THE UNIVERSITY *of* EDINBURGH

Numerical modelling of unbonded post tensioned concrete structures in fire including explicit modelling of creep in prestressing steel tendons

James Lee

For the consideration of the degree title Doctor of Philosophy

UNIVERSITY OF EDINBURGH

2016

Lay summary

Unbonded Post Tensioned (UPT) concrete structures are generally large, multi-storey, open plan buildings, typically used for offices. These structures consist of concrete floor slabs supported by concrete columns. Concrete is weak in tension, when stretched, but strong when compressed. Support is therefore required for the base of concrete floor slabs, where they are stretched, due to bending under the loads placed on the floor. UPT concrete structures include high tensile steel cables, known as tendons, placed through greased ducts which are cast into the concrete slabs during construction as a means of support. These tendons are anchored at one end of the slab and then pulled and fixed against the opposite end. This squeezes the slab and reduces how much it can bend under floor loads. It also means that the slabs can either be longer, thinner or carry more load than regular concrete slabs. When the base of a UPT concrete floor slab is exposed to a fire the steel tendon inside will heat up and then cool down as heat penetrates and then leaves the slab. The temperature the tendon reaches depends on the amount of concrete between itself and the base of the slab as well as the duration of the fire. Steel, when heated, loses stiffness, its breaking strength reduces and its elastic behavioural yield force also reduces. If a steel cable breaks the compressive support it provides to the slab is lost and the concrete slab will be exposed to greater tensile stretching forces, which may in turn cause it to crack excessively and possibly snap in places. As a result of this UPT concrete structures must be designed in accordance with European design codes which specify how much concrete must be cast below the tendon duct to protect it from dangerous temperatures. When the temperature in the steel becomes high enough such that the tendon can no longer behave elastically its breaking strength can however continue to reduce with time, even if the temperature remains constant. This phenomenon is known as *creep*. The European design codes do not give any information on how to design a UPT concrete building to withstand the effects of creep in steel tendons. Through a progressive computational modelling study, beginning with the modelling of an isolated steel tendon, this thesis explores methods to consider creep in steel tendons within UPT concrete structures exposed to fire. It is however not clear whether the effects of creep in steel tendons within a UPT concrete structure could significantly increase the likelihood of a structural collapse during a realistic fire scenario. Having identified a method of accounting for creep and validated this against experimental data, a UPT concrete slab followed by a complete UPT concrete structure are modelled to assess whether creep in the steel tendons does increase the likelihood of a UPT concrete slab breaking. This is achieved through comparing the degree to which a UPT concrete slab bends when exposed to fire if the steel tendon is modelled according to European design codes, without consideration of creep, versus models where creep is explicitly considered in steel tendons. Two different manufacturing standards of steel tendon are considered, to see if one is more susceptible to creep than the other. The outcomes of this study show with respect to one particular manufactured standard of steel, creep can be significant and increase slab bending during a 90 minute fire by 9% when the tendon is protected from the fire by 3cm of concrete. This is compared to the case where creep is not explicitly considered within the steel tendons. The other manufacturing standard of steel however shows a high resilience to creep. UPT concrete slabs using this standard of steel do not show a significant increase in bending even when exposed to a 120 minute fire with 2.5cm of concrete protection to the tendon.

Declaration

It is hereby declared:

1. All work contained in this thesis has been solely carried out by the author.
2. This work has not been submitted for any other degree or professional qualification

Signed:

JAMES ALISTAIR LEE

Abstract

Due to the unbonded nature of tendons to the slab within Unbonded Post Tensioned (UPT) concrete structures, tendon stress relaxation under heating affects all regions of the slab spanned by the tendon; not just in the locality of the fire. The numerical modelling of bonded and unbonded post tensioned concrete structures in fire has been performed to some degree, notably by Bailey and Ellobody. The consideration of elevated temperature creep to the relaxation of tendon prestress however, has not been considered. This thesis attempts to incorporate a uniaxial creep strain rate function of stress and temperature into the commercial FE software package Abaqus, compatible for use within the in-built multiaxial metal plasticity constitutive framework. What follows is a validation study of the Harmathy's uniaxial creep strain accumulation function via the modelling of stress relaxation in isolated, tensioned and heated prestressing steel tendons, against experimental data. From here, UPT concrete slab models are analysed whilst exposed to a standard fire temperature-time curve and subsequently allowed to cool. Tendon prestress relaxation and resulting UPT concrete slab deflection is compared, where tendon creep is explicitly modelled, as opposed to implicitly covered by Eurocode 2 determined temperature dependent stress-strain curves. Following this, a large scale continuous one-way spanning UPT concrete structural model is developed to consider global structural behaviour resulting from localised fire, where realistic boundary conditions such as beam rotation and deflection are permitted. The ignorance of explicit elevated temperature creep consideration, in prestressing steel tendons, is commonly justified through the implicit accountability stated within Eurocode 2 temperature dependent stress-strain curves. This however is not completely true; Eurocode 2 states implicit accountability only holds should the tendon be heating at a rate within the bounds of 2^{o}C/min to 50^{o}C/min. Where only heating of a UPT concrete slab is considered, evidence from this thesis suggests Eurocode 2 determined stress-strain curves can implicitly account for accumulated creep strain up to limited temperatures. Prestressing steel tendons are however embedded within a concrete slab through which thermal gradients build up during fire. This means heat transfer can continue to the tendon, increasing its temperature post-fire at an ever decreasing rate until it reaches its peak. Should post-fire cooling behaviour not be considered, continued tendon heating and subsequent creep strain accumulation will be ignored. Further, during the transition from heating to cooling within the tendon, it will be exposed to elevated temperatures with a rate of change below 2^{o}C/min, whereby Eurocode 2, as stated cannot implicitly account for creep. It is shown, a significant degree of subsequent relaxation of prestress, UPT concrete slab deflection and concrete damage in hogging can occur during this phase of post-fire behaviour, where the tendon temperature peaks during its transition from heating to cooling. In order to justify non consideration of creep, it should be shown tendon temperature will remain suitably low throughout the entire heating-cooling regime to which the UPT concrete slab is exposed. This must be achieved through adequate specification of minimum concrete cover to tendons to limit tendon temperature exposure for a given parametric fire curve duration, including the potential continued rise post-fire. Evidence within this thesis identifies 350^{o}C as a critical temperature whereby the explicit consideration of tendon creep does not significantly increase predicted prestress relaxation and subsequent UPT concrete slab deformation, compared to implicit creep consideration from Eurocode 2. The manufacturing standard to which prestressing steel

tendon strands are produced has been shown experimentally by Gales to significantly influence their susceptibility to elevated temperature creep. This is reflected by Gales determining differing creep parameters as a function of stress for incorporation in Harmathy's uniaxial creep strain function. Modelled prestress relaxation of isolated, tensioned and heated tendons within this thesis is therefore significantly reduced when tendons are manufactured to a yield stress of 1860MPa according to the BS 5896 standard, as opposed to the ASTM A416 standard. As a result Eurocode 2 determined stress-strain curves implicitly account for accumulated creep strain during heating, at 10^{o}C per minute, up to approximately 400^{o}C for grade 1860 ASTM A416 manufactured tendons and 500^{o}C for grade 1860 BS 5896 standard tendons. The aforementioned critical temperature of 350^{o}C does not in actuality apply to necessary explicit creep consideration for UPT concrete slabs modelled with grade 1860 BS 5896 standard tendons. This temperature however remains a design temperature limit, owing to the potential onset of microstructural recrystallization beyond 400^{o}C and the associated degradation of mechanical properties that coincides. The reasons for such differing elevated temperature creep and stress relaxation behaviour between the two manufacturing standards of prestressing steel wires and strands has been postulated within this thesis to be due to differing chemical compositions. This relates specifically to large relative differences of phosphorus and sulphur found in wires manufactures to each standard as tested by Gales.

Table of Contents

Table of Figures

1. Introduction

The main purpose of this thesis is to explicitly model the effect of creep in prestressing steel tendons on the structural behaviour during fire of Unbonded Post Tensioned (UPT) concrete structures. Owing to the unbonded nature of the tendon-slab contact, elevated temperature stress relaxation can reduce tensile support and slab compression over the entire continuous span covered by the tendon. Therefore a localised fire may have non-local consequences. Creep has the potential to contribute significantly to the inelastic strain accumulated within the tendon; as the tendon is essentially fixed in length this manifests as a relaxation of elastic strain and consequently mechanical stress. However, the consideration of creep explicitly within the elevated temperature relaxation process and within elevated temperature structural steel in general is usually ignored. This is partly due to design codes such as Eurocode 2 [1] stating that creep is implicitly accounted for in temperature dependent stress-strain curves covering elastic and inelastic domains. This makes it convenient to ignore if analysis is only focussed on the temperature rise portion of a standard fire curve. But in part creep is ignored due to a general lack of understanding of creep and a lack of realisation that it may even be a factor in elevated temperature structural steel behaviour. As a result this thesis aims to additionally provide a fundamental background to creep through describing the microscopic material mechanisms from which it emerges and the constitutive relations in place to represent it. Once a suitable means to account for creep is established compatible with numerical modelling then explicit creep models may be validated and incorporated into material definitions for prestressing steel tendons within UPT concrete structural models.

Eurocode 2 [1] provides temperature dependent reduction factors to be used in the determination of complete stress-strain curves for prestressing steel. Naturally however temperature-dependent stress-strain curves cannot account for yield state evolution with time at constant temperature (as would result due to creep). This is accepted within Eurocode 2 [1] and as such it is stated should heating rate fall out with the range $2°\mathrm{C}/min \leq \dot{T} \leq 50°\mathrm{C}/min$ creep should be explicitly considered in prestressing steel exposed to fire. Within this range stress-strain temperature dependent reduction curves are said to implicitly account for creep. No guidance is however given to explicitly consider creep. With respect to a standard fire curve, the heating rate within a prestressing steel tendon embedded within a concrete slab, bonded or unbonded, is not likely to become exposed to heating rates outside this range within a reasonable time scale. Therefore it is generally convenient to ignore the effects of creep assuming the code will implicitly cover any concern. This firstly assumes the Eurocode 2 [1] temperature-dependent reduction factors and resulting yield curves are sufficiently conservative to implicitly account for creep but, possibly more importantly, it ignores the effects of cooling. During a fire below the base of a concrete slab, thermal energy accumulates within the slab, once the fire ceases this energy is still present and thermal gradients still exist. Therefore there may be continued heat transfer within the slab towards the top as well as to the base. As such the tendon temperature profile must go through a phase of elevated-temperature exposure where the heating rate is below 2^{o}C per minute. There must therefore exist a time period, should tendon temperature be sufficient, where creep-induced tendon relaxation may compromise structural integrity, either locally or in extreme cases globally. The ignorance of cooling, particularly

post long duration fires where tendon temperature has become large, is difficult to justify. It is particularly concerning to 'conveniently' ignore cooling as a means to avoid consideration of creep.

Should Eurocode 2 [1] not be sufficient to account for transient heating elevated-temperature creep, egress times and structural fire ratings may be affected. Should cooling not be considered both short-term and long-term structural integrity post-fire may be significantly underestimated. As a result within this thesis it is aimed to:

1. Present an overview of creep from an internal behavioural perspective and present the constitutive model and relations used to represent this behaviour.
    a. This aims to inform a general understanding of creep in metals particularly related to steels to the reader and those who wish to account for creep.
2. Determine whether Eurocode 2 [1] inelastic stress-strain curves can implicitly account for creep during transient heating as stated (within the $2℃/min \leq \dot{T} \leq 50℃/min$ heating range).
3. Ascertain an accurate means of explicitly accounting for creep in prestressing steel tendons suitable to numerical modelling of structures.
4. Compare the effects on UPT concrete structures of neglecting to explicitly account for creep, particularly if cooling is considered.
5. Present any additional structural behaviour data of relevance resulting from detailed models of one way spanning UPT concrete structures exposed to fire.

The first two working chapters (Chapter 2 and Chapter 3) of this thesis focus exclusively on point one above; providing a general understanding and description of creep in metals. This is of great importance to understand situations where creep may be of concern in structures and provides a basis from which to begin accounting for its effects. The remaining chapters present a modelling study using information from the first two chapters as a basis to determine a function to account for creep in prestressing steel tendons. The verification of this function provides a means to explicitly model creep in prestressing steel tendons in larger UPT concrete structural models. From this point numerous possibilities arise with respect to potential modelling studies directed to contribute to the understanding of UPT concrete structures when exposed to elevated temperatures. As part of the validation study of an explicit creep model, the accuracy of Eurocode 2 [1] inelastic stress-strain curves to implicitly account for creep is also explored.

A more detailed overview of the structure and flow of this thesis will be introduced shortly; firstly however a brief history of UPT concrete construction is presented, highlighting the concerns over fire safety that in large part are the driving forces behind this thesis. The structural and architectural benefits that make them such a popular choice of building today are also presented as a means of highlighting the importance to ensure their integrity during fire. Following this an overview and introduction to creep is presented including reasons for its neglect and current state of understanding. This includes reasoning for the increased collaboration between material experimentation, larger scale experimentation and numerical modelling.

1.1 UPT concrete structures; a history of construction and fire safety

UPT concrete slab structures are an extremely popular means of construction of multi storey buildings such as offices, car parks, apartment buildings and transfer structures in modern times. Having first appeared in the 1960's [2] the use of Post Tensioned (PT) slabs either bonded or unbonded is now commonplace. This statement is applicable to North America, Australia, the Middle East and the UK, or indeed any established or upcoming area of commerce. In California it is the number one choice for concrete floors ([3]). The use of modern formwork systems reducing floor construction cycle times makes this type of construction far easier to implement than in the past. Therefore in addition to the many structural and architectural benefits that will be listed below it is also highly useful to the client wanting quick construction times with quicker occupation of the building.

In case of non-familiarity with this type of structure a UPT concrete slab is a concrete slab cast around hollow ducts placed within a formwork; through these ducts high-tensile prestressing steel tendons are placed. These tendons can span over multiple bays. Ducts can be positioned within the formwork to allow the tendons to take a parabolic profile within the slab once cast. In this manner they can be positioned to hog over supports and sag in the midspan; thus following the bending moment profile across the bays. Once the concrete has set these tendons are anchored at one end and tensioned against the slab at the opposite side of the span. This allows compressive stress to be applied to portions of the slab which would otherwise experience tensile bending stresses under flexural loading; crack propagation can then be reduced and the effective load-resisting cross-sectional area can be increased.

If required, additional standard reinforcement may also be placed within the formwork; the more steel tendons used the less reinforcement that is required. Internal spans may sometimes be specified without any additional sagging reinforcement. In one-way spanning structures it would always however be necessary to include some transverse reinforcement and depending on eccentricities across the supports, most likely hogging longitudinal reinforcement. As hogging spans are generally smaller than sagging spans, tendon eccentricities with respect to the top surface of the slab are usually significantly larger than their sagging counterpart, meaning a smaller ultimate moment. The tendon is anchored at either end of the span of a series of continuous spans and post tensioned (i.e. tensioned once the concrete has been cast and reached a suitable strength) to apply a compressive stress to the slab. This compressive stress however produces tensile lateral stresses within the concrete in proximity to the anchors, and as such bursting reinforcement must also be placed within the slabs at anchored ends. Within sagging regions the axial compressive stress created through the slab by the tendons helps move the neutral axis towards the base of the slab under bending reducing the tensile region within the concrete. Therefore greater loads can be accommodated, or a longer span at a given deflection or load. Alternatively thinner slabs may be used for a given deflection or load.

A tendon typically consists of a strand consisting of seven high tensile yield prestressing steel wires helically woven around one another with strand diameters typically within the range of 9mm to 15mm. As the unbonded term suggests the tendons are not bonded to the sheath within the duct. The duct is lubricated, allowing relative longitudinal motion between the tendon and the sheath and

thus the concrete slab. There will inevitably be some frictional resistance, but this should be minimal owing to the lubrication.

Within two-way spanning slab structures punching shear capacity is increased through hogging the tendon over the supports in both dimensions of the slab plane. Thus the flexural strength and punching shear capacity of a concrete slab can be much increased for a given depth of cross section. Through control and specification of the degree of post-tensioning it is possible to gain a high degree of control over the amount of deflection and cracking within a slab across its span.

1.1.1 Structural and Architectural benefits

Structurally, UPT concrete slabs can reduce cracking and crack propagation. They can increase shear and punching shear capacity and reduce deflections. This means greater spans can be covered by a slab and/or slab depth can be reduced. The main advantage therefore of UPT concrete slabs is the increased span-to-depth ratio possible with this type of construction.

From a structural performance perspective this can allow fewer columns, allowing larger spans and thus fewer foundations. A reduction in building height is possible through a reduced floor depth, or alternatively an extra floor may be possible over a standard ten-storey structure [3]. The structure as a whole may also be lighter due to the thinner slab depths, which reduce the overall dead load being transferred to the foundations. It is also possible to integrate services into ducts cast into the slab, and therefore increase the ceiling height.

The architect or designer can then exploit this type of structure to create large open-plan column-free spaces to be partitioned however the client wishes. Light penetration can be maximized and passive solar gain strategies optimized.

1.1.2 Safety concerns

Despite numerous tests in North America in the 1960s there is still a large gap in data and knowledge of the true structural behaviour of UPT multibay concrete slab structures in fire. A range of noted case studies, including a fire in Bangkok in 1987, two fires at Parmelee elementary school in California in 1965, and a fire at Kearney plaza, Portland, Oregon in 1999, have prompted a drive for more research into the performance of UPT structures in fire amongst certain authors [4]. In the first two cases localised concrete cover spalling led to tendons being locally exposed to fire, resulting in tendon rupture in the first case. A further case study of a UPT concrete slab exposed to fire in Tel-Aviv in 2000 has also been reported, where a tendon ruptured after concrete cover spalling directly exposed a tendon to fire [5].

Case studies such as these highlight the concern that has led to the aim of this thesis, namely understanding and modelling the effect of temperature on cold-drawn steel tendons in UPT concrete slabs. As mentioned above a tendon may span multiple bays of a structure, therefore a

localised fire can lead to global issues if significant damage to tendons occurs. The advantage of computational modelling in this context is the ability to perform parametric studies to highlight potential differences and the consequences of underestimating the effect of creep on tendon stress relaxation.

Typically in standard reinforced concrete slabs, building codes such as Eurocodes or British Standards prescribe a minimum concrete cover to the steel reinforcement. Generally UPT concrete slab construction will adhere at least to these guidelines with regard to providing cover to steel tendons. However the use of modern high strength concretes, and the possibilities for substantially thinner concrete slabs afforded by this and UPT construction raise issues that have not yet been adequately addressed in codified design relating to fire. The main issue is quite possibly the increased likelihood for spalling in high-strength concretes, exposing tendons directly to fire.

The main issue regarding the localised exposure of a tendon to fire or an elevated temperature is the loss of tensile stress in the tendon. This loss, as alluded to earlier, can then span the entire tendon length leading to load redistribution throughout the entire span. In the extreme case this loss of relaxation of tendon stress may lead to tendon rupture, if the tendon relaxes such that grain growth leading to tertiary creep (Section 2.2.4) is facilitated.

Current design codes such as Eurocode 2 [1] state that details provided pertaining to prestressing steel are valid within heating rates of 2^{o}C to 50^{o}C per minute; outwith this range factors such as creep should be explicitly considered. This implies that creep will be implicitly accounted for within that heating range. The concern here however, is that these curves will be used to implicitly account for elevated temperature creep outside of this range. Of further concern is the ignorance of the effects of cooling and the transition from heating to cooling within tendons. It is during this phase of thermal exposure where creep could be a significant contributor to the relaxation of tendon prestress. This ignorance could potentially result in far greater stress relaxation within operational prestressing steel tendons than predicted; the consequences being an overestimation of structural integrity and load capacity in fire conditions (and post-fire). Any loss of tendon stress due to creep strains are irrecoverable, therefore on cooling the structure may be permanently weakened along the length of the tendon and anywhere else that has sustained structural damage due to underestimated load redistribution.

1.2 Creep

Part of the reason that the consideration of creep in certain elevated temperature structural situations is neglected may be due to a general lack of understanding of the phenomenon and a lack of realisation that it may even be a factor. As relatively little guidance exists on its effective consideration in steel at elevated temperatures, it is necessary to present an overview of available literature and information on how to account for creep. There is however a greater understanding of creep, documented within applied material science, plasticity and mechanics journals and literature, than most structural engineers realise. Much of this literature describes mathematical material models based around previous experimentally observed yield response data. The most mathematically concise way to formulate this data into a multiaxial framework to quantify material

yield response generally involves the use of tensors and tensor calculus. The reader quickly becomes bombarded with equations containing multiple indices and mathematical terms relating to tensor analysis and vector spaces. Much of this mathematics is previously unheard of to the standard structural engineer taught to think in linear elastic terms. As such much of this information regarding creep and plasticity in general is inaccessible to the typical structural engineer, and in many cases there is no knowledge of its existence. In actuality a firm constitutive model and framework to account for, and quantify, creep deformation over time in three dimensions exists as an extension of general classical plasticity frameworks such as the Von Mises framework. The main input required into such a model is a function determining the norm or magnitude of the creep strain rate. This is a uniaxial creep strain rate function through which using a deviatoric stress (rather than a directional stress) such as the Von Mises stress (which effectively represents the norm or magnitude of the deforming stress component) then represents the magnitude or norm of the deformation rate. With respect to classical plasticity, temperature-dependent stress-strain curves exist for a wide range of metals and steels, negating the need to understand either the internal material mechanisms or constitutive relations governing plastic behaviour. For instance from a computational modelling perspective a multiaxial constitutive framework is usually in-built within commercial Finite Element (FE) software packages, and as such the user is only required to input a stress-strain curve. With respect to creep however whilst a constitutive model and framework exists the equivalent stress-strain curve to input does not. In place of the standard temperature-dependent elastic-plastic stress strain curves the aforementioned definition of a uniaxial creep strain rate function is required. This may then effectively represent the creep strain rate norm or magnitude should a deviatoric stress such as the Von Mises stress be used. However these functions are generally very specific to the type of material and very sensitive to stress, temperature and strain rate bounds. As such these uniaxial functions have largely to be determined experimentally, relating to the specific case required for analysis. In this regard it may be viewed that within applied physics the experimental and mathematical work has already been done in determining a general multiaxial framework for structural and mechanical creep analysis. The final piece of the jigsaw has however been, and has to be, left to the structural engineer and the specific case they are analysing; this being to determine a uniaxial creep strain rate function of various external and internal variables relating to the material and structural case of interest. There are relatively well-documented empirical uniaxial relationships between stress, temperature and what is known as secondary creep strain rate resulting from experimental observation. For these relationships to be useful in a specific situation the specification of various constants is required which can only be determined from experimental data. This is generally the area missing in being able to account for creep; the understanding of the requirement for uniaxial creep strain rate magnitude functions specific to the material of concern and appropriate constant determination. It should be noted however that work has recently been done in this area by Gales [6] and to a certain extent many years ago by Harmathy and Stanzak [7] with respect to prestressing steels. As the function of use defines creep strain accumulation including primary and secondary creep (to be covered in Chapter 2) rather than strain rate at a given time they appear rather complicated at first glance, and do not easily fit within a constitutive framework. On differentiating with respect to time and rearranging however they reduce and simplify dramatically towards the generally observed empirical relationships and fit well within the multiaxial constitutive model. Their data and functions will be elaborated within both parts of this thesis and converted and presented within a more user friendly framework (strain rate form) with respect to numerical modelling and consideration of creep in general.

To many, the importance of the internal material and constitutive theoretical background detailed within the early part of this thesis may seem redundant. Of sole importance, it may be thought is the description of a blind function including necessary caveats and means to account for creep, covering as many specific cases as possible; the theoretical and experimental basis to this function is less relevant. On the surface this seems perfectly acceptable; after all the main concern of this thesis is the consequences of creep in prestressing steel tendons on UPT concrete structures, not the material process of creep. However in this case it would not be possible to understand the effect of creep in prestressing steel tendons or in structural steel in general and wider structural consequences; merely to quantify and hope all bases are truly covered. For example the internal material evolutions of steel with accumulating creep strain can have significant effects on long-term behaviour and structural integrity; yield state and ductility are significantly altered. Understanding of a phenomenon allows the prediction or anticipation of potential problems, it allows the understanding of when creep may and may not be an issue. It also provides a basis for developing means of accurate quantification. Attempting blind quantification in the absence of understanding often leaves an increased degree of exposure to unforeseen problems. The awareness of these problems, their solutions and prediction is then developed from hindsight not foresight.

The modern day tools available to the structural engineer with respect to large-scale and small-scale material experimentation coupled with computational modelling capabilities should make understanding of complex structural behaviours ever more possible. It does however appear that there is still little collaboration between these three, in a concise manner, to get to the route of a particular behaviour. Understanding internal material behaviour allows the understanding of how a material will behave at yield with respect to stress and temperature. Numerical modelling incorporates material models developed around experimental observations of material yield behaviour. These models allow the visualisation of principal stress and principal strain directions which can inform as to how a structure may deform and fail. Large scale experimentation can provide far more accurate quantification of these mechanisms and statistical variation. Numerical modelling outcomes can allow streamlining of experimentation and narrowing of applied boundary conditions in the light of observed behaviour. All three then fit together and contribute to developing concise and much more cost effective means of researching and understanding structural behaviour.

1.3 Thesis structure and flow

The structure of this thesis is based around presenting and addressing the objectives listed at the start of this introduction. The importance of ascertaining a general understanding of creep has been described earlier in this introduction, this understanding is essential if it is desired to anticipate when creep may be of concern and understand its implications. Chapter 2 therefore describes the internal microstructural behaviour in metals giving rise to external time evolving creep deformation and how it is influenced by stress and temperature. This understanding should allow an assessment to be made as to when creep may and may not be of concern in a structural steel fire situation. From this point forward the means to account for creep is presented and described. As was detailed in the previous section a constitutive uniaxial model and multiaxial framework providing a means of

analysing creep from a continuum perspective is well established. This framework describes the constitutive relations between the norm (magnitude) of the creep strain rate and multiaxial creep strain rate (the creep strain rate tensor). The constitutive model and relations are presented in Chapter 3, highlighting the role of the engineer to determine and provide a uniaxial creep strain rate function compatible with the constitutive framework. Towards the end of Chapter 3, once the constitutive model and multiaxial framework have been clearly defined, commonly observed empirical relationships between creep strain rate, stress and temperature (as well as accumulated plastic strain in some cases) are described. These may be fitted to experimental data to determine constants specific to the situation. It should be noted, commonly used inelastic temperature dependent stress strain curves are based on experimental data with suitable factors of safety applied for use in design situations regarding element sizing for example. It may be prudent to expand this to experimentally define and determine constants within the bounds of trusted empirical uniaxial creep strain rate formulations for use when creep may need to be explicitly considered. Chapter 3 culminates by presenting the Harmathy [8] uniaxial creep strain representation with which constants specific to various types of prestressing steel have previously been determined [6] [7]. Converting this representation to strain rate form reveals similarity to common empirical relations and ensures compatibility with the established multiaxial constitutive framework. Chapter 2 and Chapter 3 are largely dedicated to covering the first objective listed at the start of the introduction. These chapters set the basis for understanding what creep is and how to potentially account for it. The remaining chapters primarily focus on presenting a modelling study based around addressing the remaining points.

Chapter 4 presents modelling studies addressing the second and third objectives listed at the beginning of this introduction. Experimental stress relaxation data for prestressing steel tendons obtained from tests performed by MacLean [9] is used throughout this chapter. As such, there exists a set of data that may be used as a benchmark for both Eurocode 2 [1] temperature-dependent inelastic stress-strain curves and an explicit creep model as material input data within relatively simple FE models replicating the experiments. It should be noted that all FE models are developed and analysed using the commercial FE software package Abaqus. Firstly, relaxation models are performed using the Harmathy creep strain rate function and derivatives. The purpose of this being to validate an explicit uniaxial creep strain rate function for future inclusion within the material definition of prestressing steel tendons in large scale UPT concrete structural models (Objective 3). This has the added benefit of providing a means of demonstrating the contribution to relaxation of tendon prestress that creep may make during both transient and steady state heating. Following this models are performed using only Eurocode 2 [1] inelastic stress-strain data tabulated as a function of temperature within the tendon material definition. This addresses Objective 2; determining whether Eurocode 2 [1] inelastic stress-strain curves can implicitly account for creep during transient heating as stated (within the $2℃/min \leq \dot{T} \leq 50℃/min$ heating range). Next, a comparison of predicted tendon prestress relaxation, with respect to tendons produced according to ASTM A416 [10] and BS 5896 [11] manufacturing standards is presented. In turn, the predicted stress relaxation from these models is compared to the predicted stress relaxation using Eurocode 2 [1] derived stress-strain curves, implicitly accounting for creep. From here, an analysis of the contribution that primary and secondary creep phases make to the overall deformation, and within what temperature ranges they are relevant is performed. The potential significance of this analysis

will emerge through Chapter 2, with respect to the material processes at large and their effects on material integrity.

Following the validation of a uniaxial creep strain rate function large-scale UPT concrete structural models including creep as an explicit part of the prestressing steel material definition are developed. Chapter 5 focusses on ascertaining the consequences of neglecting to account for creep in the analysis, design and determination of fire ratings in UPT concrete structures (Objective 4). Unfortunately, due to time constraints this analysis is limited to isolated UPT concrete slab models. A large range of minimum concrete covers to tendons and standard fire durations are considered as part of a comprehensive parametric study on this matter. Very importantly complete cooling of the UPT concrete slabs has been modelled. Thus structural behaviour during phases of elevated-temperature low-transience tendon exposure can be considered and the explicit effects of creep-induced relaxation clearly visualised. Prestressing steel tendons manufactured to two alternative institutional standards are considered within these slabs; ASTM A416 [10] grade 1860 prestressing steel, on which MacLean's experiments were performed, and BS 5896 [11] prestressing steel. Experimental data exists for both types of prestressing steel with respect to transient creep tests by Gales [6]; this data is used to assist accurate modelling of creep.

Following the modelling of isolated UPT concrete slabs a generic one-way spanning UPT concrete structural model has been developed within Abaqus. The development and analysis of this model forms the content of Chapter 6 addressing the final objective listed at the beginning of this introduction. Utilising symmetry only a quarter of this structure has been modelled, reducing computation. Given time constraints the number of parameters modelled on this structure has also been limited. The main focus of this chapter is therefore on addressing the concerns and limitations arising from the UPT concrete slab models of the previous chapter. Naturally when structural elements are isolated for the purposes of experiment or modelling, recreation of realistic boundary conditions and accountability of load transference effects to other parts of the structure are not possible. Chapter 6 then focusses on determining and analysing areas of potential structural failure and damage within a realistic structure when fire is incident on a section of the continuous slab base; creep is explicitly modelled in prestressing steel tendons throughout. These models are particularly detailed, as with the isolated UPT concrete slab models quadratic continuum elements have been used to model the continuous slab behaviour. This allows out-of-plane effects that may be expected to occur in the vicinity of columns to be modelled. This type of element is particularly useful for modelling bending in general, due to a quadratic shape function (quadratic interpolation of internal element coordinates from nodal coordinates) allowing element curvature and shape variation. They also ease numerical convergence problems with respect to tendon-slab contact, permitting a coarser and less computationally expensive mesh. It is hoped the data resulting from this detailed analysis may inform future modelling and experimental studies with respect to UPT concrete structures and reinforced concrete (RC) structures in general.

2 Metal material microstructure and behaviour giving rise to creep

Within this section the general material microstructure of metals is explored, and its intricacies and imperfections which give rise to plastic and creep behaviour discussed. In general this is related to steel and particularly prestressing steels with respect to later chapters in this thesis. When temperature becomes an additional external variable the line between classical plasticity and viscoplasticity, commonly known as creep, becomes increasingly blurred, giving way fully to creep with increasing temperature. In fact when material mechanisms giving rise to plasticity in general are considered and explored with an understanding of temperature effects, it becomes possible to take a much more holistic view of plasticity. This chapter starts, in Section 2.1, by overviewing the material microstructure of metals in general. Ultimately it is various imperfections and irregularities within the material microstructure that are responsible for macroscopic plastic and viscoplastic (creep) behaviour. Section 2.2 overviews the internal material mechanisms involving these material defects that lead to macroscopic inelastic deformation. This includes a description of the internal base energy state of a metal created by the energy stored in all the localised strain fields formed around the various material defects and impurities referenced in Section 2.1. Following this the restoration process is discussed whereby the material goes about reducing its internal energy state through various stages of internal deformation assisted by externally applied stress and temperature. Finally classical plasticity and creep are related to the restoration process and its respective components. Section 2.3 describes the commonly observed empirical relationships between creep strain rate, stress and temperature. These form the basis for modelling and predicting creep strain rate in metals.

2.1 The internal microstructure of metals

In order to understand the material mechanisms giving rise to plasticity in metals in general, and ultimately steel, it is necessary to have an understanding of the material microstructure. Metals are often described as having a polycrystalline microstructure; this means a granular structure with each grain and subgrain consisting of a regular *crystal lattice* arrangement of atoms. A crystal lattice is an ordered, periodic, three dimensional array of atoms, spreading over multiple atomic distances [12]. Each atom is bonded to its nearest neighbours, depending on how many bonds it is able to form. Figure 2-1 shows an image depicting the typical polycrystalline granular microstructure of a metal, such as steel, illustrating grain boundary misalignment.

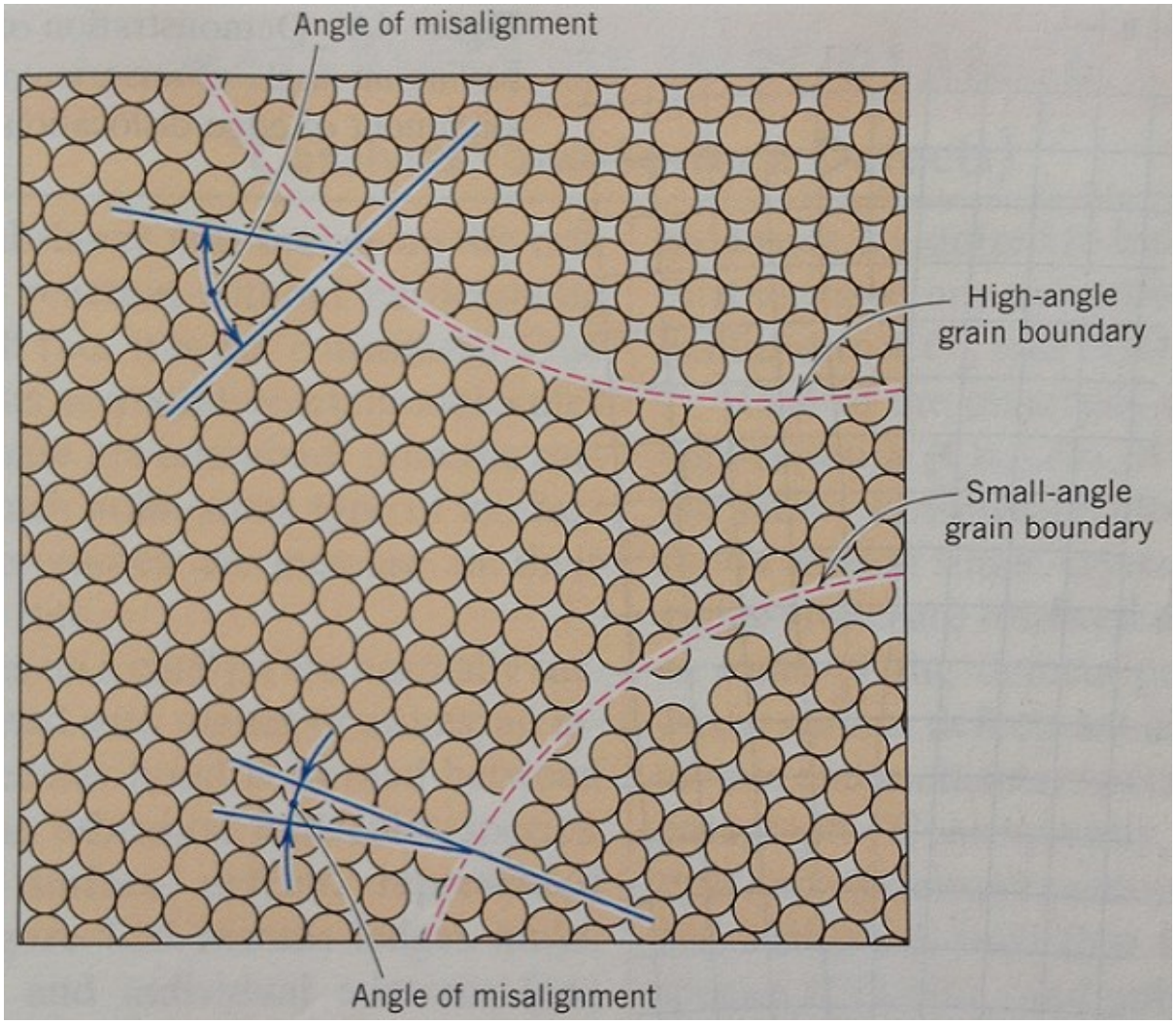

Figure 2-1; Polycrystalline microstructure of metals [12].

An alternative way to visualise such microstructures is through bubble rafts. A bubble raft consists of the creation of a layer of bubbles on a surface of a soap solution on a tray of some sort. This method of representing and visualising the microscopic behaviour of metals was developed by Sir Lawrence Bragg and J. F. Nye in 1947 [13] and has proven one of the most useful ways to this day to visualise and understand metal microstructure. A series of bubble raft images are displayed in Figure 2-2, taken from [13] and [14]. What is noticeable is the granular formation that is assumed, consisting of

regular crystalline regions of bubbles, mimicking atoms, offset at various angles from each other. The boundaries between the grains are clearly disordered. In particular, Figure 2-2c bears a striking resemblance to the surface of a metal.

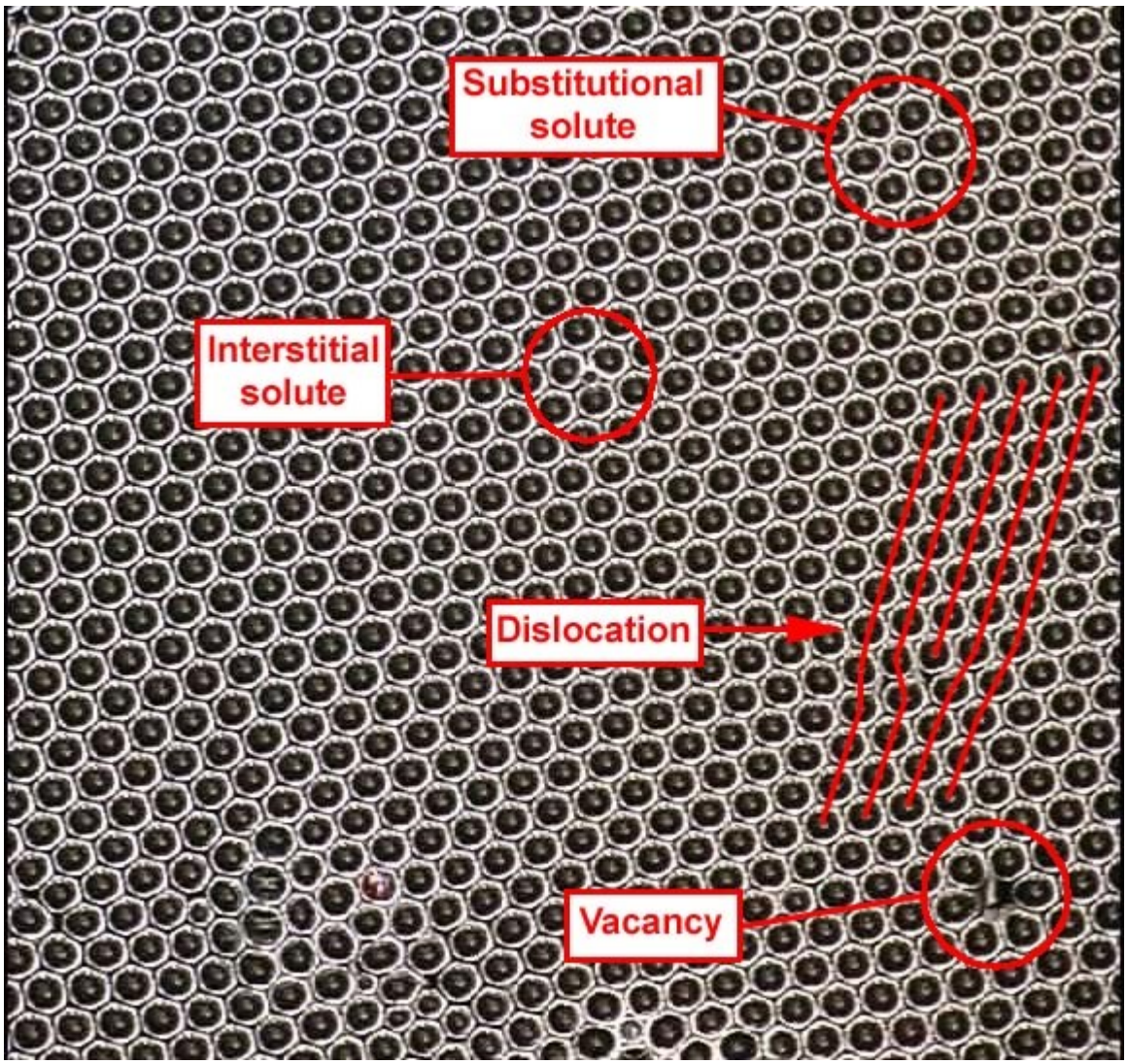

Figure 2-2; Bubble raft images [13] [14]; a) Bubble raft depicting various lattice imperfections [14]

b) Fault lines between offset crystalline regions. Vacancy upper right [13].

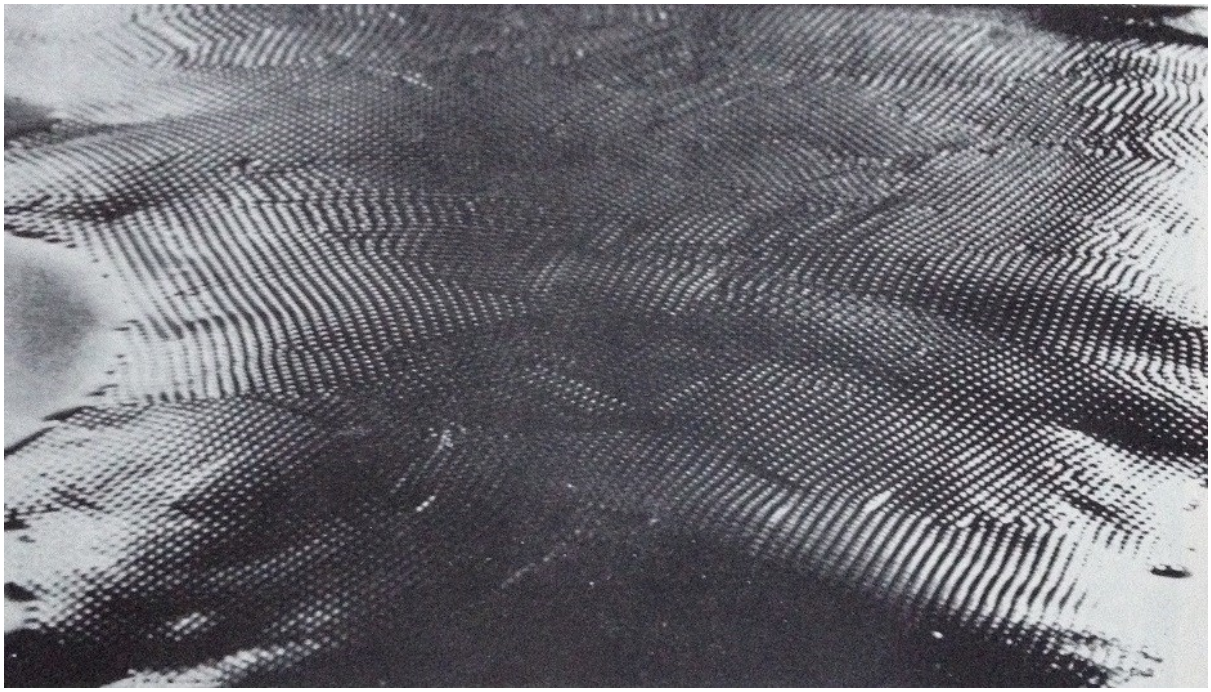

c) Oblique view of a bubble raft displaying significant similarity to a metallic surface [13].

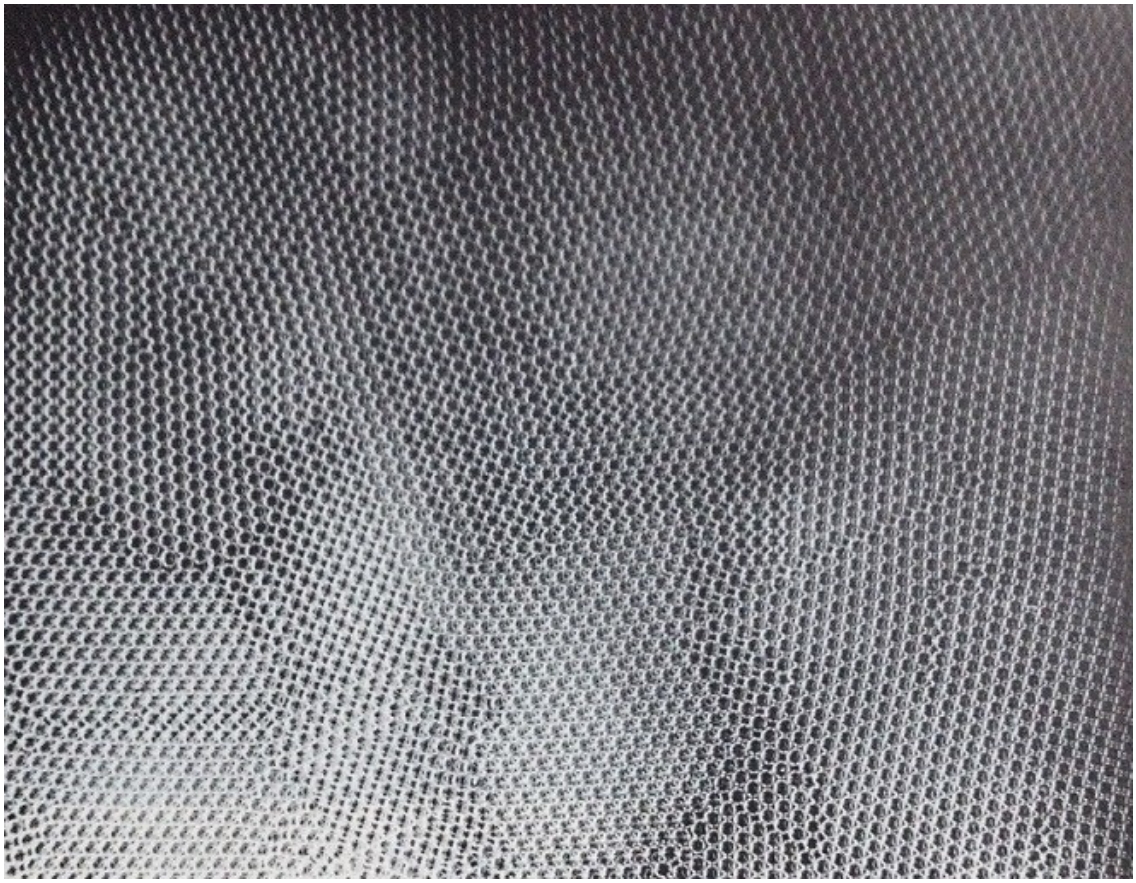

d) Normal view of a bubble raft surface; a variety of clear and vague cells and subgrains [13]

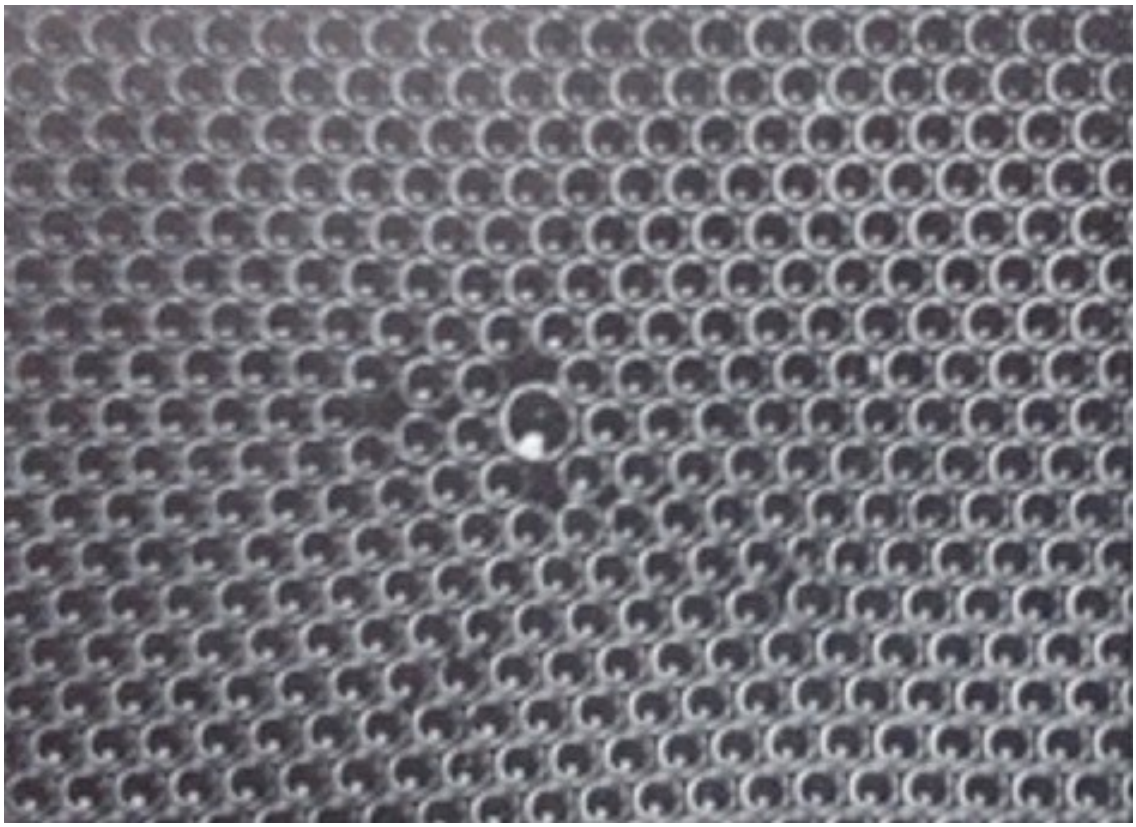

e) A larger bubble representing the effect of an impurity in a metal [13].

Imperfections can be noticed within the regular crystalline grains themselves; examples are displayed in Figure 2-2a [14]. Substitutional and interstitial solutes are essentially impure atoms (therefore different from the majority of the crystal) introduced in solution form often deliberately as alloying elements for reasons that will be outlined in Section 2.1.3. They are often found at grain boundaries if they are larger than the regular atoms where they are better accommodated, but can still be found within a lattice also [13]. Pure lattice imperfections generally fall into two categories; dislocations and vacancies, these will be explained in terms of their origins and roles in plasticity next.

2.1.1 Dislocations

A dislocation is a type of imperfection that often appears in a crystal lattice as visualised in the various images of Figure 2-2. Typically they come in three forms; *edge dislocations*, *screw dislocations* and *mixed dislocations*. In practice dislocations may bear characteristics of both screw and edge, and as such are often mixed (Figure 2-4). Figure 2-3, taken from [12], shows an illustrated example of an *edge dislocation* within a crystal lattice and its motion under an externally applied shear stress across a *slip-plane.* The dislocation is a form of gap in the lattice where a row of atoms terminates prematurely; the last atom in the row is missing a partner for its remaining bond. If an externally applied shear stress is large enough, this atom may be pushed to a point where it is closer to a fully bonded atom than another of that atoms neighbours which is fully bonded; thus the bond switches and the dislocation moves one step along the slip-plane. Typically the dislocation will then move along the entire length of the slip-plane, assuming the shear stress remains, until it either reaches a grain boundary or is obstructed by another lattice irregularity (such as an impurity or another dislocation). This motion of a dislocation along a slip-plane is known as *dislocation glide* and is responsible for the plastic strains associated with classical plasticity; this is explained in more detail in Section 2.2.3. The migration of a dislocation along the entire slip-plane results in a lattice deformation of one unit step, as noted in Figure 2-3. It can be seen in the example in Figure 2-3, the dislocation reaches the end of the slip-plane, a regular ordered crystal is realised.

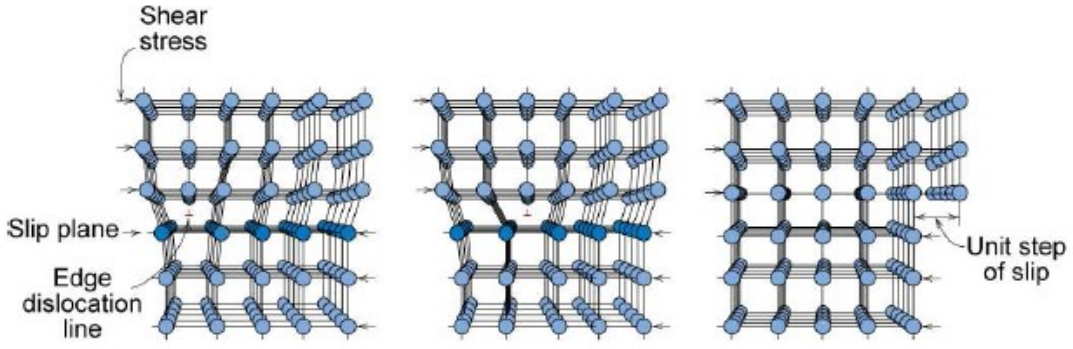

Figure 2-3; Dislocations, slip-planes and dislocation motion [12].

A screw dislocation results from a layer of atoms twisting with respect to its adjacent layer at some point. An example of this, combined with an edge dislocation, is displayed in Figure 2-4, again taken from [12]. It should be noted the motion along a slip-plane in this case is essentially the same as for an edge dislocation.

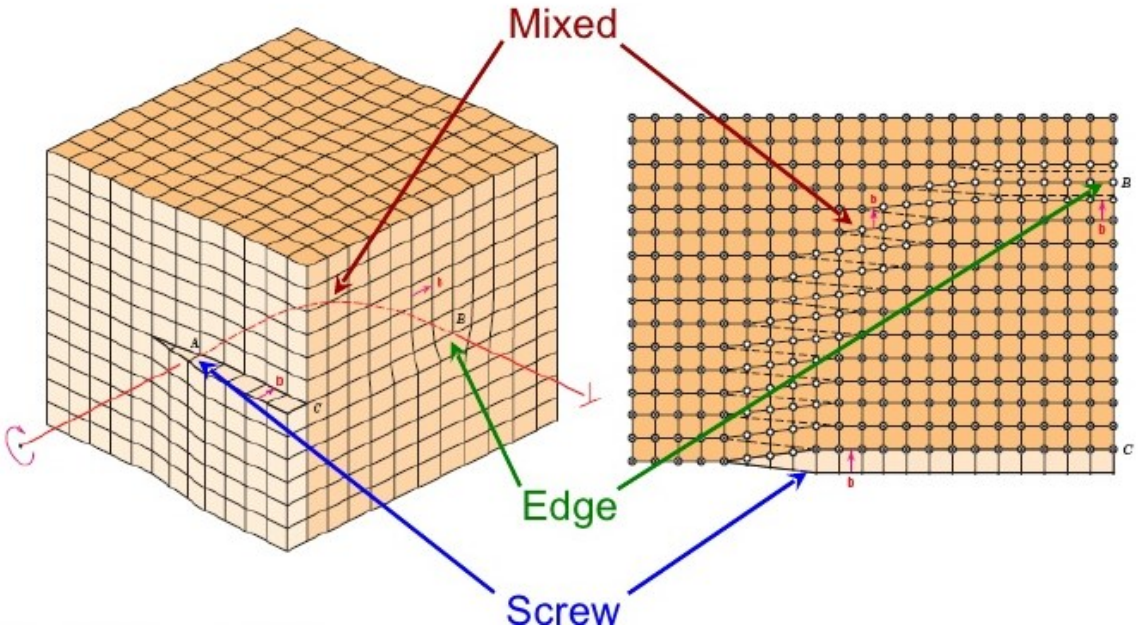

Figure 2-4; Edge, screw and mixed dislocations [12].

Ultimately motion of a dislocation across an entire slip-plane does not influence the elastic behaviour of the material. The material will be permanently deformed in its new state, but will still behave elastically below a threshold stress; the elastic behaviour being governed by the strength of the bonds between the atoms. Referring back to the bubble raft images and descriptions from Figure 2-2, it is noted that many dislocations can lie within a crystal lattice (Figure 2-2a,b,c,d) and this lattice may contain impurities also (Figure 2-2a, e). Dislocations may also have different orientations and polarities, noting that rows of atoms extend in three dimensions; thus rows may prematurely terminate in three dimensions, leaving three different possible orientations for edge dislocations within a lattice. Each row can also terminate prematurely in opposing directions or opposite polarities, leaving six possible different orientations of edge dislocation. These dislocations, when stimulated to move, may collide and *pile up*, hardening the material, or they may annihilate those of opposite polarity, restoring a row. Further to this, when impurities are added into the material in the form of different atoms, with extra or fewer bonds as precipitates or solutes, all this acts to restrict dislocation motion along a slip-plane as in Figure 2-3.

2.1.2 Vacancies

Visualisations of vacancies can be noted in the bubble raft image Figure 2-2a, and can be seen in Figure 2-5 below. The term vacancy refers to a vacant space within a crystal lattice where an atom is missing. The concentration of vacancies within a crystalline structure is noted to be strongly dependent on temperature, via an Arrhenius relationship [12] (Equation 2-1).

$$N_v = Nexp\left(\frac{-Q_v}{kT}\right)$$

Equation 2-1

In Equation 2-1, N_v represents the concentration of vacancies in a given volume of material, N represents the number of atomic sites, Q_v is the energy required to form a vacancy, k is the Boltzmann constant and T is the temperature in Kelvin [12]. When referring to creep, it is often noted in literature that the *activation energy* of creep, closely matches that of *self-diffusion* or *lattice diffusion*, particularly in *power law* creep (*power law* creep and this significance will be discussed later in Section 2.3) [15] [16]. The diffusion processes named, refer to the diffusion of species such as impurities through a solid material; an example may be the diffusion of interstitial or substitutional carbon atoms in steel (Figure 2-2a). Bragg and Nye [13] described through their bubble raft representations, that it appears that impurities, rather than moving themselves through a lattice under a disturbance to the material, will remain roughly in place while the grains and lattice re-orient themselves to accommodate these impurities at grain boundaries. They also describe the possibility that gaps in a lattice, now referred to as vacancies, may play a role in diffusion and reducing energy barriers in areas of a material around impurities. In these regions local strain fields are created through the distortion created by the impure atoms of a different size. These provide an obstacle to the motion of dislocations along a slip-plane. Thermally-induced vacancies then can assist the internal motion of dislocations and the internal restructuring about impurities. They appear to do this through a mechanism known as *dislocation climb*; the vacancy provides a vacant atomic space in the vicinity of an obstacle for another atom to 'climb' into, allowing a dislocation to effectively circumvent an obstacle and continue to 'glide'. The rate of self-diffusion of *species* referred is described by Equation 2-2.

$$D = D_0 exp\left(\frac{-Q_D}{RT}\right)$$

Equation 2-2

As with the concentration of vacancies at a given temperature, the diffusion of species through a solid is described by an Arrhenius relationship. Where in Equation 2-2, D represents the diffusion rate in m^2/s, D_0 is a stress dependant normalising constant, also in m^2/s, Q_D is the activation energy of self-diffusion in Joules per mole, R is the universal gas constant ($J/molK$) and T is the temperature in Kelvins. It should be noted that Equation 2-1 uses the molecular form of an Arrhenius relationship, whilst Equation 2-2 refers to the energy per mole. The rate of diffusion of species in a solid material, as a function of temperature, then seems to be mathematically at least, very consistent with the concentration of vacancies. Again, the significance of this and the apparent close ties between Equation 2-2 and *minimum creep strain rate* or *steady state creep strain rate,* in power law creep (when a power law stress dependence for D_0 is applied), will be discussed in Section 2.3.

2.1.3 Impurities

Examples of how impurities may lie within a lattice are illustrated in Figure 2-5. Free atoms lying within the lattice are known as interstitials, these may be pure (same atoms as the rest of the lattice but unbonded) or impure. Substitutional impurities are impure atoms substituted within a lattice for a pure atom; therefore they are bonded but may be a different size to other atoms, creating local stresses and strains within the bonds. Figure 2-5 also displays an example of a vacancy where an atom is missing from the lattice, leaving a gap or space. Lastly a dislocation can be observed in Figure 2-5, it should be noted this is an example of a different orientation to the dislocation in Figure 2-3.

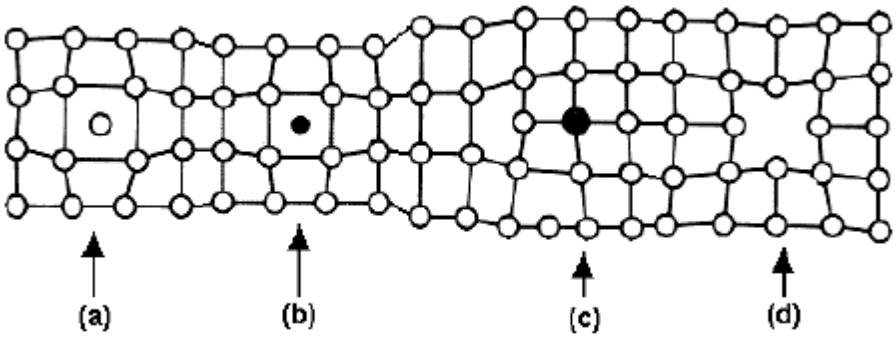

Figure 2-5; a) Self interstitial, b) Impure interstitial, c) Impure substitutional, d) Vacancy [17].

As is well known, steel is not a pure metal, it is predominantly iron alloyed with carbon, the carbon typically making up to a maximum of 2% of the mass. As a reference, high-tensile steels, used as wires in cables, are typically alloyed in the region of 0.8% to 0.9% carbon and usually also contain manganese (Mn) and/or vanadium (V). On occasion silicon (S) and/or chromium (Cr) may be used. The addition of such alloys has the effect of restricting dislocation motion thus reducing the materials susceptibility to plastic deformation; this may often come at the expense of ductility. Large impurities may often be located at grain boundaries; Bragg and Nye [13] state it is rare to find them lying within a grain. This is such that it takes less energy to accommodate an impurity at a grain boundary, where there is more space to accommodate them [13]. A material will naturally adjust, if disturbed, to find a lower energy state if possible, and as such will seek to form its granular boundaries about such impurities. Discussion of such energy reducing adjustments will take place in Section 2.2.1. The presence of an impurity of a different size (particularly larger) at a grain boundary restricts the ability for the boundaries to align under load, again restricting the ease of plastic deformation. It should be noted that it is also possible to soften a material through certain alloying.

Further to strengthening or stiffening through introducing alloyed impurities, work hardening is typically undertaken to deliberately introduce more dislocations into a metal; the more dislocations the less distance they can travel along a slip-plane before colliding and piling up with others. The result of this, as with certain alloying, is it takes far greater force to elicit a given plastic strain, but this again often comes at the expense of ductility.

It is intriguing to read the paper presented by Bragg and Nye [13] on the bubble raft model to note their postulations on observations and how accurate to representing metals they really appear to be. For instance, the vacancies noted in Figure 2-2a and Figure 2-2b; at this time they are not labelled vacancies; it is postulated that they may well exist in metals also and that they, 'may play a part in processes such as diffusion or the order-disorder change by reducing energy barriers in their neighbourhood, and act as nuclei for crystallisation in an allotropic change' [13]. Such a statement appears to be very accurate. With respect to creep their role in reducing energy barriers in their neighbourhood, as will be elaborated on shortly, seems to be the main mechanism initiating elevated temperature creep in metals.

2.2 Inelastic deformation in metals

Within Section 2.2 the role of the microstructural defects described in Section 2.1 with respect to inelastic material deformation and ultimately creep is presented. Externally applied stress and thermal conditions, through mechanisms that will be discussed in Section 2.2.2, allow these defects to be gradually eliminated. This in turn removes the localised strain fields around such defects and releases the internal energy stored within them. The microstructure also tends to also re-orient itself such that interstitial impurities are accommodated at points where localised stress and strain fields are minimised; this again minimises the intrinsic internal energy state of the metal.

It is the process of a metal seeking to reduce its *internal* or *base* energy state under external stress and/or temperature that gives rise to global inelastic deformation. As such the concept and the roles of dislocations, grain boundaries and impurities in influencing a metals base energy state are discussed firstly in Section 2.2.1. The microstructural evolutions and processes which are permitted in metals when stress and/or temperature is applied, allowing internal energy state reduction, are then discussed in Section 2.2.2. This material process is known as *restoration*, whereby the material seeks to restore a uniform regular crystal lattice throughout its entirety.

Both classical plasticity and creep relate directly to internal energy state reduction and the restoration process. Classical plasticity can be related to the early stages of the restoration process and is discussed in Section 2.2.3. Creep is often referred to as consisting of three phases relating to the evolution of strain rate with time; these are known as primary, secondary and tertiary creep. These three phases relate to the various stages across the entirety of material restoration and are discussed finally in Section 2.2.4. Both classical plasticity and creep relate to the restoration process and internal energy state reduction. It is however the influence of temperature that permits the restoration process to continue beyond its early stages and significant time evolving inelastic creep deformation to occur.

2.2.1 Internal energy states; 'reducing material base energy state'

The process of a metal seeking to reduce its internal energy state ultimately results in creep under appropriate external loading and thermal conditions. In Figure 2-2a, it is possible to notice distorted bubbles, most noticeably in the bottom left. These distortions, to their otherwise circular shape, build up from distortion of the crystal lattice around irregularities, impurities, dislocations and grain boundaries when the rafts are tightly packed. A bubble in a regular crystal region under no external force may experience no physical stress. In a distorted region, around dislocations or impurities or other lattice irregularities, it may be elongated through a combination of compression and stretching. This means it is experiencing a local stress field which is inducing a local strain field upon it and its neighbours that does not exist in other parts of the raft. As a result there exists a stress gradient between these local regions, extending in all directions to the unstressed or uniformly stressed regions. Stress gradients result in forces; if the raft is settled and there is no internal motion the forces within these local stress fields must be balanced by equal and opposite forces. If it is imagined that the obstruction creating the local stress field is removed but the bubbles are held in their distorted form by the application of a fictional force, then there is work done in maintaining this distortion. The force applied to maintain the distortion multiplied by the magnitude of the distortion, equals the energy or work done (work = force x distance). This imaginary work is equal to the energy stored in these local strain fields associated to these distortions. In a metal at rest, the internal or base energy state then can be defined as equalling the sum of the energy stored in all these local strain fields associated with all these internal forces. This internal energy state then represents a form of potential energy associated to the material. The first law of thermodynamics relates internal energy to heat and internal work as Equation 2-3

$$\Delta U = Q - W$$

Equation 2-3

In Equation 2-3, *ΔU*, represents the change in internal energy, *Q*, represents the thermal energy and *W*, represents the work either done internally by the system on its surroundings or vice versa. The various defects outlined previously (impurities, dislocations, grain boundaries, etc) are often described as *energy barriers* against the motion of dislocations, as extra energy is required to allow passage through or around the local strain fields they create. Therefore in an adiabatic environment (no exchange of thermal energy, *Q*), an increase in work internally, to allow a dislocation to overcome an energy barrier, must be associated by an equivalent decrease in internal energy. Similarly, again in an adiabatic environment, if a materials internal energy state is somehow reduced, *ΔU* becomes negative, and work is done by the material on its surroundings. This work will induce material deformation. When a dislocation moves, this is a permanent plastic deformation, as has been described in Section 2.1.1. Internal work must have been done to elicit this plastic deformation; this results in a reduction of internal energy. Conservation of energy during material motion can be expressed through Equation 2-4 [18].

$$\frac{d}{dt}\int_V \rho U dV = \int_S \underline{\tau} \cdot \underline{\dot{X}}\, dS + \int_V \underline{f} \cdot \underline{\dot{X}} dV - \frac{d}{dt}\int_V \rho\, \underline{\dot{X}} \cdot \underline{\dot{X}} dV$$

Equation 2-4

Equation 2-4 equates the rate of change of internal energy, *U*, summed over the volume, *V*, of the material, to rate of change of external work and the associated kinetic energy of the deformation. The right hand side of Equation 2-4 expresses the external rate of change of work done on the material through associated surface tractions, τ, acting on the material surface, *S*, and body forces, *f*, acting on each summed volume element, *V*. To complete the internal-external energy balance the kinetic energy associated to the rate of material deformation, $\dot{\underline{X}}$, is added. From Equation 2-4, if no body forces or surface tractions exist, any decrease in internal energy must manifest as a global deformation with a rate of increase in kinetic energy matching the rate of decrease in internal energy. It can be seen from Equation 2-4, that a change in internal energy state will influence the motion of the material. Considering Cauchy's equation of motion for a material deformation (Equation 2-5), in conjunction with Equation 2-4, it is possible to derive the energy Equation 2-6 [18].

$$\frac{d}{d\underline{X}} \cdot \underline{\sigma} + \underline{f} = \rho \frac{d\dot{\underline{X}}}{dt}$$

Equation 2-5

$$\rho \frac{dU}{dt} = \underline{\underline{\sigma}} : \underline{\underline{\dot{\varepsilon}}}$$

Equation 2-6

With respect to creep, it is therefore clear how a change in internal energy effects strain rate. As dislocations and impurities, as well as other irregularities create local strain fields, the energy stored in these strain fields when the material is unloaded make up its base internal energy state. If some of these obstacles are removed, energy is released from the base state and internal motion results; this is what is meant by a material reducing its internal energy state. The material then will deform externally as it restructures internally according to Equation 2-6. A material will always seek to minimise its internal energy state [19]. As a material seeks to reduce its internal energy, at each time step, it should then be theoretically possible through calculus of variations to find the set of material displacements that are associated with this. This process is however more complicated than it first appears, requiring accurate representations of internal stress components such as the internal yield state and internal viscous stress state (Chapter 3).

The influence of heat on internal energy state of a material is implied through Equation 2-3. Whilst it may appear an increase in heat absorbed by a material may increase internal energy through thermal excitation, it may also through certain mechanisms, cause an increase in internal work and subsequent reduction in internal energy. From Section 2.1.2, the concentration of vacancies is related to temperature via Equation 2-1. It was described how vacancies facilitate a mechanism known as dislocation climb; this allows dislocations to overcome obstacles such as other dislocations and impurities. Through giving atoms a vacant space in which to move, the presence of vacancies then allows a material to re-orient around obstacles, relaxing local strain fields; internal energy state as such can be reduced through heating. The relaxation and energy release from one local strain field may then destabilise adjacent localised strain fields, through unbalancing forces holding the internal microstructure in equilibrium. This can facilitate an ongoing process of destabilisation and subsequent release of internal energy from the material as it re-orients to find a new minimum internal energy state based on the change in heat and internal work (Equation 2-3). Videos of such internal motion and the resulting chains of motion, within bubble rafts, can be observed after

disturbance from [14], and other video sourcing websites. Within classical plasticity, the time taken for this re-orientation is assumed as instantaneous. In some of the videos referenced, it is however noticed the time taken for such re-orientation is clearly far too long to be treated as instantaneous. In fact Bragg and Nye [13] observed bubble rafts of certain bubble dimensions, post 'vigorous stirring', continuing to evolve even after 25 minutes; beyond this time the bubble integrity could not be maintained (due to diffusion of air through their boundaries). As this internal restructuring is not in effect instantaneous, then a static, minimum internal state has not been reached instantaneously either, and thus the external deformation state must also be continually evolving (Equation 2-4). Therefore there is a continuous release of external kinetic energy. This phenomenon is creep. Classical plasticity and creep both essentially result from enough energy being put into the material through loading, heating, or a combination of both, to facilitate the process of reduction of internal base energy state. This is somewhat analogous to a ball stuck behind a rock on a hill; its potential energy is based on the altitude it is stuck at. If an intervention releases it from behind the rock it rolls down the hill along the path of least resistance, reducing its potential energy state along the way. This potential energy is converted to kinetic energy as it rolls; it may of course get stuck behind other obstacles on the way, or it may go on indefinitely (until it reaches its lowest possible altitude) dependent on external conditions. This analogy, and process of material internal energy state reduction, relates directly to the material processes described by the restoration process, in Section2.2.2. Ultimately it is the occurrence of the three constituents of the restoration process, *recovery*, *recrystallization* and *grain growth* that give rise to creep in metals, and its (sometimes) distinct phases.

2.2.2 The restoration process

The restoration process refers to the internal microstructural processes a material goes through in order to reduce its internal energy state to the minimum possible (Section 2.2.1); a regular crystal lattice throughout its entirety. In other words, the material attempts to 'restore' a regular crystalline microstructure of the lowest energy state possible. Reduction or minimisation of base energy state is typically facilitated by either loading or thermal effects. Under large external loads a slip-plane (Figure 2-3) can be distorted enough such that a dislocation moves position and glides along a slip-plane to a lower energy location. Increased temperature can reduce bond stiffness and increase vacancy concentration (Equation 2-1).

The basis for restoration has already been outlined in Section 2.2.1; stored energy in local strain fields, usually around dislocations, impurities and grain boundaries, is released allowing dislocations to move, and under external load (or gravity) the material to deform. All local stress and strain fields should ultimately align with the global stress-strain field (created from loading or gravity) such that all energy barriers are eliminated and the material can only display linear elastic behaviour. In reality this ultimate state is never reached, with the metal being left with a microstructure of large grains with high angle offsets which are difficult to align. Often contained within these grain boundaries, post-restoration, are impurities. It is within the vacant spaces of the grain boundaries that they are least disturbing to the overall microstructure and thus they are stored in the 'least energy' location. Under a global stress field created by an external load the bulk of the material will stretch in a

direction dictated by this field as it orders and arranges itself in the most efficient manner through grain alignment.

Typically restoration involves three sometimes overlapping processes; *recovery*, *recrystallization* and *grain growth*. Under loading the material is globally deforming, recovery and recrystallization in this case are known as *dynamic recovery* and *dynamic recrystallization*. When static, either after loading or having only been heat treated, they are known as *static recovery* and *static recrystallization*. The overall process is illustrated in Figure 2-6 [17].

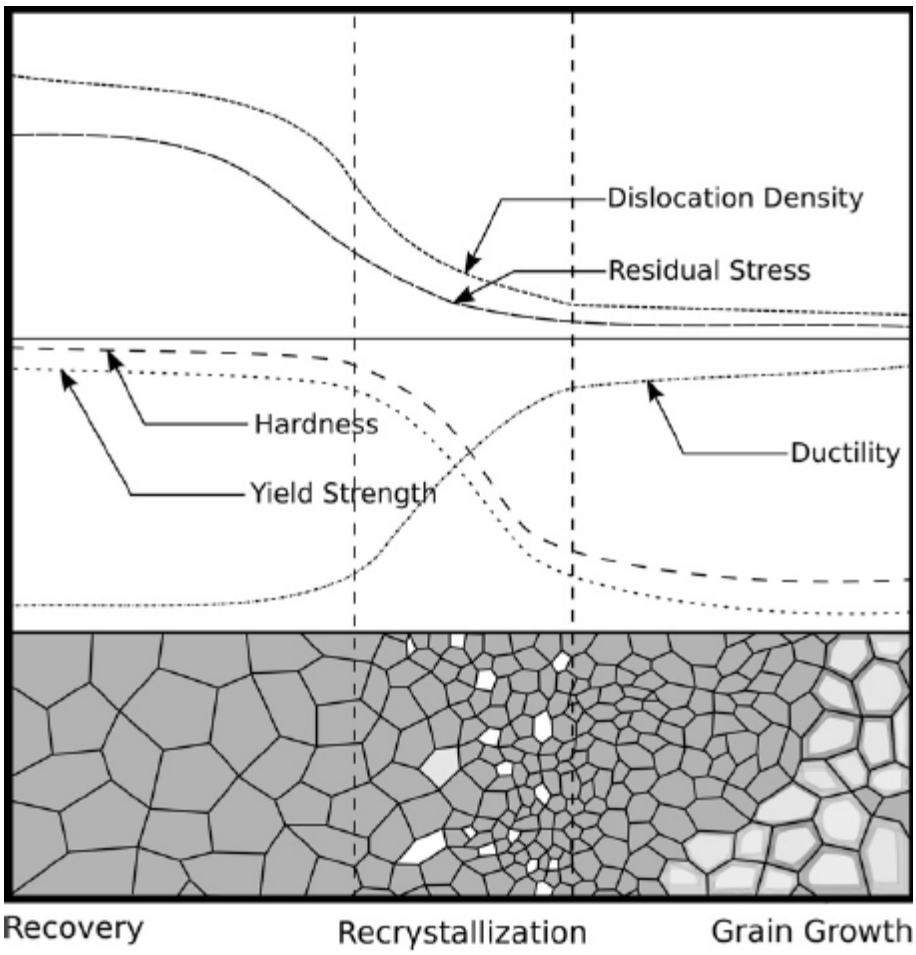

Figure 2-6; The restoration process [17]

As can be observed, the restoration process also results in a significant drop in yield strength and hardness, accompanied by a significant increase in ductility. As such, the stage of the restoration process the material is at strongly dictates the inelastic response of metals to load and heating. The recovery process is usually associated with microstructure change through dislocation motion; often this is possible to some degree without thermal aid under loading, this is classical plasticity. With temperature, a reduction in bond stiffness and the increased presence of vacancies destabilises the stress gradients mentioned in Section 2.2.1. This occurs about dislocations and obstacles, unbalancing the local internal forces and allowing the dislocations to move. The material reduces its energy state in doing so.

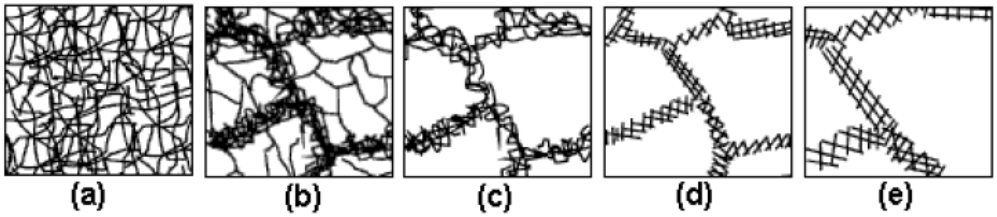

Figure 2-7; Stages of the recovery process [17]

Figure 2-7 shows an illustrated concept of the recovery process [17] leading to decreasing dislocation density and recrystallization. It largely consists of the motion of dislocations under glide and vacancy assisted climb, as they move and re-align to form cells and subgrains. Consider a standard polycrystalline metal, made up of grains of regular crystals, at various offsets, with numerous dislocations and vacancies within each grain, such as in the bubble raft images of Figure 2-2. Should an external force be applied, that is sufficient enough to allow dislocations to glide; dislocations will eventually begin to pile up. This pile up will be caused by a backup of dislocations against grain boundaries, each other, and particularly around large impurities; the result is the emergence of vague lines of dislocations within the existing grains (Figure 2-7a).With the thermal assistance of vacancies these dislocations can begin to overcome one another through dislocation climb. Lines of dislocations become increasingly more defined as dislocations of opposite polarity meet and annihilate leaving clearer crystalline cells within the existing grains (Figure 2-7b, c). These cells become cleaner, or more regular, as remaining dislocations migrate towards cell boundaries, again thermally assisted by vacancies, forming subgrains within the original grain structure (Figure 2-7d, e). At this stage the material microstructure hasn't undergone a significant visible change when viewed through an optical microscope. The original grain boundaries still dominate the visible microstructure. During the recovery process a material may well have hardened to some degree; this is strain hardening.

The migration of dislocations into distinct lines and the formation cells and subgrains from them, initiate recrystallization (Figure 2-6). Recrystallization is noted to start from *sites of nucleation*, often around large impurities; a new finer grain structure evolves from these *nuclei* [12] [17]. This coincides with the observations of Bragg and Nye [13] noting that large impurities appeared to be accommodated at grain boundaries, where there is more 'space' to accommodate them, requiring less stored energy. In fact this process of nucleation is really the overlap of recovery leading to the beginning of recrystallization created through the formation of cells (Figure 2-7a, b, c). Dislocations pile up around large impurities that they cannot move beyond (energy barriers), forming vague lines in numerous directions; and thus cell formation which leads to subgrain formation proliferates from those points. The dislocation density drops as illustrated in Figure 2-6 (also Figure 2-7c, d, e) as those dislocations of opposite polarity annihilate each other, creating more and more clearly defined subgrain boundaries. As the subgrain boundaries become clearer, the stress gradients from them to the rest of the metal decrease and the energy state decreases; these subgrain boundaries may then align as internal forces between them are released. This is the point where the original granular structure becomes less distinct, as lots of smaller subgrains and grains emerge within. Ultimately the original grain structure disbands leaving a slightly less ordered material with a smaller granular structure. This correlates with optical microscopy observations from MacLean [9] of prestressing steel single wire strands undergoing static recrystallization facilitated by temperature. Up to around

400°C, no major change of microstructure was observed, during which time it is likely the recovery process had been proceeding. As the temperature approached 500°C and 600°C the material exhibited a less defined original granular structure with the emergence of a finer granular structure being exhibited. At 700°C the material now exhibited a new fine granular structure.

Recrystallization is however not instantaneous. Bragg and Nye [13] noted the recrystallization of bubble rafts after 'vigorous stirring' to continue for as much as 25 minutes (they also note to observe beyond 25 minutes is difficult as bubbles shrink due to diffusion of air through their boundaries). It is strongly recommended to view bubble raft recrystallization on video upload websites to appreciate this behaviour.

The size of the new subgrains and grains formed during recrystallization appears to be linked to the original dislocation density of the metal, and thus the yield stress. A higher dislocation density tends to mean a higher number and density of cells; as a result these form with a smaller diameter (Figure 2-7a, b). It has also been observed that irrespective of initial dislocation density, the density of moving mobile dislocations appears proportional to a square of the applied shear stress [15]. The diameter of subgrains formed within aluminium through the recovery process has also appeared to be inversely proportional to a power of the applied stress, this appears close to 2 [20]. Therefore a higher yield stress metal, subjected to higher loads, will typically restore to a finer granular structure.

Grain growth emerges from the increased alignment of the finer, new grains, now formed through recrystallization. At this point a substantial amount of stored strain energy around dislocations and obstructions has been released and the metal is at a low energy state. It is thus highly ductile and of much lower yield strength; therefore under loading it will deform rapidly. The various impurities present, particularly those larger interstitial foreign atoms (Section 2.1.3), are remaining energy barriers and now find themselves occupying space at high energy, high angle offset boundaries. This usually marks the end point of restoration; a low energy state, low dislocation density, polycrystalline microstructure of large grains at high angle offsets. Under loading the deformation will have been rapid at this latter stage leading to this point at which time cracks could be expected to occur at these boundaries, this could result in eventual rupture.

2.2.3 Classical plasticity

From the discussion of dislocations in Section 2.1.1 and their role in the recovery part of the restoration process discussed in Section 2.2.2 the mechanisms of classical plasticity have already been described; by the motion of dislocations along a slip-plane. Elastic yield is breached at the point where a lattice is distorted to such a degree that a dislocation is prompted to move along a slip-plane. The strain resulting from this motion (dislocation glide) is irrecoverable plastic strain. Once elastic yield has been reached, typically many dislocations will be prompted to *glide* in grains of similar alignment, in various crystalline portions of the metal.

As has previously been stated, the motion of a dislocation across a slip-plane results in a deformation equivalent to a *unit step* or one atomic spacing. This represents a sudden acceleration

of total strain with respect to applied stress. This phenomenon is often neglected in stress-strain curves. Figure 2-8 shows a real, typical, stress-strain curve for mild steel. This is the nature of the stress-strain curve obtained through uniaxial tensile load tests, as opposed to an idealised version used for coded design purposes. It shows an initial rapid increase in total strain once elastic yield is exceeded that can be attributed to the sudden uninhibited motion of dislocations prior to pile up.

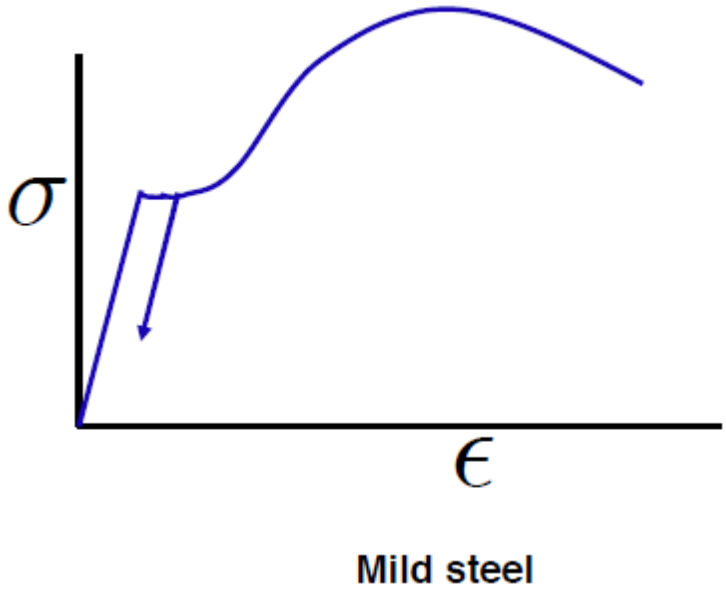

Figure 2-8; A 'real' stress strain curve for mild Steel

The density of dislocations and the immovable nature of impurities limit the mobility of dislocations before they pile up with one another. This pile up, and decrease in mobility is represented further along the total strain evolution of Figure 2-8 as the stress required to induce further strain rapidly increases again. This phase of behaviour in classical plasticity is known as strain hardening. When a metal is deliberately work hardened prior to functional use, by working and stressing in a manner to increase the number of dislocations, the purpose is to reduce dislocation mobility such that the initial acceleration of strain observed in Figure 2-8 is less pronounced. Prestressing steels are an example of this; the dislocation density is so high that mobility is minimal and plastic strain prior to rupture is very small.

It should be noted that even during strain hardening the material is still lowering its base energy state; every plastic deformation results from the release of some locally stored energy. As dislocations pile up, the effective energy barriers they create become larger and more difficult to overcome. It therefore simply takes more force to release these energy barriers, and in some cases rupture may happen first.

As was covered through discussion of the recovery component of the restoration process in Section 2.2.2, dislocation pile up is relieved through thermal effects; most notably this is through the increased concentration of vacancies with temperature (Equation 2-1) facilitating dislocation climb. From this point in the restoration process the time taken for internal re-orientation and therefore accompanied global deformation becomes longer and increasingly ongoing. There is however difference in yield strength between an already loaded metal which is subsequently heated (such as

structures in fire) and a metal which is heated and then suddenly loaded. In the latter case the rate of diffusion of vacancies within the metal prior to loading will be far less than in the former case (Equation 2-2) through the absence of a global stress field across the metal microstructure. Therefore the loaded metal, which is then heated, will have moved further along the restoration process with a possible reduction in yield strength and increase in ductility (Figure 2-6). When a pre-heated metal however is suddenly loaded there is a sudden pile up dislocations followed by sudden rupture as there is not sufficient time for vacancies to diffuse and relieve the congestion of dislocations. In such a case a greater yield load is observed, but accompanied by a less ductile response at the same temperature. The loaded metal which is then heated has actually been experiencing elevated temperature creep, whether this is observable or not depends on the magnitude of the temperature, rate of heating and load magnitude.

2.2.4 Primary, Secondary and Tertiary Creep

Time dependent creep strain evolution is often referred to as consisting of three phases relating to strain rate at constant stress and temperature. These phases are known as the primary, secondary and tertiary creep. These phases relate to the respective components of the restoration process (recovery, recrystallization and grain growth) with some degree of overlap. Figure 2-9 displays a classic image of primary, secondary and tertiary creep strain accumulation with time under steady state external stress and temperature conditions.

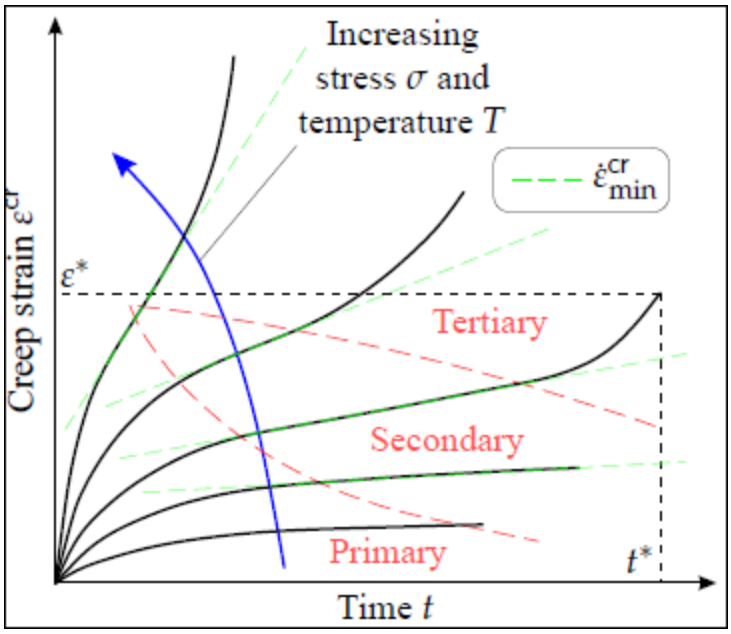

Figure 2-9; Primary, Secondary and Tertiary creep [16]

Primary creep can be largely attributed to the recovery component of restoration (Figure 2-6).The primary creep phase involves rapid strain accumulation, attributed to dislocation motion as they become initially mobile; this strain rate then decelerates as dislocations pile up. This leads to the

secondary phase of creep strain accumulation (which is facilitated by increased temperature). Primary creep therefore is the same mechanism as classical plasticity. At ambient temperature primary creep and classical plasticity are entirely analogous where the strain rate is so rapid to be treated as instantaneous. As temperature increases the recovery process is permitted to evolve to some degree beyond dislocation pile up following Figure 2-7. Material deformation then may continue to evolve with time depending on the stress and temperature magnitudes as vacancies diffuse through the microstructure permitting dislocation climb. This primary creep phase is typically small in duration compared to the time to rupture of metals under a tensile load. The magnitude of the primary creep strain accumulated, compared to the total creep strain, is also often small, dependent on the type of metal. This relates to the dislocation density and the distance mobile dislocations are able to travel prior to piling up. Yield strength may increase during this period owing to strain hardening.

The secondary creep phase begins when the material strain rate during the primary phase decelerates to a steady state strain rate under constant external loading and thermal conditions. The intersection of the red dashed lines with green dashed lines in Figure 2-9 highlights the separation of the creep phases. The strain rate during the secondary phase is often termed the *minimum creep strain rate* or the *steady state creep strain rate*; this reflects that under steady state external conditions, this is the 'minimum creep strain rate' observed. This phase appears to coincide with recrystallization in ASTM A416 [10] prestressing steel when comparing the observed onset of recrystallization by MacLean [9] with the onset of modelled secondary creep strain accumulation. This will be shown later through the modelling of isolated, prestressed steel tendons, using an experimentally verified creep strain rate function (Section 4.4.5). For recrystallization to begin the recovery process must be allowed to evolve towards cell and subgrain formation which requires the presence and diffusion of vacancies. As vacancies are temperature induced (Section 2.1.2, Equation 2-1) recrystallization and secondary creep can only be facilitated at elevated temperatures. The magnitude of the required temperature is however dependent on the magnitude of the applied stress. Empirical relationships observed from experiment between stress, temperature and creep strain rate are presented in Section 2.3. There is a degree of overlap between recovery and recrystallization with respect to the restoration process. As such it is likely that in particular the early stages of secondary creep involve an overlap of recovery and recrystallization mechanisms whereby a period of strain rate equilibrium is achieved with recrystallization slowly beginning to dominate. Secondary creep strain evolution tends to dominate total creep strain evolution and deformation time. Recrystallization, as was noted in Section 2.2.2 is a time evolving process, its likely dominance in facilitating secondary creep in metals therefore could explain the dominance of secondary creep in these respects.

The tertiary phase is usually associated with a re-acceleration of strain rate, leading to failure (rupture). This phase most likely occurs during the grain growth phase illustrated in Figure 2-6; at this stage the material ductility is maximal whilst the yield strength and base energy state are minimal. Grains grow as the newly formed subgrains and grains from recrystallization align under a globally applied stress field. Vacancies continue to assist this process through smoothing the grain boundaries. This process of increasingly rapid alignment accelerates strain rate and increased ductility. It is likely significant necking may occur immediately prior to this as larger angle grain offsets are forced to align resulting in large increases in longitudinal strain and large induced lateral

strains. This leads to damage effects being observed as grains that cannot align, separate from one another, leaving cracks with ultimate rupture.

At very high temperatures or heating rates, as observed in Figure 2-9, the primary and secondary phases may not be very distinct at all with respect to strain rate. The recovery part of the restoration process at high temperatures or high heating rates should occur very rapidly due to high vacancy concentrations allowing dislocations to 'climb' and overcome barriers extremely quickly. This can lead to annihilation and recrystallization without a significant drop in strain rate.

Under transient heating or loading conditions the primary, secondary and tertiary creep phases may not be distinguishable; it is still however beneficial to refer to primary, secondary and tertiary creep as a means of separating deformation mechanisms. Confusion can arise under such transient external conditions when, as is often the case, secondary creep is referred to as steady state creep or minimum creep strain rate. Under transient external conditions, secondary creep strain rate is also transient as it is a function of stress and temperature (Section 2.3).

2.3 Empirical stress and temperature relationships to creep strain rate

The previous discussion in Section 2.2.3 has highlighted dislocation motion, in the form of a gliding action along a slip-plane, as responsible for plastic strains in the regime commonly known as classical plasticity. It has been established that impurities, grain boundaries and the pile up of dislocations, create local stress and strain fields that act as an energy barrier, preventing further travel of dislocations. If these energy barriers cannot be overcome by dislocations, under increasing load, the material will likely rupture as no more plastic strain is possible.

In order to overcome an energy barrier, energy has to be put into the system. When heating is involved, a unit volume of the material will 'receive' energy proportional to the temperature via the materials specific heat capacity (itself a function of temperature). It appears this energy manifests itself physically in overcoming an energy barrier through reducing the stiffness of atomic bonds (reducing elastic yield stress) and particularly through increased concentration of vacancies related to temperature according to Equation 2-1. Therefore under heating, a metal such as steel has a mechanism (dislocation climb) that can assist and allow the restoration process to progress beyond dislocation pile up towards recrystallization. As recrystallization evolves with time, then yield strength decreases and ductility increases with time. Therefore, under load the material deforms over time; this process is observed as creep. The next step is to discuss experimentally observed relationships between external applied stress and temperature conditions to creep strain rate.

It has been noted that in high-yield metals, typically subjected to high loads, dislocation density is high. It seems logical and has been observed [15] [20] that high dislocation densities will result in limited mobility and a denser formation of smaller diameter cells and subgrains. In cases of high initial dislocation density and high load it should then be expected that relatively small plastic strains will occur through dislocation motion due to the limited mobility their density allows. Therefore small relative creep strains may occur in the primary phase. A low yield stress material, on the other

hand, subjected to a high temperature, should see significant initial plastic strain through dislocation motion with the formation of larger cells and subgrains. Large subgrains should result in a lower total subgrain boundary length throughout the metal, but being offset at larger angles (Figure 2-1). As the applied stresses are relatively low then high temperatures are required to provide the energy to overcome the energy barriers. Thus creep in metals at low stress seems, and indeed is, thermally dominated. The process then is very similar to the granular restructuring required for species diffusion throughout a metal as defined by Equation 2-2.

At higher stress, larger amounts of work are put into the material through the load, when assisted by vacancies this allows energy barriers to be released and creep observed at lower temperatures. With smaller subgrains offset at lower angles less energy is required for alignment; stress effects can begin to dominate. Vacancies are necessary to facilitate cell formation and alignment, but only to the degree that stress can then force this alignment. So creep at higher stresses may be viewed, perhaps not as stress dominated, but heavily stress dependant. Now, commonly observed empirical relationships through experiment, between creep strain rate, temperature and stress will be presented.

2.3.1 Temperature dependence

Some external factors influence internal factors, the obvious one being temperature and its effect on vacancy concentration (Equation 2-1) and bond stiffness (elastic yield stress). It was stated earlier in Section 2.1 that under certain external temperature and stress conditions creep strain rate appears to be predictable in a manner very similar to Equation 2-2. The normalising diffusion rate constant, D_0, in Equation 2-2, has a stress dependence directing the diffusion and influencing its rate. It has been observed in many metals when subjected to creep tests at constant stress and at temperatures, above 0.5 times the metals melting temperature, that minimum creep strain rate does indeed relate strongly to Equation 2-2. By plotting the natural logarithm of the strain rate against the reciprocal of the temperature, the *creep activation energy* of the metal can be determined (Figure 2-10). Within the above temperature range, the recorded activation energy for many metals appears to match closely that of self-diffusion in Equation 2-2 [16] [21]. This is indicative of a metal subjected to low stress and high temperature, such that the concentration and diffusion of vacancies is the dominant factor in releasing energy barriers. It is during these external conditions where large creep strains are noted in the primary phase. As minimum creep strain rate can be strongly linked to an Arrhenius relationship in many metals just reinforces the importance of vacancies in the recovery process and possibly further into recrystallization. After all, it appears to be largely due to vacancies that cell formation and thus subgrain formation can be initiated, thus setting the basis for recrystallization to progress.

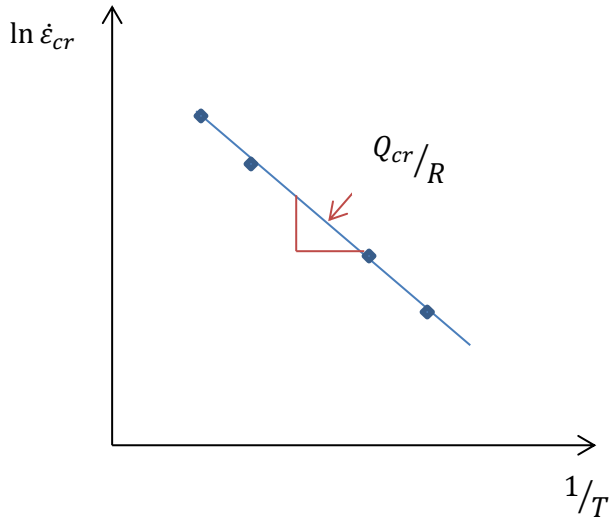

Figure 2-10, Determination of creep activation energy

The concept of creep having an activation energy in the above form is somewhat misleading; the activation energy within the Arrhenius relationship is merely a constant, determining the magnitude of the effect of temperature on creep strain rate. Ultimately creep is 'activated' dually by stress, being applied beyond the yield state, and the influence of temperature. The combination of global stress state and temperature can be viewed as providing the energy to initiate creep, especially as energy needs to be put in to release local strain fields. A constant relating to this energy of activation should then be tied to the combination of stress and temperature on creep strain rate, rather than only to the temperature component. In higher dislocation density metals, typically used in high stress applications, the energy associated to the work done by the applied force is significant enough to relieve energy barriers at lower vacancy concentrations, and thus lower temperatures. This within the scope of an Arrhenius relationship manifests itself as a higher activation energy [15] resulting in, and reflecting, the smaller influence of temperature at a given creep strain rate. The concentration of vacancies at a given temperature should however be the same (unless stress is a factor in their creation!), implying the activation energy constant should be the same. The higher activation energy for power law breakdown creep (Section 2.3.2) may then reflect the lower temperatures involved to initiate creep. The bond stiffness, dependant on the particular metal, may not be able to influence behaviour as much, in terms of initiating dislocation motion and creep at these low temperatures hence the higher activation energy. This of course would depend on the particular metal and the evolution of first elastic yield with temperature.

2.3.2 Stress dependence

The stress dependence of the secondary or minimum creep strain rate during many tests appears to often follow a power law and is thus known as *power law creep*. At higher stresses this is observed to break down as the power exponent becomes increasingly large [15] [16]. Often in those cases an exponential stress dependence is found to become more appropriate, leading to the term *power law breakdown* creep [22] [23]. Power law and power law breakdown relationships between secondary creep strain rate and applied stress, that can be fitted to experimental data, depending on stress and temperature range, are noted in Equation 2-7 and Equation 2-8 [15] [16] [22] [23]. Equation 2-7 is generally restricted to creep at temperatures above 0.5 times the melting temperature whilst Equation 2-8 is generally considered applicable at temperatures beyond 0.3 times the melting point [15] [16]. It has been stated by Harmathy [8] however that the relationship to the Arrhenius function appears also to work in Carbon steels at slightly lower relative temperatures in the range 400°C - 700°C. In this case, the secondary or minimum creep strain rate can be shown to match Equation 2-8 (Chapter 3.3) but with a greater activation energy than that of self-diffusion [15].

$$\dot{\varepsilon}_{cr} = \dot{\varepsilon}_0 (B\sigma)^n exp\left(\frac{-Q_{cr}}{RT}\right)$$

Equation 2-7

$$\dot{\varepsilon}_{cr} = \dot{\varepsilon}_0 exp(B\sigma_A) exp\left(\frac{-Q_{cr}}{Rt}\right)$$

Equation 2-8

In both equations, $\dot{\varepsilon}_{cr}$, represents the creep strain rate, $\dot{\varepsilon}_0$, is a rate constant with units of t^{-1}, and σ, is the applied stress. The value, *B*, is a constant with units of stress^{-1}, necessary to dimensionally balance the equation. It may itself be a function of accumulated creep strain, representing strain hardening behaviour, and distinguishing between transient primary and steady state secondary creep strain rate, should temperature and stress be constant. Q_{cr}, is the activation energy of creep. The constant, *R*, is the universal gas constant whilst *T* is the temperature in Kelvins. In Equation 2-7 the power exponent, *n*, is a constant dependent on temperature and stress, at low stresses it may be in the region of 3, whilst at high stresses can extend beyond 20. As stated above, at such high stresses the power law representation Equation 2-7, begins to breakdown, and the power law breakdown exponential form of Equation 2-8 is assumed. In some cases a hybrid algorithm using a power of a hyperbolic sine stress function is used, this reduces towards the power law form of Equation 2-7 at lower stress and towards the power law breakdown form of Equation 2-8 at higher stress. An example of this is displayed in Equation 2-9; typically the constants, *B*, and, *n*, are chosen such that when $B\sigma > 1.2$, Equation 2-9 tends towards a power law breakdown form (Equation 2-8) and when $B\sigma < 0.8$, towards a power law (Equation 2-7) [15].

$$\dot{\varepsilon}_{cr} = \dot{\varepsilon}_0 (\sinh B\sigma)^n exp\left(\frac{-Q_{cr}}{Rt}\right)$$

Equation 2-9

It should be noted however, that when expanding the hyperbolic sine function in a Maclaurin or Taylor series, only odd powers are obtained. At lower values of $B\sigma$, tending towards zero, large power terms of the expansion tend to be negligible, thus only small power terms are significant. An appropriate choice of the power n, applied to the hyperbolic sine function can allow a suitable choice or series of powers to be effectively used as stress rises.

2.4 Summary

The internal material defects that give rise to creep and plastic behaviour in general have been described in this chapter (Section 2.1.1, Section 2.1.2 and Section 2.1.3). This includes their roles (dislocations in particular) in creating a materials base energy state, through effectively creating energy barriers against internal motions. The release of these energy barriers results in plastic deformation. When a chain reaction of release is induced, largely facilitated thermally by vacancies and a reduction in bond stiffness, the ongoing release of internal energy manifests externally as an ongoing release of kinetic energy from the work being done to maintain the deformation; the result is creep. The internal material evolution, through this process of energy state minimisation, is described as the restoration process (Section 2.2.2). Its constituents are the recovery, recrystallization and grain growth. The recovery process largely describes the behaviour attributed to classical plasticity but also primary creep strain evolution. Recrystallization evolves over far longer periods of time; the energy released from the material through this process appears to be responsible for secondary creep strain evolution. Ultimately this leads to tertiary creep as the recrystallization process evolves into grain growth. It is very important for structural integrity to prevent recrystallization occurring and evolving in metals; yield stress decreases significantly whilst ductility increases significantly during this process.

Secondary creep strain rate, in a uniaxial manner, is generally observed in metals to relate externally to stress through a power law or power law breakdown representation (Equation 2-7, Equation 2-8). The temperature dependence within these representations is generally described by an Arrhenius relationship, probably highlighting the importance of vacancy concentration and diffusion on facilitating the restoration process, and thus creep.

3 Constitutive modelling of creep

In the constitutive representation of classical plasticity, deformations are assumed to break the laws of physics and occur instantaneously. Relating this to the content of the previous chapter, classical plastic deformations result from dislocation movement or glide. Dislocation motion along a slip-plane is rapid (as can be seen from bubble raft videos); lasting only till it hits an obstruction. At low temperatures there is little follow up motion and subsequent microstructural changes possible. With respect to classical low-temperature plasticity, there is generally then a sudden inelastic deformation followed by elastic behaviour once more, should the load not increase further; an instantaneous assumption suffices. As this deformation is assumed instantaneous, then should the external stress state force energy barriers to be released, internal material re-orientation must also occur instantaneously. As a result of this the internal stress state must match the external applied stress state. That is to say, a force acting on a given area of material creates a global stress field across the material, therefore internally, if all the newly created stresses felt by the atoms and grains are summed, they will match this stress given by the force multiplied by the area. The energy or work put in externally is then matched again by the sum of the energies in the newly created strain fields. Once the elastic yield state or stress is exceeded the internal stress state then immediately evolves to become the new yield state. The constitutive model for classical plasticity thus dictates the yield stress state must always match the external stress state and, as described in Appendix A; stress states cannot exist outside the yield surface.

During creep as has been noted in Chapter 2 the total internal energy state is continually evolving; the initial release of an energy barrier creates a chain of subsequent releases should the temperature be sufficiently elevated (Section 2.2.1). As such there is a continuous release of internal energy which is externally matched by the kinetic energy of the ongoing global deformation and any change in external work from applied forces (Equation 2-4). Unlike classical plasticity therefore, the external stress state also contains an inertial term as displayed in Equation 2-5; the total internal stress state matches the external stress state including the inertial forces. To represent continuous motion, the constitutive model for creep splits the total internal stress state into a static yield force and a *viscous* damping force associated to the rate of the deformation.

This chapter presents the generally accepted constitutive model of creep otherwise known as *viscoplasticity*. This includes a conceptual model representing the internal behaviour giving rise to creep through an analogous continuum representation. Within this representation, the creep deformation evolving over time, as internal motion and reorientation progresses, is related to a damping pot with the viscosity of the damping fluid representing an equivalent or effective viscosity of internal motions. In this respect, the non-static internal material is treated as a Newtonian liquid with an effective viscosity. It is thus easy to see how the term viscoplasticity arises. This model will be discussed in detail in the following Section 3.1. Once viscoplastic or creep strain rate is related to this effective viscosity and the *viscous stress,* effectively yielding a strain rate magnitude, a framework is required to predict the multiaxial deformation rate. As was stated in the introduction, Section 1.2, a constitutive framework is well established, this is an adaptation of the classical plasticity framework in consideration of the viscoplastic constitutive model. This is presented in Section 3.2. Within Section 3.2 the adaptations to classical Von Mises constitutive framework overviewed in Appendix A are presented; allowing stress states to exist outside the yield surface

such that viscous stress and resulting creep may be accounted for. This framework provides the methodology behind modelling creep or viscoplastic behaviour in three dimensions in commercial Finite Element software packages. It is advised that should the reader be unfamiliar with the constitutive framework of classical plasticity that they read Appendix A; Classical plasticity constitutive relations, prior to reading this section.

Having defined the constitutive framework for viscoplastic modelling at the start of Section 3.2 the constitutive theory of multiaxial viscoplastic behaviour is defined in Section 3.2.1. In Section 3.3 existing models for the *creep strain rate magnitude* otherwise known as the *flow rate*, *gradient of the viscoplastic potential*, *plastic multiplier* or *norm of the viscoplastic strain rate* tensor are presented.

3.1 The constitutive model and equation of motion

Figure 3-1 presents a one dimensional conceptive illustration of the respective constitutive models for classical plasticity and creep or viscoplasticity. The classical elastic-plastic model consists of a spring fixed at one end connected to a friction slider in series. Elastic behaviour is represented by the spring, behaving according to Hooke's law. Inelastic behaviour is represented by the friction slider. The system is loaded such that the loading force creates an equal and opposite reaction at the fixing, and thus at any point a cut is made. When a force greater than the elastic yield is applied to the system, the friction slider instantaneously displaces a distance determined by its coefficient of friction. The system then behaves elastically once more, with the force producing the friction slider displacement being the new elastic yield stress or force. This yielding force is felt equally across the spring and friction slider, therefore the equivalent internal yield force equals the total external force applied to the system. The friction sliders new displacement is permanent, representing an irrecoverable plastic deformation. The coefficient of friction of the slider can evolve as a function of its displacement in order to represent strain hardening or softening.

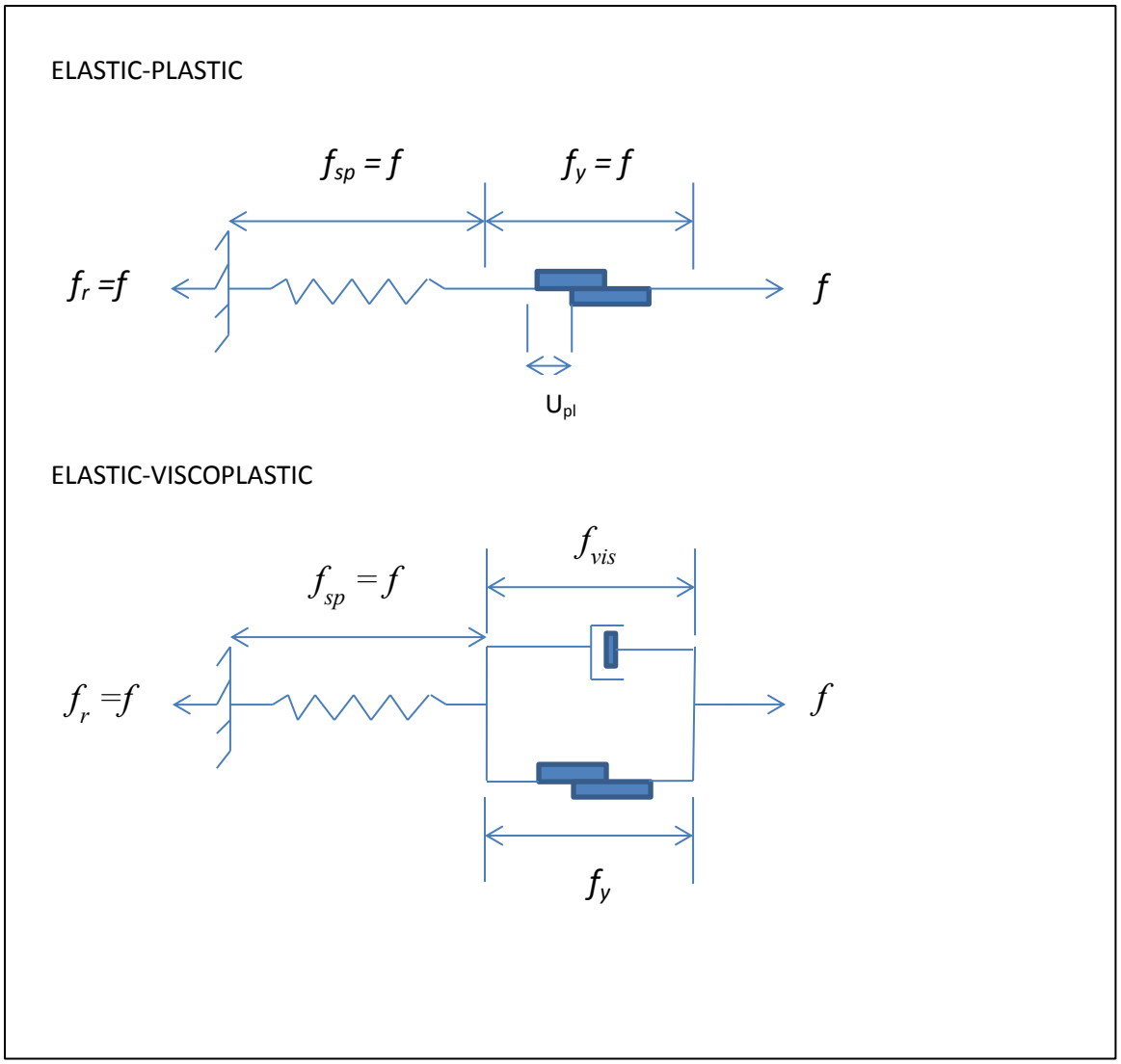

Figure 3-1; One dimensional conceptual visualisation of viscoplasticity or creep

The elastic-viscoplastic representation consists of the same spring fixed at one but connected to a friction slider whose motion is damped (by the illustrated damping pot). Plastic behaviour is thus represented by the combined friction slider and damper system; the addition of the damping pot damps and delays the displacement response of the friction slider should elastic yield be exceeded. As the friction slider and dashpot are connected in parallel with one another they are then subjected to separate forces or stresses. These two internal forces sum to the total force or stress applied to the system minus an inertial force, assuming the system is not static. These internal force components are termed a *viscous force*, f_{vis}, across the damper, and a *static yield force* (or state), f_y, across the friction slider.

Once yielding and displacement of the friction slider has begun, the internal yield force does not equal the total applied force as it would classically; this is an extremely important point to note and will be elaborated on shortly.

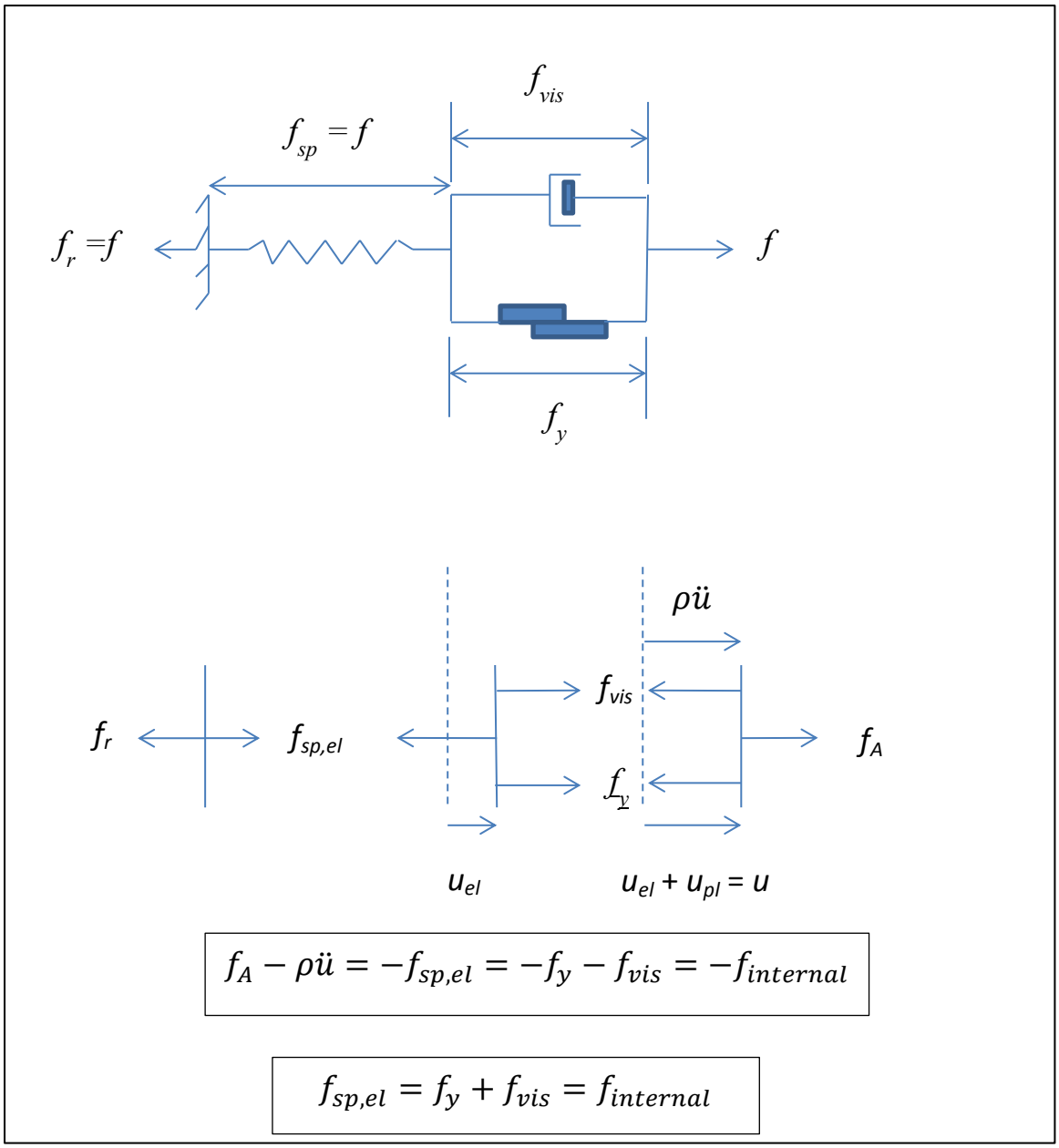

Figure 3-2; Force vector plot of the one-dimensional elastic-viscoplastic constitutive model.

Figure 3-2 shows a force vector plot, and associated displacements, representing the physical behaviour of the elastic-viscoplastic constitutive model from Figure 3-1. The external applied force, f_A, minus the inertial force it creates through the displacing of the centre of mass of the system, equals the sum of the internal forces as shown in Equation 3-1. It should be noted the total internal force acts as a restoring force in the opposite direction to the external applied force, hence the negative sign on the right hand side of Equation 3-1. Rearranging Equation 3-1 shows it to match Cauchy's equation of motion (Equation 2-5). It should be noted that the total internal force in Equation 3-1 is equal to the gradient of internal stress fields as displayed in Equation 2-5.

$$f_A - \rho\ddot{u} = -f_{internal}$$

Equation 3-1

It is then possible to construct an equation of motion representing viscoplastic deformation in terms of the external force applied to the system, and the internal restoring force components associated to the friction slider and dashpot shown in Figure 3-2; this is displayed in Equation 3-2.

$$f_A - \rho\ddot{u} = -f_y - f_{vis}$$

Equation 3-2

Equation 3-2 is representative of a unit volume of material of density, ρ, if the friction slider displaces at such a variable rate that accelerations are noticeable an inertial force according to Newton's second law must be included. Within Equation 3-2, f_A, represents the external force applied to the system, f_y, is the internal elastic-plastic yielding force across the friction slider, f_{vis}, is internal viscous force across the damper and ρ, the density of the material being represented, $\ddot{u}$ is the acceleration of the centre of mass displacement. The parallel friction slider and dashpot system are in series with the spring; whatever force is applied to the overall system then is felt fully by the combined friction slider and dashpot system, and also by the spring (plus any inertial force induced by the applied force).

If the material is deforming at a rate $\dot{u}$, multiplying Equation 3-2 by this rate yields the energy conservation Equation 2-4. This shows the rate of internal work by the internal yield and viscous forces (f_y and f_{vis}) to match the rate of change of internal energy (note for an adiabatic system with $Q = 0$, $\Delta U = -W$). The constitutive model of course does not represent the role of heat with respect to the internal energy and equation of motion; this must be included via its effects on the yield and viscous states. The force-displacement curves illustrated in Figure 3-3 further highlight the difference in internal yield state response to external forces between the elastic-plastic and elastic-viscoplastic models of Figure 3-1.

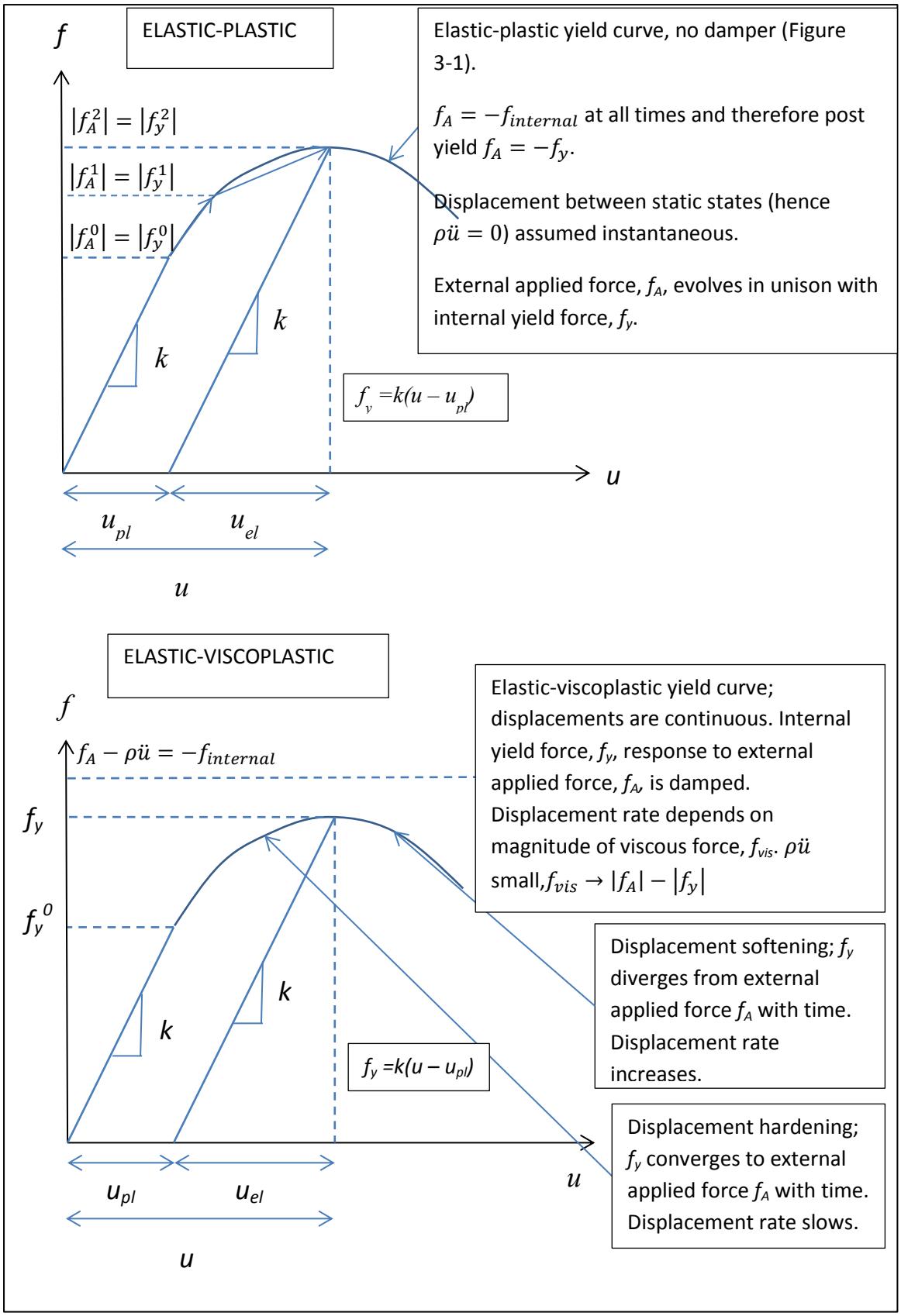

Figure 3-3; Elastic-plastic and elastic-viscoplastic uniaxial force-displacement curves

In the elastic-viscoplastic model, once the total internal force, $f_{internal}$ (Figure 3-2), exceeds first elastic yield, f_y^0, the internal deformation response to the external applied force is damped; the internal

material response is constantly evolving and is not static (Section 2.2.1 and 2.2.2). If the internal material response was to become static the internal yield force f_y, then would have 'caught up' with the external applied force f_A. The viscous force, f_{vis}, at this point would equal zero. The internal viscous force therefore tends towards the difference between the total internal force and the internal static yield force at a given time. This can be clearly visualised in Figure 3-3 by considering the difference between the applied force line and the yield curve.

The viscous force across the damper, as is standard in fluid mechanics relates to deformation rate via a dynamic viscous drag coefficient, *c*; this deformation rate is the rate of displacement of the friction slider, as the damper does not act on the spring. The plastic deformation rate represented by the friction slider displacement rate, $\dot{u}_{pl}$, then relates directly to the viscous force across the damper, f_{vis}, via an effective dynamic viscous drag coefficient, *c*, in one dimension as in Equation 3-3. The negative sign indicates that the viscous force acts in the opposite direction to the displacement and displacement rate.

$$f_{vis} = -c\dot{u}_{pl}$$

Equation 3-3

It is thus noted, considering stress-strain as opposed to force-displacement, viscoplastic or creep strain rate relates directly to the magnitude of the equivalent internal viscous stress. The elastic-plastic yield force across the friction slider, f_y, relates to the spring stiffness, *k*, as displayed in Figure 3-3 via Hooke's law (Equation 3-4).

$$f_y = k\left(u - u_{pl}\right)$$

Equation 3-4

Substituting Equation 3-3 and Equation 3-4 into Equation 3-2 yields the differential equation of motion Equation 3-5.

$$f_A = \rho\ddot{u} + c\dot{u}_{pl} + k\left(u - u_{pl}\right) = \rho\ddot{u} + ku + c\dot{u}_{pl} - ku_{pl}$$

Equation 3-5

Equation 3-5 appears very similar to the type of differential equation typically encountered in engineering mathematics tuition of a damped mass on a spring; here however, the spring is not damped and deforms separately to the friction slider, owing to the series connection.

Above all, from Figure 3-3 it should be noted that internal yield state, f_y, during a viscoplastic deformation must be lower than that of an equivalent instantaneous classical plastic deformation for the same applied load increment. Therefore treating a material subjected to external loading and thermal conditions that may induce viscoplastic behaviour (creep), in a classical manner, may result in yield strength being overestimated. Recrystallization in particular as may occur under prolonged heating under load is associated with a drop in yield stress and increase in ductility (Section 2.2, Figure 2-6). It is this ongoing recrystallization process over time which prevents a locked static yield state being reached due to an ongoing release of internal energy barriers and restructuring to a lower energy internal state (Section 2.2.1 and 2.2.2).

3.2 The constitutive framework of creep modelling

In this section the constitutive framework of viscoplasticity, in consideration of the viscoplastic constitutive model and the total internal stress state, consisting of yield and viscous stress components (Equation 3-1 and Equation 3-2), is detailed. As noted in Section 1.2 of the introduction, this framework is well established, ultimately providing a constitutive representation and means to relate the norm (magnitude) of the creep strain rate to the multiaxial creep strain rate.

As detailed in Appendix A, yield criteria in metals are often dictated by where the internal stress state lies with respect to a yield surface. Within classical plasticity, an assumed property of metals is that yield is invariant to hydrostatic stress. Yield is therefore reached if the total internal stress state (matching the external applied stress state) reaches a point on a cylindrical surface surrounding a hydrostatic axis in principal stress space (Figure 8-2). In a one-dimensional system this is equivalent to the total internal stress matching the first elastic yield stress, f_y^0, as indicated in Figure 3-3. As yield is invariant to hydrostatic stress, the radius of the cylinder may then be related to uniaxial tensile yield values for a material to determine if yield has been reached; this will be detailed shortly, and in Appendix A. Relating to Section 3.1, Figure 3-1 and Figure 3-3, in classical plasticity the internal yield stress is identical to the total internal stress, once linear elastic behaviour has been surpassed, and is equal and opposite to the external applied stress state; there is no viscous stress state. Therefore should yield be exceeded the yield surface representing the internal yield state in three dimensions is assumed to instantaneously expand radially, in the same manner as the yield curve in the elastic-plastic force-displacement curve of Figure 3-3. The total internal stress state therefore remains on the yield surface. Stress states are not permitted to exist beyond the yield surface in classical plasticity.

Figure 3-4 displays the same Von Mises yield surface of Figure 8-2 in Appendix A, illustrating the total internal stress state that now consists of both yield and viscous stress components (Equation 3-2), as they lie with respect to the cylindrical surface. Once the total internal stress state reaches a point on the yield surface inelastic behaviour ensues. As the cylindrical yield surface still represents the internal yield stress component, then the total internal stress state, once linear elastic behaviour has been exceeded must lie beyond this surface to account for viscous stress. This is in the same manner as the total internal force in the elastic-viscoplastic one dimensional force-displacement curve of Figure 3-3 lies above the yield curve. The evolution of radius of the yield surface is damped in the same manner as motion of the friction slider is damped in Figure 3-1.

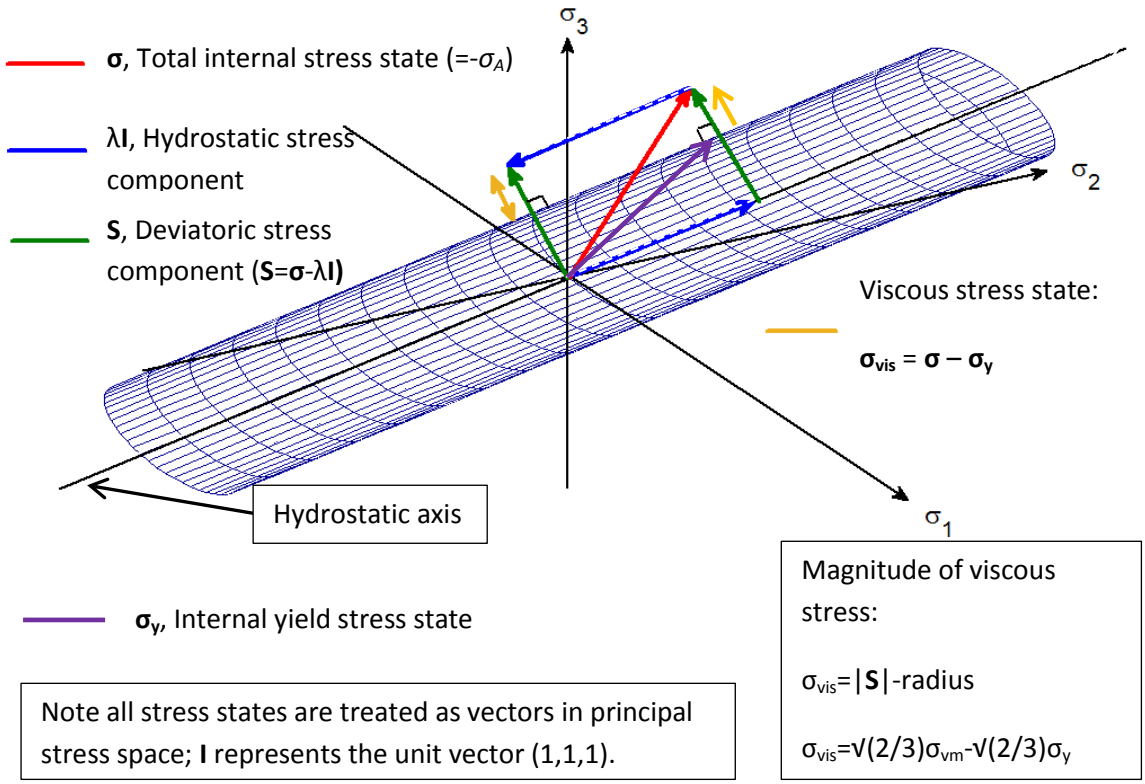

Figure 3-4; The Von Mises yield surface with viscoplastic total stress state allowed to lie outside the surface

The radial stress component of the total internal stress state, dictating yield and driving the yielding deformation, is the deviatoric stress component. As detailed in Appendix A; Classical plasticity constitutive relations, deviatoric stresses lie in a radial plane perpendicular to the hydrostatic axis (noting hydrostatic stress in metals is not assumed to contribute to yielding behaviour). The viscous stress as illustrated is the difference between the total internal stress state and the internal yield state just as described in Section 3.1 (Figure 3-3). As plastic flow in metals is termed *associated* flow (meaning the plastic strain vector lies perpendicular to the yield surface), the viscous stress must be purely deviatoric and lie perpendicular to the yield surface (between the total internal stress state and the internal yield state). The viscous stress is often alternatively referred to as the *overstress*, referring to its magnitude being the radial distance perpendicular from the yield surface to the total internal stress state.

The Von Mises stress represents the magnitude of the total deviatoric internal stress state (radius from the hydrostatic axis to the total internal stress state). The deviatoric magnitude of the yield state is the radius of the yield surface. The radius of the yield surface is shown to be $\sqrt{2/3}$ of the uniaxial yield stress (Appendix A, Equation 8-5). As a result of this the Von Mises stress represents the magnitude (norm) of the stress deviator tensor multiplied by a factor of $\sqrt{3/2}$ (Appendix A, Equation 8-6). This aligns it with a materials stated uniaxial tensile yield stress to determine if a yield state has been reached. Bearing this in mind then a factor of $\sqrt{2/3}$ must also be applied back to the Von Mises stress to represent the radial deviatoric stress magnitude of the total internal stress state. The magnitude of the viscous stress then can be represented as in Equation 3-6.

$$\sigma_{vis} = |S| - radius = \sqrt{2/3}\,\sigma_{vm} - \sqrt{2/3}\,\sigma_y$$

Equation 3-6

Should a viscoplastic strain rate magnitude, as a function of viscous stress be defined (in a form later to be determined), it is then necessary to compute the multiaxial plastic flow from it. As stated earlier and illustrated in Figure 3-4, the flow should be perpendicular to the yield surface in principal strain space; the same direction as the vector formed by the principal deviatoric stresses. The multiaxial plastic flow or creep strain rate, $\dot{\varepsilon}_{ij}^{cr}$, is then defined in Equation 3-7.

$$\dot{\varepsilon}_{ij}^{cr} = \dot{p} n_{ij}$$

Equation 3-7

The tensor, n_{ij}, is the flow direction tensor, which when multiplied by the viscoplastic strain rate magnitude, $\dot{p}$, gives the creep strain rate tensor, representing multiaxial creep strain rate. As the direction of the flow is in the same direction as a vector formed by the principal stresses of the stress deviator tensor (perpendicular to the yield surface); the flow direction tensor can be defined directly from the stress deviator tensor as in Equation 3-8. It should also be noted the creep strain rate tensor, $\dot{\varepsilon}_{ij}^{cr}$, is naturally also a symmetric tensor, and may also be represented as a vector of principal strain rates in principal strain rate space.

$$n_{ij} = \frac{1}{\sigma_{vm}}\frac{3}{2}S_{ij} = \sqrt{\frac{3}{2}}\frac{\underline{\underline{S}}}{\left\|\underline{\underline{S}}\right\|} = \sqrt{\frac{3}{2}}\frac{S_{ij}}{\sqrt{S_{ij}S_{ij}}}$$

Equation 3-8

As the Von Mises stress is the denominator in Equation 3-8, it is equivalent to dividing the stress deviator tensor S_{ij}, by its norm, as shown (its vector magnitude when considering principal stresses). When considering the stress deviator tensor as a vector in principal stress space the flow direction tensor becomes a vector $\sqrt{3/2}$ times the stress deviator unit vector.

Substituting the middle form of Equation 3-8 into Equation 3-7, implies further that the strain rate parameter $\dot{p}$, is equal to the norm of the viscoplastic (creep) strain rate. In fact the viscoplastic strain rate magnitude, $\dot{p}$, is often referred to as the norm or length of the viscoplastic strain rate. It is also often known as the viscoplastic multiplier, as it relates the direction of plastic flow to the rate of plastic flow.

$$\dot{p} = \sqrt{2/3}\left\|\underline{\underline{\dot{\varepsilon}}}^{cr}\right\| = \sqrt{2/3\,\dot{\varepsilon}_{ij}^{cr}\dot{\varepsilon}_{ij}^{cr}}$$

Equation 3-9

The above descriptions detail the main processes with which constitutive viscoplastic theory is applied conceptually and mathematically to ultimately describe a multiaxial creep strain rate in a material at a given point. In most Finite Element (FE) software packages this is the methodology used. The total internal stress state at various points throughout the modelled structure is converted into hydrostatic and deviatoric components. The Von Mises stress is computed, and should it exceed

the uniaxial tensile yield stress at each subsequent time increment of the analysis, at any point in the material, the flow direction is computed. The user will define, or there will be an in built algorithm for the viscoplastic strain rate norm, $\dot{p}$, as a function of the Von Mises stress and temperature, and possibly accumulated plastic strain. This will also be computed at each time step by the software. The user therefore is responsible for determining a uniaxial creep strain rate function, through which the Von Mises stress is used in place of a directional stress component. Finally a creep strain rate tensor will be formed from Equation 3-7; this allows the deformation to be computed explicitly for the forth coming time increment. If at various points throughout the modelled structure, equilibrium cannot be found with respect to the numerous computed nodal displacements, an implicit numerical integration method is used to find the optimal equilibrium nodal displacements at the end of that time increment possible. This generally involves directly computing nodal displacements over the time increment from the creep strain rate tensor and then continually adjusting in an incremental manner to find the least energy orientation of all nodal displacements.

The software does not compute a viscous stress; the flow rate, $\dot{p}$, is computed from experimentally observed functions of the Von Mises stress as stated above. Such forms are often based around those presented in Section 2.3 (Equation 2-7, Equation 2-8 and Equation 2-9). Plastic yield data is commonly input into FE software by the user as a material definition, such data though is typically obtained from classical measurements not accounting for viscous stress. Any computation of viscous stress from the total internal stress state, as well as this yield data would then be inaccurate (theoretically zero). As a result classical plasticity and viscoplasticity are generally considered separately in FE software packages such as Abaqus, when both are input as material data. Whichever plasticity model produces the greatest inelastic strain within a given time increment is used. In order to compute viscous stress a set of inelastic stress-strain curves as function of strain rate as well as temperature would in some way have to be determined through material creep tests.

The following Section 3.2.1 presents details of some of the more fundamental points relating to constitutive viscoplastic theory and formation. This is primarily for reference, but within is highlighted idealised representations of the gradient of the viscoplastic potential (creep strain rate) as a function of viscous stress. It is hoped these forms with constants determined utilising a least energy approach could yield more theoretically concise and accurate viscoplastic gradient functions (creep strain rate functions). The use of a least energy approach in this manner, to determine constants, may also allow constants to be computed as a function of strain rate themselves (possibly allowing Laplace transforms to utilised), or as functions of temperature or stress, thus allowing creep strain rate functions operable over a wide range of strain rates to be determined. This may inform more accurate determination of uniaxial yield stress curves as a function of strain rate as well as temperature, allowing a more holistic approach to material and structural plastic behavioural modelling and accountability. The above procedures would require experimentally determined creep strain rates.

3.2.1 Constitutive viscoplasticity theory

It was mentioned in the introduction to Chapter 3, that the creep strain rate magnitude $\dot{p}$ is often labelled the gradient of the *viscoplastic potential*. The creep strain rate tensor representing

viscoplastic flow in Equation 3-7 is more precisely defined within viscoplastic theory from a viscoplastic potential function, Ω (Equation 3-10). The viscoplastic strain rate norm, $\dot{p}$, is defined as the gradient of this potential function with respect to the viscous stress magnitude (Equation 3-11). This is much like the gravitational acceleration, g, is the gradient of the gravitational potential, φ, ($=gz$) with respect to position, z. The flow direction tensor, n_{ij}, is then the rate of change of the viscous stress with respect to each individual stress component (Equation 3-12).

$$\dot{\varepsilon}_{ij}^{cr} = \frac{\partial\Omega(\sigma_{vis})}{\partial\sigma_{ij}} = \frac{\partial\Omega(\sigma_{vis})}{\partial\sigma_{vis}}\frac{\partial\sigma_{vis}}{\partial\sigma_{ij}} = \dot{p}n_{ij}$$

Equation 3-10

$$\dot{p} = \frac{\partial\Omega(\sigma_{vis})}{\partial\sigma_{vis}}$$

Equation 3-11

$$n_{ij} = \frac{\partial\Omega(\sigma_{vis})}{\partial\sigma_{ij}}$$

Equation 3-12

Possible representations for the gradient of the viscoplastic potential, $\dot{p}$, will be discussed and presented in the following sections. However a few potential options and considerations in determining a relation between creep strain rate and the viscous stress will be outlined here first. As mentioned in Section 2.3, typically creep strain rate appears proportional to a power or exponential function of the applied stress. It may then be considered that a uniaxial model as a function of viscous stress should have similar dependence (Equation 3-13 and Equation 3-14).

$$\dot{p} = \dot{\varepsilon}_0 \langle\frac{\sigma_{vis}}{D}\rangle^n$$

Equation 3-13

$$\dot{p} = \dot{\varepsilon}_0 \langle exp\left(\frac{\sigma_{vis}}{D}\right) - 1\rangle$$

Equation 3-14

The parameter, D, is a constant with units of stress, and known as the *drag stress*, whilst $\dot{\varepsilon}_0$, is a *rate constant* with units of t^{-1}. The Macaulay brackets in Equation 3-13 and Equation 3-14 represent that should the viscous stress drop below zero (and the stress state into the elastic domain), the bracket then becomes zero and thus strain rate becomes zero. It should be noted, the subtraction of 1, in Equation 3-14, is necessary to ensure that should the viscous stress drop to zero, the creep strain rate also drops to zero (given that, $e^0 = 1$).

Briefly, referring back to Equation 3-3, an effective dynamic viscous drag coefficient, c, can be deduced, if desired, to fit with the conceptual one dimensional model of Figure 3-1, and the equation of motion, Equation 3-5. Considering Equation 3-3 in stress form and rearranging Equation 3-13 and Equation 3-14 to represent the viscous stress, σ_{vis}, as a function of plastic strain rate norm,

$\dot{p}$, and then dividing by $\dot{p}$, gives the following definitions shown in Equation 3-15 and Equation 3-16 for effective dynamic viscous drag coefficients, *c*.

$$c = \frac{D}{\dot{p}}\left(\frac{\dot{p}}{\dot{\varepsilon}_0}\right)^{1/n}$$

Equation 3-15

$$c = \frac{D}{\dot{p}}\ln\left(\frac{\dot{p}}{\dot{\varepsilon}_0} + 1\right)$$

Equation 3-16

In order to complete the equation of motion in Equation 3-5, all that would remain is for the elastic stiffness constant, *k*, to be defined. This would have to be a function of temperature.

Equation 3-13 and Equation 3-14 are forms that directly relate viscous stress to the gradient of the viscoplastic potential (creep strain rate). These forms however, as previously stated are not practical without knowledge of the true, strain rate dependent, yield stress. The extension of Equation 3-13 and Equation 3-14 towards practical use is discussed in more detail within Appendix B; Creep strain rate functions of viscous stress. For now, the further discussion of creep strain rate as a function of viscous stress is beyond the scope of this thesis.

3.3 Existing representations of the flow rate

As stated in Section 3.2, in order for finite element software to compute viscous stress for use in a creep model, accurate yield stress data derived using viscoplastic assumptions is required. Commonly yield curves as a function of temperature are determined classically where the internal yield state is assumed to match the total applied stress state. Standard forms of flow rate or creep strain rate magnitude for practical use are then typically based around uniaxial power law or exponential forms (power law breakdown) using equivalent Von Mises stress. The choice of which law to use is based around anticipated stress exposure ranges. Often the two representations of stress dependence are combined using a hyperbolic sine function of stress, which reduces to a power law at low stresses, and an exponential at higher stresses, as described in Section 2.3.2 Equation 2-9.

The commercial FE software package Abaqus, used in this thesis, offers a range of in-built algorithms for modelling the uniaxial creep strain rate in both primary and secondary regimes. The flow rates obtained are converted into a multiaxial creep strain rate tensor via the methods outlined in Section 3.2. These uniaxial creep strain rate functions are listed below in Equation 3-17, Equation 3-18 and Equation 3-19 .

$$\dot{p} = A\sigma_{vm}^{n}t^{m}$$

Equation 3-17

$$\dot{p} = (A\sigma_{vm}^{n}[(m+1)p]^{m})^{1/m+1}$$

Equation 3-18

$$\dot{p} = A(\sinh B\sigma_{vm})^{n} exp\left(\frac{-Q_c}{RT}\right)$$

Equation 3-19

As used previously, σ_{vm}, is the equivalent Von Mises stress, p, is the magnitude of the accumulated creep strain ($\dot{p}$, is the creep strain rate magnitude), Q_c, is the creep *activation energy* and T, is temperature in Kelvins. The parameters A, B, n and m are stress and/or temperature dependant constants. The constant, m, is used to predict hardening behaviour, either in a time hardening manner (Equation 3-17) or a strain hardening manner (Equation 3-18). The constant, n, is typically stress dependant; rising with increasing stress. Equation 3-19 is the only one with explicit temperature dependence; in the other forms constants must be tabulated with temperature. It is still possible to include the Arrhenius relationship within those forms by incorporating it within the constant A, and tabulating.

In order to use the algorithms effectively, constants must ideally be determined from experimental data. In the time and strain hardening cases, represented by Equation 3-17 and Equation 3-18, when stresses are high, the constant n, will rise whilst the constant A, can very often be very small causing numerical difficulties in many FE software packages.

The hyperbolic sine model Equation 3-19, is deliberately included in the Abaqus FE software package for situations where there may occur localised high stress concentrations and an algorithm is required to be able to account for a wider stress range. Again, at high stress it tends towards a power law breakdown form as in Equation 2-8, whilst at lower stresses reduces towards a form of power law similar to Equation 2-7. Equation 3-19 then provides a versatile in-built means of modelling creep should sufficient experimental data exist to determine constants. Some of these constants can also be tabulated using stress as an additional field variable via a *user defined field* subroutine if required. In order to define hardening and possibly softening effects in Equation 3-19, this must be done by tabulating with respect to a field variable; for strain hardening this field variable is plastic strain. This again requires a user defined field subroutine, extracting this strain from the model as a means to reference against tabulated data. Should any of the constants be desired to be tabulated with temperature in Equation 3-19, despite the Arrhenius function, it is also necessary to do this through a user defined subroutine.

3.3.1 Harmathy model

Harmathy [7] presents an algorithm for predicting accumulated creep strain in steels based around two stress dependent parameters and *temperature compensated time*. In this manner, accumulated creep strain can be predicted at any time, temperature and stress from one set of axes. The temperature and time variables are combined into one master variable, θ, known as the aforementioned temperature compensated time. This is displayed in Equation 3-20 as defined by Sherby and Dorn [24], with units of time.

$$\theta = \int_0^t exp\left(\frac{-Q_{cr}}{RT}\right) dt$$

Equation 3-20

At constant temperature the integral is not necessary, and the temperature compensated time becomes the time multiplied by a constant defined by the Arrhenius relationship. Conceptually, temperature compensated time could be viewed as measuring time as an accumulation of temperature induced material effects (e.g. cumulative vacancy assistance) on the restoration process or creep. Harmathy [8] presents accumulated creep strain evolution over temperature compensated time, θ, rather than real time.

The first stress dependant parameter is the Zener Hollomon parameter, Z, [25] with units of, t^{-1}, representing the gradient or rate of secondary creep strain accumulation with temperature compensated time, θ. The second parameter, $\varepsilon_{cr,0}$, represents the intercept of steady state secondary creep with the strain axis. The nature of these parameters is displayed with respect to temperature compensated time versus accumulated creep strain master curves (combining the time and temperature components) as shown in Figure 3-5.

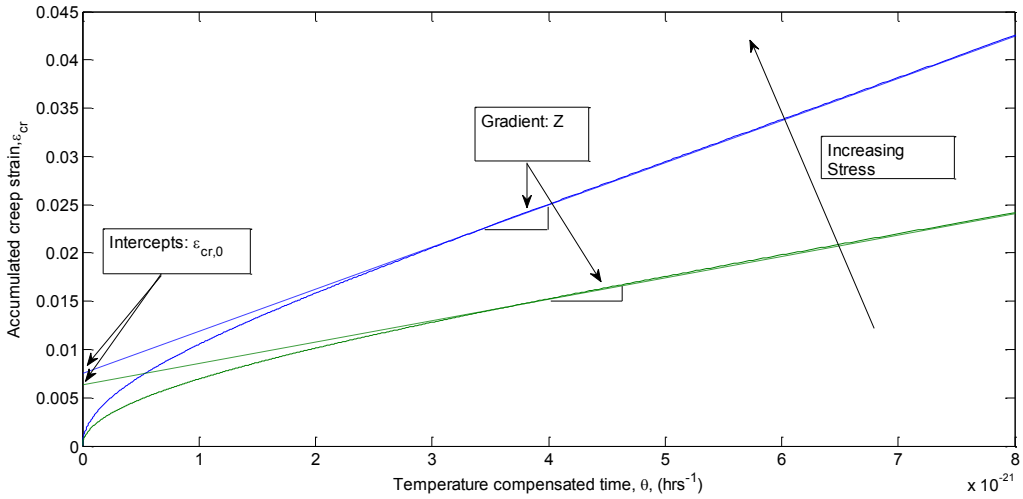

Figure 3-5; Secondary or steady state creep paramters

The Zener Hollomon parameter (gradient of Figure 3-5), Z, and the creep strain intercept, $\varepsilon_{cr,0}$, are found to increase with stress. Experiments by Harmathy and Stanzak [7] and Gales [6] have deduced the following stress relations for the Zener Hollomon parameter and creep strain intercept for prestressing steel wires manufactured to the American ASTM A421 [26] and ASTM A416 [10] standards as well as the British BS 5896 [11] standard in Table 3-1.

Steel type	Z	$\varepsilon_{cr,0}$
ASTM 421 [26]	$8.21 * 10^{13} exp(0.0145\sigma)$ Range:- (172MPa<σ<690MPa) [7]	$9.26 * 10^{-5}\sigma^{0.67}$ Range:- (172MPa<σ<690MPa) [7]
ASTM 416 [10]	$2.7 * 10^{13} exp(0.012\sigma)$ Range:- (690MPa<σ<1000MPa) [6]	$1.13 * 10^{-7}\sigma^{1.63}$ Range:- (690MPa<σ<1000MPa) [6]
BS 5896 [11]	$1.6 * 10^{12} exp(0.013\sigma)$ Range:- (690MPa<σ<1000MPa) [6]	$1.51 * 10^{-14}\sigma^{3.9}$ Range:- (690MPa<σ<1100MPa) [6]

Table 3-1; Expreimentally determined Zener Hollomon and creep strain intercept parameters

It should be noticed the Zener Hollomon parameter is identical to the power law breakdown secondary creep stress dependence described in Section 2.3.2. As such it can be seen from Figure 3-5, creep strain accumulation beyond the primary creep phase can be predicted through Equation 3-21. Differentiating by time this is identical to the empirically observed power law breakdown secondary creep form Equation 2-8.

$$\varepsilon_{cr} = z\theta + \varepsilon_{cr,0} = Aexp(B\sigma)\theta + \varepsilon_{cr,0}$$

Equation 3-21

Harmathy's uniaxial model is said to be able to represent both transient primary creep and secondary creep strain behaviour as a function of only these two secondary creep parameters ($\varepsilon_{cr,0}$ and *Z)* and temperature compensated time; this equation is displayed as Equation 3-22.

$$\varepsilon_{cr} = \frac{\varepsilon_{cr,0}}{\ln 2} \cosh^{-1} 2^{\left(Z\theta/\varepsilon_{cr,0}\right)}$$

Equation 3-22

Therefore entire primary and secondary creep curves can be determined from stress, temperature and time without any knowledge of accumulated strain effects. The justification for this revolves around assuming an effective hardening function can be determined solely as a function of the ratio of the accumulated creep strain, to the secondary creep strain intercept, $\varepsilon_{cr,0}$. This justification and derivation of Harmathy' Equation 3-22 can be viewed in [8]. This effective hardening function tends towards unity as accumulated creep strain evolves and thus Equation 3-22 tends towards Equation 3-21.

The accountability for primary creep strain and the reduction to a secondary creep model with evolving creep strain accumulation is more easily considered if Harmathy's Equation 3-22 is

converted into a rate form through differentiating with respect to time as in Equation 3-23. If the exponential form of the Zener Hollomon parameter is substituted into Equation 3-23, then it can be seen from Equation 3-24, Harmathy's equation is in fact the secondary creep strain rate form with the addition of a form of an effective *hardening parameter*.

$$\dot{p} = zexp\left(\frac{-Q_c}{RT}\right)\frac{X}{\sqrt{X^2-1}}; \quad X = 2^{z\theta/\varepsilon_0}$$

Equation 3-23

$$\dot{p} = Aexp(B\sigma)exp\left(\frac{-Q_c}{RT}\right)\frac{X}{\sqrt{X^2-1}}; \quad X = 2^{z\theta/\varepsilon_0}$$

Equation 3-24

This hardening parameter is a function itself of the secondary creep parameters the Zener Hollomon parameter, Z, and the secondary creep strain intercept, $\varepsilon_{cr,0}$, as well as temperature compensated time, θ. As the factor, X, becomes increasingly large, this parameter tends towards unity and Equation 3-23, tends towards the standard secondary creep form. It should be noted however this can be problematic when modelling, as a divide by zero is created at zero time as X, becomes equal to one. It is convenient to view the Harmathy Equation 3-22, in rate form (Equation 3-23), not least to visualise its relation to standard creep forms, but also as this form is required in most Finite Element (FE) software packages, if it is to be included via a user defined subroutine.

The Harmathy equation then appears to apply a generic primary creep strain and time hardening fitted curve to any secondary creep model based on its gradient and intercept with respect to temperature compensated time. That they can be combined in such a manner, said to predict primary creep strain behaviour in an identical form, and appear remotely accurate regardless of type of steel, stress and temperature range is dubious. Any perceived accuracy is more likely an indication that transient creep strains resulting from dislocation motion, leading to strain hardening are generally small in comparison to total creep strain. This is particularly true for high-yield, high-dislocation density metals, represented by a power law breakdown type secondary creep models (Equation 2-8). It would be interesting to see how Equation 3-22 or Equation 3-23 would hold as the stress dependence tends towards a power law secondary creep model, with a potentially more significant primary creep phase. The hardening multiplier is essentially a logarithmic fit between zero strain and the point at which it is anticipated steady state creep will ensue. The parameters, Z, $\varepsilon_{cr,0}$, and θ, could directly and indirectly represent the main material factors dictating transient primary creep, these factors being dislocation density and vacancy concentration. But the precise evolution of creep strain rate with accumulated creep strain through the primary creep phase should be determined on a case by case basis, should the primary phase be of significant concern.

If Equation 3-21, representing secondary creep strain accumulation is differentiated with respect to time this yields the secondary or minimum creep strain rate form identical to Equation 2-8. A more appropriate way to represent the transient creep strain phase may be to modify the constant B, treating its inverse as a form of *drag stress* as in Section 3.2.1, such that $D=1/B$ (Equation 3-13 and Equation 3-14). This may be represented as a function of accumulated plastic or creep strain, ε_{cr} (noted p in previous constitutive theory discussion). In this manner, the Zener Hollomon parameter would evolve towards its steady state values represented in Table 3-1, as creep strain accumulates.

The drag stress would be formed on an individual material basis improving accuracy, but its evolution with accumulated creep strain has to be experimentally determined. The term 'drag stress' then relates to the effective viscous drag on creep strain rate, a larger drag stress means slower rate and vice versa; the drag naturally increasing as dislocations pile up till it reaches a steady state value.

For example it is relatively easy to equate evolving creep strain from Equation 3-22 to Equation 2-8 and record the variation of the parameter *B*, required to maintain creep strain rate using Matlab. Figure 3-6 shows such an evolution plotting the evolution of *D*, and *B* (as represented in Equation 2-8), with accumulated creep strain for ASTM A421 [26] standard prestressing steel, through equating Equation 2-8 to Harmathy's Equation 3-22 at constant applied stress and transient heating of 5°C per minute. The Zener Hollomon parameter *Z*, for this steel is taken as displayed in Table 3-1. It is observed that the inverse of the drag stress *B*, tends towards the value 0.0145, as noted in the Zener Hollomon parameter for ASTM A421 [26] standard steel in Table 3-1. Harmathy's Equation 3-22 then does indeed tend towards the form of Equation 2-8, representing steady state secondary creep, as creep strain accumulates. Both transient and steady state creep then can be predicted with an appropriate strain dependant evolution of the factor *B*, through Equation 2-8.

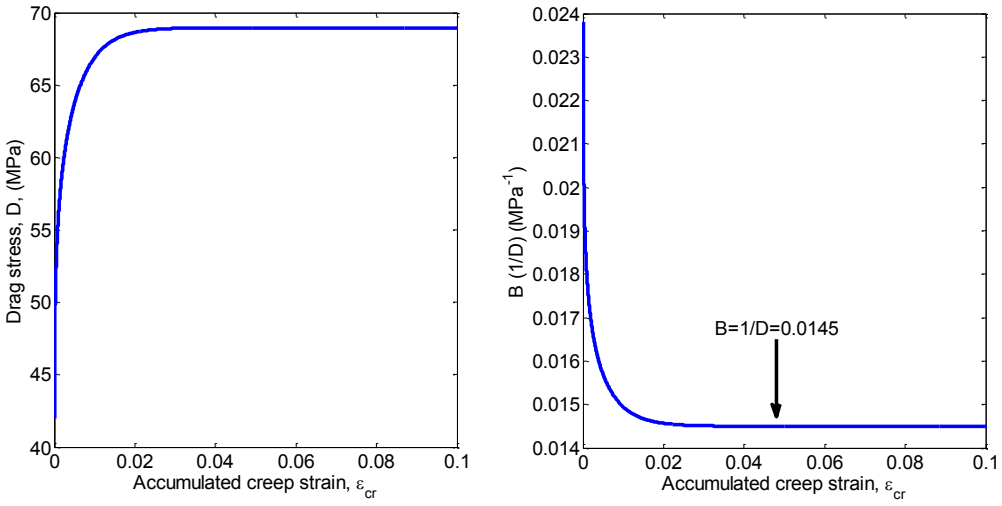

Figure 3-6; Evolution of drag stress through primary to secondary creep

3.4 Summary

The constitutive viscoplastic model presents a macroscopic, conceptual analogy, to the internal processes giving rise to creep. This is visualised by a spring representing linear elastic behaviour connected in series with a friction slider which in turn is connected in parallel to a damping pot (Figure 3-1). The constitutive representation involves a yield state which evolves with the friction slider, in parallel with an effective viscous stress state, being the equivalent stress across the damping pot. This viscous stress represents a stress state resulting from ongoing internal motion and restructuring. Creep strain rate then relates to the viscous stress associated to the viscoplastic potential of the damping pot, just as kinetic energy of the deformation relates to the square of the deformation rate. A very important point from this chapter is that the total stress state is made up of

these two stress components; yield stress and viscous stress. In classical plasticity as external stress rises so does the yield stress state in unison; if creep is ignored in certain situations then so is viscous stress, and the yield state and load capacity of the material as a function of temperature may be overestimated.

As was mentioned in the introduction to this thesis, and presented in this chapter, constitutive relations exist for the multiaxial representation of creep, subject to input of a function representing the magnitude or norm of the multiaxial creep strain rate, $\dot{p}$. This function is generally a uniaxial creep strain rate function of stress and temperature, in which a deviatoric stress component such as the Von Mises stress is used in place of a directional stress component. From the perspective of the constitutive model this should be a function of viscous stress, however this has been shown to be of difficulty practically. When an appropriate uniaxial creep strain rate function with respect to stress, temperature and accumulated inelastic strain is determined experimentally, this can be incorporated within a multiaxial constitutive framework to predict multiaxial creep deformation rate. This is most easily done numerically within a commercial FE software package that has this general constitutive framework in-built, requiring only input of the uniaxial function.

Empirical forms for uniaxial creep strain rate in metals generally relate to the forms described in Chapter 2; these being the power law or power breakdown representations most commonly observed. Harmathy [8] developed a comprehensive primary and secondary creep representation, which in strain rate form is compatible with the standard constitutive model and framework. The means of representing primary creep essentially involves the addition of a hardening parameter multiplied to a standard power law breakdown representation of secondary creep strain rate. The justification behind the formation of this hardening parameter is dubious, however constants have been developed equating this function to experimental creep strain data for numerous prestressing steels (Harmathy and Stanzak [7], Gales [6]).

4 Modelling stress relaxation in pre stressed steel tendons exposed to elevated temperature

The last two chapters detailed creep from a phenomenological perspective and a constitutive perspective. In particular the process required to explicitly account for creep in a multiaxial framework was detailed. With respect to numerical modelling this process requires the specification of a uniaxial creep strain rate function capable of representing the creep strain rate magnitude. Section 3.3 presented explicit representations for the norm or the magnitude of creep strain rate, both in-built within the commercial FE software package Abaqus, as well as representations based and adapted around empirical observation (Section 2.3). An example of this is the Harmathy [8] uniaxial model (Equation 3-22). Therefore the means exist to explicitly account for creep in prestressing steel tendons and other metals subject to experimental determination of constants. Fortunately, regarding prestressing steel, such constant determination has been performed with respect to the Harmathy uniaxial model [6] [7] (Table 3-1).

The remainder of this thesis focusses on explicitly modelling the effect of creep in prestressing steel tendons on the structural behaviour during fire of Unbonded Post Tensioned (UPT) concrete structures. All modelling studies herein are performed in the commercial FE software package Abaqus. This chapter focusses in particular on the following two points detailed in the introduction to this thesis.

- To determine and validate an appropriate explicit creep strain rate magnitude representation, for inclusion in the material definition of prestressing steel tendons within UPT concrete structural FE models.

- To ascertain whether design code (Eurocode 2 [1]) stress-strain curve, temperature reduction factors, for prestressing steel are sufficient to implicitly account for creep during transient heating.

In order to validate an explicit uniaxial creep strain rate algorithm within an FE model, experimental data must be sourced as a benchmark, and the experimental procedure mimicked within the FE model. MacLean [9] performed a series of experiments observing stress relaxation of isolated and then tensioned, prestressing steel tendon strands subject to various heating protocols. Steel tendons for prestressing concrete are typically formed from six steel wires cold drawn from high-tensile-grade steel (high-tensile yield strength), woven helically about a seventh central wire of a slightly larger diameter. The manufacturing process of tendon wires and strands, and their respective properties is covered in Section 4.1.

As the tendons are tensioned to a fixed length and therefore a fixed total strain prior to being heated, the accumulation of thermal strain must be accompanied by a reduction of elastic mechanical strain to maintain the total fixed strain. This requires the tensile stress applied to relax. Stress relaxation is covered in more detail in Section 4.2 through consideration of the individual strain components making up the total fixed strain.

MacLean's [9] experiments were performed on grade 1860 (1860MPa tensile yield strength) prestressing steel tendon strands manufactured to the ASTM A416 [10] standard; the experimental protocol is overviewed in Section 4.3. Gales [6] has subsequently determined Zener Hollomon and creep strain intercept parameters (Table 3-1) for use within the Harmathy [8] uniaxial creep strain rate model (Equation 3-22), also for grade 1860 ASTM A416 prestressing steel; all be it determined on wires (manufactured to the same design code) as opposed to strands. The difference in yield strength between wires and strands can be minimised through thermal treatment during strand manufacture. Differences do however exist in elastic modulus between wires and strands that must be considered when applying data obtained from tests on wires, to strands. This is explained in more detail in Section 4.1.

The existence of this experimental data therefore provides a unique opportunity to perform a validation study of an FE prestressing steel tendon model, explicitly considering elevated temperature creep. The experimental tendon stress relaxation curves, recorded over time by MacLean [9] (from an initial ambient applied stress of 1008 MPa), presented in Section 4.3 can be used as a benchmark for the output of models based on the experimental protocol. Following such validation the ability of Eurocode 2 [1] stress-strain temperature reduction factors to account for transient heating creep strain accumulation can be assessed. Here temperature dependent stress-strain curves are computed from the Eurocode 2 [1] guidelines and reduction factors, and input into the prestressing steel material model, in place of the explicit creep model.

It can be observed from Table 3-1, creep parameters (Zener Hollomon and creep strain intercept) have also been determined for other standard prestressing steels. These are by Harmathy and Stanzak [7] for prestressing steel to the ASTM A421 [26] standard and again by Gales [6] for grade 1860 BS 5896 [11] standard prestressing steel. They all however show a different creep strain rate response to stress and temperature (hence the differing creep parameters determined). Therefore in addition to the stated aims of this chapter, an added aim is to study the respective creep and resulting stress relaxation response under heating, at a fixed extension, of the different standards of prestressing steel. The parameters determined by Harmathy and Stanzak [7] do however date back to 1970 and were determined in an applied tensile stress range peaking at 690MPa, this is far below the operational tensioning stress of prestressing tendons in UPT concrete structures. As a result this steel is not considered in the rest of this thesis.

4.1 Tendon properties and manufacturing

Steel tendons for use in prestressing concrete are formed from winding six prestressing steel wires helically about a seventh wire to form a tendon *strand*. These wires are typically cold-drawn from high tensile yield steel rods. The process of cold-drawing will be describes shortly. The manufacturing process of the tendon strand firstly involves the formation of rods of steel, with a particular chemical composition suitable to high-yield functionality. This often involves carbon content in the range of 0.8% and subtle variations in manganese and silicon to influence mechanical properties as desired [9]. The basic composition of the rods is formed through a process of heating and slowly cooling steel. The heating is sufficient to activate a eutectoid reaction at a given

temperature whereby on cooling back below this temperature a homogeneous microstructure, consisting of alternating layers of *ferrite* (pure iron) and *cementite* (F_3C) is formed. This matrix is known as *pearlite* with ferrite forming the abundance of the micro structure by weight. The temperature whereby the eutectoid reaction takes place is approximately 720^{o}C with a carbon content of 0.8% (the transition temperature varies with carbon content). The pearlite grains are often of a platelike or elongated in form; this makes them particularly suited to cold drawing and aligning in a particular direction [9].

The formation of wires for stranding, as mentioned above, involves their being cold-drawn from the larger diameter rods. The process of cold drawing involves the steel rods being drawn through a series of dies, of ever smaller diameter, to form a wire of the desired diameter. This drawing process further increases the tensile yield strength, through strain hardening. Following this the wire is subjected to a *thermo-mechanical* treatment to improve relaxation properties [9]. A strand is formed through weaving six strands of identical diameter helically about a seventh wire of slightly larger diameter (an image of a tendon strand can be viewed in Section 4.3, Figure 4-4). It is likely that residual contact stresses between the wires will emerge as a result of the weaving process; this may result in localised stress concentrations within the strand on application of load, and alter the yield characteristics from that of the wire. This is alleviated through a further thermo-mechanical treatment involving heating the strand to 350^{o}C for a specified period of time [9] under tension. This ensures tensile load on the strand is transferred uniformly through the wires, assuming no other manufacturing defects exist. Minimum tensile yield for strands is therefore quoted as the same as that for wires. Elastic modulus is however generally not the same between wires and strands. The weaving process creates an inherent torsion within the strand and thus a degree of elastic unwinding can occur under tensile load; this effectively reduces the stiffness of the tendon. Typical differences in elastic modulus between wires and strand are around 10GPa; for example BS 5896 [11] states 205GPa may be used for design purposes involving wires, and 195GPa for strands.

Often wires and strands for prestressing concrete are manufactured and delivered to a particular grade characterised by their tensile yield strength. The chemical composition of grade 1860 (1860MPa tensile yield stress) wires manufactured to ASTM A416 [10] and BS 5896 [11] standards as used by Gales [6] in transient heating tensile creep tests are listed below in Table 4-1.

Chemical	ASTM A416	BS 5896
Carbon (C)	0.8%	0.9%
Chromium (Cr)	0.04%	0.011%
Manganese (Mn)	0.868%	0.66%
Phosphorus (P)	0.023%	0.007%
Silicon (Si)	0.450%	0.25%
Sulphur (S)	0.12%	0.014%
Nickel (Ni)	-	0.021%
Copper (Cu)	-	0.011%

Table 4-1; Chemical composition of prestressing steel tendon wires as used in transient creep tests by Gales [6].

BS 10020:2000 [27] to which BS 5896 [11] refers, issues guidelines as to permissible chemical composition ranges and maximum or minimum values of particular elements to define rods suitable to a particular purpose. It does not however specify precise compositions. This means it could be possible for tendon-wires and strand manufactured to the same standard code to have differing

chemical composition depending on the supplier of the product. Both ASTM A416 [10] and BS 5896 [11] specify maximum isothermal relaxation losses, in terms of force, of 2.5% at when loaded to 70% of the tensile breaking force for wires and strands, over 1000 hours of loading. At 80% of the maximum breaking force however, ASTM A416 [10]specifies maximum relaxation of 3.5% whilst BS 5896 [11] specifies 4.5%. In both cases the isothermal test temperature is ambient 20^{o}C, therefore elevated temperature relaxation properties may still vary significantly dependent on chemical composition. Table 4-1 shows the marked difference in chemical composition between grade 1860 ASTM A416 [10] and BS 5896 [11] standard steel used by Gales [6]. It was noted in the introduction to this chapter, the creep parameters as a function of stress determined by Gales [6] in transient heating tensile load tests varied between both the above standard prestressing steel wires. The manufacture of both grade 1860 wires and strands to ASTM A416 [10] and BS 5896 [11] standards appear very similar; each involving cold-drawing from rods, followed by a thermo-mechanical treatment. A difference in elastic modulus as a function of temperature could influence creep strain rate as 'looser' inter-atomic bonds would permit easier motion of dislocations and subgrains about obstacles. BS 5896 however states the ambient elastic modulus for wires may be taken as 205GPa [11] whereas tests by MacLean performed separately on six individual ASTM A416 [10] standard wires noted an average elastic modulus of 214GPa [9]. BS 5896 [11] standard wires however were less susceptible to creep strain accumulation with stress and temperature than their ASTM A416 [10] counterparts as tested by Gales [6]. Temperature dependent elastic modulus is however not specified with respect to either steel.

The difference in creep strain rate response to stress at a given temperature could then be due to the chemical composition of the rods used to draw the wires. Typically steel rods supplied for manufacture of high strength steel such as springs, electrodes or tyre cords are required to have low contents of phosphorus and sulphur [27]. It is however worth noting that increasing phosphorus and sulphur content is said to improve *drawability* [9]. The percentage weight of these two constituents is markedly larger in the ASTM A416 [10] standard wires tested by Gales [6] as compared to the BS 5896 [11] standard wires (Table 4-1). Impure alloying elements often act as energy barriers (Sections 2.1.3, 2.2.1 and 2.2) against internal motion or in some cases can ease internal motion. Various elements therefore are often incorporated into a steel to influence its ductility and yield behaviour. It should be no surprise therefore that variation in alloying elements included in steel or their respective concentrations will influence the rate with which a materials internal energy barriers are alleviated. Any definitive judgement at this stage as to the magnitude of the difference certain element concentrations may make however, can only be postulated.

4.2 Stress relaxation in post-tensioned tendons

When a tendon is extended to a fixed length by the application of a tensile load, and held at this length, then a fixed elastic strain is achieved; assuming the applied stress does not exceed elastic yield. If the length of the tendon is to be held constant, whilst being heated, additional strain components such as thermal strain and potentially inelastic strains will be accumulated. The tendon length is however being held constant, and therefore despite these additional strain components accumulating, total strain remains fixed. Inelastic strains, such as creep strain, may accumulate if the

elastic yield strength of the tendon drops with temperature, below the tensile stress being applied to maintain the fixed length. Considering the total sum of all the strain components is fixed, a strain equilibrium equation can be formed, as in Equation 4-1.

$$\varepsilon_0 = \varepsilon_{el}(\sigma, T) + \varepsilon_{pl}(\sigma, T, t) + \varepsilon_{th}(T)$$

Equation 4-1

In Equation 4-1, ε_0, represents the fixed strain of the tendon, ε_{el}, represents the elastic strain component, this is a function of stress and temperature , ε_{pl}, represents all plastic strains, including creep strain (hence it is also a function of time), whilst ε_{th}, represents the accumulated thermal strain through heating. Any plastic strain that accumulates during heating is irreversible, whilst thermal strains can only be removed through cooling. Therefore as the total fixed strain, ε_0, is constant, if inelastic straining ensues during heating, the elastic mechanical strain must reduce to maintain equilibrium. In order to achieve this, the applied tensile stress, maintaining the tendons length, must reduce or *relax*. This can be visualised by considering the total fixed strain, ε_0, on a stress-strain curve, as shown in Figure 4-1.

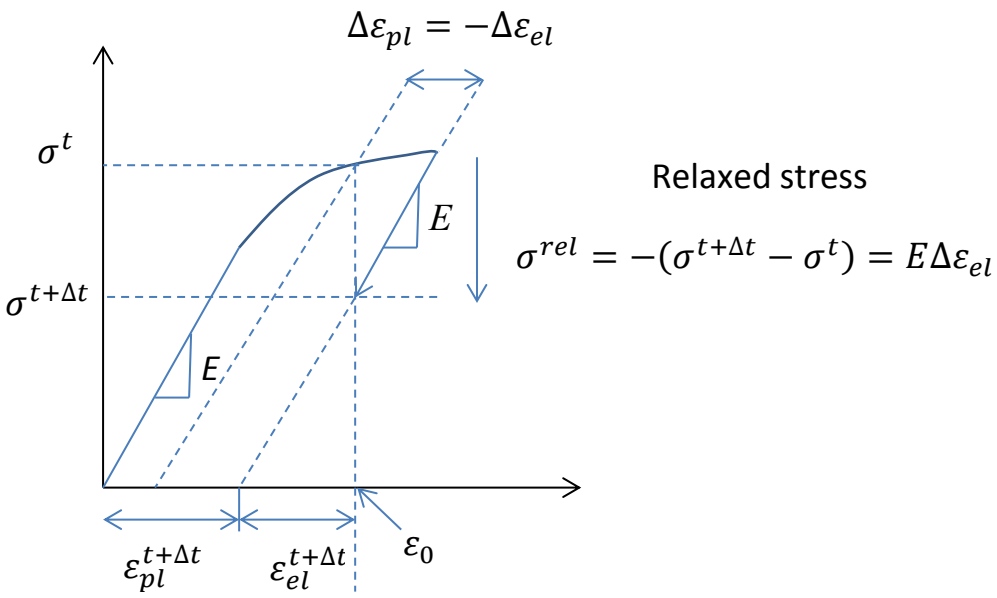

Figure 4-1; Concept of stress relaxation to maintain fixed total strain.

Figure 4-1 shows how an increase in plastic strain, $\Delta\varepsilon_{pl}$, over a small time increment, Δt, is accompanied by an enforced reduction in elastic strain, $\Delta\varepsilon_{el}$, via an elastic unloading path to maintain the total fixed strain, ε_0. The thermal strain component in Equation 4-1 is not represented in this figure for simplicity. The reduction in mechanical elastic strain is achieved through the material essentially deloading; this requires a reduction in the total internal stress state as displayed in Figure 4-1. The magnitude of the stress relaxation between stress states is displayed in Equation 4-2.

$$\left|\sigma^{rel}\right| = E(T)|\Delta\varepsilon_{el}| = E(T)\left|\Delta\varepsilon_{pl} + \Delta\varepsilon_{th}\right|$$

Equation 4-2

The reduction in internal stress must be matched by a reduction in the external applied stress to maintain equilibrium, according to Equation 3-1, noting that as the length is fixed there is no inertial force to speak of. The relaxed stress magnitude then depends on the temperature dependent elastic modulus, as shown in Figure 4-1. This representation also assumes no degradation in elastic modulus with accumulated inelastic behaviour. This may be a consideration during tertiary creep and would be a significant consideration for concrete relaxation. It should be noted Figure 4-1 is an exaggeration of the relaxation phenomenon to illustrate the elastic unloading effect with respect to stress relaxation. Increases in plastic or thermal strain are accompanied simultaneously by elastic unloading and stress relaxation, such that the stress-strain curve does not evolve beyond the total fixed strain. As creep strain accumulation is time evolving then stress relaxation due to creep is also time evolving.

4.3 MacLean's experiments

The experimental stress relaxation tests used as a data benchmark for the modelled stress relaxation curves were performed by Maclean [9] in 2007. Figure 4-2 [9] shows a schematic of the experimental set up. This details an isolated grade 1860 ASTM A416 [10], seven wire prestressing steel tendon strand, 13mm in diameter, 5390mm in length, fixed and tensioned to approximately 1000MPa. A heating furnace is placed around the centre of the tendon covering a length of 610mm (a central heated region 11% of the total tendon length). Figure 4-2 also shows the locations of various thermocouples monitoring the temperature at various points over time along the tendon. Figure 4-3 and Figure 4-4 show a full image of the experimental set up and a closer image of the load cell used to tension the tendon.

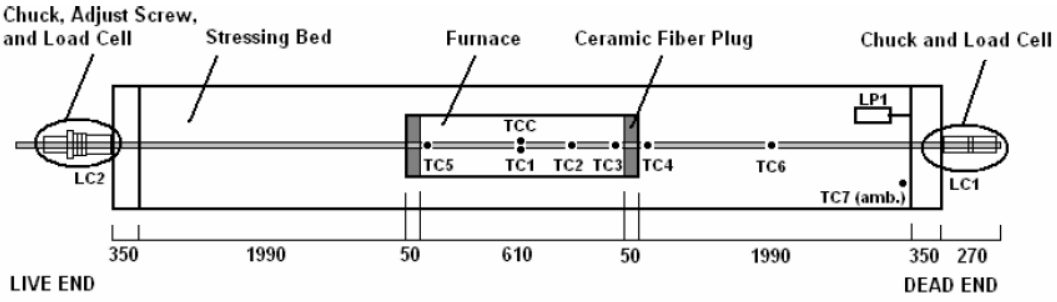

Figure 4-2; Schematic of the experimental test set up [9]

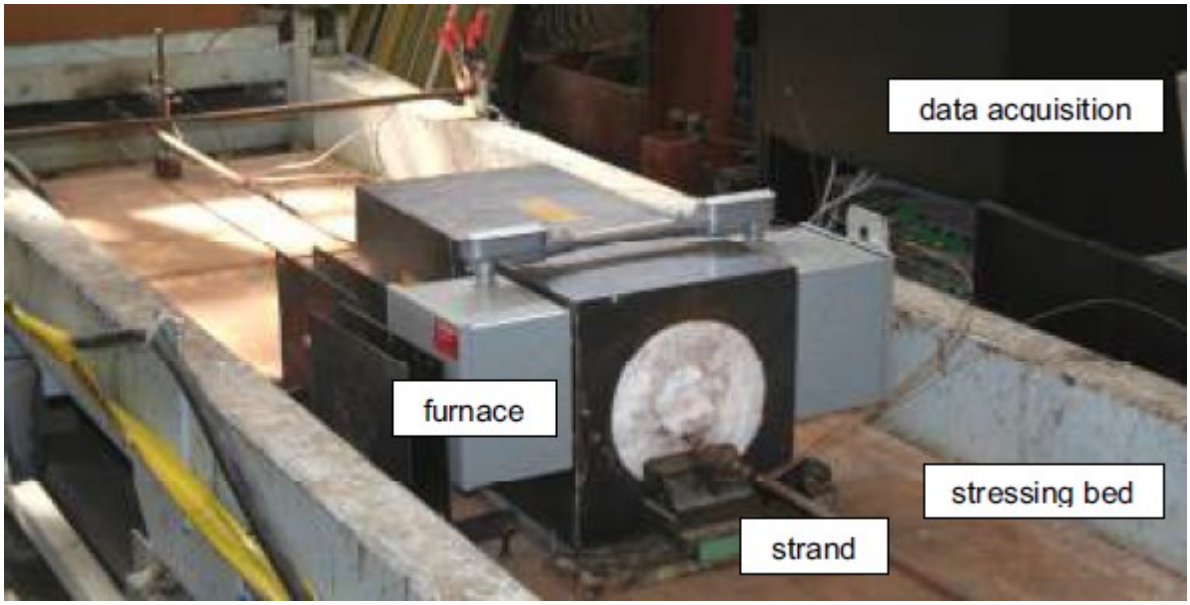

Figure 4-3; Stress relaxation test experimental test set up [9]

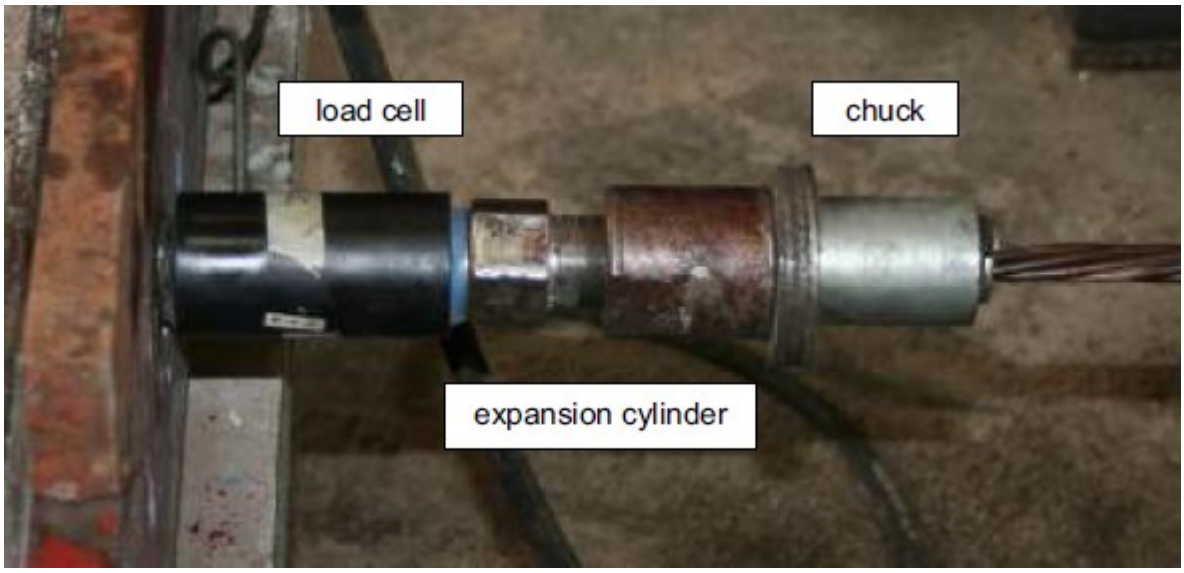

Figure 4-4; Load cell and seven strand tendon [9]

The heating protocol involved raising the temperature of the central region of the tendon within the furnace (Figure 4-2) at a rate of approximately 10^{o}C per minute, up to designated temperatures of 200, 300, 400, 500 and 700^{o}C. Once a specified temperature was reached, that temperature was maintained or *soaked* for 90 minutes before the tendon was allowed to cool naturally. Given that the tendon length is fixed, all strains accumulating with temperature must be simultaneously countered by a relaxation of the tensile stress applied, to reduce mechanical elastic strain. The accumulating strains with temperature are thermal strain and plastic strains resulting from a reduction in temperature dependent yield, of which a significant proportion is likely to be time evolving creep strain. This relaxation was monitored over the duration of the heating and cooling protocol by load cells at either end of the tendon consisting of four strain gauges each.

Figure 4-5 shows the experimental stress relaxation curves obtained for grade 1860 ASTM A416 [10] prestressing steel tendons, tensioned to approximately 1000MPa under the aforementioned heating

protocols. In all except the test heating and soaking to 700°C, the initial tensile stress recorded was 1008 MPa; the initial stress in the 700°C soak test was 975 MPa.

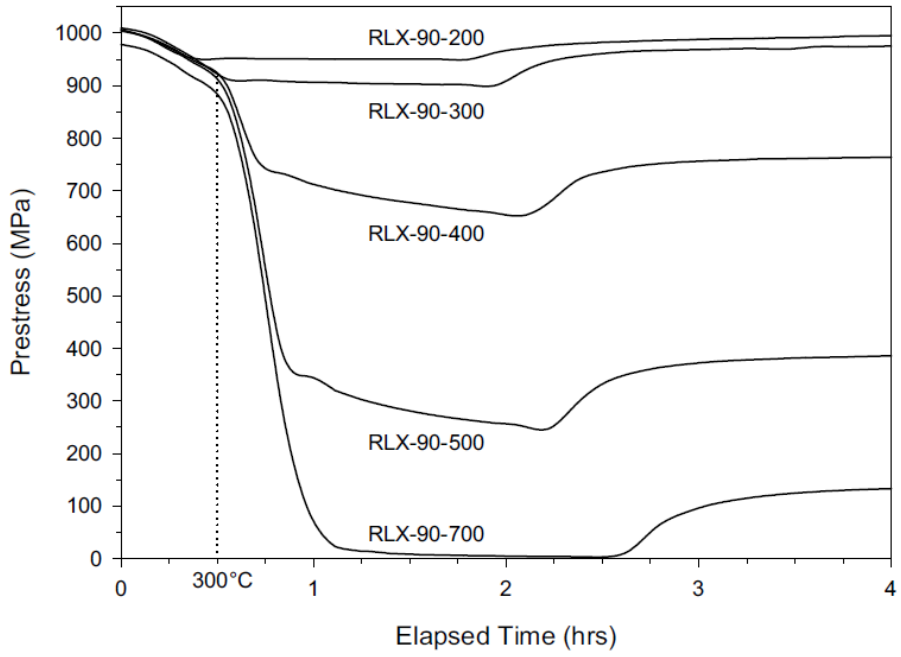

Figure 4-5; Experimental stress relaxation curves for ASTM 416 prestressing steel tedons heated at 10°C per minute to pre-designated hold temperatures of 200°C, 300°C, 400°C, 500°C and 700°C.

4.4 Tendon models

This section presents the tendon stress relaxation modelling study and the various validation studies (explicit creep models, EC2 implicit creep accountability, etc) based around MacLeans [9] experiments. Firstly, section 4.4.1 overviews the set up and details of the FE model within the commercial FE software package Abaqus. Included in this description are the various assumptions that had to be made in modelling the experimental protocol.

Section 4.4.2 begins the presentation of the various validation studies. In this section Harmathy's [8] comprehensive uniaxial creep strain model, with constants as determined by Gales [6] for ASTM A416 [10] standard prestressing steel is incorporated into a FE tendon model. The stress relaxation curves obtained from this model are then compared to those determined experimentally for the same steel by MacLean [9].

Section 4.4.2 presents modelled stress relaxation curves assuming creep is implicitly accounted for by Eurocode 2 stress-strain temperature reduction factors. Having established a set of modelled curves explicitly accounting for the contribution of creep to tendon stress relaxation, coupled with experimental relaxation curves, the ability of the Eurocode 2 to implicitly account for creep can be judged by comparison.

Following this, the modelling study moves to compare respective stress relaxation of prestressing steels manufactured to ASTM A416 [10] and BS 5896 [11] standards. Gales [6] has shown the two standard steels to have differing creep strain rate responses with respect to stress at elevated temperature. Any significant difference as a result of this, with respect to elevated temperature stress relaxation, could be an important factor in choice of tendons for prestressing concrete. This study is presented in Section 4.4.4.

Further to the above, such factors as the individual contributions made by primary creep and secondary creep strain respectively to total stress relaxation, can be explored in this chapter (via comparing secondary minimum creep strain rate models with a comprehensive primary and secondary model). This may provide further information as to the onset, and degree of recrystallization, and the potential effects on structural integrity this may have at a given tendon temperature. This is explored in Section 4.4.5.

Section 4.4.6 examines the possibility of simplifying computation through combining Eurocode 2 [1] calculated inelastic yield curves as a function of temperature with a secondary creep model. The implication here is that the Eurocode 2 [1] based curves could account for the contribution of primary creep strain to the overall inelastic strain. In turn this could eliminate the need to define a uniaxial creep model via a user-defined subroutine within Abaqus. Following this an adapted form of the standard power law breakdown secondary creep model (Equation 2-8), to incorporate primary creep strain, is developed and used within the prestressing steel material definition to model stress relaxation. This is presented in Section 4.4.7. Finally, the key outcomes from the studies undertaken within this chapter are summarised in Section 4.5.

4.4.1 Modelling procedure and set up

The modelling of tendon strands, as opposed to wires or bars, is a complicated endeavour, whereby a relatively complex (all be it repeating) geometry has to be defined, as well as the inclusion of a wire to wire contact definition. As covered in Section 4.1, contact between wires is eased to largely eliminate localised stress concentrations created by internal friction, through heating the strand under load to 350^{o}C for a specified time [9]. As such, tensile load on the strand is resisted axially through each wire, with the tensile yield characteristics of the individual wires dictating the tensile yield characteristics of the tendon strand. Both grade 1860 ASTM A416 [10] and BS 5896 [11] standard wires and strands are specified with a minimum tensile yield of 1860 MPa. This implies, with regard to yield characteristics, modelling a single wire with a diameter equal to that of the strand (13mm in MacLean's [9] tests) should produce similar results.

There is however a noted difference in elastic modulus between wires and strands. BS 5896 [11] states for design purposes the elastic modulus may be taken as 205GPa for wires and 195GPa for strands. This owes to the inherent torsion created on the strand through its helical weave when axially loaded and the unwinding effect that results. MacLean [9] measured residual elastic modulus for six grade 1860 ASTM A416 [10] prestressing steel wires, during individual tensile tests, to average approximately 214GPa at ambient temperature. Applying the same 10GPa reduction for the elastic

modulus of a strand, as displayed in the BS 5896 [11] standard, gives an assumed strand modulus of 204GPa with respect to the ASTM A416 [10] standard prestressing steel tendon.

As yield strength characteristics can be assumed to be the same between wires and strands (due to residual wire contact stresses being thermally alleviated), for simplicity and to reduce computation, it has been decided to model the tendon strand as a single wire of the same 13mm diameter as the tendon. Elastic modulus however is reduced from that specified or measured for a wire to reflect the elastic properties of a strand. This has been taken as 200GPa across all tendon models herein, irrespective of standard steel, based on the uncertainty of exact values relating to tendon strands.

The material data incorporated in the tendon models is tabulated and viewable in Appendix C, in the units used within the model. All material data, with the exception of explicit creep models and constants, has been taken or derived from various Eurocode 2 [1] reduction factors. Taking ambient elastic modulus as 200GPa, the temperature dependent modulus then computes from Eurocode 2 reduction factors as in Table 10-1.

The stress relaxation response of the tendons will be strongly dictated through the mechanical material properties input into the model. The temperature dependent elastic modulus dictates the relaxed stress from the reduction in elastic mechanical strain, with respect to maintaining total strain as described in Section 4.2. The reduction in elastic strain required to maintain a constant total strain is however dependent on the change in plastic strain (including creep strain) and thermal strain, as temperature evolves within the tendon (Equation 4-1). Thermal strain magnitude at a given temperature is dictated by (proportional to) temperature evolving thermal expansion coefficients (Table 10-2). Where classical plasticity is modelled in the absence of creep, inelastic stress-strain curves, which include the evolution of first elastic yield, are tabulated as a function of temperature within the prestressing steel material model. This first elastic yield is taken as the yield grade of both the ASTM A416 [10] and BS 5896 [11] prestressing steel wires and strands used in the various tests of Gales [6] and MacLean [9]; this is 1860MPa. From the first yield value and ambient elastic modulus, respective parts of an idealised inelastic stress-strain curve are formed following Eurocode 2 [1] guidelines. The temperature dependent evolutions of the ambient curve are computed through the multiplication of Eurocode 2 [1] temperature dependent reduction factors to the ambient yield and elastic modulus values. These values are then input into the Eurocode 2 [1] algorithm defining stress as a function of strain for the various elastic and inelastic regions of the curve. These inelastic stress-strain curves are input within Abaqus through tabulating stress with respect to inelastic strain, as displayed in Table 10-3.

The methodology by which Abaqus and other FE software packages explicitly model multiaxial creep has been detailed comprehensively in Section 3.2. This requires the user to either choose an in-built uniaxial creep strain rate function, declaring appropriate constants, or define their own uniaxial creep strain rate function via a user defined Fortran subroutine. In-built Abaqus uniaxial creep strain rate functions and other options for user definition are detailed in Section 3.3. The temperature evolution of the tendon is dictated by the various parameters involved in heat transfer. Heat transfer between the heated and non-heated part of the tendon is facilitated through thermal conductivity (Table 10-4), specific heat capacity (Table 10-5) and material density parameters (7830kgm^{-3}); again all input is tabulated as a function of temperature. Steel density is however assumed to remain constant with temperature.

In order to reduce computation further (aside from modelling the tendon strand as an equivalent diameter wire), only half the tendon length has been modelled, utilising symmetry about the centre. This is made possible by the experimental heating having being applied about the centre of the tendon. Figure 4-6 shows a schematic of the modelled half tendon.

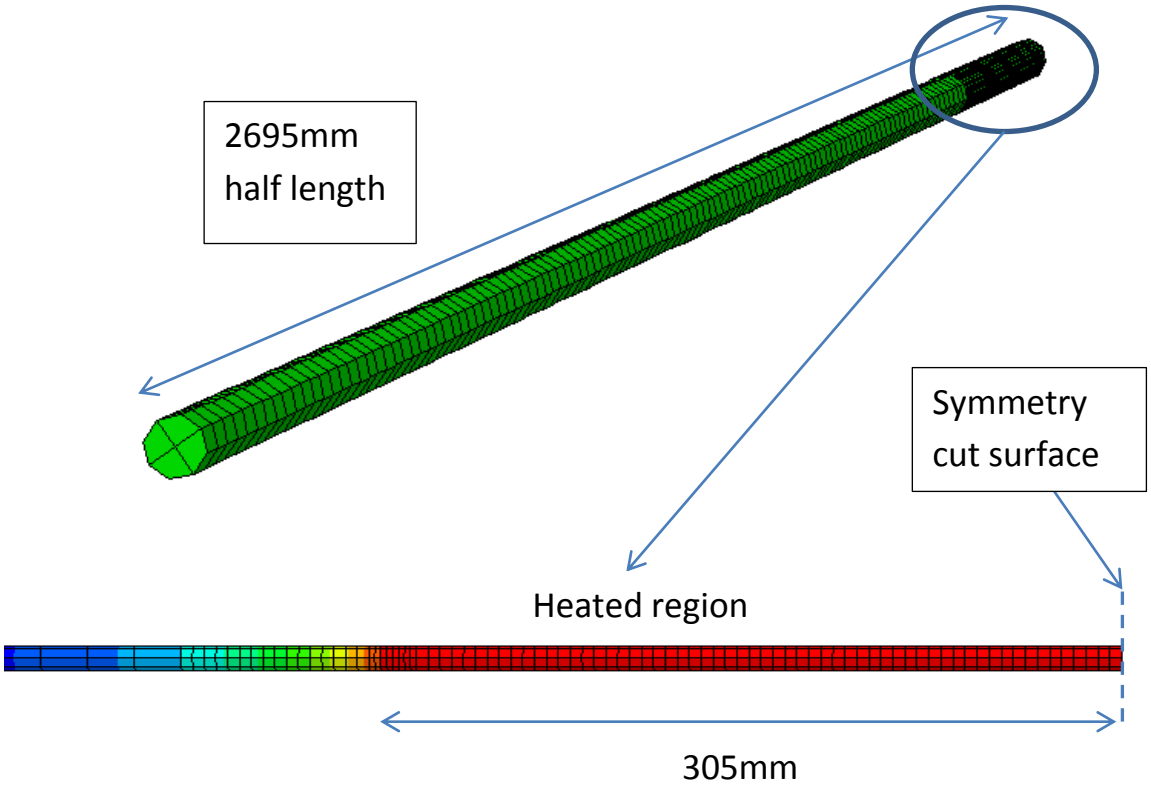

Figure 4-6; Schematic of modelled tendon half length

The modelled cross section consists of four C3D8T coupled temperature displacement elements (as such the analysis of type 'coupled temperature displacement'). A finer mesh along the tendon length was used around the heating region where the temperature gradient should be highest. In order to create the tensile stress within the tendon, an initial stress condition was specified on all elements. This created a tensile stress of 1008 MPa in each element prior to heating. The tendon was fixed in displacement at each end. The heating profile applied to the 305mm heated region of the tendon (Figure 4-6) is plotted for the 300^{o}C, 400^{o}C and 500^{o}C cases with time in Figure 4-7.

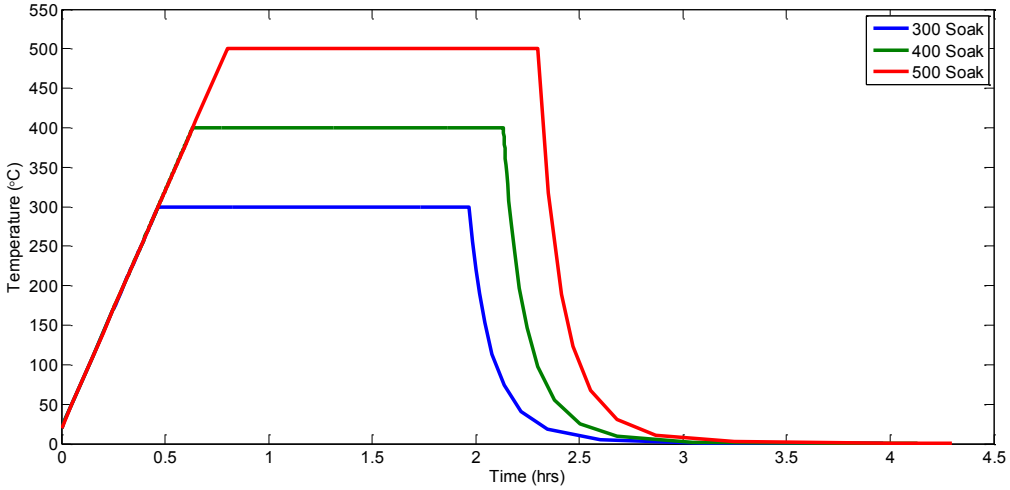

Figure 4-7; Temperature-time heating profiles applied to a 310mm half-length of the modelled tendons

These profiles involved the tendons being heated via a boundary condition applied to each node within the heated region. This was achieved through defining an amplitude curve, prescribing a heating rate of 10^{o}C per minute. This transient heating was maintained until the designated soak temperature was reached. At this point a new analysis step was started, maintaining the soak temperature for 90 minutes, as was applied in the experimental case; following this, a final analysis step to model cooling commenced. As was the case with the experiment, this was modelled as natural cooling, using a surface convective film interaction and surface radiation interaction. The accuracy of this however is hard to judge given the uncertainty as to the value of the local sink temperature in immediate proximity to the tendon, when the heating furnace was removed (to allow the tendon to cool naturally). As a result this sink temperature was taken as ambient 20^{o}C, almost certainly over predicting the initial cooling rate. The bay cooling phase with respect to the UPT concrete structural models to come, will be of importance, in this case however the tendons will be embedded within concrete, with a heat transfer model setting sink temperatures for tendon heating and cooling based on the concrete temperature.

4.4.2 Explicit creep modelling; validation of Harmathy's comprehensive uniaxial creep model

The most obvious starting point for modelling creep in prestressing steel tendons is with the Harmathy [8] comprehensive primary and secondary uniaxial creep strain model, Equation 3-22. Constants fitting this model have been determined experimentally for grade 1860 ASTM A416 [10] prestressing steel (Table 3-1, [6]). This makes the Harmathy model ideal for use in a validation study against MacLean's [9] stress relaxation tests using the same steel. These creep parameters were determined on wires as opposed to strands. Creep however, is a time evolving material process; therefore the behaviour of a single wire should be duplicated by the other six in the strand, assuming they are subject to the same stress and temperature. As mentioned in Section 4.1, localised residual contact stress between the wires should be eliminated by a thermo-mechanical treatment after the strand is woven. Any difference in global behaviour between an individual wire

and a strand should be accounted for by adjusting the elastic modulus to account for the torsional unwinding effect (Section 4.1).

With regards to compatibility within a multiaxial viscoplastic constitutive framework (Section 3.2), as used by Abaqus, the strain rate form of Harmathy's model as shown in Equation 3-23 and Equation 3-24 must be used. In order to use this model within Abaqus it is necessary to define this form within a Fortran user defined subroutine. Equation 4-3 shows the rate form of the Harmathy uniaxial creep model repeated from Equation 3-23. It may be considered easier to use an Abaqus in-built uniaxial model as detailed in Section 3.3, thus avoiding the need to code and import a model manually into Abaqus (via a user defined sub-routine). Constants however have not been determined to apply these models to ASTM A416 [10] prestressing steel. Aside from constant determination, the time hardening model (Equation 3-17) and strain hardening model (Equation 3-18), are both power law representations for use at far lower stresses than operational concrete prestressing values. There is however scope for using the in-built hyperbolic sine model (Equation 3-19) by determining appropriate constants through equating with Harmathy's model, this is explored in Section 4.4.7.

$$\dot{p} = Zexp\left(\frac{-Q_c}{RT}\right)\frac{X}{\sqrt{X^2-1}}; \quad X = 2^{Z\theta/\varepsilon_0}$$

Equation 4-3

As temperature, stress, time or a combination of the three rise, the rate form of the Harmathy Equation 4-3 reduces towards the standard, empirically observed, power law breakdown secondary creep strain rate model (Equation 2-8). This comprises the Zener Hollomon [7] [25] parameter multiplied by an Arrhenius function. The Zener Hollomon parameter and the secondary creep strain intercept, $\varepsilon_{cr,0}$, are used to define the effective hardening parameter determining the primary creep phase (Section 3.3.1). Substituting the constants determined by Gales [6] for grade 1860 ASTM A416 [10] prestressing steel (from Table 3-1) into Equation 4-3 yields Equation 4-4. The constants displayed in Equation 4-4 are defined in Mega Pascal's (MPa) for stress and hours with respect to time, temperature is measured in Kelvins. Equation 4-4 is coded into Abaqus via a Fortran user-defined subroutine; the stress must be defined as the Von Mises stress.

$$\dot{p} = 2.7E13exp(0.012\sigma)exp\left(\frac{-Q_c}{RT}\right)$$

Equation 4-4

There are three notes of caution however when deciding to use the above Harmathy model through a user-defined subroutine. Firstly in cases of highly non-linear behaviour, brought on by significant hardening or softening, or induced by highly transient external conditions, Abaqus prefers to use an implicit integration solution scheme. To allow this, Abaqus requires the derivative of Equation 4-3with respect to the Von Mises stress to be coded within the same creep user-defined subroutine. Whilst this is essentially basic calculus, the Von Mises stress appears in both the Zener Hollomon parameter *Z*, and creep strain intercept $\varepsilon_{cr,0}$, which in turn both appear in multiple parts of Equation 4-3. This implicit integration however will only be used if the user specifies the nonlinear geometry (NLGEOM) option in the step module. Therefore care has to be taken to perform this differentiation correctly. Secondly, temperature compensated time has to be considered in its integral form as in Equation 3-20 during transient heating. This requires declaring the temperature compensated time,

θ, as a state variable that is updated each time increment by the addition of the temperature compensated time differential (the Arrhenius function at the time increment temperature, multiplied by the time differential). Should temperature compensated time not be considered in integral form it will be over predicted during transient heating at each time increment, resulting in the parameter, *X*, in Equation 4-3 also being over predicted. Equation 4-3 will tend towards its steady state form of Equation 4-4 more rapidly, and potentially underestimate transient heating primary creep strain in such a case. Thirdly when the parameter, *X*, in Equation 4-3 is close to unity, a 'divide by zero' may occur within the computational algorithm; as such, a condition needs to be coded for such an occurrence. This should only occur at zero time, when creep strain rate will also be zero. Once these factors are considered, stress relaxation can be modelled in prestressing steel tendons using the Harmathy uniaxial creep strain model defined in Equation 4-4 for ASTM A416 [10] prestressing steel. Figure 4-8 shows stress relaxation curves modelled for ASTM A416 [10] isolated prestressing steel tendons, tensioned to 1008MPa (975MPa in the 700°C soak temperature model), and heated according to the temperature profiles detailed in Section 4.4.1 and Figure 4-7.

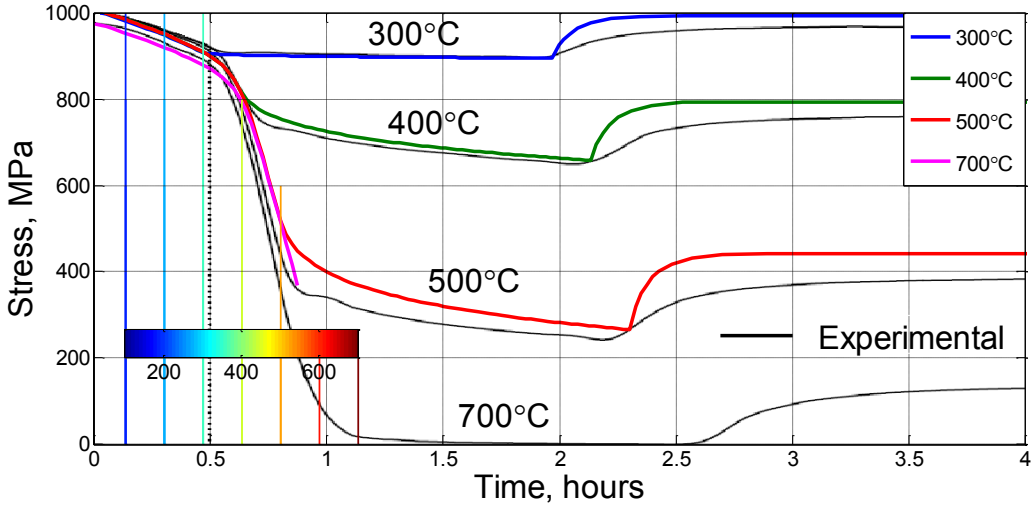

Figure 4-8; Experimental and modelled stress relaxation curves for ASTM 416 prestressing steel using Harmathy's uniaxial creep strain model in Abaqus

The FE tendon models can be seen to show a reasonable degree of accuracy with respect to the experimental relaxation curves. There is however a steadily increasing under prediction of relaxed stress as temperature rises beyond 400°C. The attempt to model stress relaxation under transient heating to the 700°C soak temperature fails just beyond 500°C, owing to the rapidity of the relaxation at this time (this is despite including the non-linear geometry option allowing implicit integration).

The modelled 400°C curve in Figure 4-8 shows reasonable accuracy, typically within a 3% error of the experimental curve, all be it an under prediction. An over prediction would be preferred generating an intrinsic factor of safety. This corresponds well with separate, non FE Fortran models by Gales [28], using the same data from Table 3-1 for ASTM A416 [10] prestressing steel, modelled against experimental stress relaxation curves for parabolic mounted 18.4m tendons. These tendons were heated about a region of 3% of the total length, predicting relaxation within a 2% error of experimental data at 400°C [6]. The 500°C curves show a far greater relative under prediction in stress relaxation; this is generally of the order of 10% with respect to the experimental curves, as

temperature progresses beyond 450^{o}C. As 500^{o}C is approached and during the early stages of the soak phase this difference extends towards 15%, but appears to reduce as the soak phase progresses.

It will not have escaped notice that the cooling portion of the modelled curves is rather inaccurate. The models specified cooling using standard convective film coefficients and radiative emissivity properties as described in Section 4.4.1. The sink temperature to which the tendons cooled, immediately post-heating was taken as ambient (20^{o}C). It is likely the realistic sink temperature in close proximity to the tendons was not instantaneously ambient and as such the modelled curves cooled too rapidly in fully recovering elastic stress. The experimental curves it appears recover this stress over a much longer time scale.

4.4.3 Stress relaxation modelled from inelastic stress-strain curves computed from Eurocode 2 stress-strain temperature reduction factors.

The following section displays modelled stress relaxation curves for prestressing steel tendons using inelastic stress-strain curves computed from Eurocode 2 [1] stress-strain temperature reduction factors. As stated in Section 4.4.1, these curves are based on an ambient curve largely defined by first yield (1860MPa for ASTM A416 standard prestressing steel) and elastic modulus (taken as 200GPa). The curves are input into Abaqus through tabulating yield stress at a given inelastic strain as a function of temperature within the prestressing steel material definition. As stated earlier these curves are assumed valid to implicitly account for creep within heating rates of 2^{o}C to 50^{o}C per minute. In order to validate this statement the modelled relaxation curves, based around the mechanical properties of ASTM A416 [10] prestressing steel strands, should therefore cover the temperature ramp phase relaxation recorded experimentally by MacLean [9].

The modelled tendons were heated according to the temperature profiles of Figure 4-7, mimicking the experimental temperature exposure within the tendon region outlined in Section 4.4.1 and Figure 4-6. The modelled relaxation curves are displayed in Figure 4-9 against the experimental relaxation curves obtained by MacLean [9]. Again it is noted the tendons were tensioned to 1008 MPa using an Initial Condition of ‘type=stress’ with the exception of the tendon heated to 700^{o}C, which was tensioned to 975 MPa as in the experimental case.

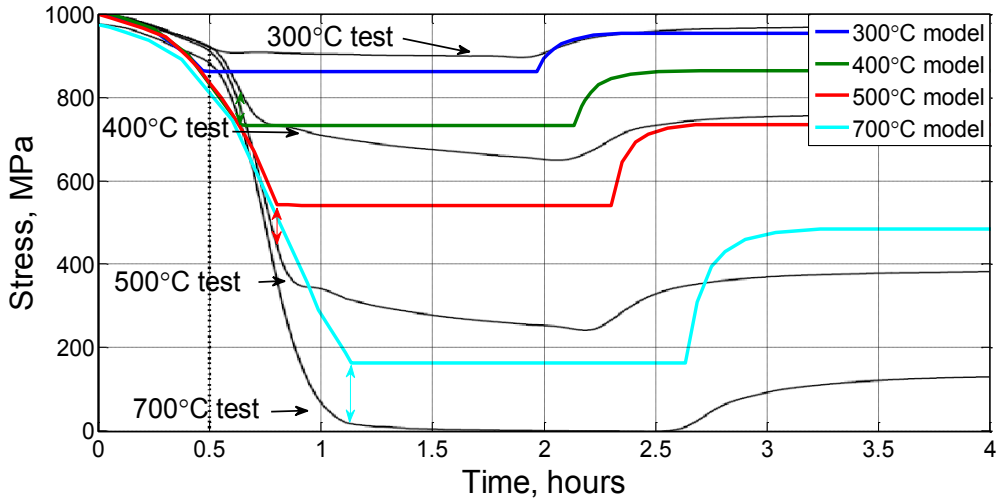

Figure 4-9; EC2 [1] predicted prestressing steel stress relaxation against experimental ASTM 416 stress relaxation curves [9].

Figure 4-9 highlights two points; firstly the Eurocode 2 [1] calculated inelastic yield curves fall short in predicting transient heating stress relaxation at 500°C by approximately 75MPa (16-17% relative to the experimental curve) for ASTM A416 [10] standard prestressing steel. Whilst at 700°C the Eurocode 2 [1] curve falls significantly short, in the region of 150Mpa. Up to 400°C stress relaxation is covered with respect to transient heating; there is not a significant factor of safety to cover any significant time dependent relaxation during the soak phase however. Stress relaxation during the soak phase is entirely attributable to creep, as thermal strain is constant; the elastic strain component of the total strain (constant) therefore must relax to account for increasing creep strain (Equation 4-1). This steady state temperature exposure does however fall out with the Eurocode 2 [1] specified heating rate domain of 2°C and 50°C per minute with respect to implicit creep strain inclusion (being 0°C per minute). It goes on to state creep should be explicitly considered at heating rates outside of the above domain (again no explicit method is provided).

With respect to ASTM A416 [10] standard prestressing steel, the Eurocode 2 [1] stress-strain reduction factors are not capable of implicitly accounting for creep during transient heating at temperatures much beyond 400°C. It should however be considered that thermal expansion coefficients dictating thermal strain also contribute to relaxation during transient heating, and will contribute to a relaxation underestimate if they themselves are under predicted. These coefficients have also been taken from Eurocode 2 [1].

In consideration of the accuracy of the Eurocode 2 [1] stress-strain reduction factors, first elastic yield, as used in the above models (Table 10-3), drops significantly to 400°C. This contributes to the over-prediction of stress relaxation within that temperature range (Figure 4-9). The same Eurocode 2 curves however predict significant strain hardening, even at elevated temperatures beyond this. This doesn't conform well with optical microscopy evidence from MacLean [9] with respect to observed recrystallization beyond 400°C; where yield stress would be expected to drop rapidly and dislocation based strain hardening should be expected to become increasingly negligible (as dislocation density declines, Figure 2-6). This elevated temperature degree of strain hardening does not correspond well with the increasingly larger under prediction of relaxed tendon prestress in Figure 4-9, as tendon temperature increases to 500°C and 700°C.

Eurocode 2 [1] does however state 350^{o}C as a critical temperature and recommends additional concrete cover to prestressing steel tendons to protect from increased exposure beyond this. Up to this temperature, the Eurocode 2 [1] determined stress-strain curves have a reasonable enough factor of safety to cover transient heating stress relaxation. Further, soak phase relaxation at 300^{o}C is not significant enough over 90 minutes to exceed the transient relaxation predicted to this temperature in the modelled curve (Figure 4-9). During the soak phase at 400^{o}C it takes approximately 10 minutes of steady state heating for the experimental stress relaxation curve to exceed the Eurocode 2 [1] relaxed stress, achieved during the transient heating phase.

In Chapter 5, FE models of isolated UPT concrete slabs subject to standard fire exposure below their base are presented. This will analyse minimum concrete covers and maximum fire durations required to prevent tendon temperature exposure reaching levels of 350^{o}C or beyond. The consequences of exceeding such tendon temperature exposure with respect to the UPT concrete slab will also be analysed. Clearly the tendon temperature will undergo varying degrees of thermal transience during fire, as at some point it has to reach a peak temperature and then cool. During these periods, where the tendon temperature plateaus for a period of time, it may be particularly susceptible to creep induced relaxation which will be difficult for Eurocode 2 [1] data to account for. It is also therefore important to consider cooling of the slab in such analyses, to monitor the complete thermal exposure of the tendon.

4.4.4 A comparison of different prestressing steels

As noted in Table 3-1, prestressing steels manufactured to differing standards exist. Other than ASTM A416 [10] standard prestressing steel strands, as tested by MacLean and modelled previously in this chapter, BS 5896 [11] is also a commonly used manufacturing standard for prestressing steel tendon wires and strands. Both these standards of prestressing steel (with stated yield strengths of 1860MPa) have been subject to transient heating creep tests by Gales [6] and subsequent creep constants in-fitting Harmathy's uniaxial model (Equation 4-3) determined (Table 3-1) as a result. ASTM A421 [26] is an older standard of steel with the creep parameters listed in Table 3-1, determined by Harmathy and Stanzak [7], based on steady state heating tests with tensile loads only to 690MPa. This is far below standard operational tendon post-tensioning loads in excess of 1000MPa.

This section focusses on the respective stress relaxation noted from grade 1860 ASTM A416 [10] and grade 1860 BS 5896 [11] standard prestressing steels subject to the same heating and experimental protocol of MacLean's [9] tests. Accuracy of modelled stress relaxation curves for grade 1860 BS 5896 standard prestressing steel can only be judged through considering the accuracy of the modelled ASTM A416 prestressing steel relaxation curves against MacLean's experiments (Figure 4-8). This of course is given that the creep parameters of both were determined by the same author [6] under identical test protocols. Figure 4-10 displays stress relaxation curves for both grade 1860 ASTM A416 [10] and grade 1860 BS 5896 [11] standard prestressing steels with creep explicitly modelled via Harmathy's Equation 4-3, using respective creep constants as determined by Gales [6] (Table 3-1). The heating protocol and modelling set up is, again, based on MacLean's experiments. Eurocode 2 [1] determined stress relaxation curves are also displayed for comparison.

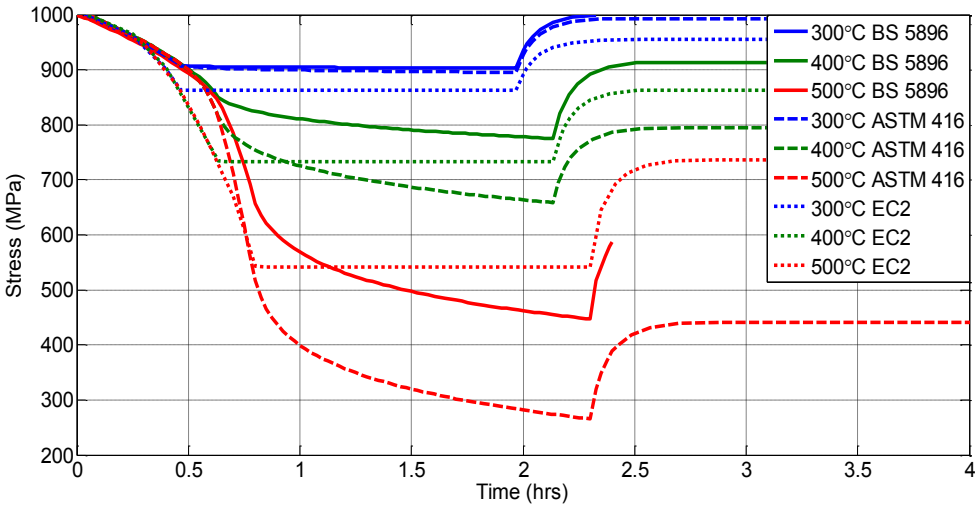

Figure 4-10; Stress relaxation curves explicitly including creep for ASTM A416 and BS 5896 standard prestressing steel compared to Eurocode 2 plastic stress strain temperature reduction curves applicable to either steel.

Firstly from Figure 4-10 it is notable the transient heating portion of the Eurocode 2 [1] curve almost encompasses the modelled curve, including creep, for grade 1860 ASTM A416 [10] standard prestressing steel at 500°C; it falls approximately 20MPa short. Neither could match the transient heating stress relaxation of the experimental curves to this temperature. Relaxation predicted from the explicit creep model was approximately 75MPa short of matching the experimental curve whilst the implicit creep Eurocode 2 relaxation model was approximately 95MPa short. The Eurocode 2 [1] curve comfortably covers transient heating stress relaxation from BS 5896 [11] standard steel to 500°C; it over-predicts stress relaxation by approximately 100MPa. The modelled stress relaxation curve explicitly accounting for creep in ASTM A416 prestressing steel was showed a 15% error to the experimental stress relaxation at 500°C in Figure 4-8. Should the BS 5896 [11] standard steel modelled stress relaxation show a similar error to equivalent experimental stress relaxation at 500°C, it should then be possible validate Eurocode 2 [1] stress-strain curves and temperature reduction factors as implicitly accounting for transient heating creep. This would produce an over-prediction relative to equivalent experimental curves of approximately 27MPa (~5% a relative increase).This is at a heating rate of 10°C per minute to 500°C, well within the $2℃ \leq \dot{T} \leq 50℃$ applicable domain of the Eurocode 2 [1] reduction factors.

Most notable from Figure 4-10 is the significant difference in elevated temperature stress relaxation between the two steel types as modelled using Gales [6] creep parameters (Table 3-1). To further illustrate this the accumulation of creep strain recorded by Abaqus, for each steel, is plotted below in Figure 4-11 for heating to and soaking at 300°C and Figure 4-12 for both 400°C and 500°C cases.

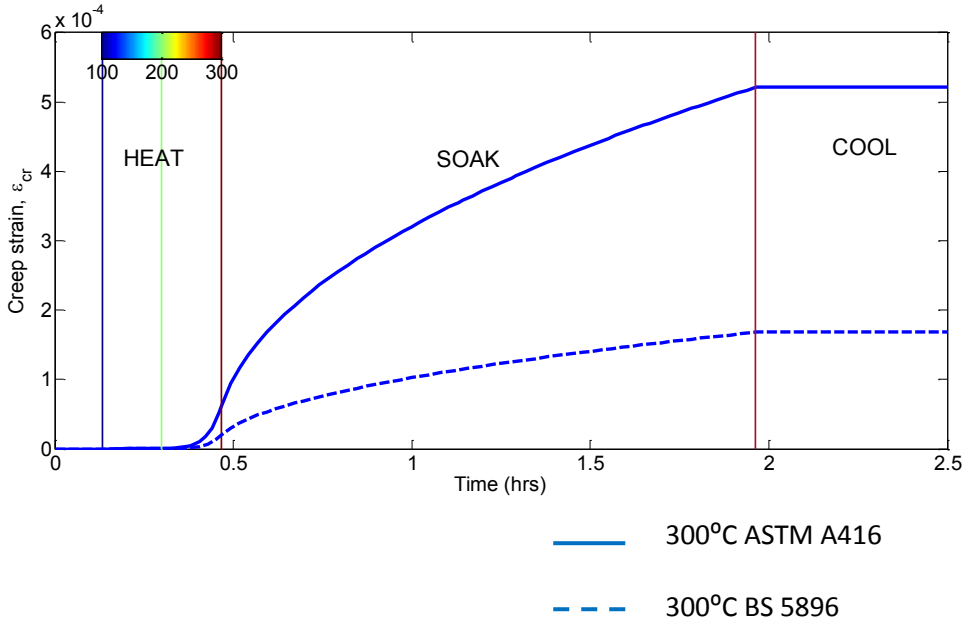

Figure 4-11; Accumulated creep strain during heating and soaking to 300°C of isolated and tensioned prestressing steel tendons.

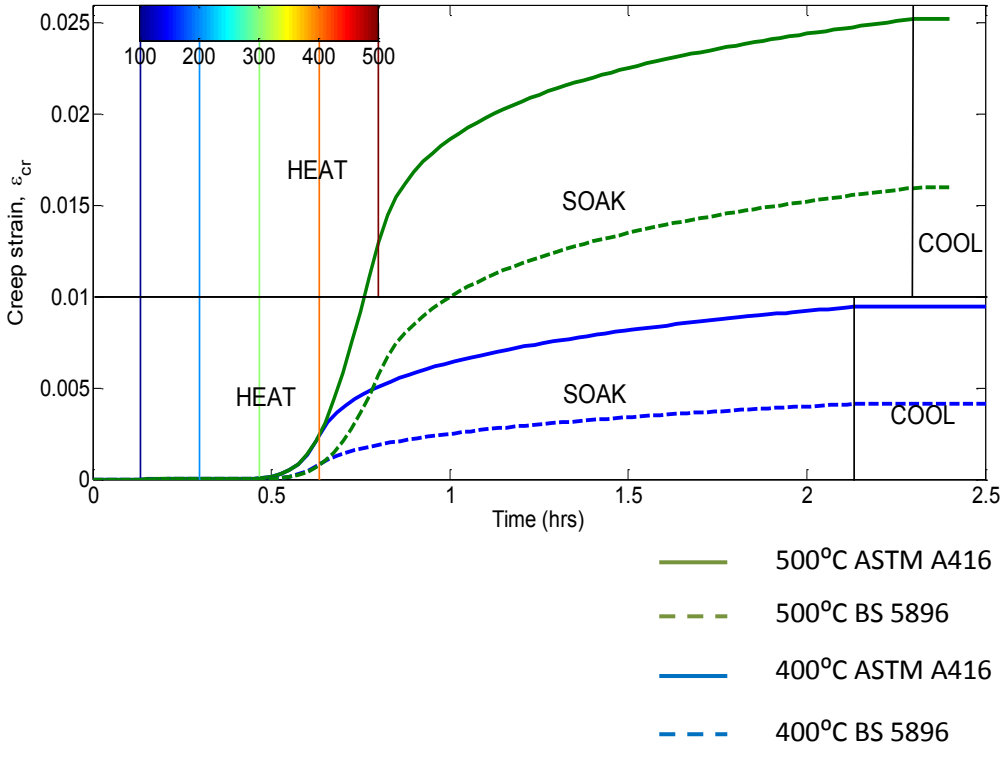

Figure 4-12; Accumulated creep strain during heating and soaking to 400°C and 500°C of isolated and tensioned prestressing steel tendons.

Figure 4-11 and Figure 4-12 both show considerable difference in creep strain accumulation between the two standard types of prestressing steel. During the transient heating phases the creep strain accumulated by the ASTM A416 [10] standard steel is double that of the BS 5896 [11] standard steel. Soaking at 300°C also shows a significantly higher rate of creep strain accumulation for the

ASTM A416 [10] standard steel. This rate of accumulation however tends to even out between the two respective standards of steel as the higher temperature soak phases progress, particularly at 500^{o}C.

It is important to note however, the greater creep strain accumulation within the ASTM A416 [10] tendon during transient heating, as compared to the BS 5896 [11] tendon, means at a given temperature prestress is higher within the BS 5896 [11] tendon. Therefore, during respective soak phase a greater stress is driving the creep strain rate in BS 5896 [11] tendons compared to the ASTM A416 [10] tendons. For example, the BS 5896 [11] prestressing steel, by the time the 500^{o}C soak phase is reached, is tensioned by approximately 655MPa compared to approximately 520MPa within the ASTM A416 [10] model (Figure 4-10). The stress dependence on creep strain rate with respect to both standards of prestressing steel tendon wires can be clearly viewed by comparing the Zener Hollomon parameters of Table 3-1. The order of creep strain magnitude also increases significantly with temperature in both cases. These are of the order 10^{-4}, when heated to and soaked at 300^{o}C, 10^{-3}, when heated to and soaked at 400^{o}C and 10^{-2}, when heated to and soaked at 500^{o}C. During cooling creep strain will continue to accumulate dependent on stress and temperature. Figure 4-11 and Figure 4-12 appear to show the accumulation to cease; this however is not the case as the rate of cooling in the modelled cases is so rapid (Figure 4-7), that the continued accumulation is both short lived and of a far smaller order.

The difference in operational stress due to differing degrees of stress relaxation with respect to both standard steels makes it somewhat difficult to make direct comparisons of the difference in creep strain accumulation. However, it is the difference in creep strain accumulation that is responsible for such a difference in stress relaxation. However, the significant difference in creep strain rate shown during soaking at 300^{o}C, in Figure 4-11, is recorded at similar tendon stress levels (approximately 900MPa). Given the difference in creep strain accumulation appears so significant, the question has to be asked as to why this is the case, especially as both steels have a specified ambient yield stress of 1860MPa. Clearly there could be structural consequences in choosing one standard of tendon over the other, with respect to behaviour of a UPT concrete slab subject to prolonged thermal exposure.

The manufacturing process of both ASTM A416 [10] and BS 5896 [11] prestressing steels appear very similar through information given in the respective standards. Details regarding the general manufacturing process of tendon strands were provided in Section 4.1. Given the similarity of the specified manufacturing process it is possible the difference in creep strain susceptibility at elevated temperature is due to the chemical composition of the supplied rods, from which the wires are drawn. Details regarding chemical composition of the ASTM A416 [10] and BS 5896 [11] standard wires, as subjected to transient heating tensile creep tests by Gales [6], were also given in Section 4.1 and Table 4-1. To summarise, there are some noticeable differences in composition between the two standard wires tested, most notably of which is the significantly larger composition of phosphorus and sulphur within the ASTM A416 [10] wires. Low quantities of both are generally specified for high strength steels ([27]), however increasing their respective concentrations within a rod can ease the cold drawing process ([9]). As cold drawing essentially involves pulling under tension, and thus lengthening a rod through increasingly narrower dies it may imply increased concentrations of phosphorus and sulphur eases tensile elongation during creep. This is however postulation at present. The ambient yield stress of both standard steel wires tested is given as the

same value of 1860MPa. Further, the maximum isothermal force relaxation allowable at ambient temperature subject to testing over 1000 hours, is actually stricter at 80% of maximum tensile breaking load, as detailed in the ASTM A416 [10] standard. This however is not a yield inducing load; the force used during cold-drawing of wires by default has to induce inelastic yielding behaviour. Further, inelastic creep is induced at elevated temperature by loads that cause inelastic yielding behaviour (noting yield stress reduces with temperature). It may then be possible the introduction of phosphorus and sulphur eases subgrain and grain alignment, but doesn't significantly affect initial ambient dislocation motion and initial post-yield inelastic behaviour. This type of inelastic behaviour where new grains form and align is very much the process of recrystallization and grain growth, associated to elevated temperature secondary and tertiary creep behaviour.

There may also be potential for prestressing steel wires and strands designed to the same standard by different manufacturers to use different chemical compositions rods for cold drawing. As noted in Section 4.1, BS 10020:2000 [27] to which BS 5896 [11] refers, only specifies chemical composition guidelines such as maximum or minimum compositions by weight, for given elements in preparing steels fit to specific purposes; not exact values. The potential for differing elevated temperature relaxation behaviour between prestressing steels manufactured to the same standard could be particularly concerning should it turn out chemical composition is significant in this matter. Whilst the ambient behaviour may therefore be very similar with respect to the ASTM A416 [10] and BS 5896 [11] standard wires tested, despite differing chemical composition, the elevated temperature post-yield behaviour is clearly somewhat different. Mandatory elevated temperature performance requirements are not specified in either code [10] [11]. The effect of differing compositions of certain elements on elevated temperature tensile yield behaviour (and thus creep) should be explored and researched in more detail.

4.4.5 Relaxation modelling from a secondary only creep model

It was implied in Chapter 2 that in high-yield stress metals, with high dislocation densities and therefore subjected to high stress loading, that the total contribution to overall creep strain from the primary creep phase may be small. This owes to the restricted distances dislocations can move prior to piling up and forming cells from where recrystallization begins. It is also possible to model secondary power law breakdown creep strain rate directly through the Abaqus in-built hyperbolic sine model (Equation 3-19), negating the need to compose a user-defined subroutine. Therefore it is worthwhile comparing a comprehensive primary and secondary creep model such as the Harmathy uniaxial model in Equation 4-3, with the secondary model it reduces to (Equation 4-4), with respect to predicting tendon stress relaxation. Secondary creep strain rate as a function of stress and temperature is defined by the respective Zener Hollomon parameters determined by Gales [6] in Table 3-1. At high stresses the Abaqus in-built hyperbolic sine model presented in Equation 3-19, reduces to the form of Equation 2-8; this is provided the power constant, n, be set to unity as represented in Equation 4-5.

$$\dot{p} = A(\sinh B\sigma_{vm})^n exp\left(\frac{-Q_c}{RT}\right) = \frac{A}{2} exp(B\sigma_{vm}) exp\left(\frac{-Q_c}{RT}\right); \qquad n = 1, B\sigma_{vm} \gg 1$$

Equation 4-5

The obvious requirement is the pre-exponential constant within the Zener Hollomon parameters of Table 3-1 be doubled when input into Abaqus to account for the division of two as shown in Equation 4-5. This allows the constant, *A*, to take on the correct effective value in the in-built hyperbolic sine model. In order to verify the use of the in-built hyperbolic sine model to represent Equation 4-4, it has been validated against a user defined subroutine explicitly coding the secondary creep strain rate power law breakdown (PLB) model, Equation 4-4. This validation is displayed in Figure 4-13 for ASTM A416 [10] standard prestressing steel alongside MacLean's [9] experimental relaxation curves.

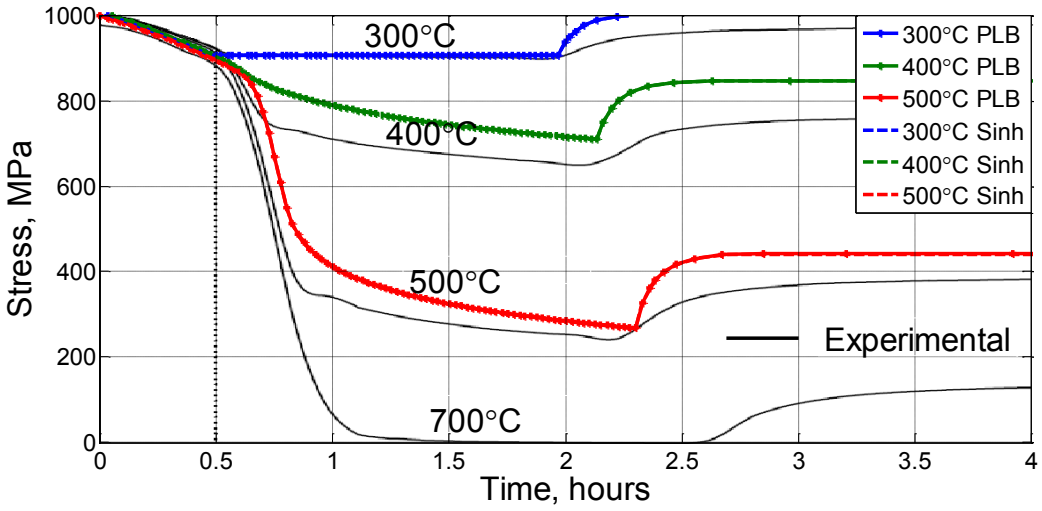

Figure 4-13; Validation of in-built hyperbolic sine model as means of including a secondary creep power law breakdown model.

The in-built hyperbolic sine model is indeed nearly identical to the secondary creep model, Equation 4-4, when the pre-exponential constant is doubled for input, as displayed in Equation 4-5. Using the in-built hyperbolic sine version of the secondary creep model also reduces computation and model preparation time, which is an added bonus.

Post this validation, the secondary creep model Equation 4-4 is compared to the comprehensive primary-secondary Harmathy model, Equation 4-3, for ASTM A416 [10] standard prestressing steel. The respective predicted relaxations are displayed in Figure 4-14 with those from the comprehensive primary and secondary creep Harmathy model, Equation 4-3, labelled *'P+S'*. The curves from the equivalent power law breakdown secondary creep model are labelled *'S'*. These curves are again plotted against the experimental relaxation curves from MacLean [9].

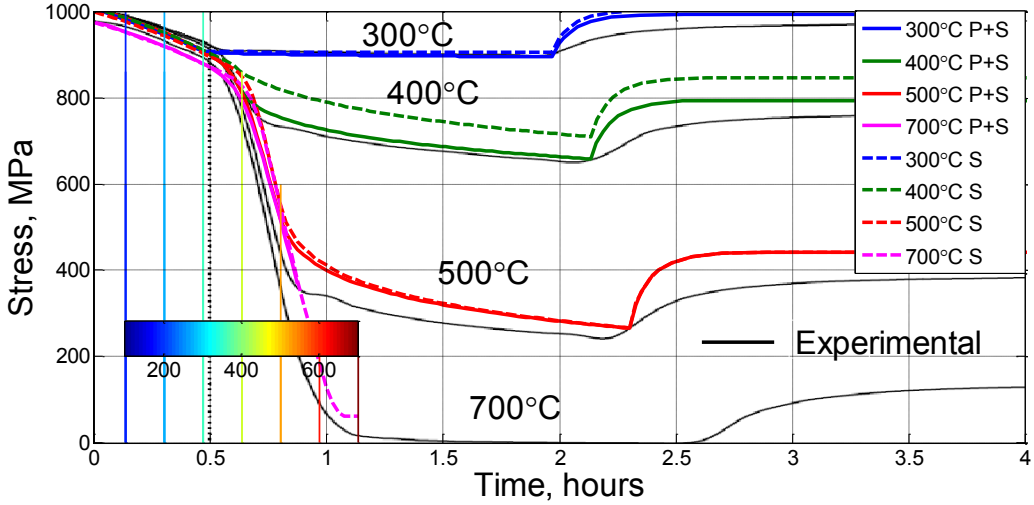

Figure 4-14; Comparison of a secondary creep only model versus a primary and secondary creep model (Harmathy) with respect to stress relaxation

The most standout point in Figure 4-14 is the difference in predicted relaxation at 400°C. This implies, given the difference in accuracy with respect to the experimental data, primary creep plays a significant role in stress relaxation between 300°C and 400°C. This corresponds well with the optical microscopy observations by MacLean [9] in comparison to the restoration process described in Section 2.2. Dislocation motion leading to strain hardening is responsible for the difference in relaxation noted (the recovery process, Section 2.2). No distinct changes in microstructure were observed to this point under optical imaging by MacLean [9] implying recrystallization has not yet begun (to any degree of significance).

The difference between the full Harmathy model Equation 4-3 and the secondary only model (Equation 4-4) up to 300°C are negligible. This implies primary creep strains up to this point, whilst definitely accumulating, are not significant enough to cause a large degree of stress relaxation unless heating time is extremely long. The early stages of primary creep strain accumulation are essentially the same material process that describes classical plasticity (but accentuated due to the emerging aid of thermally induced vacancies). It is highly likely some of this primary creep strain is implicitly covered in the elastic regime of the Eurocode 2 [1] derived stress-strain curves; this however would represent those strains, incorrectly, as recoverable. The elastic part of these stress-strain curves is input into the Abaqus models explicitly considering creep, it is the inelastic portion that is replaced by an explicit creep function.

It is also noticeable however that the relaxation modelled in both cases at 500°C tends towards the same magnitude. Beyond 400°C the comprehensive primary and secondary creep Harmathy model Equation 4-3 has most likely reduced towards the secondary model Equation 4-4. As the secondary creep model has not predicted the stress relaxation associated prior to this from primary creep, a higher stress is input than in the comprehensive model. At each equivalent time increment at such higher temperature exposure it then predicts a greater creep strain increment and thus the models converge. It also appears from Figure 4-14 that under a large enough soak time at 400°C, the same process may occur. On heating to 700°C, the secondary creep model is capable of predicting creep strain for a longer time period with respect to the constraints of the relaxation model. It however breaks down as the temperature approaches 700°C.

In order to visualise the onset of primary and secondary creep strain, a series of creep strain accumulation plots with data taken directly from the Abaqus stress relaxation models are now presented. Figure 4-15 shows a comparison of the accumulation of creep strain in the relaxation model heating to and soaking at 300°C for the comprehensive Harmathy model (Equation 4-3) and the secondary creep model (Equation 4-4). This again is taken from the modelled ASTM A416 [10] standard prestressing steel tendons.

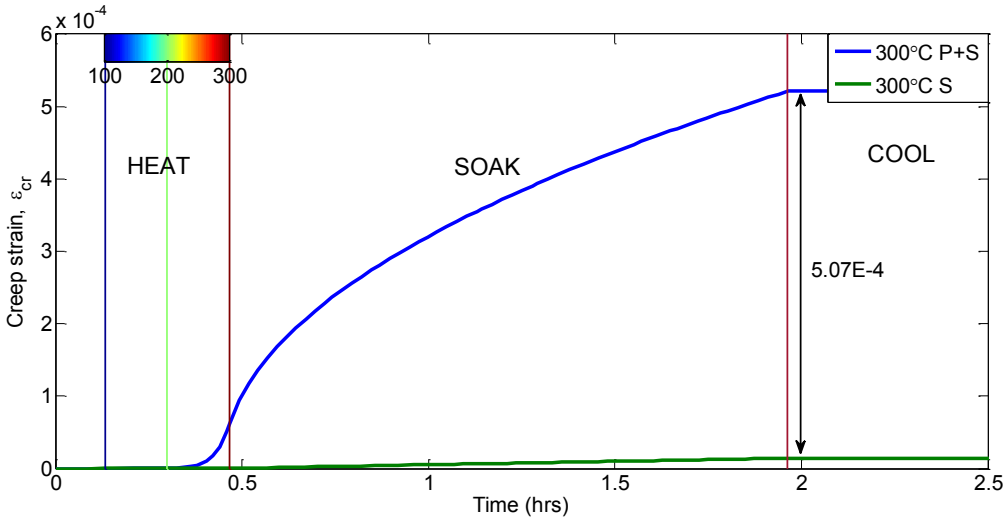

Figure 4-15; Accumulation of creep strain in relaxation models for the full Harmathy model and the secondary creep model

From Figure 4-15, the onset of noticeable primary creep strain in the modelled ASTM A416 [10] prestressing steel tendon is observed from approximately 250°C. This correlates with statements from Anderberg [29] regarding observational creep beginning at this point. The accuracy of this onset with respect to modelling is naturally down to the reliability of the experimental data used to derive the creep constants. Secondary creep strain steadily evolves during the soak phase at 300°C, but over the 90 minute heating period these strains do not materialise with any great significance at the stress applied (approximately 900MPa, Figure 4-14). Creep strain and the small degree of associated stress relaxation noted in the experimental data up to 300°C in Figure 4-8 must then be attributed almost entirely too primary creep. The magnitude of these creep strains with respect to stress relaxation are still relatively small, and as such temperature exposure to 300°C may be judged as not causing significant irreversible damage to an ASTM A416 [10] standard prestressing steel tendon (note in the experimental case the tendon is still recovering relaxed stress long beyond the 4 hours plotted).

Figure 4-16 shows the accumulation of creep strain with respect to both the full Harmathy model Equation 4-3 and the secondary creep model Equation 4-4 up to and including the remaining soak temperatures of 400°C, 500°C and 700°C (ASTM A416 [10] standard tendons).

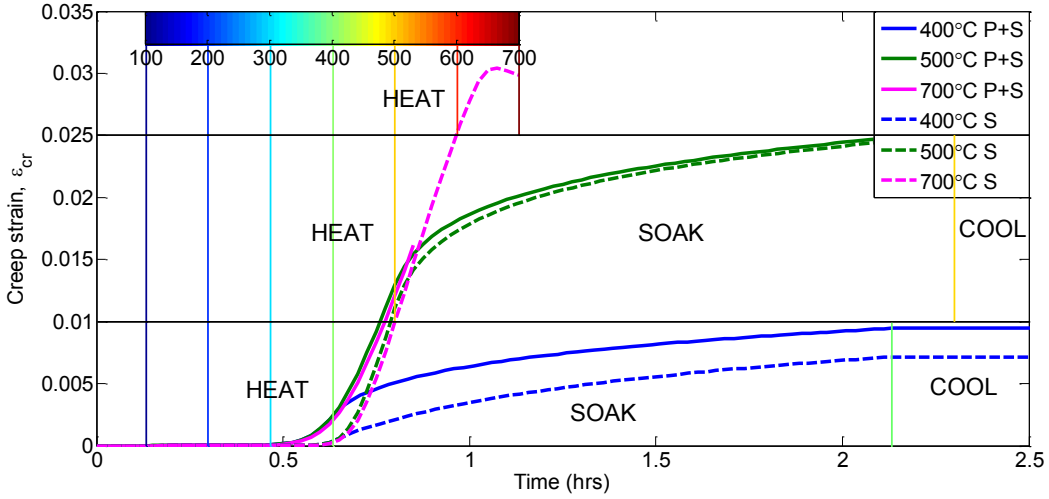

Figure 4-16; Accumulation of creep strain in relaxation models for the full Harmathy model and the secondary creep model up to soak temperatures of 400°C, 500°C and 700°C

It is firstly observed in Figure 4-16, the magnitudes of the creep strains are between one and two orders of magnitude higher than those observed up to 300°C, this increase contributes to the significant increase in stress relaxation beyond this point (Figure 4-14). Between 300°C and 400°C appears to be where the majority of primary creep strain is accumulated during transient heating. Secondary creep strains appear to become significant beyond 400°C, which yet again associates secondary creep strain accumulation to recrystallization through comparison to the microscopy observations of MacLean [9] (Section 2.2.1, Section 2.2.2).

Over short durations and temperatures reaching up to 400°C, primary creep strains should not be ignored (Figure 4-15, Figure 4-16). Care should also still be used in ignoring the effects of primary creep at temperatures beyond this point and over longer durations. It may however be possible to use Eurocode 2 [1] stress-strain temperature-dependent yield curves to account for primary creep strain accumulation in combination with a secondary creep strain model. This is explored in the following Section 4.4.6. It should be noted Abaqus will only use the larger inelastic strain increment computed at a given time, where both classical and creep plastic material models are present. It will not use both.

The previous data and discussion within this section refers only ASTM A416 [10] standard tendons. With regards to microstructural behaviour it would be useful to have an idea of when secondary creep emerges in BS 5896 [11] standard prestressing steel also. Section 4.4.4 compared temperature induced stress relaxation between BS 5896 [11] tendons and their ASTM A416 [10] counterparts. In doing so, Figure 4-11 and Figure 4-12 presented the accumulations of creep strain taken from, and contributing to the respective stress relaxation models. Figure 4-17 shows the total primary and secondary creep strain accumulated in BS 5896 [11] standard tendons recorded from the comprehensive Harmathy uniaxial creep model (Equation 4-3), compared to accumulation from a secondary creep only model (Equation 4-5). This data is taken from models heating and soaking to 400°C and 500°C respectively.

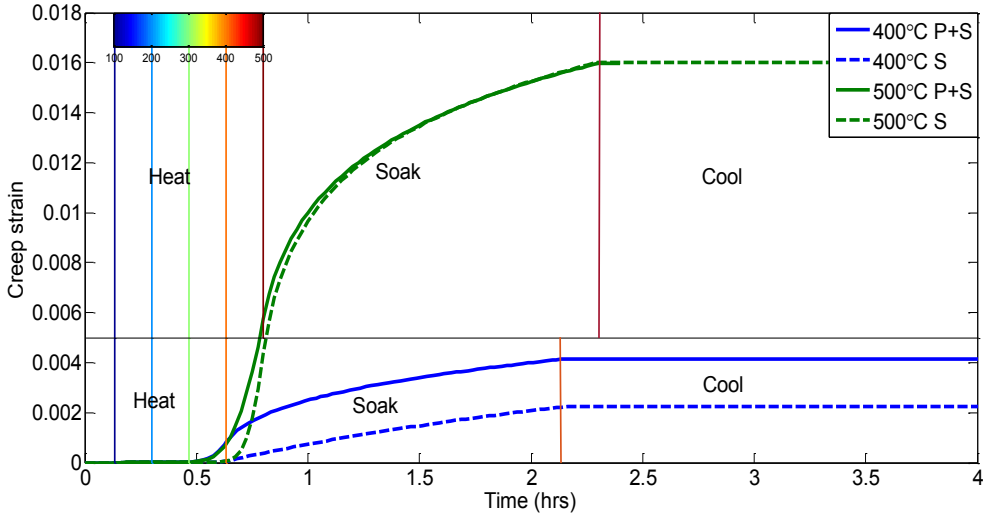

Figure 4-17; Accumulation of creep strain for BS 5896 standard prestressing steel heated to and soaked at 400°C and 500°C.

Figure 4-17 shows, much like the creep strain accumulation for ASTM A416 [10] tendons presented in Figure 4-16, that secondary creep appears to emerge from 400°C. This implies that recrystallization and its associated degradation of mechanical properties will also become observable from this point onwards in BS 5896 [11] prestressing steel.

4.4.6 Modelling simultaneous creep and classical plasticity

In the above modelling examples, plasticity has been modelled assuming the creep strain rate algorithms will account for all plastic strains accumulated. This appears to be relatively accurate in comparison to the experimental curves displayed in Figure 4-8 including the lower temperature transient behaviour below 300°C. In structural cases however, prestressing steel tendons are not strictly held at a fixed length. In a UPT concrete structure, as the slab deflects the tendon stretches and as such the internal tensile stress state should actually increase at low temperatures in the early stages of fire exposure. Under extreme load situations or the weakening of the concrete slabs flexural load resistance (possibly due to fire), the tendon could possibly be exposed to lower temperature dislocation based plastic strains. It could therefore be desirable to be able to couple classical and creep plastic models. Classical plastic strains accumulated at low temperatures should manifest through the same material mechanism as initial primary creep strains (dislocation motion) and thus they should not be allowed to superimpose in modelling. In Abaqus both classical and creep plasticity can be accounted for simultaneously. The larger plastic strain increment predicted from the two in a given time increment is that used to evolve the structural state [30].

Figure 4-18 shows stress relaxation curves for ASTM A416 [10] steel, as previously modelled against experimental data from MacLean [9]. The modelled curves combine a classical plasticity model (labelled +EC2), using the same Eurocode 2 [1] data as in Figure 4-9, with creep explicitly considered from the comprehensive Harmathy model (Equation 4-3). Relaxation curves using only the Harmathy creep model are also displayed for comparison (labelled ‘P+S’).

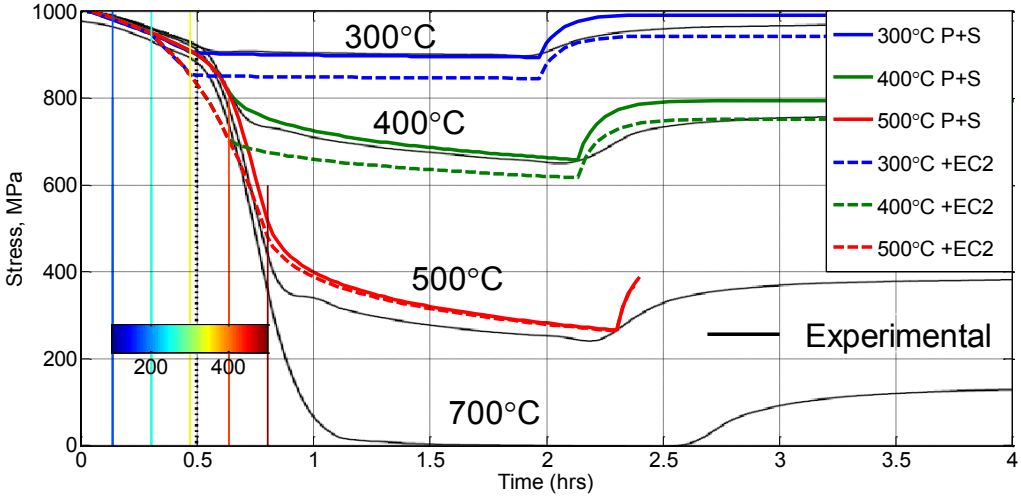

Figure 4-18; Stress relaxation modelled with simultaneous classical and creep plasticity.

It was noted from Figure 4-9, Eurocode 2 [1] computed yield curves over predict low temperature relaxation owing to a significant reduction of first elastic yield up to 400°C. This break from the experimental relaxation curves occurs at around 200°C. Modelled relaxation in Figure 4-18 towards 400°C is largely dominated by the plastic strain increments predicted from this Eurocode 2 data. As 400°C is approached the predicted creep strain increment at a given relaxed stress begins to exceed that from the Eurocode 2 [1] yield curves. Given the current accumulation of plastic strain being greater than experimentally predicted, and greater than a creep alone model would predict, this increased incremental strain contributes to increased relaxation. The modelled relaxation curve at 400°C then far exceeds the experimental curve and the creep alone modelled curve. As the temperature progresses towards 500°C creep strain is largely accumulating through secondary creep mechanisms and dominates over the classical plastic strain increment. As stress continues to relax the respective models in Figure 4-18 converge.

As mentioned in the previous section, as classical plastic strain and primary creep strain are accumulated through the same dislocation glide mechanism, it may be possible to combine Eurocode 2 [1] computed yield curves with a secondary creep model such as Equation 4-4. This can also eliminate the need to define a creep model via a user-defined subroutine as the secondary creep power law breakdown form can be represented by the Abaqus in-built hyperbolic sine model (Equation 4-5). Figure 4-19 shows a comparison of stress relaxation for ASTM A416 [10] standard prestressing steel modelled using the secondary creep model of Equation 4-4, coupled with the same Eurocode 2 [1] computed classical plasticity input data as displayed in Table 10-3 (labelled ‘S+EC2’).For further comparison purposes, the full Harmathy Equation 4-3 coupled with Eurocode 2 [1] yield reduction curves is also displayed (labelled ‘H+EC2’) alongside MacLean’s [9] experimental relaxation curves.

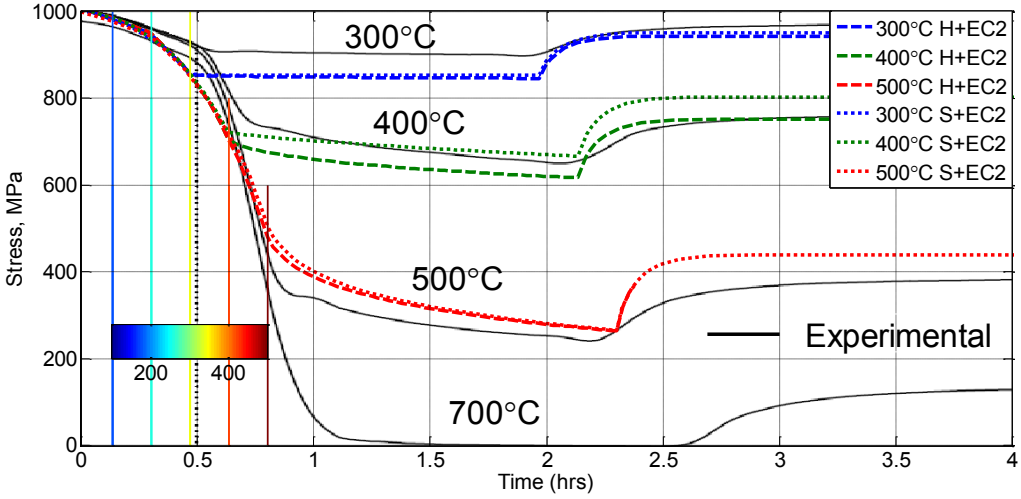

Figure 4-19; Stress relaxation modelled with simultaneous classical plasticity and Harmathy creep compared to simultaneous classical plasticity and a secondary creep model

At first glance this approach of coupling a classical plasticity model with a secondary creep model seems to be a reasonable simplification and with the absence of having to use a Fortran subroutine in Abaqus, may be more computationally efficient. It has however been noted in earlier plots such as Figure 4-15 and Figure 4-16 that primary creep strain can make a difference to stress relaxation in the 300°C to 400°C region during steady state temperature exposure. This appears to be the case with respect to the 400°C curve in Figure 4-19; where primary creep has not been explicitly modelled the rate and degree of stress relaxation is lower than experimentally observed. In a structural loading case where the tendon length is not fixed, the total internal stress state may rise beyond those in the above tests at these temperatures. As such primary creep strain effects, particularly at low heating rates may be more pronounced. So caution should be used and the situation being modelled carefully considered prior to using Eurocode 2 data to implicitly account for primary creep.

4.4.7 Additional models

In order to effectively model creep behaviour, particularly under transient external conditions, a series of constants typically have to be determined as a function of these external conditions. This usually relies on experimental data. The advantage of using Harmathy's model, Equation 4-3, is a set of constants have been experimentally determined for a variety of steels and particularly prestressing steels [6] [7]. Further, the equation reduces to a standard secondary creep form as creep strain accumulates.

The accountability for primary creep in Harmathy's equation is somewhat generic. As was mentioned in Section 3.3.1, primary creep strain evolution in Harmathy's equation (Equation 3-22, Equation 4-3) seems really to be a best fit curve between a standard secondary creep strain evolution and zero creep strain. It is largely based on the ratio of the accumulated creep strain at a given instant to the secondary creep strain intercept, $\varepsilon_{cr,0}$. This is treated as a single, temperature

compensated time dependent variable. It appears however that its accuracy may be due to primary creep strain accumulation generally being small in comparison to total creep or inelastic strain. Basing primary creep strain rate deceleration due to strain hardening as a function of accumulated creep strain is not uncommon; typically the relation is determined experimentally for individual metals or alloys. Given the possible importance displayed earlier in Figure 4-14 of primary creep strain with respect to stress relaxation in prestressing steel tendons at temperatures in the region of 400^{o}C, this may need a closer look. A more appropriate way of accounting for primary creep is to make the drag stress a function of accumulated creep or plastic strain within the exponential of the secondary model or Zener Hollomon parameter, as indicated in Section 3.3.1. Using Harmathy's model, Equation 4-3, as indicative of experimental data for ASTM A416 [10] steel, with constants determined by Gales [6] (Table 3-1), the secondary creep model Equation 4-5 is equated, allowing the inverse of the drag stress (constant, *B*, in Equation 2-8) to vary as a function of plastic strain. The form of this equation is displayed in Equation 4-6. Figure 4-20 shows these curves for increasing applied stress values.

$$\dot{p} = Aexp[B(p)\sigma]exp\left(\frac{-Q_c}{RT}\right)$$

Equation 4-6

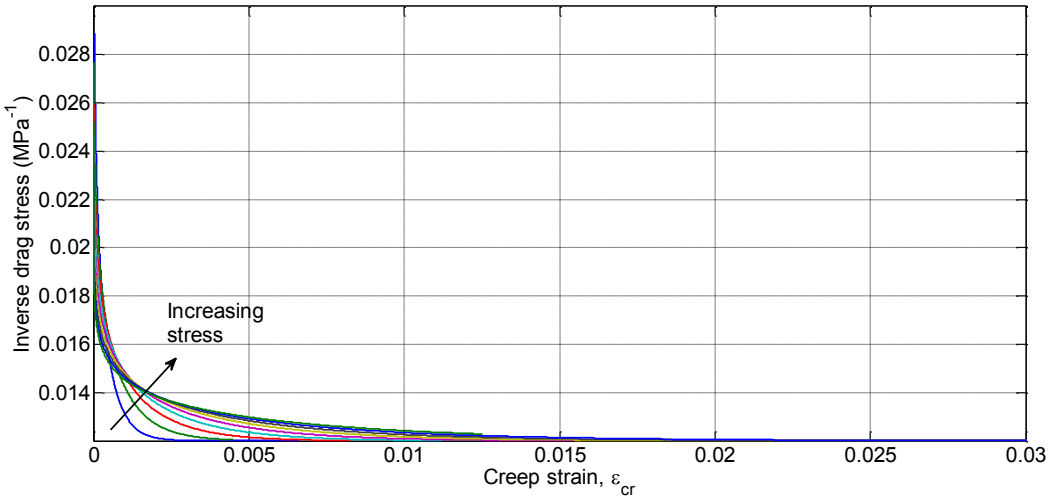

Figure 4-20; Inverse of the drag stress derived through equating the secondary creep form Equation 4-4 to Harmathy's model, Equation 4-3, at various applied stress states.

Using these curves in Figure 4-20, the inverse of the drag stress, *B*, can be tabulated within the Abaqus hyperbolic sine creep model as a function of accumulated creep strain and relaxed stress, both included as field variables. This inclusion necessitates the incorporation of a user-defined field (USDFLD) subroutine to be referenced from within the model. Figure 4-21 shows the obtained stress relaxation curves compared to Harmathy's comprehensive uniaxial model (Equation 4-3), from which the strain hardening drag stress evolution is derived. As would be expected the curves are very similar given they are equated to each other, the point here being to illustrate how a more concise definition of primary creep may be incorporated.

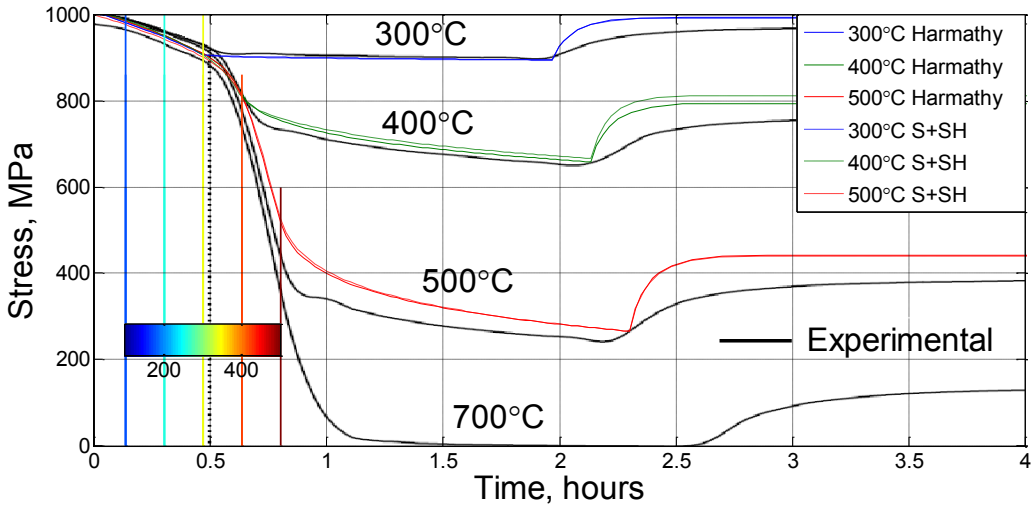

Figure 4-21; Comparison of a secondary creep model with incorporated strain hardening vs Harmathy's model

Harmathy's equation directly accounts for temperature effects through an incorporated Arrhenius function that can be broadly linked to representing the effects of vacancy concentration on creep. It does not include a direct reference as to temperature reduction effects of the elastic or shear modulus on creep strain rate. As mentioned earlier in Section 2.3 this may be implicitly reflected in a slightly higher activation energy being experimentally observed than at lower stresses and higher temperatures within the power law creep domain. The shear modulus naturally has an effect on creep behaviour, particularly in the initial primary phase as it represents the materials resistance to shear deformation, encouraging dislocation motion (Figure 2-3), as well as other lattice motions through increased lattice 'flexibility'. If the temperature dependent shear modulus, *G*, is assumed part of the drag stress, *D*, as in Equation 4-7 and extracted, then the drag stress or its inverse (Figure 4-20) relating directly to strain hardening may be approximated. Figure 4-22 shows these modified drag stress curves as a function of accumulated inelastic strain with the explicit inclusion of the temperature dependent shear modulus. These parameters are determined in the same manner as in Figure 4-20; equating a secondary creep model to Harmathy's uniaxial model (Equation 4-3) in Matlab at various constant stresses under transient heating (10°C per minute as in the previous models). The form of this new creep equation is displayed in Equation 4-8.

$$D = D'G; B = B'/G$$

Equation 4-7

$$\dot{p} = Aexp\left(B(p)'\frac{\sigma}{G(T)}\right)exp\left(\frac{-Q_c}{RT}\right)$$

Equation 4-8

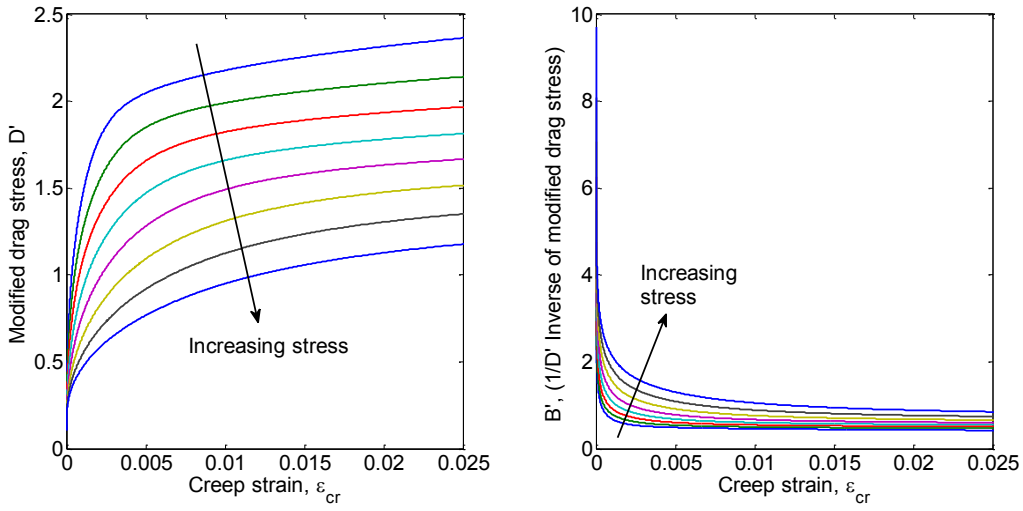

Figure 4-22; Drag stress and inverse drag stress without implicit inclusion of shear modulus vs creep strain under transient heating.

Once shear modulus is extracted in the manner shown in Equation 4-8, the overlap of the equivalent curves in Figure 4-20 is removed. The curves reflect that at lower temperatures, higher stresses are required to create a given creep strain rate and creep strain accumulation. Therefore drag stress decreases with applied stress which effectively increases the stress contribution to creep strain rate relative to the temperature contribution. For example, under steady state external stress and temperature conditions an increase in stress, whilst contributing directly to an increase in strain rate, also lowers the effective drag stress. As before the modified drag stress still requires tabulating with creep strain and stress which must be defined as field variables. Further the shear modulus could only be directly included if the model was defined as a subroutine. The above then serves more of an illustrative purpose with respect to the contribution of shear (or elastic) modulus as a function of temperature.

4.5 Summary

The key points from this chapter are summarised in the bullet points below. These relate firstly to the marked difference in creep strain accumulation and associated stress relaxation between BS 5896 [11] and ASTM A416 [10] standards of prestressing steel tendon wire and strands. The second key point to summarise is the applicability of the Harmathy comprehensive uniaxial creep strain rate model (Equation 4-3) to explicitly model creep in FE prestressing steel tendon models. This has implications for the inclusion of an explicit creep model in the prestressing steel tendon material definition of larger UPT concrete structural models. Finally, the validity of Eurocode 2 [1] derived stress-strain curves to implicitly account for creep is summarised.

- Grade 1860 BS 5896 [11] standard steel shows considerably less susceptibility to elevated temperature creep and subsequent stress relaxation than grade 1860 ASTM A416 [10] standard prestressing steel.

As the specified manufacturing processes appear to be the same, the different chemical compositions (Table 4-1) of the wires tested by Gales [6], with regards to determining creep parameters, may contribute to the difference in susceptibility to creep strain accumulation. Specific required chemical compositions are not defined in either standard, only guidelines are given. A degree of variance in chemical composition can therefore potentially exist even within prestressing steel manufactured to the same design code should steel rods be sourced from different suppliers. A difference in chemical composition is acceptable within the standards as long as certain ambient performance requirements are met by the manufacturer with respect to the finished product (Section 4.1). Elevated temperature stress or force relaxation performance requirements are not specified by either ASTM A416 [10] or BS 5896 [11] standards. The influence of chemical composition on elevated temperature creep and subsequent stress relaxation should therefore be explored further. This is of particular importance if the potential for differing fire performance exists even within prestressing steels designed to the same code, by different manufacturers (sourcing steel from different companies).

- Harmathy's comprehensive explicit creep model (Equation 4-3) validates well in predicting the contribution of inelastic strains to stress relaxation (Section 4.2, Equation 4-1, Equation 4-2) at temperatures up to 400^{o}C for ASTM A416 [10] prestressing steel tendons. This is to within 3% of the experimental relaxation curves of MacLean [9]. This accuracy reduces as temperature increases to as much as 15% by the time 500^{o}C is reached. The experimental relaxation curve profiles are however closely mirrored (Figure 4-8).

- Eurocode 2 [1] temperature reduction factors for computing inelastic stress-strain curves, fail to implicitly account for the contribution of creep to stress relaxation during transient heating to 500^{o}C, when compared to the experimental curves for ASTM A416 [10] standard steel. They do however cover the contribution of creep during transient heating to stress relaxation to 400^{o}C, when compared to the experimental curves.

  When Eurocode 2 [1] inelastic stress-strain curves are used to implicitly account for creep in BS 5896 [11] standard tendons, modelled stress relaxation during transient heating is greater than that predicted using an explicit creep model to 500^{o}C (Figure 4-10). If similar errors to experimental curves are to be assumed for BS 5896 [11] as with ASTM A416 [10], given creep constants are determined by the same author [6], transient heating creep should be considered implicitly accountable for this standard of steel (to at least 500^{o}C).

  The Eurocode 2 [1] determined stress-strain curves potentially misrepresent inelastic behaviour at elevated temperature. Lower temperature creep appears to be implicitly accounted for by a significant reduction in elastic yield stress up to 400^{o}C. Increasingly significant levels of strain hardening are however predicted as temperature rises and elastic yield drops. This degree of strain hardening continues well beyond 400^{o}C. This doesn't conform well to optical microscopy evidence from MacLean [9] with respect to observed recrystallization from this temperature, where yield stress would be expected to drop rapidly and strain hardening should be expected to become increasingly negligible. This

elevated temperature degree of strain hardening contributes to larger under prediction of relaxed tendon prestress as tendon temperature increases towards 500^{o}C and 700^{o}C in Figure 4-9 (Section 4.4.3).

5 One-way spanning UPT concrete slabs exposed to fire

Chapter 4 demonstrated there a reliable model to explicitly model creep in prestressing steel tendons within UPT concrete slabs and structures. This was demonstrated in stress relaxation models of isolated, prestressed tendons, subject to transient and then steady state thermal exposure. These models were compared to experimental data [9]. There is a 10-15% relative under-prediction in stress relaxation at 500^{o}C dependent on the stage of transient or steady state temperature exposure. However, despite this the explicit inclusion of a creep strain rate definition for a specific type of prestressing steel is considerably more accurate than assuming creep will be implicitly accounted for by Eurocode 2 [1] stress-strain curves (Section 4.4). It is also possible to account for creep strain accumulation and subsequent stress-relaxation during steady state heating.

The main goal in this chapter is to include a validated explicit uniaxial creep strain rate function within the prestressing steel tendon material definition of UPT concrete slab FE models. This allows the structural behaviour during fire of UPT concrete slabs to be compared when creep is explicitly modelled within the prestressing steel tendons as opposed to creep strain being assumed implicitly covered within Eurocode 2 [1] stress-strain curves. This requires consideration of slab-tendon temperature evolution post-fire as the compartment beneath the slab cools. The Eurocode 2 [1] guidelines state elevated temperature creep within prestressing steel should be considered at heating rates below 2^{o}C per minute. As the tendon transitions from heating to cooling the rate of change of temperature it experiences must drop below this. Therefore, the Eurocode 2 implicit creep coverage is only really valid if only the heating phase of fire exposure is considered. During a fire thermal gradients build up within a concrete slab meaning continued heat transfer to tendons and a resulting temperature increase can occur post-fire. The consideration of cooling, post-fire is therefore an important area of analysis to investigate potential continuation of UPT slab deflection and damage resulting from continued tendon prestress relaxation.

Possibly the most significant outcome of Chapter 4 was the difference in susceptibility to creep strain accumulation and the subsequent differences in prestress relaxation between grade 1860 ASTM A416 [10] standard manufactured tendons and grade 1860 BS 5896 [11] standard tendons. With the explicit consideration of creep in the prestressing steel tendon material definition of FE UPT concrete slab models, the behavioural differences, during and post-fire, can be compared dependent on the choice of prestressing tendon.

The main factors affecting the temperature exposure of the tendon are concrete cover and fire duration and as such these form the basis of a series of parametric studies, where both grade 1860 BS 5896 [11] and grade 1860 ASTM A416 [10] prestressing steel tendons are considered and compared. ASTM A421 [26]prestressing steel has not been considered owing to the constant determination from [7] being limited to 690MPa, and the significant scatter in data used to determine the given constants. The parametric studies undertaken are listed below:

- Three different minimum concrete covers; 25mm, 30mm and 35mm.
  Three different durations of standard fire exposure on the base of the slab at each concrete cover; 60 minutes, 90 minutes and 120 minutes with complete cooling of the UPT slab post fire.

The modelling process consists of two parts; firstly a heat transfer analysis determining temperature-time profiles at every nodal coordinate of the UPT concrete slab and tendon assembly. Secondly a mechanical model reads in the output from the heat transfer model allowing temperature dependent material properties to be updated at each time increment. The temperature-time curve representing the incident fire, as used in the heat transfer analysis, is the standard fire curve detailed in Eurocode 1 [31]. This is the only fire curve used in this analysis. This is by no means ideal as it creates a degree of rigidity with respect to the temperature-time curves of the tendon considered within the slab. For now however the modelling study will simply focus on varying the timescale of standard fire exposure on the base of a UPT concrete slab. Studies involving alternative and arguably more realistic fire temperature-time curves are a potential area of further analysis in the future. Further details regarding the use of the standard fire curve and its limitations are provided in Section 5.2 where the heat transfer analysis is presented. In addition most FE analysis on reinforced concrete structures in general is performed using plane stress shell elements and as such sectional behaviour cannot always be observed in detail. Out of plane stress-strain action that may occur around columns for instance cannot be viewed using shell elements. Further, out of plane effects that may result from restrained thermal expansion of the heated region such as lateral tensile strains induced through biaxial compression cannot be visualised. Details regarding the modelling set up will be provided in the next section. A factor not directly considered here is direct tendon exposure to fire resulting from concrete spalling. The possible consequences however may be deduced by considering the possible temperature exposure.

5.1 Model details

The following models have been created and analysed using Abaqus version 6.12. They have been designed following the guidelines of Eurocode 2 [32] with respect to slab dimensions and the cross-sectional area of standard, or prestressing reinforcement required. The slab models presented are somewhat of a hybrid between an isolated internal span slab and an isolated external span slab. UPT concrete structures may be designed if sufficient numbers of PT tendons are used such that no additional tensile sagging reinforcement is required within internal spans. This is a concern where the unbonded nature of the tendons means should their tensile stress relax there remains no additional tensile reinforcement for the slab. In order to simplify the modelling scenario an isolated internal span slab has been modelled such that no additional sagging rebar need be specified. The boundary conditions for the slab are set to mimic that of a beam; although this imaginary beam is fixed in terms of rotation. Anchors have been included in the model in order to create the compressive longitudinal effect desired, as well as the vertical ‘hard’ contact effect created from the draped nature of the tendon when tensioned. In addition to the anchors, bursting reinforcement has been added to prevent possible numerical failure due to localised tensile damage.

The models are based around a 10 by 6 metre, one-way spanning in the long direction, UPT concrete structure. The design involves a 250mm thick slab, which under the design load and working tendon stress requires ten tendons for one six metre cross-span on 600mm separations to ensure no additional longitudinal reinforcement is required when designed according to Eurocode 2 [32]. The tendon profiles are smooth parabolas determined through the minimum concrete cover

requirement for the particular model and the locations of points of contraflexure, where the tendon is designed to pass through the slab midsection depth. The gradient of the tendon at this point is maintained such that the hogging concrete cover is determined from a continuous parabolic profile function. Points of contraflexure (zero bending moment) were determined using Matlab whereby a script was developed applying the direct stiffness method to subframes, determining bending moment envelopes corresponding to every possible combination of variable and dead load. Within end spans the first point of contraflexure is typically slightly closer to the support than in internal spans.

The models utilise symmetry such that only a quarter of the slab is modelled. Boundary conditions are applied to the cut longitudinal face of the slab, restricting displacement in the longitudinal one-way span direction (x-axis) and rotation about the slab depth axis (y-axis) and the transverse axis (z-axis). The cut transverse face is restrained in displacement in the transverse direction as well as rotation about the x and y-axis. In fact the slab has been restrained against displacement entirely in the z-direction; this prevents thermal expansion and bowing about the cut x-face (when the entire transverse z width of the slab is heated). The main reason for applying this restraint is to aid numerical convergence, both decreasing run time and aiding model completion. In actuality the addition of this restraint means identical results should be achievable through modelling a single strip of slab, symmetric about one tendon.

It should be noted this is primarily a parametric study. Representing realistic structural restraint conditions either through modelling or experiment on isolated slabs is always a difficult task (unless the fire is small and central with respect to slab dimensions). The consequences of neglecting creep in prestressing steel tendons will be considered in more realistic structural conditions in the next chapter. The imaginary beam creating the slab support boundary condition is 500mm in width. In order to represent an internal span half of this should be modelled, however it aided numerical convergence to model the full beam support width. This reduces the effective span of the slab but is convenient for an end span where the point of contraflexure is closer to the first support than for an internal span.

The slab has been loaded with a uniform pressure load on the entirety of the top surface. The magnitude of the load is 5KN/m^2; this being made up of a 2KN/m^2 floor load and 3KN/m^2 variable load. Gravity is modelled as a body force with concrete density input as a function of temperature (Table 11-1, Appendix D; Concrete material parameters).

Figure 5-1 shows an image of the modelled quarter slab displaying dimensions and boundary conditions. The imaginary beam support, whilst fixed in rotation, is allowed to displace in the x-direction. This condition is modelled as a series of nodal simple supports across the slab-beam contact area; the freedom to roll in the x-direction is to aid numerical convergence.

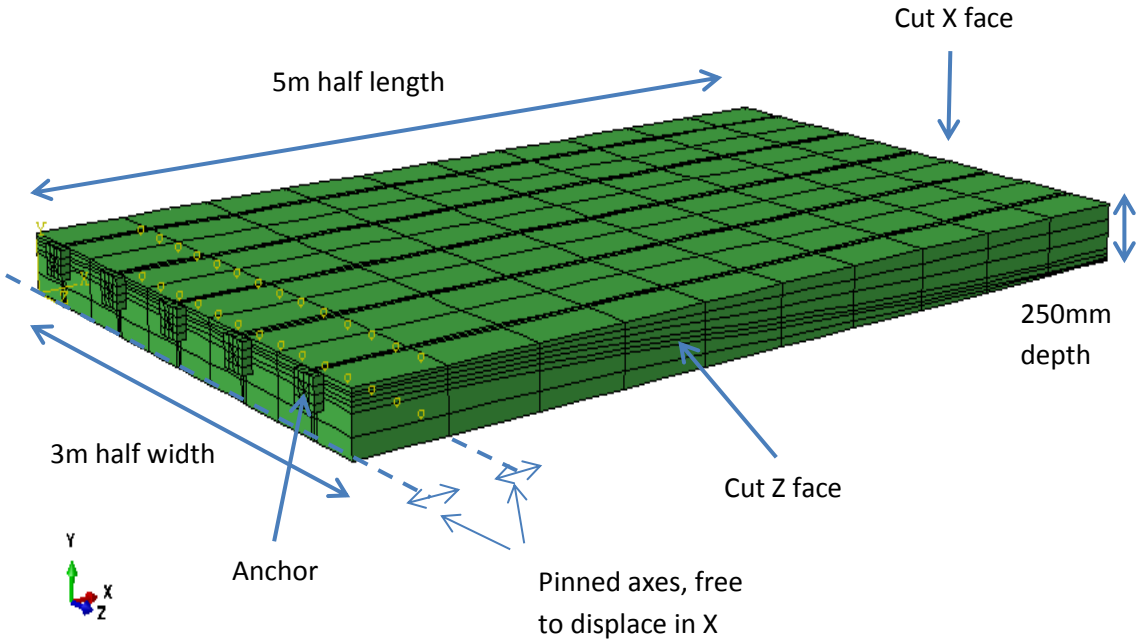

Figure 5-1; Modelled slab views, dimensions and boundary conditions

Typically models of slender slabs (high span-depth ratio) use plane stress shell elements with a number of section points specified to account for compressive and tensile bending stresses throughout the depth, so as to compute the total element response in flexure. However it is not possible to consider tendon slab contact with such elements. The combination of restrained thermal expansion, compression through post tensioning of tendons, hard contact between the tendon and slab and the applied load on the top of the slab mean complex sectional behaviour may ensue and vary along the length of the slab. It is particularly likely this type of behaviour could occur about supports such as columns. The model therefore uses solid continuum elements C3D8 for tendons and anchors whilst quadratic C3D20 elements are used for the slab. Continuum elements are particularly useful for contact problems and non-linear problems involving plasticity and potentially large displacements; they lend themselves particularly well to concrete problems as such. Quadratic elements as used in modelling the concrete slab have a non-linear quadratic distorting capability under stress, and thus are able to resolve out-of-plane strains within an element. These are very accurate at considering localised stress concentrations and behaviour with a coarser mesh than if linear elements such as C3D8 elements were used. This is facilitated by a quadratic shape function (quadratic interpolation of element internal coordinates from edge and corner nodes) allowing the element to bend and distort, suiting it to bending problems [30]. Linear continuum elements display constant volumetric stiffness; that is to say parallel edges cannot change length with respect to one another during a deformation. This can be limiting in considering out of plane effects (out of slab plane in case of this study). Contact between the tendon and the slab is defined via a master slave relationship with ‘hard’ normal contact and ‘frictionless’ tangential contact; the stiffer steel tendon surface being the master and the concrete ducts modelled through the slabs being the slave surface (Figure 5-2). The use of quadratic C3D20 elements for the concrete slab ensures a coarser nodal mesh for the slave surface assisting the contact computation.

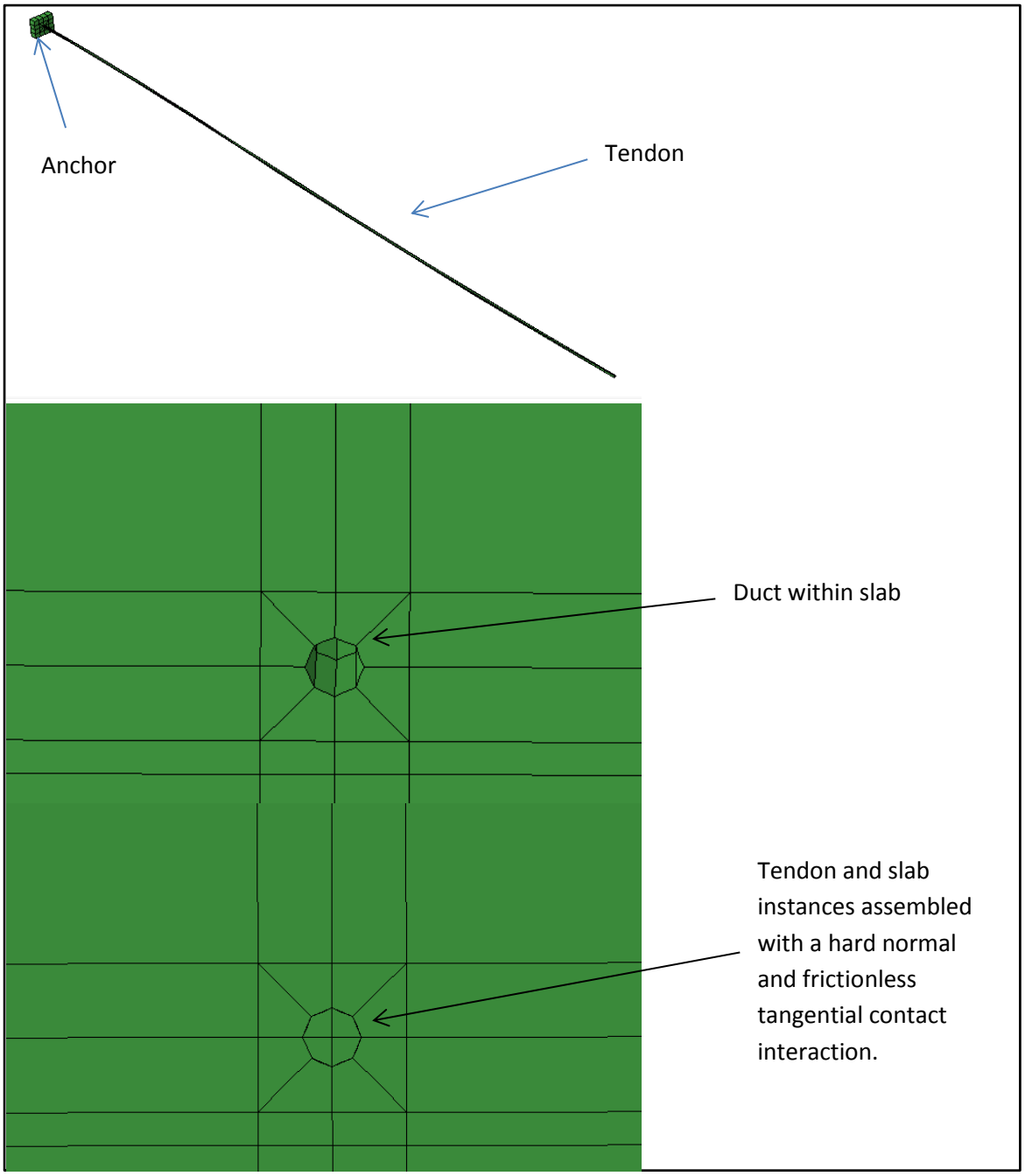

Figure 5-2; Tendon, slab duct and their combined assembly

Bursting reinforcement is modelled using truss elements embedded within relevant local quadratic concrete elements (Figure 5-3). Figure 5-3 displays the internal structure of the slabs highlighting the internal tendon profile and bursting rebar. The model as stated earlier has been designed to a 250mm depth for a 25mm tendon cover slab, with 10 tendons spanning one-way accommodated within a single 6 metre span. The specification of this tendon density ensures no longitudinal standard rebar need be included for an equivalent internal span. The tendons are placed individually on 0.6m separations. To compare the effect of varying concrete covers on tendon temperature during a standard fire and the resulting UPT concrete slab structural effects, rather than keep slab depth constant, ultimate moment capacity has been kept constant. The 30mm and 35mm concrete

cover slabs then are slightly thicker than the 250mm of the 25mm cover slab (255mm and 260mm respectively).

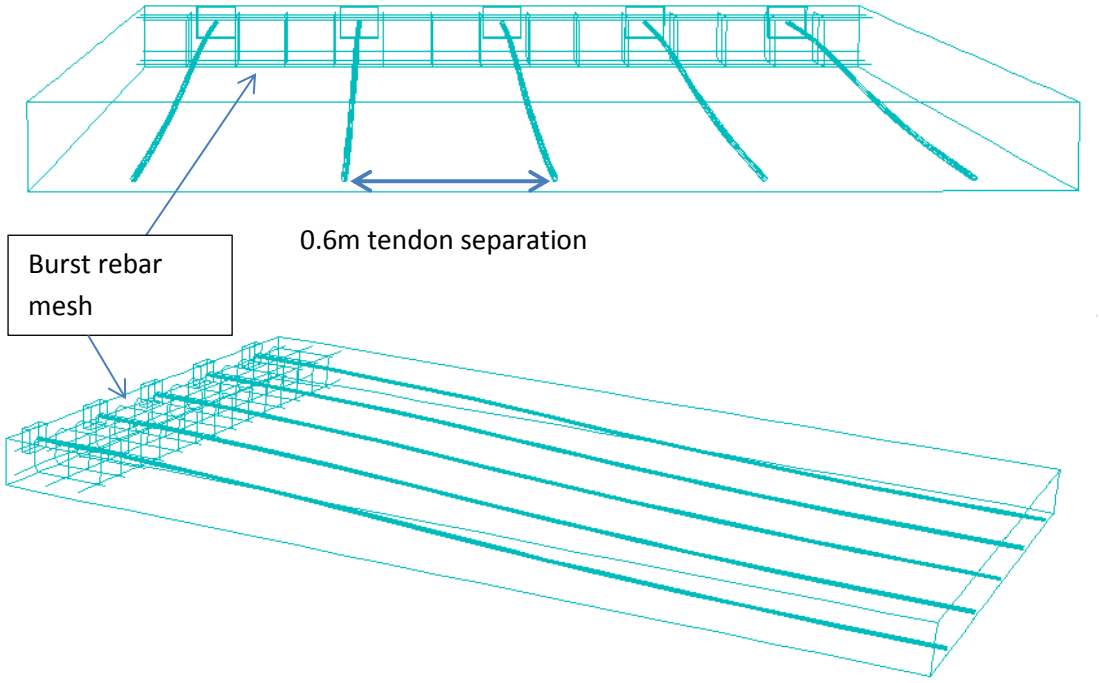

Figure 5-3; Internal slab structure

Material parameters and assumptions

The thermal and mechanical properties used for the prestressing steel are as detailed in Appendix C, Prestressing steel material parameters. It should be noted that in the forthcoming slab models, standard units of time (seconds), stress (Pascal's) and distance (metres) were used as opposed to hours, MPa and mm in the previous chapter. With respect to prestressing steel material parameters, classical plasticity has also been included to account for any potential 'cold' tendon plastic behaviour. That is to say, tendon plasticity at elevated temperatures below those at which creep is significant and dominant. As was described briefly in Chapter 4, Abaqus couples classical and viscoplasticity such that only the larger predicted plastic strain increment is used; it does not sum the respective inelastic strain components. From the material behaviour described in Chapter 2, it should be recalled that these behaviours are not separate entities and thus Abaqus deals with it appropriately. The only limitation is the material data input. The uniaxial creep strain rate function used is the uniaxial Harmathy model (Equation 4-3) encoded within Abaqus via a user-defined subroutine. Abaqus uses this uniaxial model as a function of Von Mises stress; this effectively computed the magnitude of the creep strain rate within the constitutive framework described in Section 3.2.

Thermal and mechanical concrete properties used are detailed in Appendix D; Concrete material parameters. Eurocode 2 [1] details stress-strain curves for concrete in compression. This curve consists of an initial ascending branch which displays approximately linear elastic behaviour at small

strains. Beyond the peak of the ascending branch the curve softens linearly to zero stress at the ultimate strain. The peak stress, the strain at peak stress and ultimate strain are all functions of temperature. Elastic modulus is not explicitly defined, it is however a required parameter within Abaqus. Values input for elastic modulus are obtained through taking the tangent modulus of the Eurocode 2 curves at zero strain; these are tabulated in Table 11-2. Abaqus requires uniaxial inelastic compressive stress-strain curves to be input with stress tabulated against inelastic strain. This data is taken from the Eurocode 2 [1] stress-strain curves from 0.1% strain; inelastic strain is taken as zero at this point. Uniaxial compressive inelastic stress-strain curves with temperature are tabulated in Table 11-7. Tensile yield stress as a function of temperature is listed in Table 11-8 (Appendix D; Concrete material parameters).It will be noted that softening behaviour of the inelastic concrete yield curves with respect to tensile behaviour is not modelled and instead ideal plasticity is assumed. This unfortunately does not represent accurate concrete behaviour with respect to approximating and representing cracking associated to tensile displacements and resulting softening with increased strain, but significantly increases the chance of numerical convergence during implicit backward Euler integration. The first entry in these tabulated stress-strain curves in combination with the tabulated elastic modulus values dictates the uniaxial elastic behaviour.

The elastic-plastic division of material response to loading is determined based on the position in principal stress space of the material stress state (at a given point) with respect to a modified drucker-prager yield surface. The yield function is defined by [33] with modifications by [34]. Unlike the Von Mises yield surface typically used with metals this represents material yield as a function of hydrostatic stress as well as deviatoric stress (amongst other factors). When the hydrostatic stress component is low this results in brittle behaviour whilst at higher hydrostatic stresses, behaviour is more like that of a ductile metal [18] [30]. Generally in structural situations the hydrostatic stress is relatively low, resulting in tensile cracking and compressive crushing behaviour with evolving plastic strain. The dimensions of the yield surface and thus the form of the yield function are defined dually through the specified uniaxial compressive and tensile yield stresses mentioned above combined with an in-built *concrete damaged plasticity* model within Abaqus. This model requires the specification of five parameters to complete the definition of the yield surface and also to define the flow potential, the values of these parameters are listed in Table 11-6, Appendix D; Concrete material parameters. The plastic flow (accumulation of plastic strain) is *non-associated* to the yield state/surface; this means it does not necessarily flow perpendicular to the yield surface or parallel to the direction of the deviatoric plane. Therefore a separate function (the flow potential) or surface defines the direction of the flow via its rate of change with respect to change in stress state. This flow potential is the hyperbolic Drucker-Prager function; its value is a function of the hydrostatic and deviatoric stress invariants and is defined with respect to two of the five parameters within the concrete damaged plasticity definition; the dilation angle and eccentricity.

The yield surface itself, as already stated, is defined by uniaxial tensile and compressive yield stresses as well as the definition within the concrete damaged plasticity model of the ratio between biaxial compressive yield and uniaxial compressive yield (usually taken as 1.16). This parameter essentially allows definition of the peak radius of the conical yield surface along its compressive meridian. A further parameter defines the ratio of this compressive meridian radius to the tensile meridian of the yield surface; thus defining the cross section of a cut through the conical surface. The remaining parameter defined within the concrete damaged plasticity model is a *viscosity parameter*; this essentially damps and delays the plastic displacement response of the concrete. The

main reason for the inclusion of this parameter is to ease numerical convergence problems with respect to softening behaviour of concrete in tension. Tensile softening behaviour associated to cracking can result in large sudden displacements; something often difficult to resolve numerically when a global equilibrium state is to be found at the end of each time increment. A non-zero viscosity parameter allows a given plastic strain to accumulate over time rather than instantaneously. Should the material be softening the stress state can then effectively exist temporarily outside the yield surface, evolving towards it. This allows a converging local and global equilibrium state to be more easily found with each increment. Over very large time periods, with a sufficiently small viscosity parameter, the solution should evolve towards that of the zero viscosity parameter solution [18] [30]. This may cause problems in highly transient thermo-mechanical analyses however, where time is not available for the solution to tend towards the zero solution. It is often easier to achieve convergence by simply assuming ideal plastic tensile behaviour combined with the inclusion of rebar.

A very important material response of concrete under load, with particular consequences on cooling behaviour, has not been explicitly considered within this thesis. The behaviour of note is known as load induced thermal strain (LITS). Generally speaking, LITS refers to a number of different strain components related to various phenomenological behaviours observed within heated concrete. The largest strain contributor to LITS is known as transitional thermal creep (TTC) [35]. This strain component evolves with time (hence the reference to creep) under first heating of loaded concrete. Its magnitude is the difference between total strain observed when concrete is heated under load, compared to total strain when concrete is held at a steady state temperature and then loaded (Figure 11-2, [36]). TTC is often referred to as transient creep strain (TCS); it is also often labelled as transient strain or transient creep. Strictly speaking TCS refers to the sum of TTC and another LITS component known as drying creep [35]; the latter component is generally far smaller than the TTC contribution and therefore taken as negligible. The main impact of TTC when added to the total strain component of concrete is its irrecoverable nature. Further, it generally evolves relatively early in the heating process and as a result creates a stress-strain curve with a far shallower gradient in its ascending branch than is representative of its true or pure elastic behaviour. As mentioned earlier in this section, elastic modulus is often determined from the gradient of the tangent to the stress-strain curve through zero strain. This can result in an *apparent* elastic modulus (dependent on temperature) being determined and used in design or computational analysis, below that of the *actual* elastic modulus [35]. Neither the irrecoverable nature of TTC strain, nor a reduced elastic modulus, is necessarily a problem when only heating is considered; total strain and resulting stress evolutions will be predicted through the stress-strain curves used. On cooling or unloading however, the irrecoverable nature of TTC strain and use of an apparent reduced elastic modulus can seriously impact the predicted behaviour. Firstly strength, displacement and damage recovery will be overestimated whilst elastic recovery will take far longer to occur [35].

Eurocode 2 [1] states TTC strain to be implicitly accounted for within the mechanical strain component of the specified temperature dependent stress-strain curves. This is much like the inclusion of creep strain in prestressing steel is said to be implicitly covered by the design code stress-strain curves. As with prestressing steel, implicit TTC coverage is accountable within the heating range $2℃/min \leq \dot{T} \leq 50℃/min$. The limitations with the Eurocode 2 [1] assumptions are firstly, the TTC accumulated during the ascending branch of the Eurocode 2 stress-strain curves

below 0.1% strain will be taken as elastic and recoverable when input within a commercial FE software package such as Abaqus. Secondly, during the transition between heating and cooling within the concrete, the heating rate will drop below 2^{o}C per minute; as TTC is time evolving, strain will continue to accumulate. Thirdly, as stated earlier, the temperature dependent elastic modulus is not explicitly defined within Eurocode 2 [1], it is however necessary to be defined within a concrete material model for FE computation. The Eurocode 2 compressive concrete stress-strain curves do not represent the true elastic behaviour of concrete due to the addition of TTC strain within the ascending branch of the curves. This means an under-estimated elastic modulus at a given temperature may be used within an FE model if determined from the initial gradient of these curves.

Work by Gernay [36] has adapted the Eurocode 2 [1] implicit TTC accounting stress strain curve to a version excluding TTC strain. The TTC strain is considered explicitly as an independent, inelastic strain component of the total strain. Its magnitude is based on experimentally determined proportional relationships to the ratio of the current stress to the peak cube stress. This partition of TTC strain has the advantage of allowing an actual elastic modulus to be determined tangential to the initial part of the ascending modified stress-strain branch, and allows unloading and cooling behaviour to be considered in terms of actual recoverable and irrecoverable mechanical strain. The explicit TTC strain is itself used to partition the modified stress-strain curve from the Eurocode 2 implicit version. The addition of a method such as the above to explicitly consider TTC strain and actual elastic behaviour is a possible future addition to the models presented herein. Given the importance attached in this chapter to compartment cooling, both the effect of elevated temperature creep strain on continued tendon relaxation and the effect of LITS on further irrecoverable concrete damage are essential additions, particularly for analysis related to performance based design.

5.2 Heat transfer analysis

The behavioural modelling of UPT concrete slabs exposed to fire is a two stage process. A heat transfer model determines temperature-time profiles at nodal coordinates throughout the slab-tendon assembly. Following this, a mechanical model reads in these temperatures at each time increment (using interpolation where necessary) in order to update temperature dependent material properties and analyse structural response to load and fire. The heat transfer analysis also provides useful data for analysis in its own right; in this study the temperature-time profile of the prestressing steel tendons is of particular interest as is the effect of concrete cover and fire duration on its magnitude and heating rate. The mechanical model, as well as considering the structural consequences of choice of concrete cover and the effects of fire duration, also considers the choice of prestressing steel used. BS 5896 [11] and ASTM A416 [10] manufacturing standards of prestressing steels have different viscoplastic responses to temperature and load as experimentally shown by Gales [6] (Table 3-1); differences in creep induced stress relaxation between the two were shown in the previous chapter (Section 4.4.4, Figure 4-10). In the absence of respective material data (with the exception of creep constants) distinguishing the prestressing steels, Eurocode 2 [1] data for prestressing steel relating to both heat transfer and general mechanical properties are used. The heat transfer models presented then only consider concrete cover and fire duration (not steel type)

as variable parameters and as such these models are assumed applicable to both BS 5896 [11] and ASTM A416 [10] standards of prestressing steel.

In the heat transfer model, rather than reduced integration continuum structural elements (C3D8R) for the tendon DC3D8 continuum heat transfer elements must be used in their place, whilst DC3D20 quadratic continuum heat transfer elements are used for the concrete slab elements. Heat transfer between the slab-tendon 'gap' is modelled using *gap conductance* and *gap radiation* interaction properties. In the latter case both the slab concrete surface and the tendon prestressing steel surface are assumed to have an emissivity of 0.7. The gap radiation interaction property requires the input of an effective view factor; this refers to the amount of radiation incident on the slave surface from the master surface (in the heat transfer models the concrete duct is taken as the master and the tendon surface the slave, these rolls reverse for the mechanical model) . The interaction requires the effective view factor to be tabulated with gap distance; this must involve an effective view factor of unity when the gap distance is zero, ensuring all radiation from the master is incident on the slave. There is also the requirement that a gap distance whereby the view factor reaches zero is specified; at which point no radiation from the master surface reaches the slave surface; this has arbitrarily been set at 1mm. This essentially means all radiation leaving the duct surface is incident on the tendon as the gap distance under no load, during the heat transfer model, is zero. The gap conductance interaction also requires a gap distance or surface clearance at which point the conductivity across the gap is to be zero. This has also been arbitrarily set at 1mm; the surface conductance has been taken as the ambient conductivity of the concrete detailed in Table 11-4, Appendix D; Concrete material parameters taken from Eurocode 2 [1].

The purpose of this analysis is predominantly to study the effect of creep within prestressing steel tendons explicitly on the behaviour of UPT concrete slabs. Specifically this is compared to models using yield curves computed using Eurocode 2 [1] temperature reduction factors within the prestressing steel material model (said to implicitly account for creep at heating rates between $2^{o}C$ and $50^{o}C$ per minute). Bearing this in mind it is not desirable to heat the slab near the supports where structural actions may occur masking the consequences of excessive tendon relaxation. Therefore the models presented focus on heating around the point of minimum concrete cover in the centre of the slab span (about the longitudinal cut-x-face, Figure 5-1). This allows effects of load and moment re-distribution to be explored about supports and other areas of the structure resulting from tendon relaxation, and whether any of this behaviour is enhanced when tendon creep is explicitly considered.

The heat transfer model has been completed using a two stage approach; firstly a simple slab was modelled exposed to a standard fire on its base and allowed to heat via convective and radiative interactions. Secondly a full model of a UPT concrete slab was modelled with the previously determined base temperatures, as a function of time, defined as nodal boundary conditions on the desired base region of the slab. A full three-dimensional heat transfer analysis was preferable to a simple one-dimensional analysis in order to compute nodal temperatures along the parabolic tendon and tendon-duct profiles. These could then simply be read into the mechanical model through referencing the heat-transfer output database. Conductive coefficients, material density and specific heat are all defined as functions of temperature and tabulated in Appendix C, Prestressing steel material parameters and Appendix D; Concrete material parameters. The specific

heat capacity values for concrete as a function of temperature are tabulated in Table 11-5 and plotted in Figure 11-1; these relate to a moisture content of 1.5% by mass within the concrete.

An often overlooked factor in structural fire modelling is the structural response during cooling post fire; these models have attempted to address this. Naturally once a fire ceases there still exist thermal gradients within the slab and thus further heat transfer through conduction must continue to occur in a direction dictated by these gradients. The base of the slab cools via convection and radiation at a rate dependent on the sink temperature of the air in immediate proximity to the slab base. As the base cools steep thermal gradients begin to emerge promoting heat transfer back towards the slab base. At some point post-fire therefore, the tendon will begin then to cool as thermal gradients deeper within the slab reverse in direction. The time it takes post-fire until the tendon begins to cool depends on how rapidly these thermal gradients reverse. Factors affecting this include the nature of thermal gradients created by the temperature-time profile of the fire at various points on the surface of the slab base. Other factors are the rate with which the air sink temperature cools in immediate proximity to the slab base.

The implications of continued tendon temperature increase post-fire are multiple:

- Continued tendon temperature rise will increase tendon relaxation and thus increased UPT concrete slab deflection and damage post-fire.
- The tendon will go through a phase of lower-transience temperature exposure where creep could play a significant role on increased tendon relaxation.
- Tendons may become exposed to temperatures where microstructural evolutions such as recrystallization begin, degrading mechanical properties such as yield strength and increasing ductility.

Modelling of cooling can often be tricky with respect to achieving numerical convergence to a global structural or thermal equilibrium state. This is particularly true during highly transient heating phases and the transition between heating and cooling when thermal gradients reverse. In order to attempt to model cooling parametric temperature-time curves from Eurocode 1 [31] relating to air sink temperature cooling have been considered. The accuracy of the curves depends on numerous details relating to the compartment being considered; these mainly include the area and height of openings with respect to the total area of the surfaces enclosing the compartment and the thermal material properties of the surfaces. These material properties include material density, specific heat and thermal conductivity as they relate to heat transfer. The type of building to which the modelled UPT concrete slabs of this chapter would form has not been considered, and as such functional and aesthetic details relating to windows and openings are not considered. The slabs modelled are of a high span-depth ratio however, suggesting the building would perhaps be somewhat open-planned. The value of the main parameter, Γ [31], combining the above physical and material properties determining the cooling curve has been chosen purely to allow convergence within the mechanical model throughout cooling. Highly transient cooling resulting from a sharply declining sink temperature leads to large thermal gradients at the base of the slab and rapid changes in direction of thermal gradients progressively through the slab. This results in rapid drops and changes in thermal expansion and therefore rapid stress changes from compression to tension and vice versa, these significantly affect the structural response of concrete. The values of, Γ [31], chosen to achieve convergence likely reflects a situation where air temperature cools particularly slowly. The

consequences of this will be presented shortly with respect to tendon heating and cooling curves within a UPT concrete slab; possible structural effects are postulated within the mechanical results section.

5.2.1 Slab temperature profile

An area of the modelled UPT concrete slab base of 6 metres by 6 metres square has been heated via a standard fire temperature-time curve [31]. Using symmetry to reduce the size of the model this becomes a 3 metre by 3 metre region. The standard fire temperature-time curve is represented by Equation 5-1 with the time in minutes and temperature in ^{o}C.

$$T = 20 + 345\log_{10}(8t + 1)$$

Equation 5-1

Figure 5-4 shows the standard fire curve plotted with time. The 60, 90 and 120 minute heating cut off points are also displayed, showing where they intersect the curve.

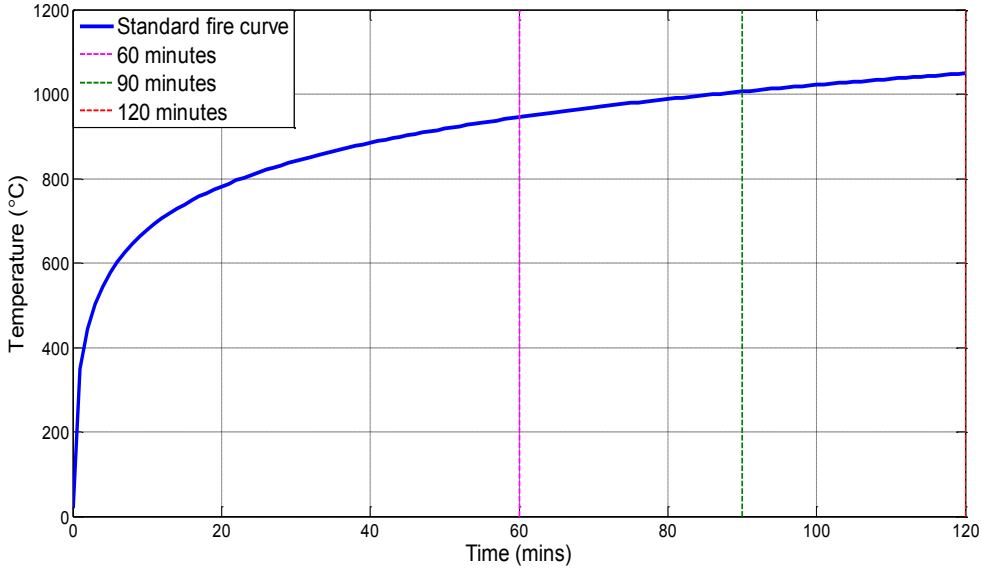

Figure 5-4; The standard fire curve

The gas temperature displayed by the standard fire curve temperature-time curve is incident on the slab base through radiation and convection. The curve acts as the sink temperature within the compartment. The convective heat transfer coefficient used was 25W/m^{2}K to the base of the slab whilst the emissivity of the concrete was taken as 0.7. The heated region of the base of the quarter slab is displayed in the contour plot Figure 5-5 showing the temperature distribution throughout the slab thickness after a 90 minute exposure to a standard fire (30mm cover to prestressing steel tendons).

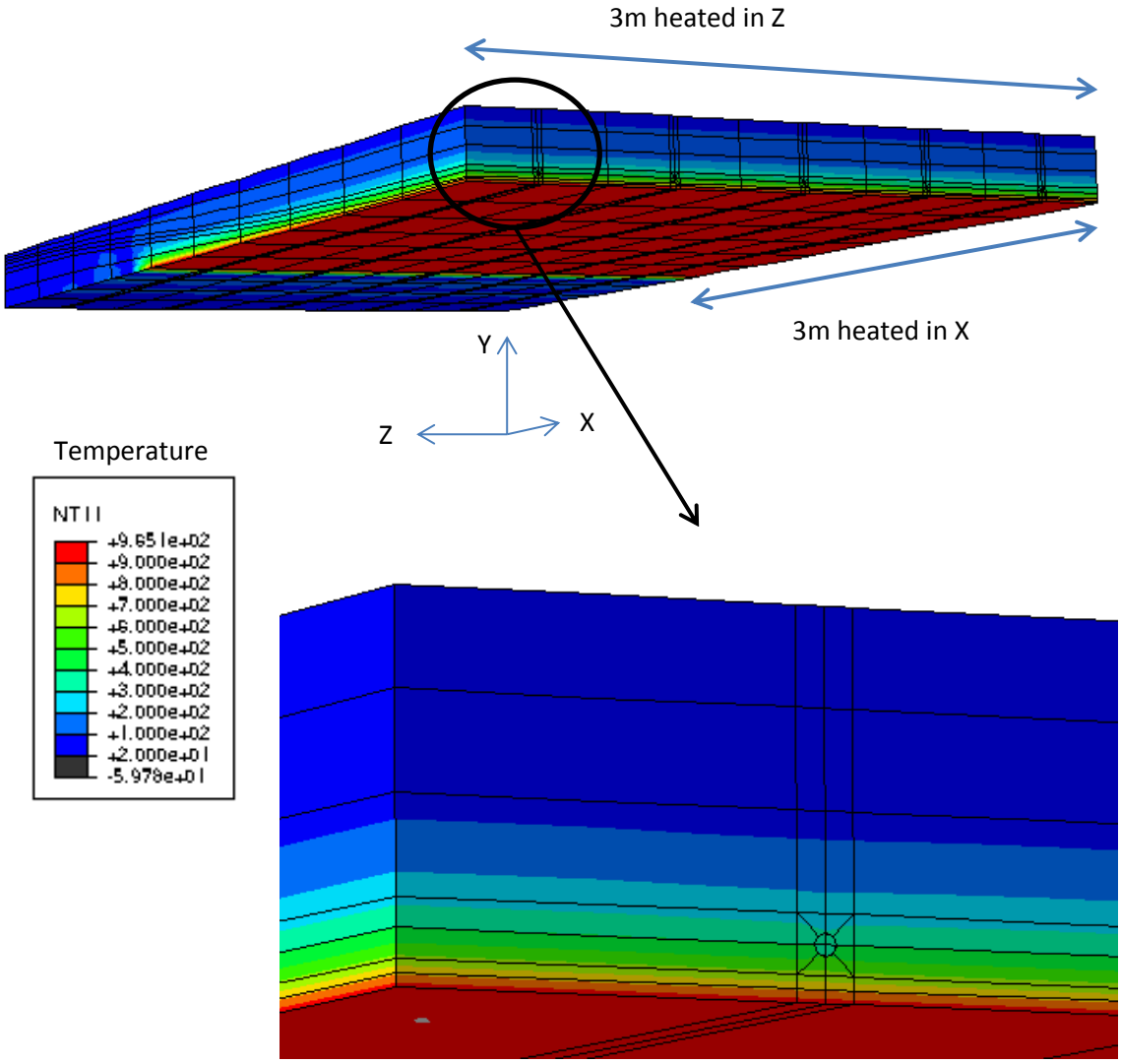

Figure 5-5; Heated slab base after 90 minutes exposure to a standard fire

The evolution of temperature over time throughout various sections of the slab depth is displayed in Figure 5-6 for a slab exposed to a 90 minute standard fire on its base. The case displayed refers to a model with a minimum concrete cover to the tendon of 30mm (37.85mm tendon centre); the tendon temperature evolution is also displayed. The cooling portion of the curves shown in Figure 5-6 refer to a situation where the air sink temperature in immediate proximity to the slab cools from a peak gas temperature after the 90 standard fire of approximately 1006^{o}C to 20^{o}C in around 81 minutes. It should be noted that temperature-time curves for concrete often display kinks corresponding to a temperature increase spike just beyond 100^{o}C. These correspond to large sudden increases in specific heat capacity for high moisture content concrete as moisture boils. A significant increase in heat is absorbed within the concrete at this point and the slab temperature increases more rapidly as a result for a short period of time, until the specific heat capacity returns rapidly to its original level. The concrete modelled within this study has a moisture content of 1.5% by mass; the specific heat capacities used as a function of temperature are listed in Figure 11-1. Whilst there is a spike in specific heat capacity just beyond 100^{o}C, it is not significant enough to produce a noticeable spike in concrete temperature at this point; particularly not at the resolutions showed

within the following temperature-time plots. At higher concrete moisture contents this spike in specific heat capacity is significantly larger.

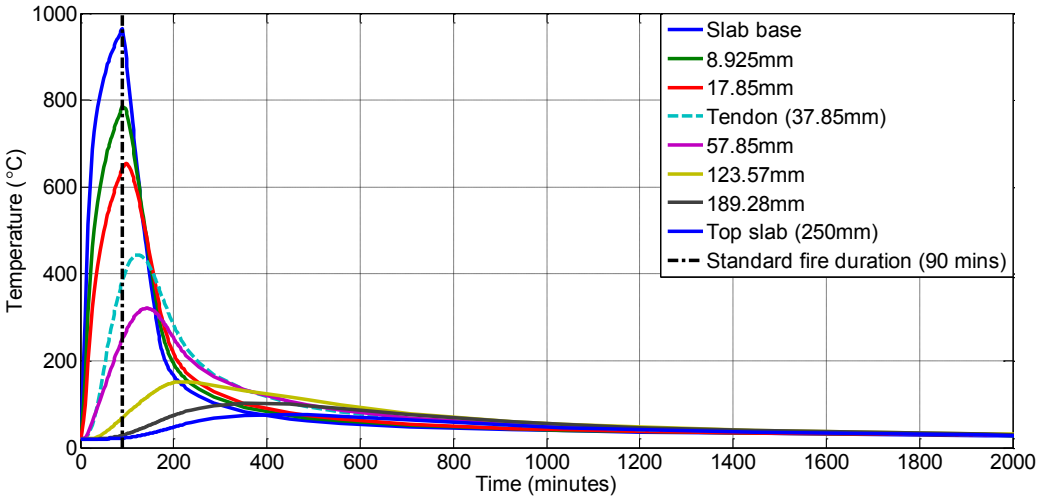

Figure 5-6; Slab temperature evolution throughout its depth (from base) under 90 minute standard fire and natural cooling

The slab depths at which the temperature-time profiles are displayed in Figure 5-6 refer to nodal coordinates throughout the depth as modelled. The gradient of the standard fire curve displayed in Figure 5-4 is initially very large, as the gas temperature increases rapidly. Within the slab, as shown in Figure 5-6, the temperature in close proximity to the base heats rapidly creating steep thermal gradients. These promote significant heat transfer in the lower parts of the cross-section. Thus the lower portions of the slab displayed, up to 17.85mm from the base in Figure 5-6, also heat rapidly. As the standard fire curve begins to plateau, heat penetrates further through the depth of the slab and the temperature through the cross-section gradually increases. Once the standard fire has ceased base cooling begins almost immediately as the air sink temperature drops below the slab base temperature. As the slab base cools, thermal gradients within the slab begin to change direction. This change of direction can take some time however. The rate with which thermal energy leaves the slab from the base depends on the magnitude of the thermal gradients at its proximity. If the air sink temperature cools slowly, thermal gradients towards the base of the slab will be shallow and thus it will take longer for heat to leave the slab and the thermal gradients deeper within to reverse. Therefore even once the standard fire has ceased, at depths further within the slab, pre-existing thermal gradients are still driving heat further upwards, increasing temperature. It is noted in Figure 5-6 that the tendon temperature therefore continues to rise after the standard fire ceases. The evolution of the tendon temperature is analysed in detail in the next section (Section 5.2.2).

The cooling behaviour displayed in Figure 5-6 results from a slow linear rate of air temperature cooling proximity to the slab base. This results in a slowly decreasing sink temperature which dictates convective and radiative cooling magnitudes from the base. The cooling modelled may be regarded as an extreme case of slow cooling, but allows numerical convergence of mechanical models using this heat transfer data. Further to this, it illustrates the possible effects on structural behaviour should cooling of a compartment be particularly slow for any reason. Figure 5-7, Figure

5-8 and Figure 5-9 show plots displaying temperature-time curves at a slab depth of 37.85mm (tendon centre depth from base) during standard fire exposures of 60, 90 and 120 minutes respectively. These curves are computed with different rates of sink temperature cooling post-fire to view the difference this has on slab temperature evolution at the above tendon depth (30mm of concrete cover, 37.85mm centre). The curves were obtained from simple one-dimensional heat transfer analyses.

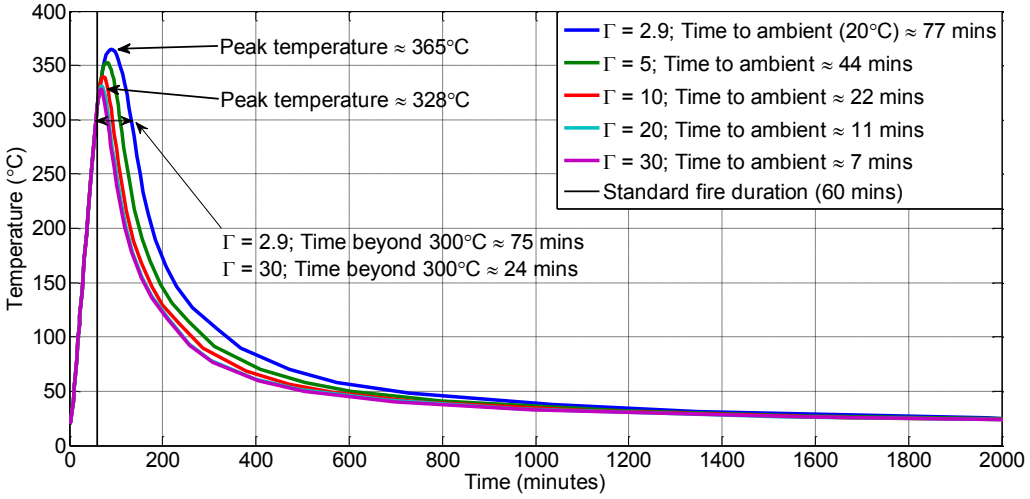

Figure 5-7; Simple slab temperature at 37.85mm from base for a 60 minute standard fire with varying degrees of post fire air temperature cooling.

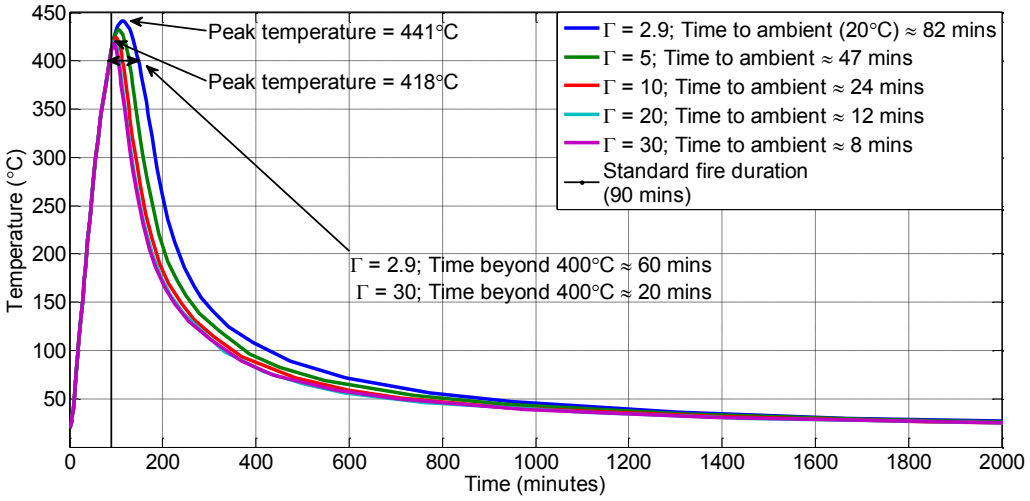

Figure 5-8; Simple slab temperature at 37.85mm from base for a 90 minute standard fire with varying degrees of post fire air temperature cooling.

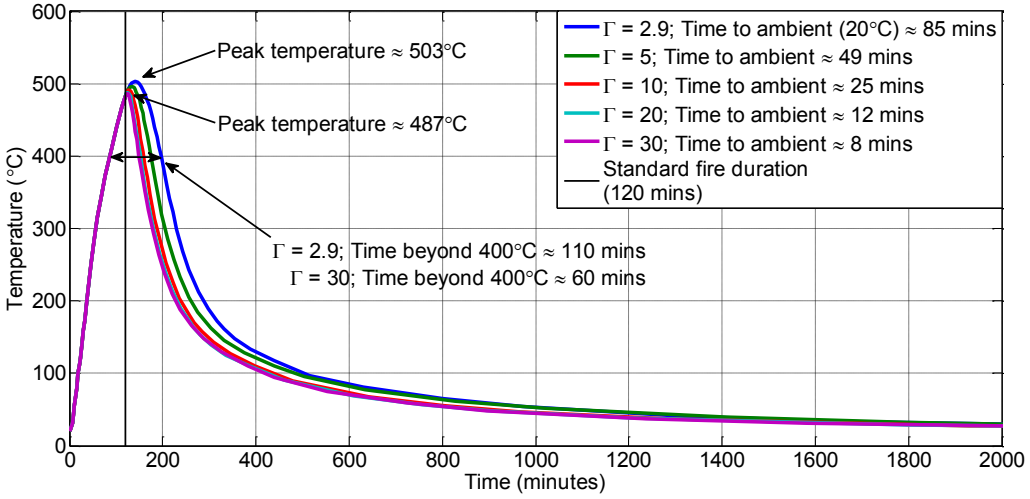

Figure 5-9; Simple slab temperature at 37.85mm from base for a 120 minute standard fire with varying degrees of post fire air temperature cooling.

These plots show a significant difference in peak temperature reached at a depth of 37.85mm from the base of the slab dependent on the rate of air sink temperature cooling within the compartment. They also show the exposure time to elevated temperatures can also be significantly altered by the rate of compartment cooling. It is however noticeable the difference in peak temperature and duration of elevated temperature exposure is more significant when cooling is considered after shorter duration fires. For example, Figure 5-7 shows temperature-time curves at a tendon centre depth of 37.85mm when a 60 minute standard fire is incident on the base of a UPT concrete slab. As thermal gradients are relatively steep post-fire in this scenario between the base of the slab and the tendon depth, significant heat transfer continues when the rate of air cooling is slow. The temperature at the depth the tendon would lay rises by just over 50^{o} in the slowest cooling case. When the rate of external sink cooling is rapid, the temperature at this tendon depth does not rise as significantly, approximately 15^{o} in the quickest cooling case. In this case the time of exposure beyond 300^{o}C is one third of that noted in the slowest cooling scenario.

For a longer standard fire exposure such as 120 minutes as shown in Figure 5-9, significantly more heat has been incident and penetrated within the slab during the fire. The temperature evolution of the slab base closely follows the evolution of the standard fire curve (Figure 5-4), as time increases it then begins to plateau. As it does this, heat transfer continues further within the slab, internal temperatures rise and thermal gradients within the slab become shallower. The rate of compartment cooling then is less significant on the peak magnitude of the temperature reached at the tendon depth within the slab post-fire (approximately 16^{o}C between both extreme cases), as compared to the 60 minute standard fire case of Figure 5-7. This owes to the shallower thermal gradients at this time and slab depth and thus the lower rate of potential continued heat transfer. As such the peak temperatures also do not increase significantly beyond that reached during standard fire heating. The rate of cooling does still have a significant effect on the time of elevated temperature exposure at the tendon depth however. In the slowest cooling case, temperature at the tendon centre depth remains above 400^{o}C for approximately 110 minutes. In the rapid cooling case this time frame of exposure is reduced 60 minutes (Figure 5-9). These differences again relate to the shallow nature of the thermal gradients between the slab base and the tendon after the 120 minute

standard fire. The faster the base of the slab cools the faster thermal gradients reverse and heat can dissipate from the tendon depth. The following section describes tendon temperature evolution within the UPT concrete slab model detailed in Section 5.1, with a relatively slow rate of compartmental cooling corresponding to a Γ [31] parameter of 2.9.

5.2.2 Tendon temperature profiles

The aim of the following parametric heat transfer models, aside from providing temperature-time data for input in subsequent mechanical models, is to study the effect of concrete cover and fire duration, as well as cooling post-fire on tendon temperature. It is the aim later to relate wider UPT concrete slab behaviour and damage to tendon temperature and associated relaxation. A further aim is to observe tendon heating rates to ascertain under what circumstances within the definition of Eurocode 2 [1] tendon creep should be modelled explicitly. This relates to identifying points during heating and cooling when tendon heating rate falls below 2^{o}C per minute.

One of the critical points to look for with respect to concrete cover and fire duration are the likelihood of the tendon temperature exceeding 400^{o}C, and for what duration. At this point it is likely recrystallization may begin with an associated loss of yield strength and increase in ductility (Section 2.2). From the previous chapter, in Section 4.4.3 and Figure 4-9 it can be observed that Eurocode 2 [1] stress-strain curves cannot adequately account for creep induced tendon stress relaxation in ASTM A416 [10] standard prestressing steel far beyond 400^{o}C, even at heating rates beyond 2^{o}C per minute. For the BS 5896 [11] standard prestressing steel, explicit creep accountability would appear from Figure 4-10 to only be required at very low heating rates approaching steady state tendon temperatures of around 500^{o}C.

The parametric studies undertaken within the heat transfer analysis are as follows.

- Three different minimum concrete covers; 25mm, 30mm and 35mm.
- Three different durations of standard fire exposure on the base of the slab at each concrete cover; 60 minutes, 90 minutes and 120 minutes with complete cooling of the UPT slab post fire.

Figure 5-10, Figure 5-11 and Figure 5-12 show obtained tendon temperature profiles (temperature taken at tendon centre) from the heat transfer parametric studies detailed above, along with approximated heating rates obtained from temperature and time increments. Each plot displays the point at which the standard fire ceases. A further vertical line shows the point in time where the heating rate drops below 2^{o}C per minute. The temperature profiles for prestressing steel tendons in Figure 5-10, Figure 5-11 and Figure 5-12 are all based on thermal parameters in Eurocode 2 [1] for a generic prestressing steel. It is assumed thermal parameters relating to heat transfer as well as convective and radiative heating for both ASTM A416 [10] and BS 5896 [11] standards of prestressing steel are similar and can be approximated by this Eurocode 2 data [1].

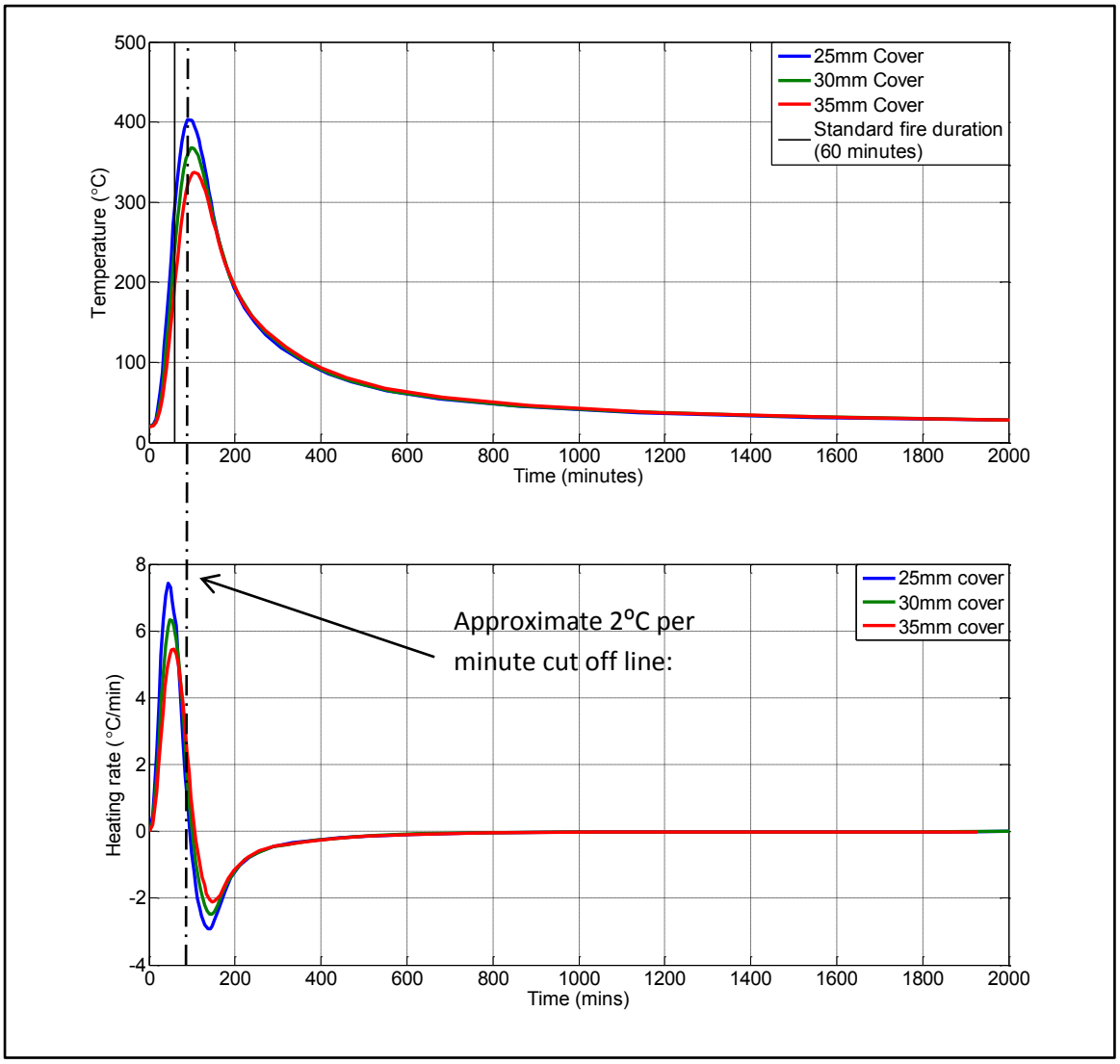

Figure 5-10; Tendon temperature and heating rate with time within a slab subjected to a 60 minute standard fire

Cover (mm)	Temp after 60 min fire	Peak temp (°C)	Peak time	Duration beyond 400°C	Time at 2°C/min	Temperature at 2°C/min
25	293	403	90 mins	15 mins	83 mins	~385°C
30	240	368	101 mins	0	86 mins	~354°C
35	197	337	105 mins	0	91 mins	~323°C

Table 5-1; Temperature-time data for UPT concrete slabs of 25mm, 30mm and 35mm tendon concrete cover exposed to a 60 minute standard fire

The key details from the curves in Figure 5-10 are summarised in Table 5-1. It is again noticeable immediately that peak tendon temperature is not reached for some time after standard fire exposure of the slab base has ceased. This is as expected after exposure to a 60 minute standard fire as detailed in the previous section (Section 5.2.1).

25mm cover: - The tendon temperature in a UPT concrete slab with minimum concrete cover of 25mm barely reaches 400^{o}C when the slab is exposed to a 60 minute standard fire. With a more rapid rate of compartmental cooling it is likely tendon temperature will fall well short of this critical temperature (Figure 5-7). With the air temperature cooling curve used, this results in a 15 minute exposure at the point of minimum concrete cover beyond 400^{o}C; this is not likely to be long enough with a peak temperature of 403^{o}C to produce any significant degree of recrystallization. Post heating of the slab with the modelled compartmental cooling curve, an approximate 60 minute period exists (at 25mm concrete cover) where the heating rate within the tendon is below 2^{o}C per minute and the tendon temperature is greater than 300^{o}C. Naturally this period will be reduced with a more rapid rate of compartment cooling. During this period it would be expected primary creep strain may still accumulate (Figure 4-15 and Figure 4-16) and induce continued stress relaxation. By definition this is a scenario which should warrant explicit creep accounting under Eurocode 2 [1].

30mm and 35mm cover: - At larger covers the tendon temperature never reaches 400^{o}C. From the previous chapter and theory presented in earlier chapters, at all these concrete covers, tendons may experience time evolving stress relaxation attributed to primary creep. None should exhibit any significant plastic and creep strain induced relaxation beyond that which Eurocode 2 [1] could implicitly cover.

At all concrete covers considered it appears a 60 minute standard fire will not induce significant microstructural change within the tendons beyond that which may actually harden the tendon. If cooling is considered, as it should be, all cases by definition of Eurocode 2 [1] should involve the explicit consideration of creep. However based on tendon temperatures observed it is unlikely neglecting to do so will result in a significant under prediction of tendon relaxation. This will be considered in more detail when comparing mechanical models.

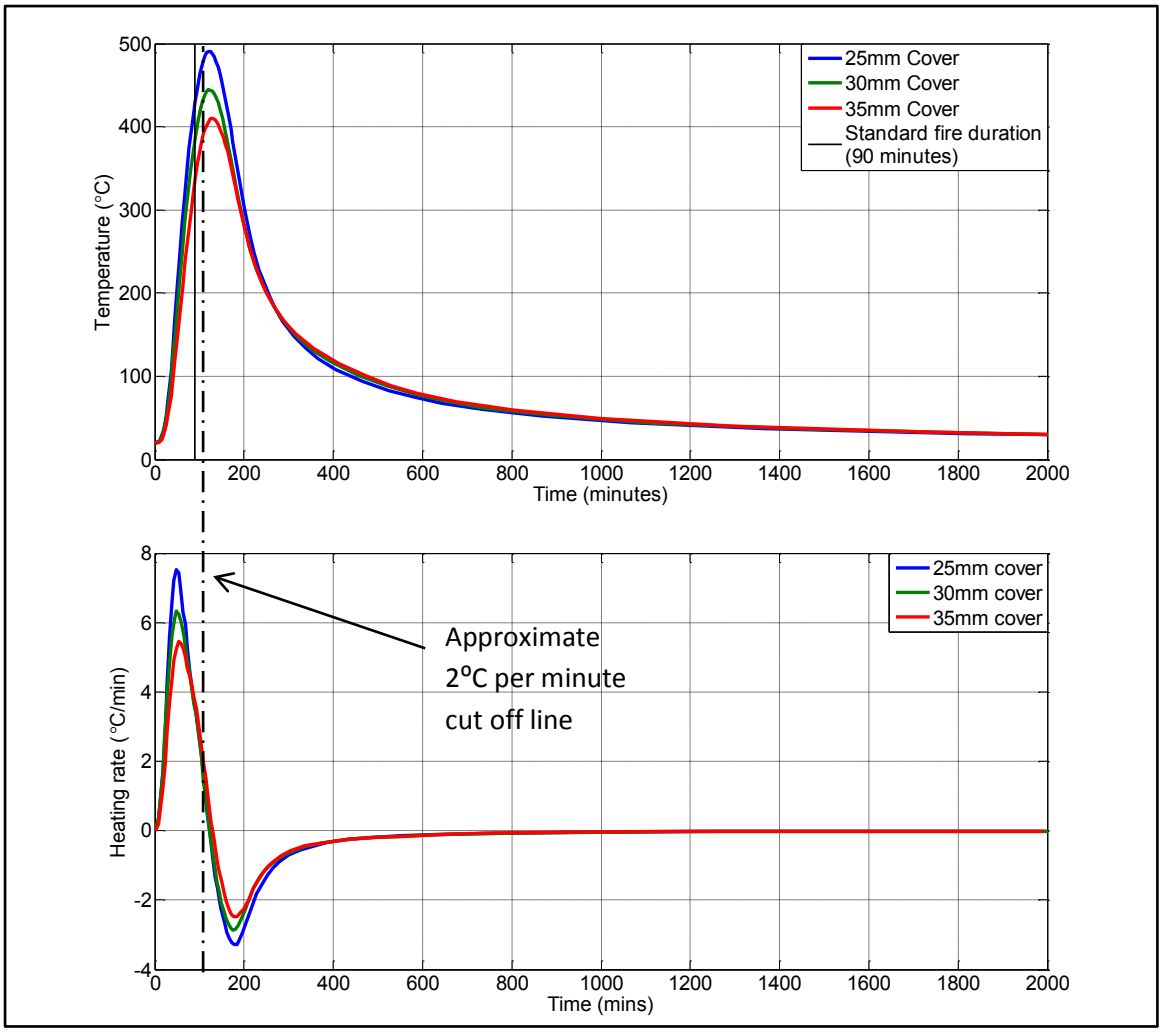

Figure 5-11; Tendon temperature and heating rate with time within a slab subjected to a 90 minute standard fire

Cover (mm)	Temp after 90 min fire	Peak temperature	Peak temp-time	Duration beyond 400°C	Time to reach 400°C	Time at 2°C/min	Temperature at 2°C/min
25	429	491	121	87	83	106 min	~474°C
30	384	444	121	61	95	105 min	~426°C
35	335	410	128	30	115	109 min	~390°C

Table 5-2; Temperature-time data for UPT concrete slabs of 25mm, 30mm and 35mm tendon concrete cover exposed to a 90 minute standard fire

When a UPT concrete slab is exposed to a 90 minute standard fire below its base the degree of concrete cover and rate of compartmental cooling now become very important with respect to tendon temperature exposure.

25mm cover: - From Figure 5-11 and Table 5-2 it is shown at a minimum concrete cover to the tendon of 25mm the tendon temperature exceeds 400°C before the standard fire has ceased. Under the rate of compartmental cooling modelled this leads to a peak temperature of 491°C. Further, the

tendon temperature reached as heating rate drops below 2^{o}C per minute is 474^{o}C and does not drop below 400^{o}C for a further 64 minutes. So in this case there is significant potential for secondary creep induced tendon relaxation and the beginnings of microstructural recrystallization. This is far beyond the capability of Eurocode 2 [1] to implicitly account for creep particularly with respect to ASTM A416 standard prestressing steel tendon as implied by Figure 4-10.

30mm cover: - At 30mm minimum concrete cover the rate of compartmental cooling becomes important. For example, 400^{o}C is not reached until after the standard fire has ceased. Through comparison with Figure 5-8, it is likely compartment cooling rate could impose on ultimate tendon temperature reached and the duration of elevated temperature exposure to which it is subjected.

35mm cover: - Here a conservative rate of compartmental cooling allows the tendon temperature to exceed 350^{o}C at a low rate of thermal transience for approximately 76 minutes. The tendon temperature barely exceeds 400^{o}C for any significant length of time.

Figure 5-11 implies at all three concrete covers there will be a noticeable difference in tendon relaxation with respect to ASTM A416 [10]standard prestressing steel should creep be accounted for, or not. The consideration of cooling again highlights the potential for creep induced tendon relaxation with elevated temperatures being reached at low heating and cooling rates (<2^{o}C) for reasonable time periods. It is not likely that significant differences in tendon relaxation will be observed with respect to BS 5896 [11] standard prestressing steel should creep be explicitly modelled or not.

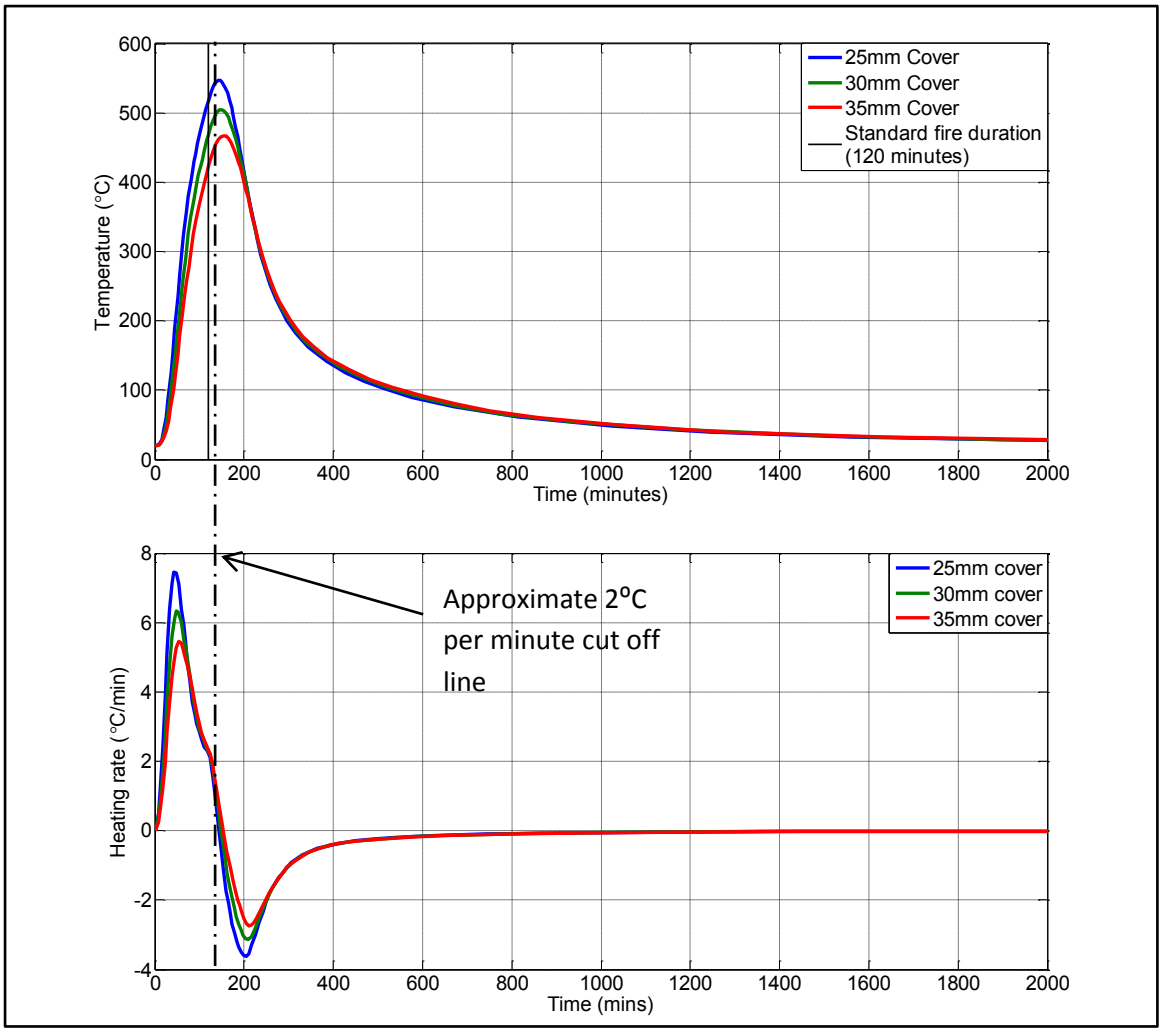

Figure 5-12; Tendon temperature and heating rate with time within a slab subjected to a 120 minute standard fire

Cover (mm)	Temp after 120 min fire	Peak temperature	Peak temp-time	Duration beyond 400°C	Time to reach 400°C	Time at 2°C/min	Temperature at 2°C/min
25	517	548	143	125	80	125 min	~527
30	468	505	150	108	95	126 min	~480
35	422	467	154	89	111	128 min	~441

Table 5-3; Temperature-time data for UPT concrete slabs of 25mm, 30mm and 35mm tendon concrete cover exposed to a 120 minute standard fire

Figure 5-12 represents tendon temperature-time curves during and after incidence of a 120 minute standard fire below the UPT concrete slab base. Naturally this duration shows the greatest potential for explicit creep induced stress relaxation within prestressing steel tendons for the parametric models considered.

25mm cover: - For ASTM A416 [10] standard prestressing steel Figure 4-9 and Figure 4-10 show as temperatures tends towards 500°C, despite the heating rate being greater than 2°C per minute,

Eurocode 2 [1]stress-strain curves cannot implicitly account for creep. Stress relaxation occurs rapidly during transient heating at such temperatures. Whilst rapid compartmental cooling could reduce the duration of significant elevated temperature exposure beyond 350^{o}C or 400^{o}C and exposure time at a heating rate of less than 2^{o}C per minute, the magnitudes of the temperature reached will induce significant tendon creep strain accumulation.

30mm cover: - A slow rate of compartmental in this case may be the difference between significant and insignificant differences in tendon stress relaxation. The case above shows a significant period of time where the tendon exposure is greater than 400^{o}C, indeed it is in proximity of 500^{o}C for a reasonable length of time. There is also a significant time period where tendon temperature is significantly high and heating rate is below 2^{o}C per minute. With a rapid rate of cooling these exposure times and peak tendon temperature would be expected to reduce somewhat, and thus may reduce the potential impact and significance of the explicit creep induced tendon relaxation.

35mm cover: - The tendon temperature reached after 120 minutes of standard fire exposure to the slab base is 422^{o}C. Under the compartmental cooling rate modelled a peak temperature of 467^{o}C is not reached till 34 minutes after this point. In this case the tendon is exposed to a temperature beyond 400^{o}C for approximately 89 minutes which is comparable with the 90 minute soak times modelled in the previous chapter. It is observed however from Table 5-3 the heating rate in Figure 5-12 does not drop below 2^{o}C per minute for another 17 minutes. It is likely up to this point based on Figure 4-9 that Eurocode 2 could account for tendon relaxation up to this point leaving 72 minutes where by its own definition creep should be explicitly considered. Whether or not this period of time and extra relaxation would be of significant consequence within a wider UPT concrete slab context will be analysed in the next subsection.

In many ways the conclusions of this heat transfer analysis are fairly simple; to avoid significant secondary creep induced tendon relaxation in all but the most extreme fire situations (including slow compartmental cooling) at least 35mm minimum concrete cover should be specified. This limits the likelihood of 400^{o}C being exceeded and microstructural changes due to recrystallization commencing. MacLean recommends however, tendons having being exposed to temperatures greater than 300^{o}C should be replaced as a factor of safety against significant material microstructural change. This also accounts for those changes that could not be visualised through microscopic examination. Eurocode 2 [1] specifies 350^{o}C as a critical design temperature for unbonded tendons, whereby 15mm of concrete cover should be added to the ambient design value as a prevention measure against this exposure level. It doesn't specify that tendon temperature evolution post-fire should be considered however.

5.3 Mechanical modelling

Figure 5-10, Figure 5-11 and Figure 5-12 show when a UPT concrete slab is heated for significant standard fire durations, it is possible for tendons to become exposed to elevated temperatures significant enough for creep to be a considered a major contributor to tendon stress relaxation. They highlight, after standard fire exposure to the base of UPT concrete slabs, tendon heating rates will fall below 2^{o}C per minute post-fire whilst the temperature can remain sufficiently elevated to evoke

significant creep strain. By the definition of Eurocode 2 [1], creep should be explicitly considered below this heating rate in the elevated temperature analysis of structural prestressing steel.

Now the attention turns to mechanical UPT concrete slab models, reading in the heat transfer data from the models presented in Section 5.2.2, in an aim to qualify and quantify the effects (if any) of neglecting to explicitly account for creep in prestressing steel tendons. Firstly the general structural behaviour with respect to compressive and tensile stress strain patterns is presented, highlighting potential failure modes and other notable observations. This general behaviour is necessary to provide context to the compared deflections and inelastic tensile concrete strains when creep is and is not explicitly considered within the prestressing steel tendon material model. It should be noted this general behaviour is the same across all parametric studies; it is the magnitudes of various stresses and strains observed in particular areas that differ with parameter. Once this data is analysed and the broad UPT concrete slab behaviour under loading and fire is understood, the parametric study comparing mechanical behaviour with and without explicit creep modelling within the tendons can be presented.

5.3.1 Sectional data and failure mechanisms

Within this section the general structural behaviour observed during the modelling of the UPT concrete slabs subject to a base fire and top surface loading is overviewed. Naturally, concrete tends to resist and transfer load to supports in compression, being unable to transfer any load of significance in tension. The tendons act dually as a compressor of the slab across its span direction, assisting the concrete transfer load, and as tensile reinforcement (noting no additional reinforcement is specified in these models). The compressive and tensile stress distributions and their evolution during fire throughout the slab, particularly in the span direction, then are particularly important in understanding how the slab transfers load throughout a fire. A series of contour plots of a modelled UPT concrete slab with 30mm of minimum concrete cover to the tendons and subject to a 120 minute standard fire are displayed in Appendix F; Slab sectional compression-tension profile evolutions. The purpose of Figure 13-1 and Figure 13-2 is to illustrate how compression and tensile lines evolve throughout the slab in the direction of span with temperature and with tendon relaxation. This should give an idea of how flexural load is resisted and transferred from the slab to beam supports (given the minimal load capacity of concrete in tension) and may give an idea of how a slab is likely to fail. Initially at ambient temperature, after tendon tensioning and under load the slab is predominantly in compression; as a large load has been uniformly distributed in these models there are small tensile regions in hogging and sagging. These tensile strains are however small and elastic.

As heating progresses thermal expansion restrained by cold regions of the slab and support boundary conditions induces compressive stresses across the base of the slab, as temperature increases within the slab these compressive stresses also progress deeper within the slab. A tensile region evolves along the longitudinal dimension of the slab through the centre of the section, where in hot regions restrained thermal expansion is cancelled by tension created by slab deflection. About the centre of the slab (the cut in Figure 13-1 and Figure 13-2), the top surface is naturally compressed under bending, thus both top and bottom surfaces are in compression resisting flexural

deformation of the slab. It is therefore unlikely the slab will fail about its centre unless the compressive stresses become high enough to initiate significant crushing. It is also unlikely that failure will occur in this region due to buckling of a compressive line in the span direction, as both top and bottom surfaces about the centre are in compression. The load transference mechanism is in fact potentially very complicated in UPT concrete slabs. In addition to the above points the tendons, whilst applying a compressive stress to the slab are also capable of acting as a tensile membrane transferring slab loading to the supports where anchored or draped in a continuous span. So it would appear failure during heating is highly unlikely to occur anywhere near the centre of the slab and instead near the supports where the greatest concrete tensile stress will accumulate.

Concrete failure is most likely to occur in the direction of maximum principal inelastic tensile strain; cracks would be expected normal to this direction. It should be noted that as described later in Section 6.1, plastic flow in concrete is non-associated to the yield surface; principal inelastic tensile strain and crack propagation will not necessarily align with principal tensile stress directions. It may then be possible for concrete to reach elastic yield in shear (along the shear meridian) but failure direction and crack orientation be dictated by maximum principal inelastic tensile strain. Figure 5-13 shows the magnitude and direction of maximum principal inelastic tensile strain throughout the slab at 120 minutes of standard fire application.

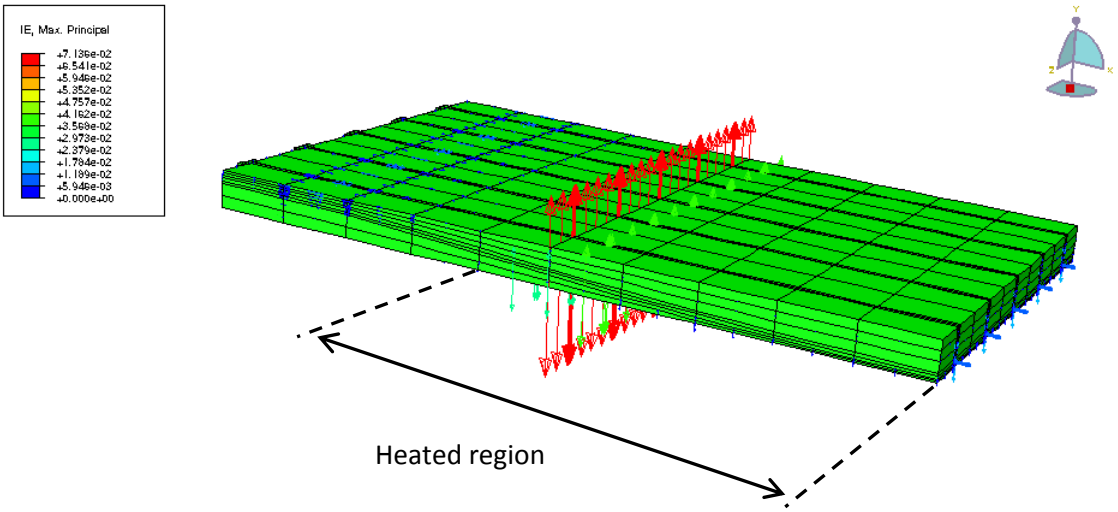

Figure 5-13; Principal inelastic tensile strain directions and magnitudes after a 120 minute standard fire

Perhaps unexpectedly the dominant strains displayed in Figure 5-13 are normal to the base plane of the slab. These maximum principal inelastic strains are representing the strain state of nodes on and near the base of the slab in a particular strip 0.5m from the edge of the heated region. This observed behaviour is discussed shortly, in Section 5.3.1.2. It should be noted when viewing Figure 5-13, double headed arrows propagate centred on nodal points within the slab and as such, arrows appearing to propagate from the top surface actually are double headed arrows, implying tension from nodes along the base. The other main area of damage and most significant with respect to slab deflection and failure, is observable in hogging near the top surface of the slab. As such this region will be analysed firstly in Section 5.3.1.1. Other areas of potential damage are noticeable around tendon ducts in tendon-slab contact areas; in particular these are located in sagging and hogging areas of maximum slab curvature.

5.3.1.1 Hogging damage

Large scale failure or collapse of the slab it would appear is most likely to occur in the hogging tensile region of the slab. It is observed in Figure 13-1 through the entirety of the heating process the concrete in the hogging region is in tension. Figure 5-14 shows a contour plot of a modelled UPT concrete slab showing significant tensile longitudinal plastic strain (PE11) development along a strip of the top surface of the slab, near the sliding beam support. The plastic strain evolution within this strip is plotted with time for a 30mm concrete cover slab and a 25mm cover slab (which failed to complete the cooling phase); both are exposed to a 120 minute standard fire. This region is approximately 750mm from the anchorage end of the slab. These plastic strains are particularly high and imply significant tensile cracking is likely to have occurred.

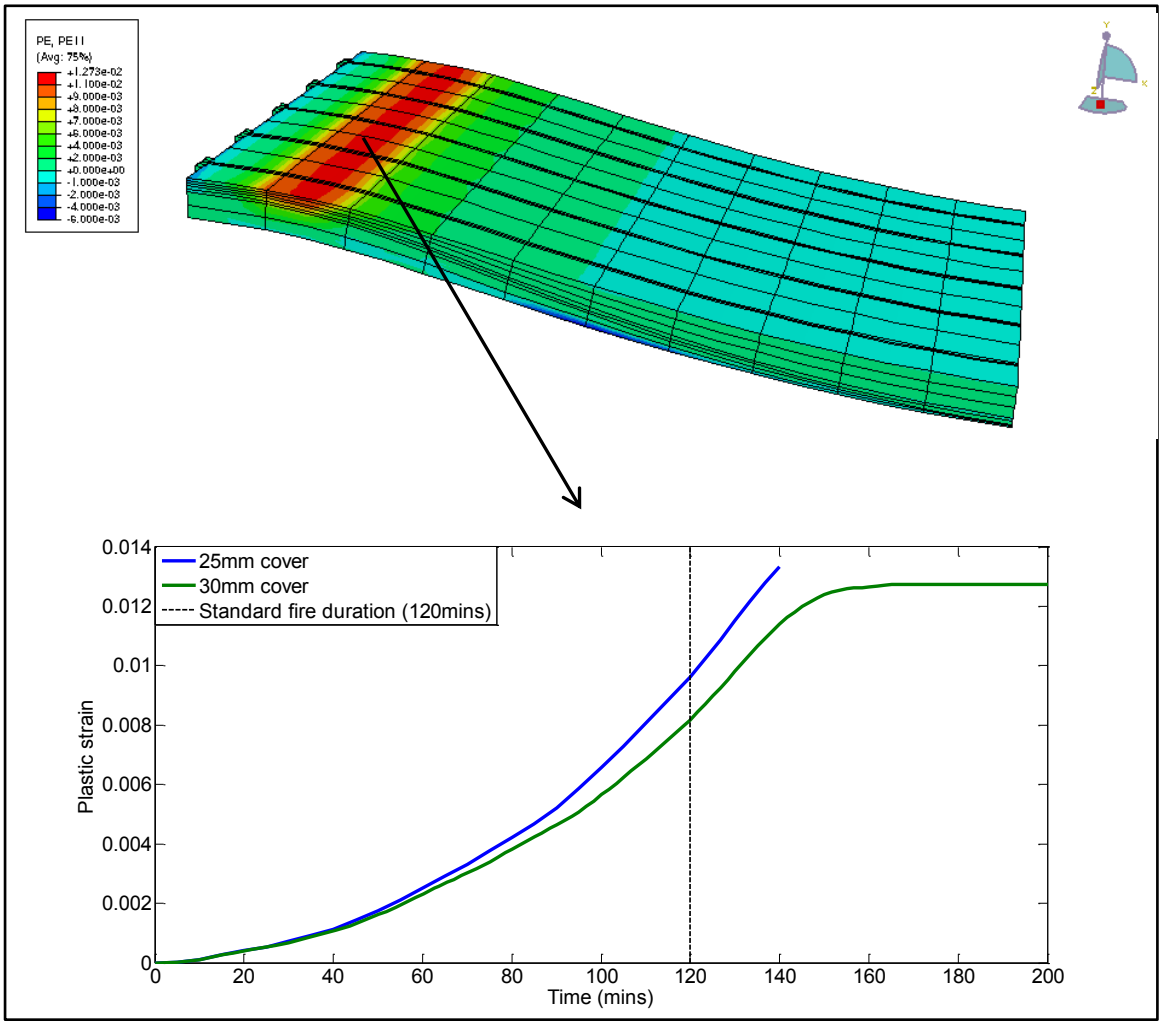

Figure 5-14; Longitudinal plastic strain contour plot and tensile plastic strain evolution for 25mm and 30mm concrete cover UPT slabs exposed to a 120 minute standard fire

To confirm this Figure 5-15 shows a transparent image of the slab, cut 0.75m into the span from the anchored edge, displaying maximum principal inelastic tensile strain magnitude and direction. The cut corresponds to the region of peak hogging shown above in Figure 5-14. This shows significant

maximum principal inelastic tensile strain in the longitudinal span direction, decreasing in magnitude with depth from the top surface. This indicates the likelihood of large openings at the top surface with the gap reducing but still open deep within the slab. There is also shown significant tensile damage radially about the tendon ducts in this hogging region.

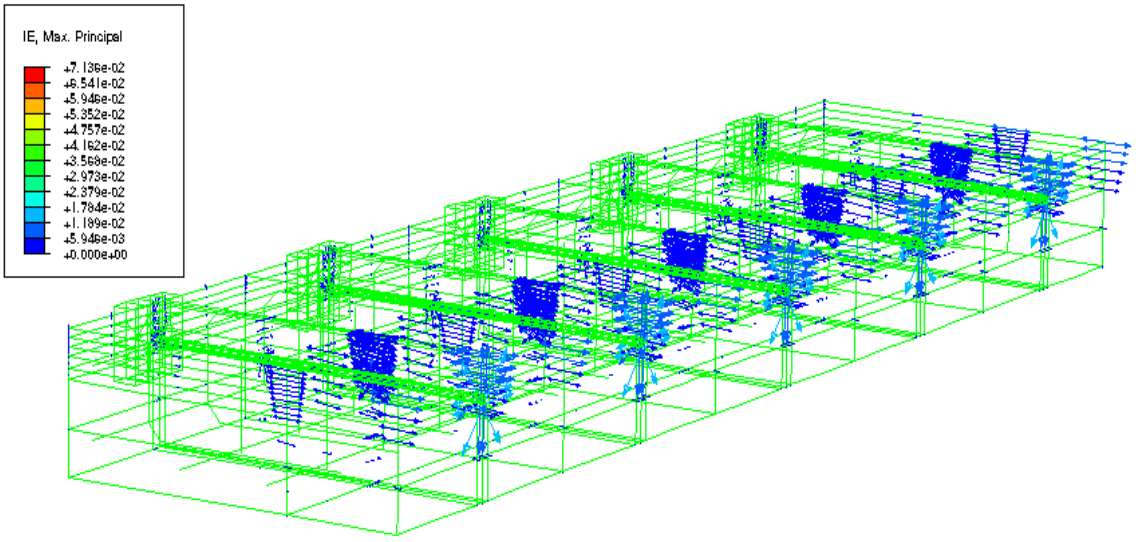

Figure 5-15; Slab cut 0.75m from the anchored edge showing maximum principal inelastic tensile strain in hogging

Figure 5-15 shows the depth to which plastic strain is experienced in tension. Figure 5-16 shows the evolution of plastic strain at various depths from top to bottom of the slab (30mm cover to tendon, 120 minute standard fire exposure) within this area of interest. This shows nearly the entire slab along this plane in the vertical y-axis has experienced a degree of tensile yield, although on comparison with the contour plots of Figure 13-1 and Figure 13-2 in Appendix F; Slab sectional compression-tension profile evolutions, a compressive region does remain between the bottom two points as plotted in Figure 5-16. As a note of realism, whilst the magnitude of plastic strain and potential for significant tensile yield is clearly high in these models, the sliding beam boundary condition does not permit beam rotation. Depending on column and beam design and their dimensions, this should reduce the potential for tensile yield in this region of the slab (if these supports are over designed against rotation and displacement, yield is more likely in the slab). With the inclusion of hogging rebar, concrete tensile damage could be further reduced. Tensile hogging yield may then be a problem over internal supports where rotation is restricted by the cold span on the other side. This will be explored in the next chapter on large one way spanning models.

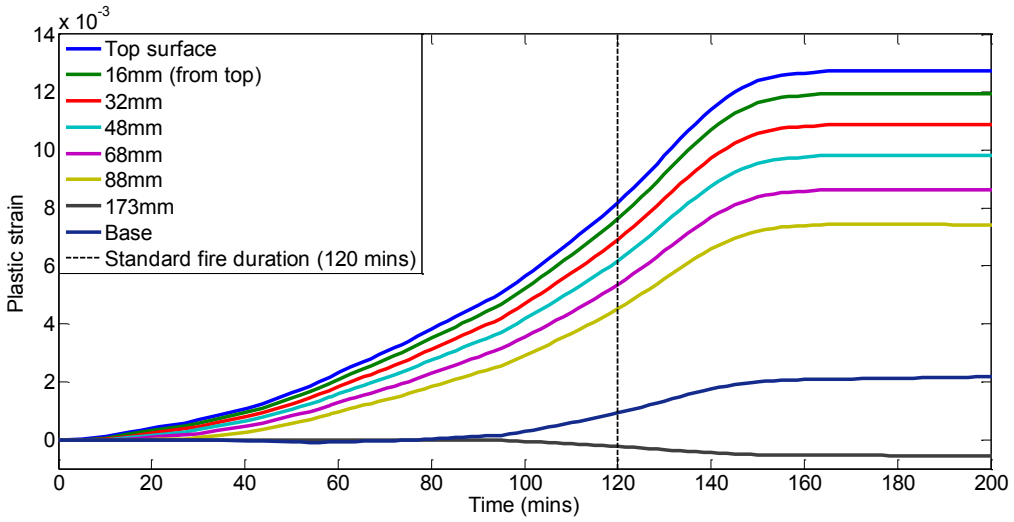

Figure 5-16; Longitudinal plastic strain evolution from the slab top surface to the base, 0.75m from anchored end (30mm concrete cover explicit creep model, 120 minute standard fire exposure).

The observed plastic strains remain as permanent tensile damage but should not affect the compressive behaviour of the slab normal to any cracks if and when these regions become re-compressed as cooling progresses. Within the model, uniaxial tensile concrete material properties have been input representing ideal plasticity (the reasons for this were discussed in Section 5.1), with uniaxial tensile yield being 10% of uniaxial compressive yield; this allows large deformation within the region of concern but prevents the models from explicitly picking up cracking behaviour and potential collapse about this region. Instead the likelihood of cracking and their orientation must be approximated from the consideration of the planes normal to maximum principal inelastic tensile strain directions and their magnitudes. The peak plastic strain occurs as one might expect at approximately the same time as peak deflection; as will be elaborated on shortly this occurs during the early stages of cooling (Figure 5-14, Figure 5-16) after the standard fire has ceased (as the tendon temperature continues to rise for a certain time and thus relax).

5.3.1.2 Out of plane behaviour

As shown in Figure 5-13, significant out of plane maximum principal inelastic strains are noticed in a specific area on and near the base of the slab. Figure 5-17 shows this region in more detail. It is noticed smaller maximum principal tensile strains exist all along the heated region implying lateral inelastic behaviour is induced throughout with a significantly amplified area in a clear locality.

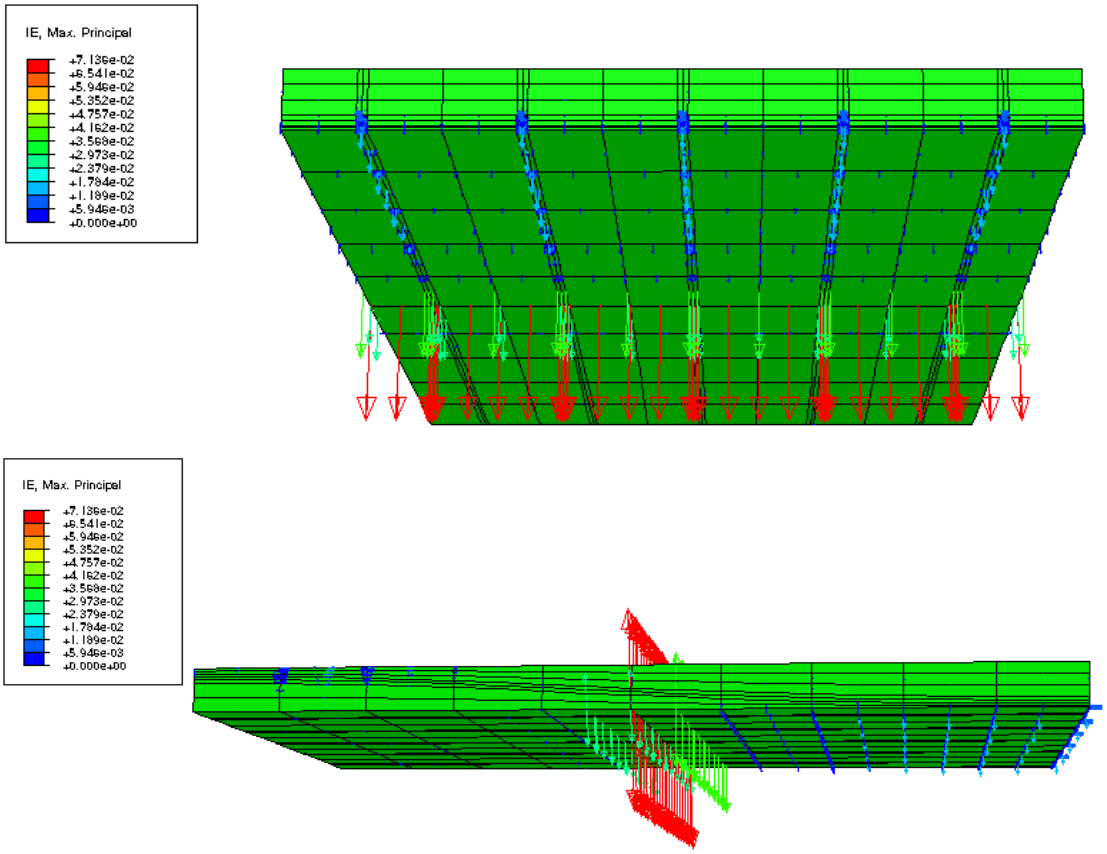

Figure 5-17; Large maximum principal inelastic tensile strains on base of slab

Referring to Appendix F; Slab sectional compression-tension profile evolutions, it is also observed in Figure 13-1 and Figure 13-2, between approximately 2100 and 2400 seconds (35 – 40 minutes) a tensile (longitudinal) stress band appears on the base of the slab at this location. The longitudinal inelastic strain is however compressive at this point. Figure 5-18 shows a longitudinal plastic strain contour plot across the slab base. This region or strip displaying longitudinal inelastic compressive strain and larger lateral out of plane tensile strain lies approximately 0.5m from the edge of the heated zone.

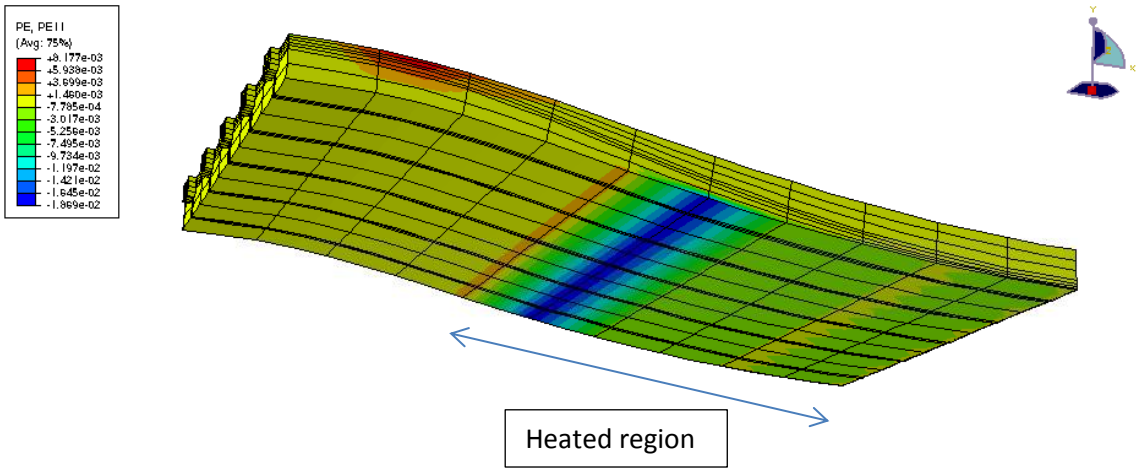

Figure 5-18; Localised failure strip

Figure 5-19 shows the evolution of longitudinal, transverse and lateral normal stresses within this region as well as the equivalent hydrostatic stress. Figure 5-20 shows the evolution of normal inelastic strain at the same point within the failure strip as well as maximum principal inelastic strain; note this is almost completely aligned in magnitude with the lateral strain perpendicular to the slab base, as can also be visualised from Figure 5-17.

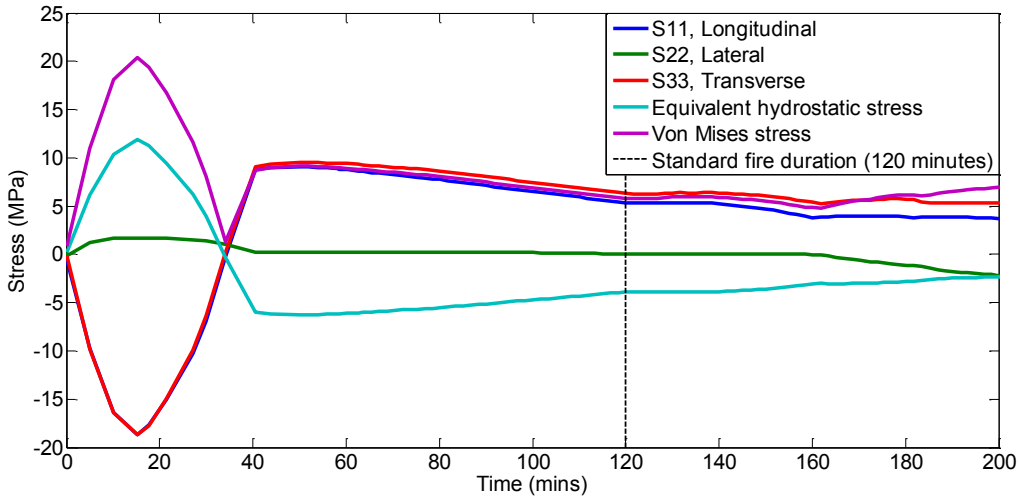

Figure 5-19; Equivalent hydrostatic, Von Mises and normal stress evolutions

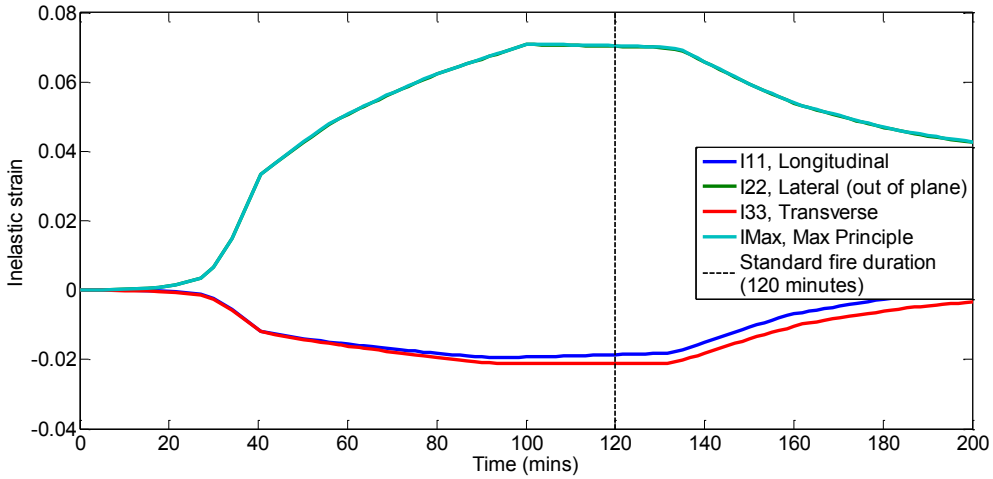

Figure 5-20; Plastic strain evolution

This region of significant lateral tensile plastic flow appears to emerge, from Figure 5-20, after around 15 minutes. However it is not until after 30 minutes that it rises significantly. The tensile strain is mirrored in terms of evolution by significant rises of in-plane compressive strains. This implies the large lateral tensile strains are induced through a state of biaxial compression and relate to the in-plane strains via Poisson's ratio. Naturally, inelastic deformation is restrained vertically upwards by the slab above, leaving the only inelastic flow option as out from the base of the slab. Cracking would be expected normal to this principal tensile stress direction and as such would be in-plane with the slab.

After around 35 minutes the stress state in the failure strip effectively represents a hydrostatic tensile state, as simultaneously the equal magnitude biaxial plane stresses rapidly changes from compression to tension. Complete brittle behaviour may be expected at this point in this region with plastic flow normal to the slab base. The equivalent hydrostatic stress state is also plotted in Figure 5-19 noting that the hydrostatic stress is defined as $\lambda=-1/3tr(\sigma)$, and as such a tensile state is represented by the negative domain. At other points on the hot surface the same general behaviour as described above also progresses. Maximum principal inelastic tensile strain is noted across this region as displayed in Figure 5-17, but far lower in magnitude. Figure 5-21 shows a comparison of stress and inelastic strain evolutions at a nodal point on the base of the amplified region and a node elsewhere on the heated region of the base. The general observance of out of plane tensile strain is understandable given thermal expansion is restrained longitudinally and transversely as well as from the cold regions of the slab above. The material has to deform out of plane in order to conserve volume.

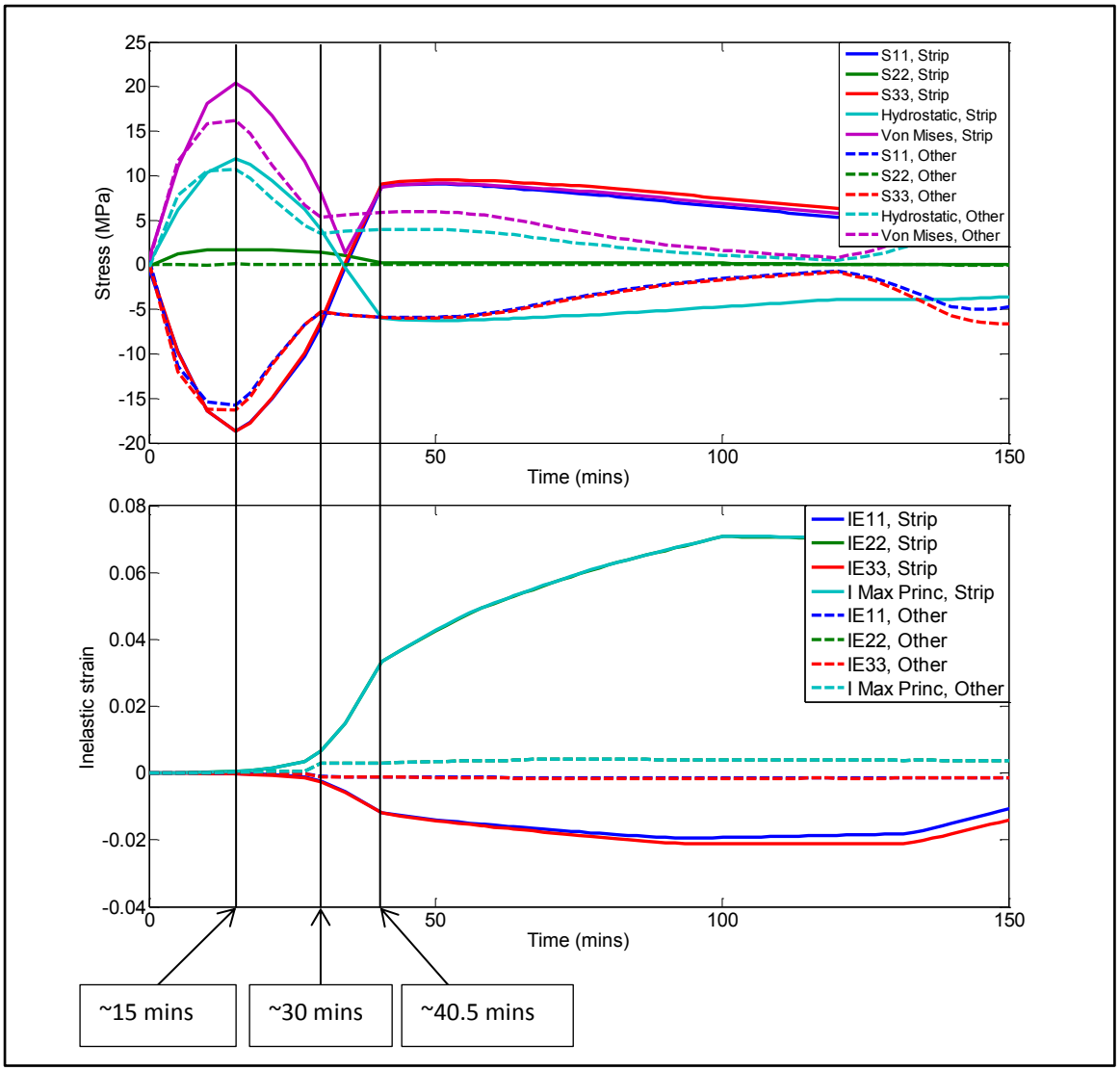

Figure 5-21; Comparison of stress and inelastic strain evolutions at a heated node within 'failure strip' and a node within the heated zone in general

From Figure 5-21, within the heated region in general, a degree of out of plane behaviour due to the Poisson effect, as detailed above is observed. This behaviour settles to an equilibrium in-plane biaxial compression state after around 30 minutes, whereby the ongoing increase in restrained thermal expansion is cancelled by the ongoing increase in deflection. Within the specific amplified region no such equilibrium is found between 15 and 40 minutes. The combination of restrained thermal expansion and ongoing deflection cannot resolve, leading to a significant build-up of potential energy stored by the large in-plane compressive stresses. This energy is released, largely transferred to the out of plane tensile strain field, as the in-plane stress drop to zero after approximately 35 minutes. Of course, should ideal plasticity not have been modelled with respect to the concrete tensile behaviour and strain softening allowed this energy may be released mainly as kinetic energy.

The location of this region of amplified out of plane principal tensile strain does not appear to be random. It occurs 0.5m from the edge of the heated zone where there exists a sudden boundary between hot and cold concrete. For example Slab models with 25mm concrete cover have been performed with a 4 metre longitudinal heated region about the slab centre (2m from symmetry cut)

and an 8 metre longitudinal heated region (4m from symmetry cut). In both cases the same localised stress-strain behaviour as displayed in Figure 5-19 and Figure 5-20 is observed, again 0.5m from the end of the heated region (longitudinally). The time of onset of this behaviour however decreases if a smaller longitudinal heated region is modelled. Should the entire slab base be heated, it is likely, if this region and behaviour emerges, that it will be located in close proximity to the support and take a longer time to be observed. This could contribute to failure in the proximity of the supports. This behaviour is noted in all slab models presented in this chapter and in the larger one way spanning models presented in the next chapter (again 0.5m from the edge of the clearly defined heating zone). The onset of this behaviour appears to be relatively independent of concrete cover to the tendons but it must be born in mind that ultimate moment is kept consistent within different cover models by adjusting slab depth.

5.3.2 Comparison of UPT concrete slab behaviour with creep explicitly considered vs implicitly considered (Eurocode 2 [1]) in prestressing steel tendons.

Having overviewed the general observed sectional response of the UPT concrete slab to flexural deformation under load, heating and cooling, attention can now be paid to the consequences of neglecting to account for creep in the prestressing steel tendons. Of particular focus is the difference in hogging damage and its effects on slab deflection. The heat transfer models presented in Section 5.2 have shown that tendon temperature and tendon heating rate (Section 5.2.2) are such that creep should be explicitly considered. This is with regard to analysis in Chapter 4 and Eurocode 2 [1] guidelines ($\dot{T} \leq 2$℃ per minute).

The following pages show plots displaying the evolution of slab deflection with tendon stress where creep is and is not explicitly modelled within the tendon for the parametric studies previously performed. This behaviour is plotted alongside temperature evolution. It is again noted the tendon creep models use the rate form of the uniaxial Harmathy uniaxial model (Equation 4-3) and appropriate constants from Table 3-1, dependent on steel type. When creep is not explicitly considered, inelastic behaviour is modelled through the input of yield curves computed from Eurocode 2 [1] guidelines and temperature reduction factors. The recorded differences in peak relaxed stress and recovered central deflection are displayed on the plots for each parametric study. Firstly, data from parametric studies modelling UPT concrete slabs with ASTM A416 [10] standard prestressing steel tendons is presented followed by slabs using BS 5896 [11] standard tendons.

5.3.2.1 UPT concrete slab behaviour with ASTM A416 prestressing steel tendons; creep explicitly considered vs implicitly considered (Eurocode 2)

The following series of plots present the evolution of slab deflection with tendon stress where creep is and is not explicitly modelled. Firstly plots are displayed for 60 minute standard fire exposure at each concrete cover (25mm, 30mm, 35mm), followed by 90 minute standard fire exposure plots and finally 120 minute standard fire exposure plots.

60 minute standard fire

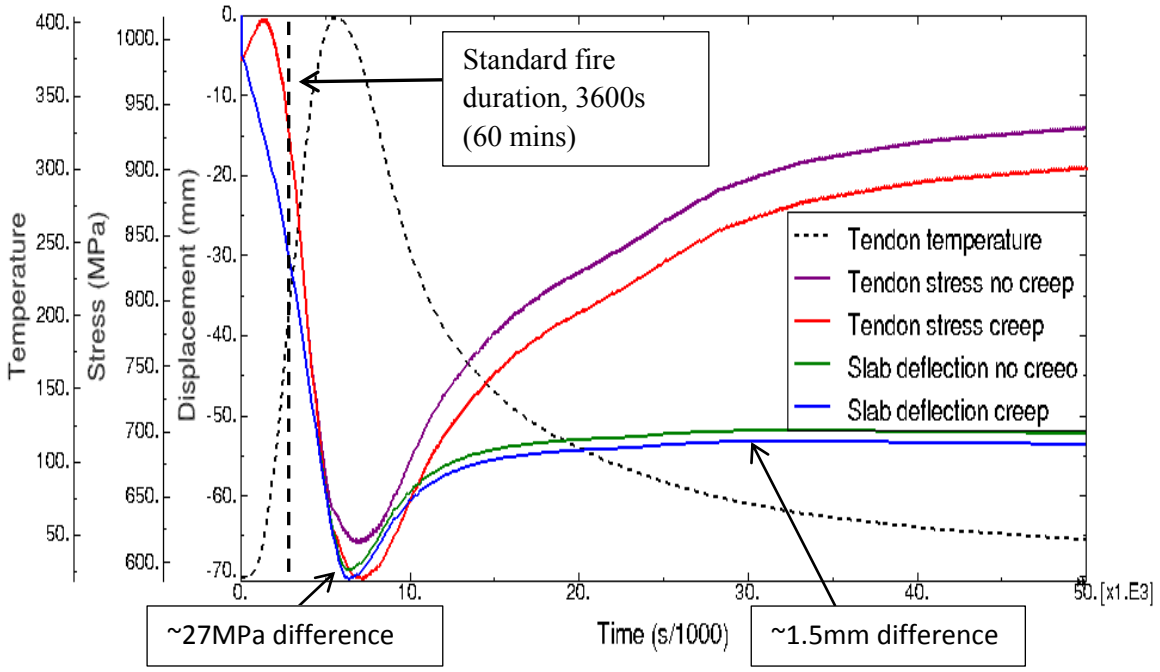

Figure 5-22; Tendon stress versus slab deflection with and without explicit creep modelling, 25mm minimum cover, 60 minute standard fire.

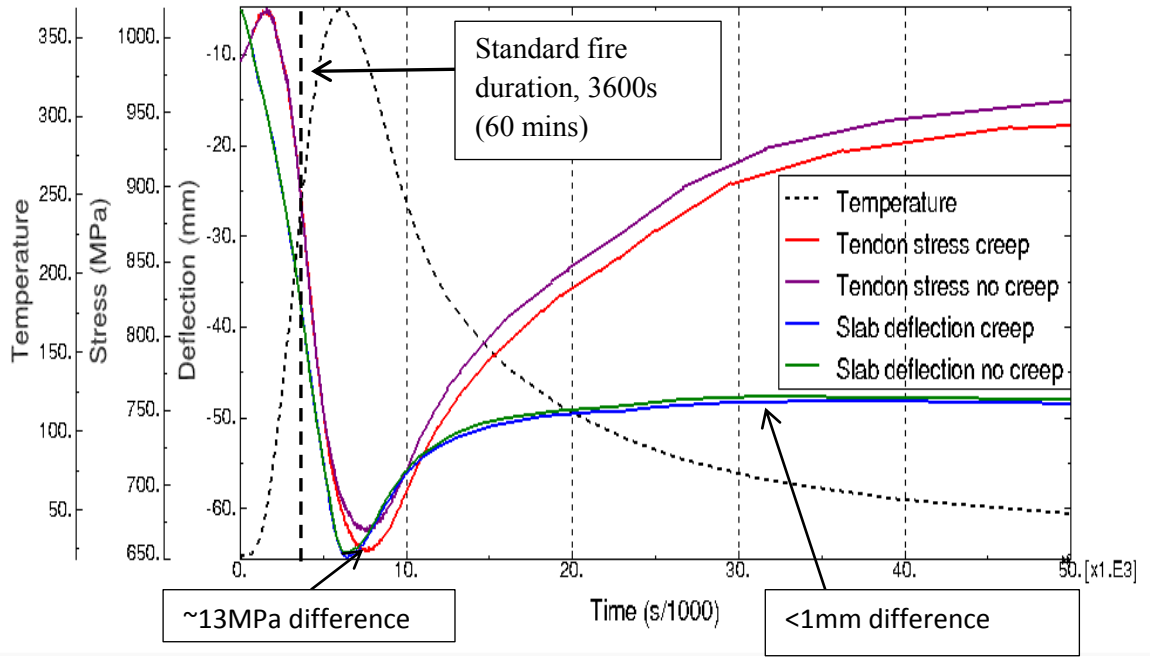

Figure 5-23; Tendon stress versus slab deflection with and without explicit creep modelling, 30mm minimum cover, 60 minute standard fire.

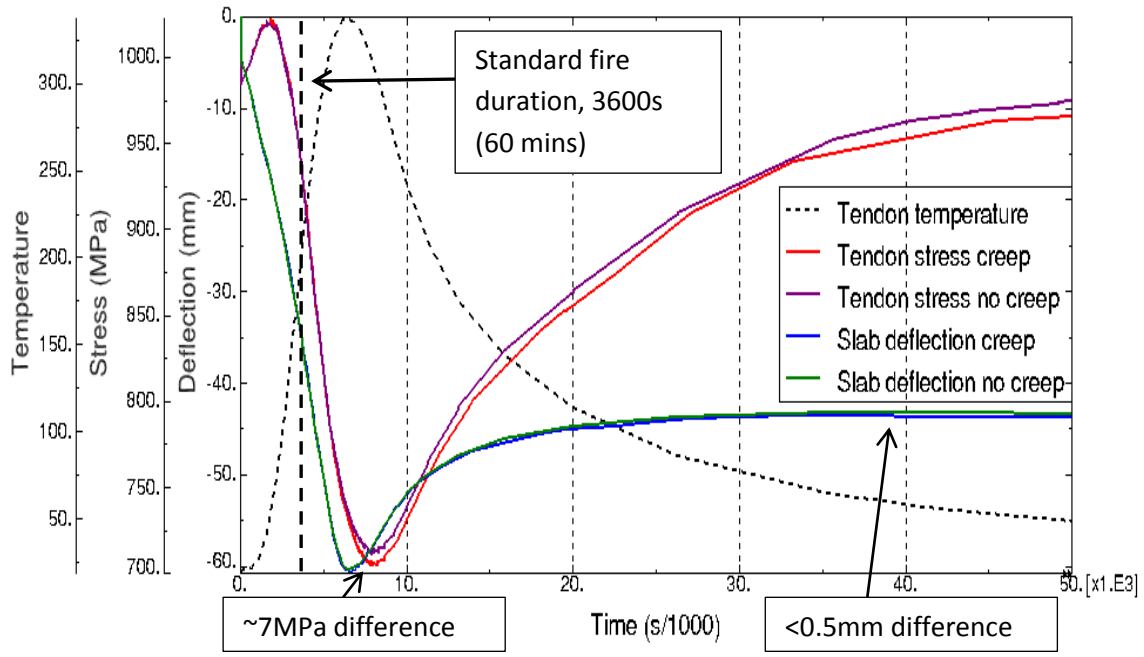

Figure 5-24; Tendon stress versus slab deflection with and without explicit creep modelling, 35mm minimum cover, 60 minute standard fire.

90 minute standard fire

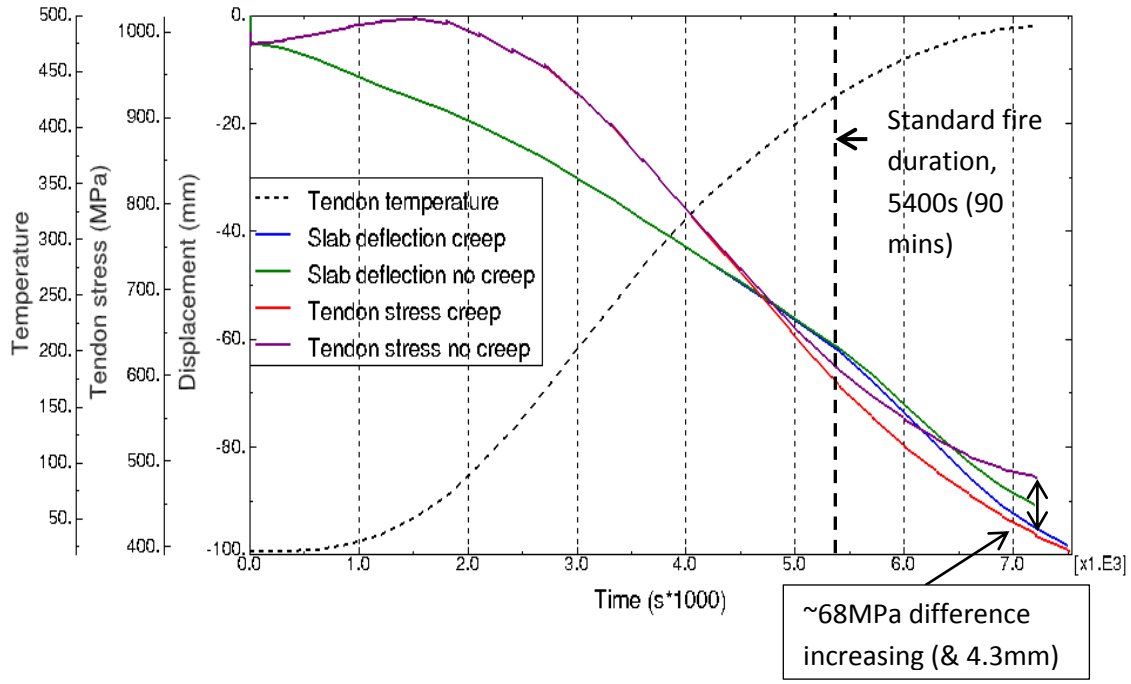

Figure 5-25; Tendon stress versus slab deflection with and without explicit creep modelling, 25mm minimum cover, 90 minute standard fire.

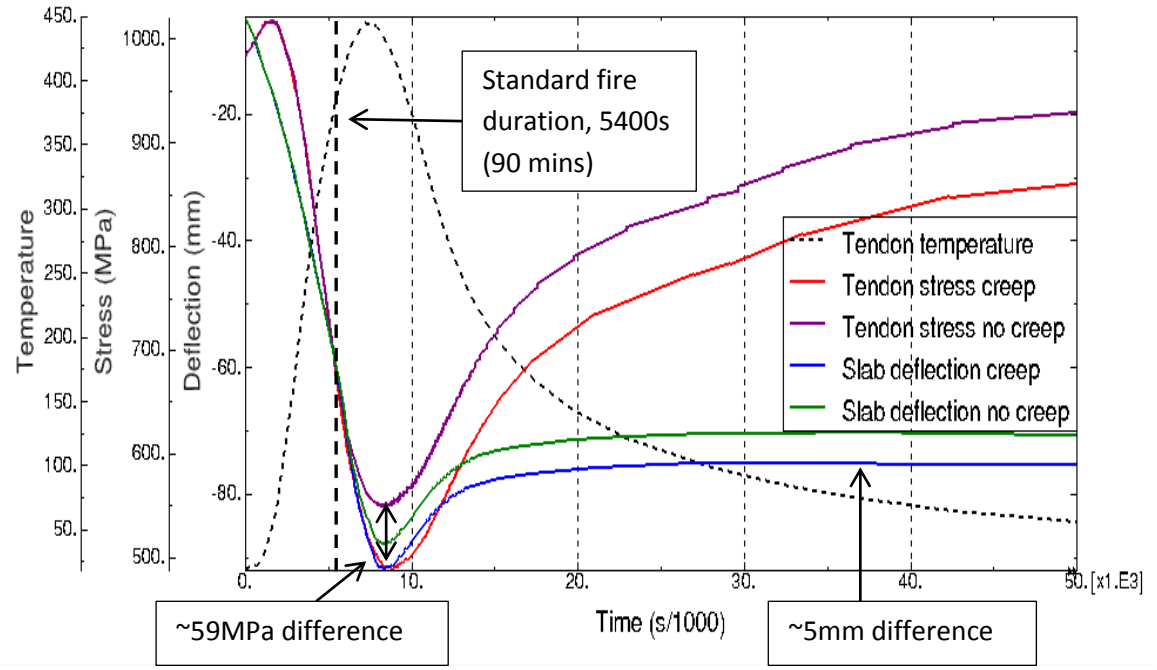

Figure 5-26; Tendon stress versus slab deflection with and without explicit creep modelling, 30mm minimum cover, 90 minute standard fire.

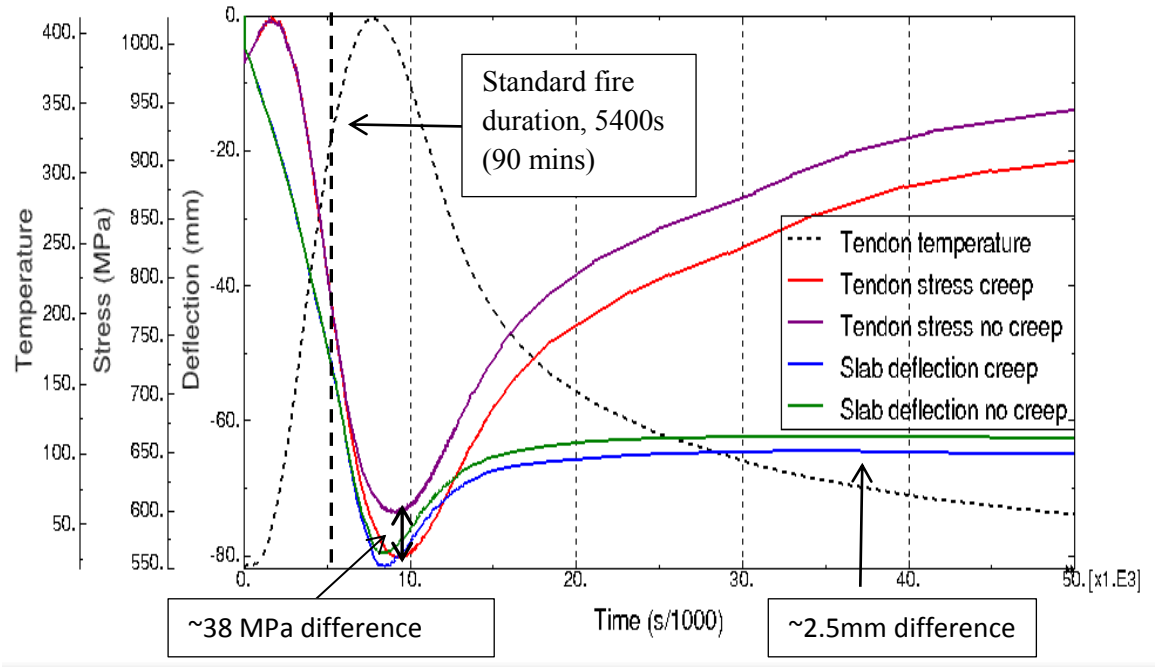

Figure 5-27; Tendon stress versus slab deflection with and without explicit creep modelling, 35mm minimum cover, 90 minute standard fire.

120 minute standard fire

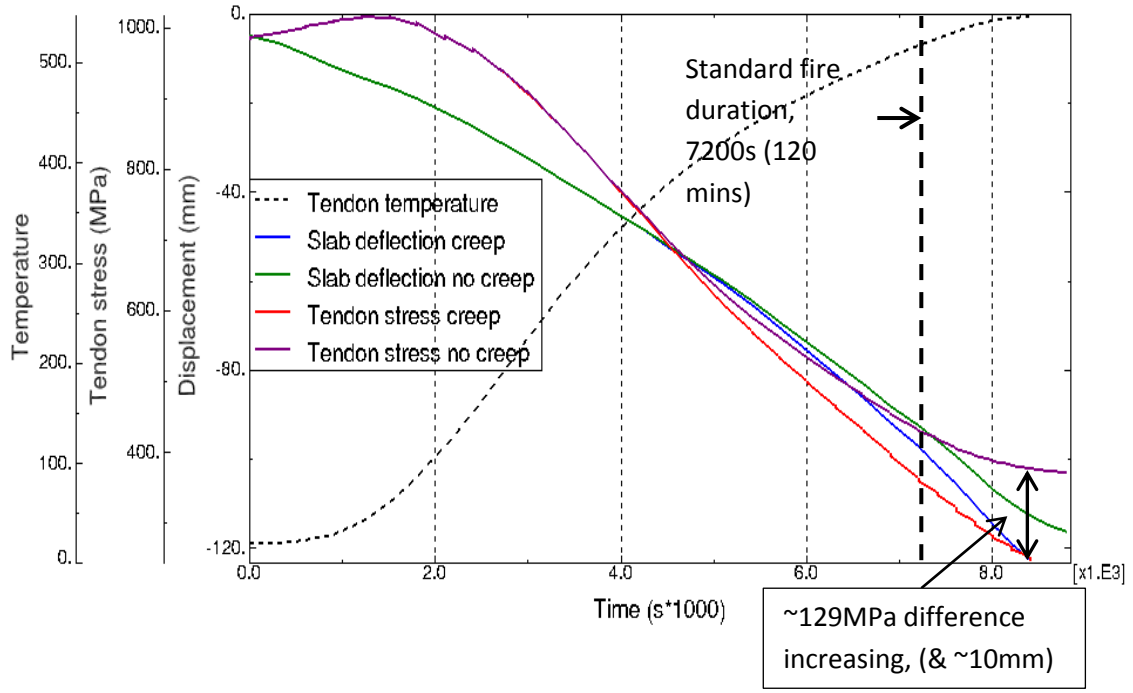

Figure 5-28; Tendon stress versus slab deflection with and without explicit creep modelling, 25mm minimum cover, 120 minute standard fire.

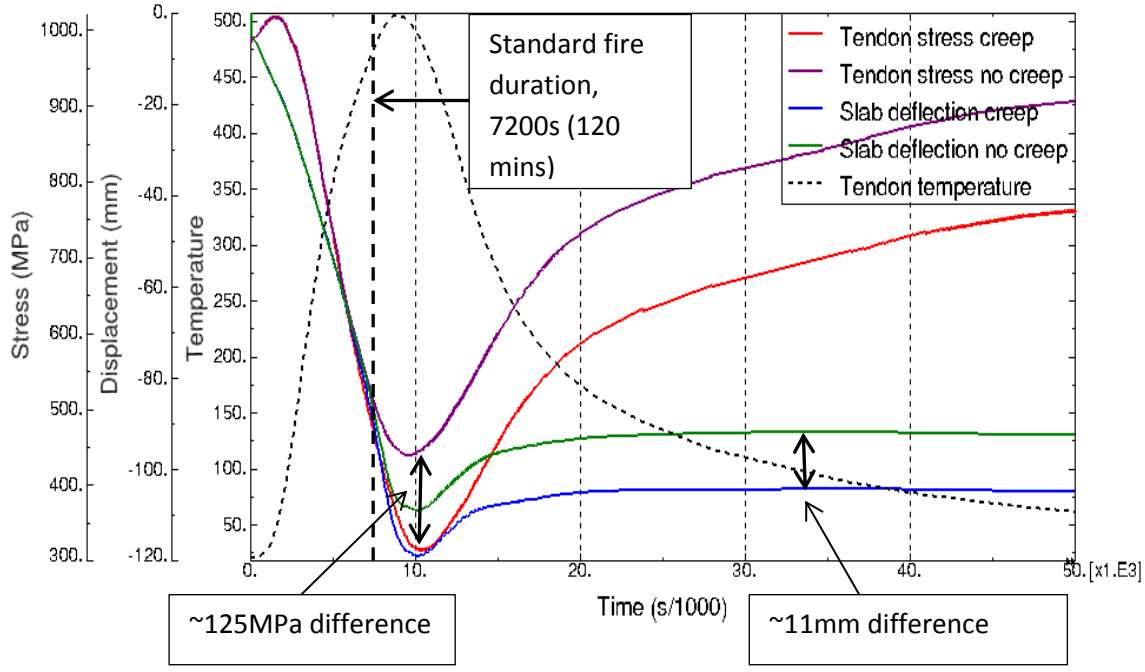

Figure 5-29; Tendon stress versus slab deflection with and without explicit creep modelling, 30mm minimum cover, 120 minute standard fire.

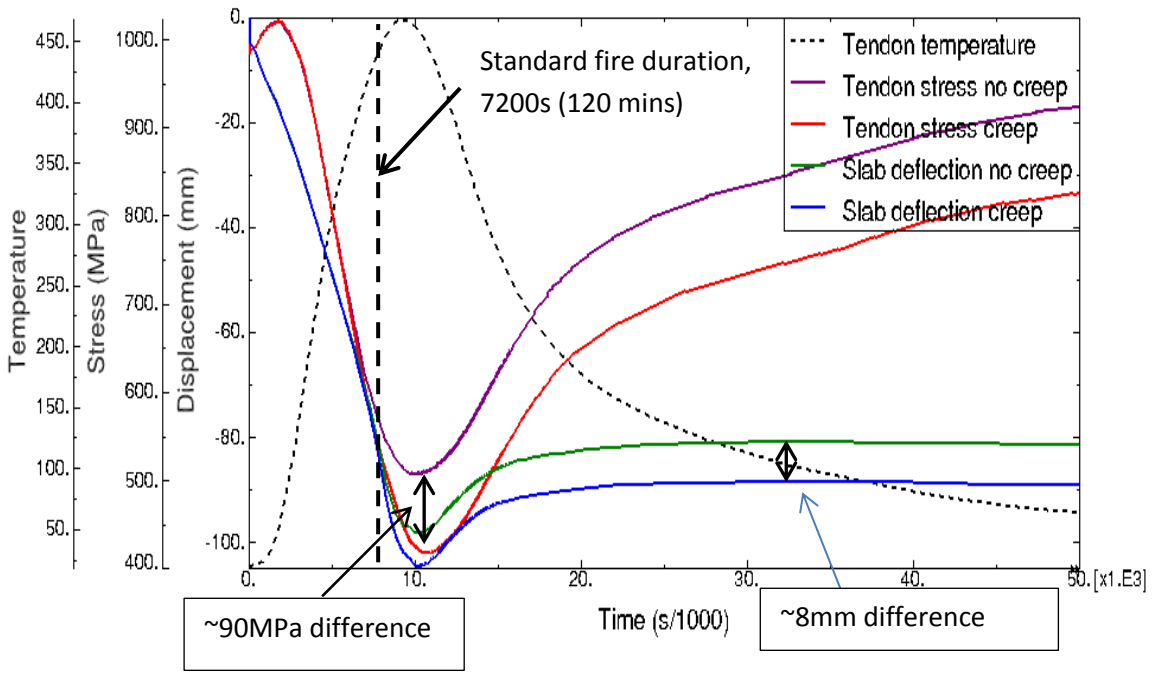

Figure 5-30; Tendon stress versus slab deflection with and without explicit creep modelling, 35mm minimum cover, 120 minute standard fire.

Firstly in all the above plots, as expected, the tendon stress rises during the early stages of heating as slab deflection increases, whilst the tendons remain relatively 'cold'. Regarding creep it is noted tendon relaxation in nearly all cases does not significantly differ between creep and non-creep models until after the standard fire has ceased. The notable exception is the most extreme case modelled; a 120 minute standard fire with 25mm of minimum concrete cover to the tendons. In this case the tendon temperature exceeds 500°C. It has been noted in Chapter 4 with respect to ASTM A416 prestressing steel that Eurocode 2 [1] did not seem to be able to implicitly account for transient heating creep strain as temperature rises towards 500°C.

In other cases it is clear the difference in stress relaxation between explicit creep consideration and implicit creep consideration accumulates as tendon heating rate drops and tendon temperature approaches it peak. This tends to happen during compartment cooling but may also occur if a standard fire is allowed to continue even further than the 120 minute limit of the studies in this thesis. As the standard fire curve plateaus significantly thermal gradients throughout the slab become increasingly shallow and thus tendon heating rate will slow. For most of the parametric studies performed here, the Eurocode 2 [1] guidelines would appear effective; creep must be explicitly accounted for when heating rate falls out with the bound $2℃ \leq \dot{T} \leq 50℃$ per minute. This highlights the importance of accounting for cooling. The heat transfer models showed through Figure 5-10, Figure 5-11 and Figure 5-12, the tendon temperature to reach its peak during compartment cooling, and heating rate to drop below 2°C per minute after the standard fire has ceased. The above plots now clearly show, it is during this cooling period that tendon relaxation peaks in the time vicinity of peak tendon temperature (or shortly after), with low heating rate creep to have a significant influence during this time. It is only during the consideration of compartmental cooling that the importance of explicitly considering creep is noticeable.

Slab central deflection is noted largely to closely follow tendon stress relaxation. Although it can be observed in certain cases, peak deflection and peak times do not entirely coincide. These cases seem to be at shorter standard fire durations and increased concrete cover. Generally, increased tendon relaxation clearly leads to increased slab deflection. It does however take a fairly significant difference in stress relaxation with respect to implicit versus explicit creep accountability to produce a notable deflection difference. As tendon relaxation deviates most in the early stages of cooling, after standard fire exposure between implicit and explicit creep models, then so does the difference in predicted central deflection. As the tendon cools and elastic modulus is recovered, along with recovery of concrete elastic properties (in compression), a degree of deflection is recovered. However tensile and compressive concrete damage remains, as well as a reduction in longitudinal slab compression from the permanent relaxation suffered by the tendon. A large portion of the peak slab deflection also remains.

The shorter the standard fire duration the greater the continued increase in post fire relaxation and slab deflection. This is particularly observable in the 60 minute standard fire plots Figure 5-22, Figure 5-23 and Figure 5-24. In these cases the thermal gradients are steep between the base and the tendon as the standard fire curve incident on the slab base has not begun to significantly plateau at this point; therefore there remains a significant degree of continued heat transfer into the slab. This behaviour with respect to standard fire duration was discussed in Section 5.2.1. Despite this, the ultimate temperatures reached are not quite significant enough to yield considerable creep strain that cannot be accounted for implicitly by Eurocode 2 [1] derived inelastic stress-strain curves. These differences would be further reduced under an increased rate of compartmental cooling.

Of the parametric studies considered and based on the above plots, those showing the greatest necessity to consider creep explicitly are the slabs exposed to 90 and 120 minute standard fires. Section 5.3.1 showed a possible failure mechanism occurring in hogging as a large sectional depth of the slab near the beam support experiences a significant degree of tensile inelastic strain. The following plots display the difference in tensile inelastic strain accumulated in hogging within the main damaged region of the slab (displayed earlier in Figure 5-14 of Section 5.3.1), when creep is and is not explicitly considered. These plots are presented for all 90 and 120 minute standard fire exposure parametric studies as well as a 60 minute exposure with 25mm concrete cover.

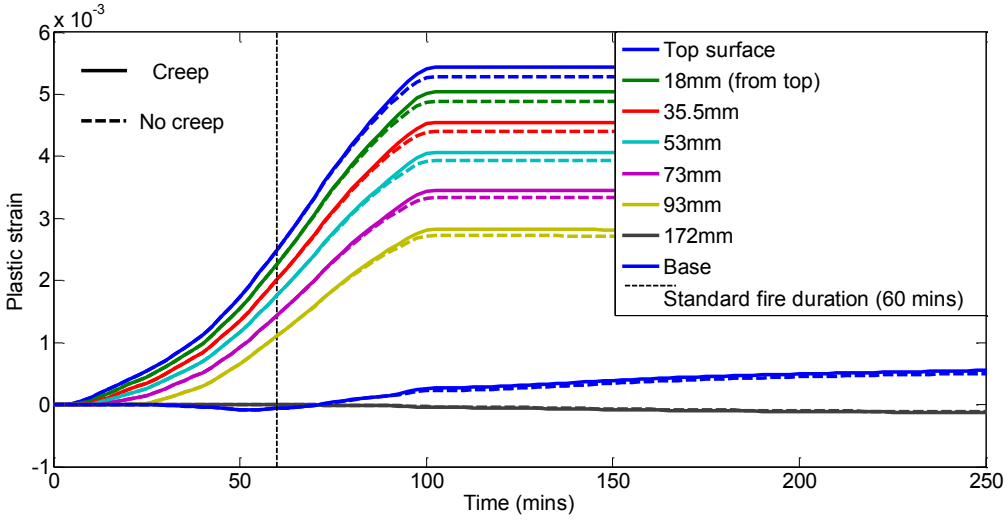

Figure 5-31; Longitudinal plastic strain, 25mm cover, 60 minute standard fire

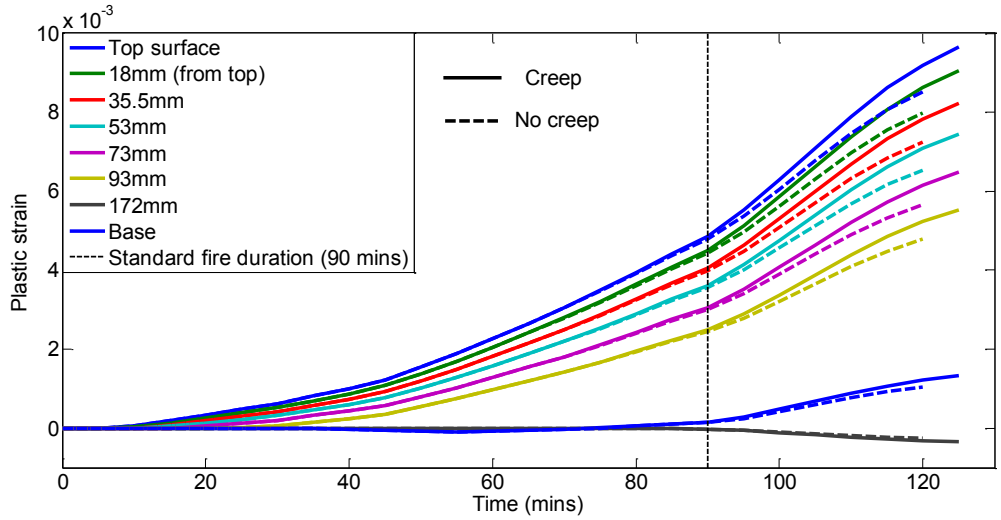

Figure 5-32; Longitudinal plastic strain, 25mm cover, 90 minute standard fire

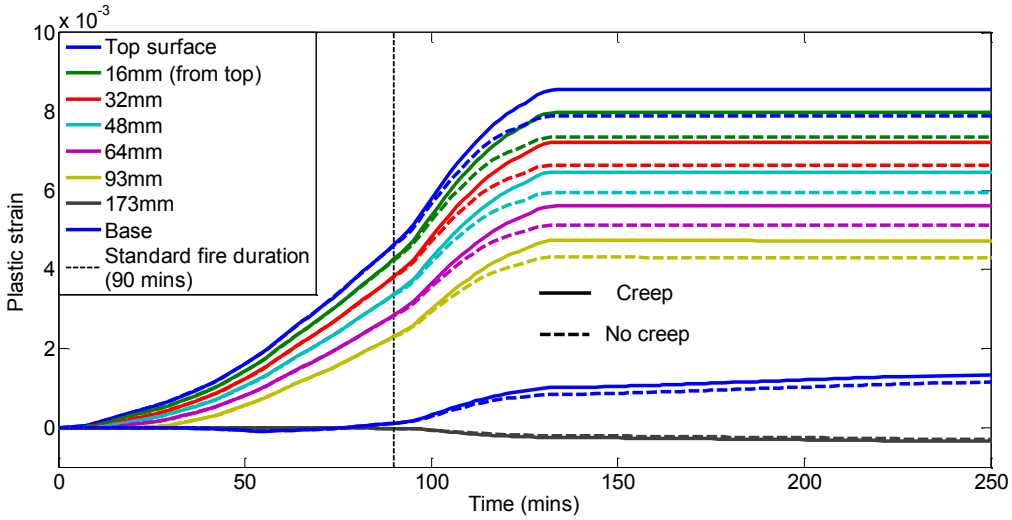

Figure 5-33; Longitudinal plastic strain, 30mm cover, 90 minute standard fire

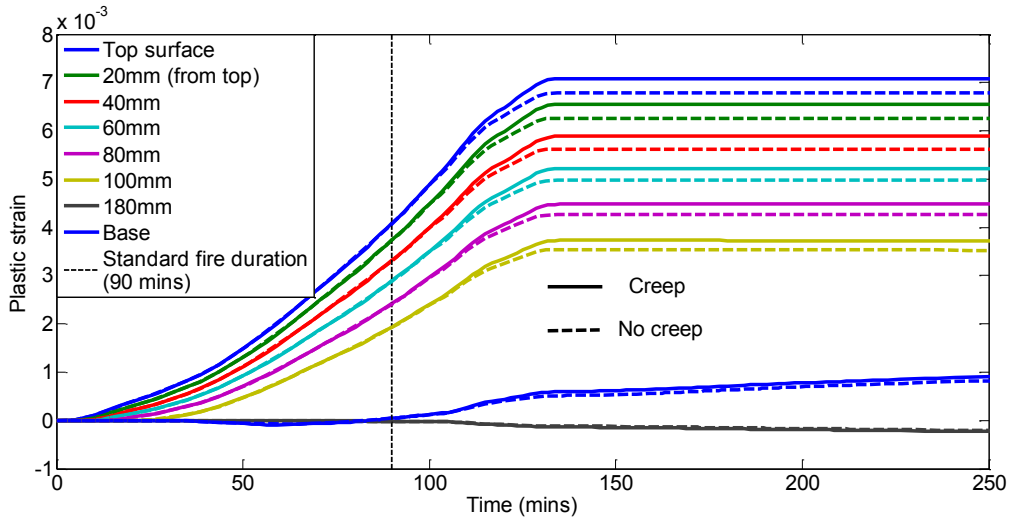

Figure 5-34; Longitudinal plastic strain, 35mm cover, 90 minute standard fire

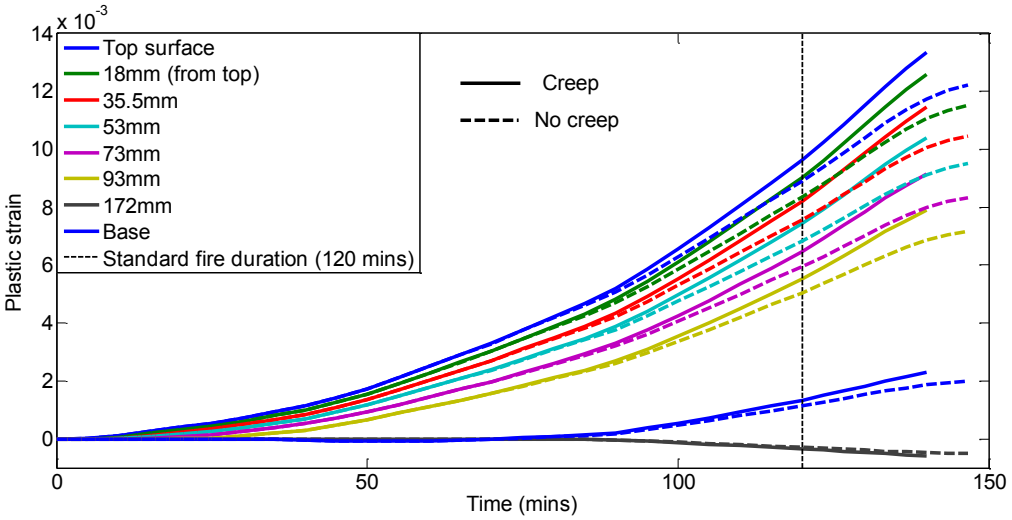

Figure 5-35; Longitudinal plastic strain, 25mm cover, 120 minute standard fire

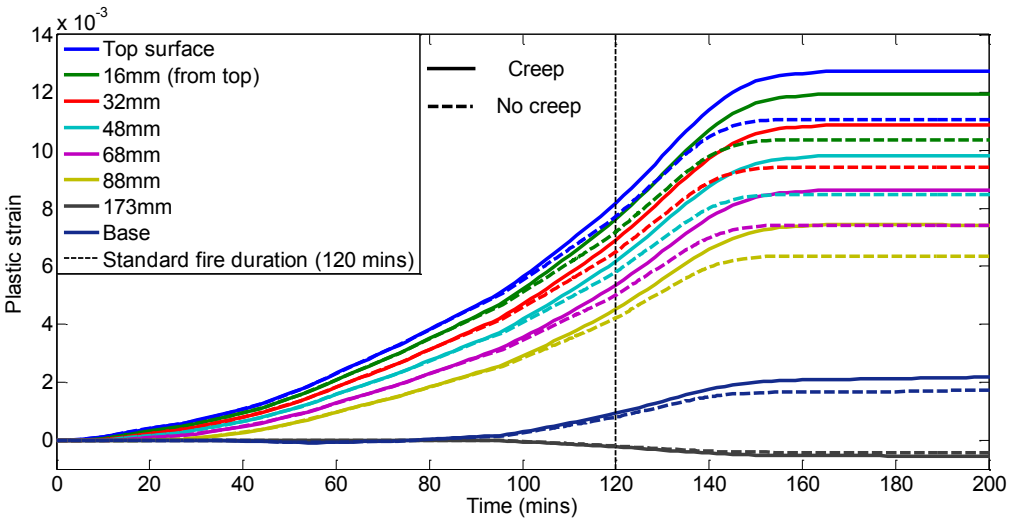

Figure 5-36; Longitudinal plastic strain, 30mm cover, 120 minute standard fire

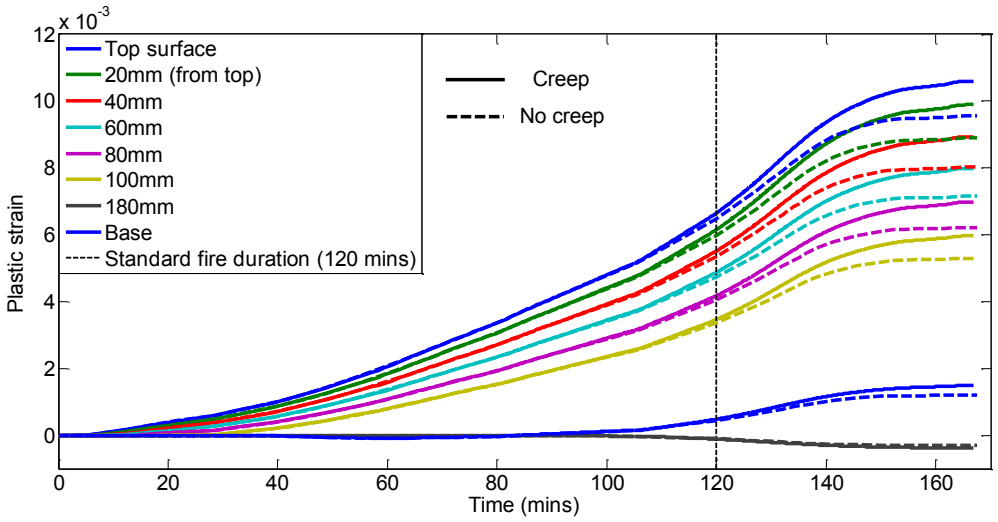

Figure 5-37; Longitudinal plastic strain, 35mm cover, 120 minute standard fire

The above plots show, corresponding to differences in tendon relaxation and slab deflection between creep and non-creep models shown in Figure 5-22 to Figure 5-30, that differences in plastic tensile strain accumulation largely occurs after the respective standard fires have ceased. Again the notable exception being the most extreme case shown in Figure 5-35; a 120 minute standard fire on a slab with 25mm minimum concrete cover to the tendon. As this case evolves into the compartment cooling phase the strain accumulations appear to be diverging significantly.

Figure 5-36 shows a 30mm concrete cover slab exposed to a 120 minute standard fire, this also shows an emerging difference in accumulated tensile plastic strain prior to the standard fire extinguishing. It evolves into a significant difference as peak deflection is reached. It is these 120 minute standard fire cases that produce the largest tensile strains and the largest differences in predicted tendon relaxation (peak difference is approximately 125MPa at 30mm cover) and slab deflection when creep is not explicitly modelled. Therefore it is these cases in which neglecting to explicitly consider tendon creep could be most significant with respect to under estimating likelihood of failure, or time to failure. It is also a noticeable point that the difference in slab deflection, as compared to the difference in tendon relaxation does not seem as large, but hogging tensile plastic strain does. For example a 30mm cover, 90 minute standard fire model shows an approximate 10% increase in tendon relaxation if creep is explicitly accounted for (Figure 5-26), and just slightly less than this increase in tensile plastic strain accumulation in hogging (Figure 5-33). The deflection increases by close to 7% however. In this respect it is worth noting the draped nature of the tendons which also have the intention of providing tensile support to the concrete in hogging and sagging. Restrained thermal expansion within the slab and its effect on the slab curvature is naturally one means by which deflection is slightly influenced by other factors than tendon relaxation (smaller heated regions may lead to a tendency towards the above percentages aligning more). Even in the case of rapid compartmental cooling it is likely at all the concrete covers presented, when exposed to a standard fire for 120 minutes, the tendon temperatures will become exposed to dangerous magnitudes for significant durations. The effect of this is microstructural change, degradation of mechanical properties and substantial stress relaxation.

It is observed in Figure 5-25, Figure 5-28, Figure 5-32 and Figure 5-35 that 25mm minimum concrete cover models exposed to 90 and 120 minute standard fires failed to maintain a numerically converging equilibrium state through the cooling phase. These models aborted just prior to peak tendon temperature being realised. This does not necessarily represent structural failure but does most likely represent a large degree of transience with respect to displacement in local regions of the slab.

The case of a 25mm cover UPT slab exposed to a 90 minute standard fire highlights particularly the effect of slow compartment cooling. This case fails to converge from approximately 30 minutes into cooling at which point accumulated tensile plastic hogging strain has increased significantly, as has tendon relaxation and slab deflection. A more rapid rate of compartment cooling would influence the increase in tendon temperature and high temperature exposure time. This may help negate the significant (approximately doubling) rise in hogging tensile plastic strain during cooling prior to numerical failure and possible associated potential structural consequences. Neglecting creep in this case does not seem to produce quite as significant difference as the 120 minute standard fire studies however.

For all standard fire durations, structural integrity with time increases with concrete cover. Over 60 and 90 minute standard fire durations 35mm concrete cover should prevent significant or dangerous microstructural changes within the tendons, especially considering these models considered a highly conservative compartmental cooling curve. However, it may be worth considering the tendons in these cases will have been exposed to primary creep and undergone a degree of strain hardening, making them less ductile and more brittle under (very) extreme cold loading. As outlined at the end of Section 5.2.2, MacLean recommends tendons should be considered damaged and thus replaced if exposed to temperatures beyond 300^{o}C. This prevents any possibility of recrystallization (usually occurring beyond 400^{o}C) and associated yield reduction and ductility increases, it also prevents the microstructural dislocation based evolutions associated to primary creep from progressing significantly. These could place the tendons further along the restoration process (Section 2.2) path should they be subject to reheating. None of the concrete cover models presented here prevent a tendon from reaching temperature exposures of greater than 300^{o}C subject to the standard fire durations applied to the slabs. Eurocode 2 [1] states 350^{o}C as a critical design temperature for unbonded prestressing steel reinforcement, recommending an additional 15mm of concrete cover from ambient to design to prevent such exposure. It specifies a greater critical temperature should only be used if more accurate methods are used to determine the effects of increased deflections. The only modelled case which prevents such temperature exposure is the UPT concrete slab with 35mm of minimum cover to tendons subject to a 60 minute standard fire (Figure 5-24). At larger standard fire durations, 35mm tendon cover will allow longer egress times. It is however difficult to see grounds for specifying less than 35mm concrete cover unless fire risk and suppression techniques are deemed sufficient to limit fire duration to below 60 minutes. This is however based only on models considering a standard fire temperature-time curve. Should a realistic fire impose greater heat on the base of a slab during this time frame this number may have to be reviewed.

5.3.2.2 UPT concrete slab behaviour with BS 5896 standard prestressing steel tendons; creep explicitly considered vs implicitly considered (Eurocode 2)

Having presented mechanical UPT concrete slab model data with ASTM A416 [10] standard prestressing steel tendons, attention now turns to mechanical behaviour using BS 5896 [11] standard prestressing steel tendons. From Chapter 4 it is noted BS 5896 [11] standard prestressing steel tendons display significantly smaller creep strain accumulation than those developed to the ASTM A416 [10] standard (Figure 4-11 and Figure 4-12). As a result, tendons manufactured to this standard were shown to display a much reduced relaxation of prestress. As such Eurocode 2 [1] stress-strain curves can account for transient heating creep strains up to around 500°C with respect to this steel, and are conservative enough to account for steady state temperature exposure for up to 90 minutes at 400°C (Figure 4-10). Based on the tendon temperature profiles from Section 5.2.2 then only 90 minute and 120 minute standard fire and cooling heat transfer models have been applied to the following mechanical models, and only 25mm and 30mm concrete covers considered. The tendon temperatures in other cases simply are not deemed sufficient to indicate any difference should creep be explicitly considered within the tendons or not.

90 minute standard fire

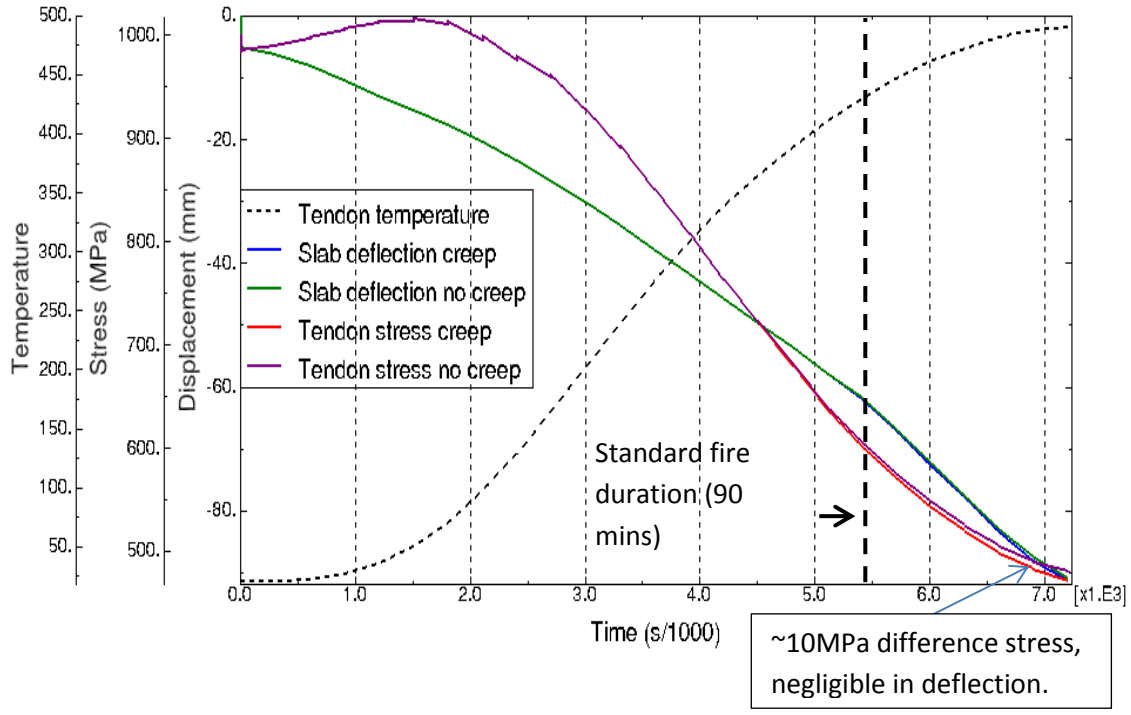

Figure 5-38; Tendon stress versus slab deflection with and without explicit creep modelling, 25mm minimum cover, 90 minute standard fire, BS 5897 prestressing steel.

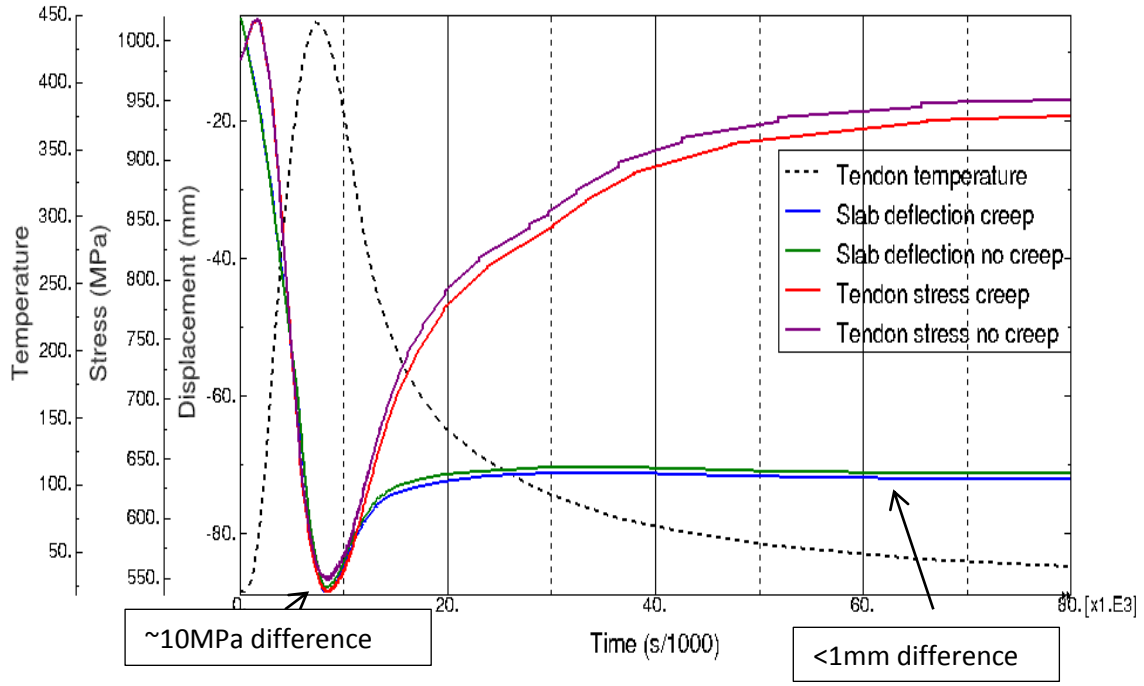

Figure 5-39; Tendon stress versus slab deflection with and without explicit creep modelling, 30mm minimum cover, 90 minute standard fire, BS 5897 prestressing steel.

120 minute standard fire

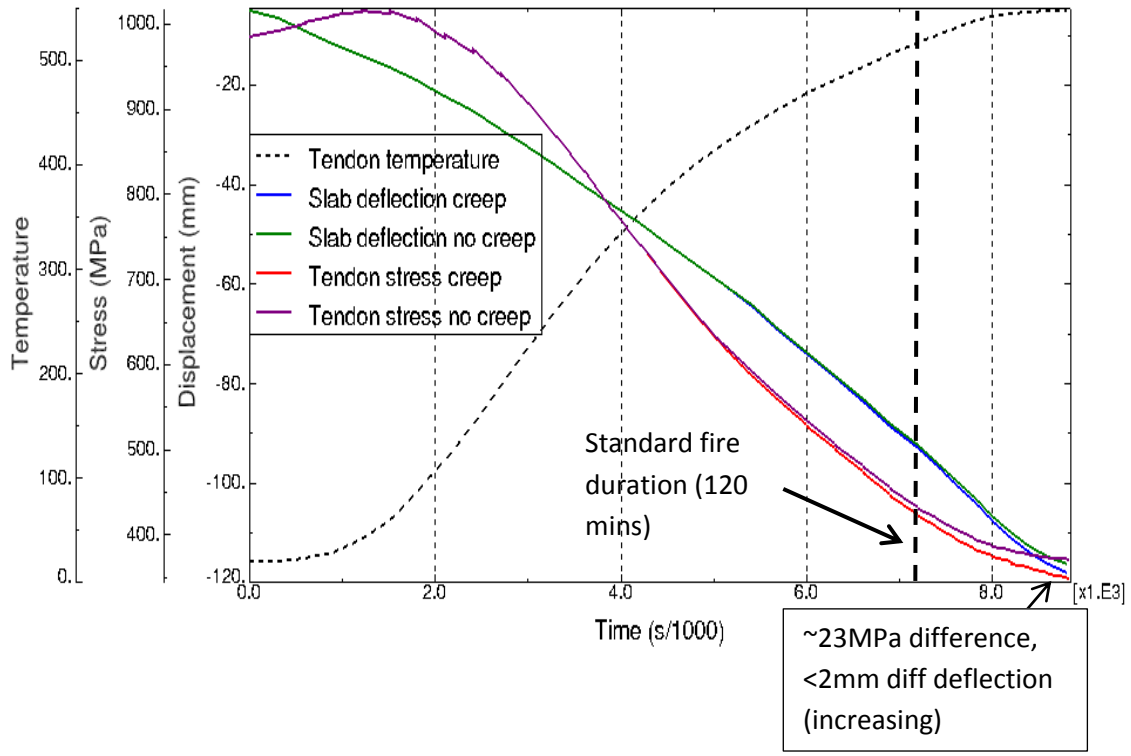

Figure 5-40; Tendon stress versus slab deflection with and without explicit creep modelling, 25mm minimum cover, 120 minute standard fire, BS 5897 prestressing steel.

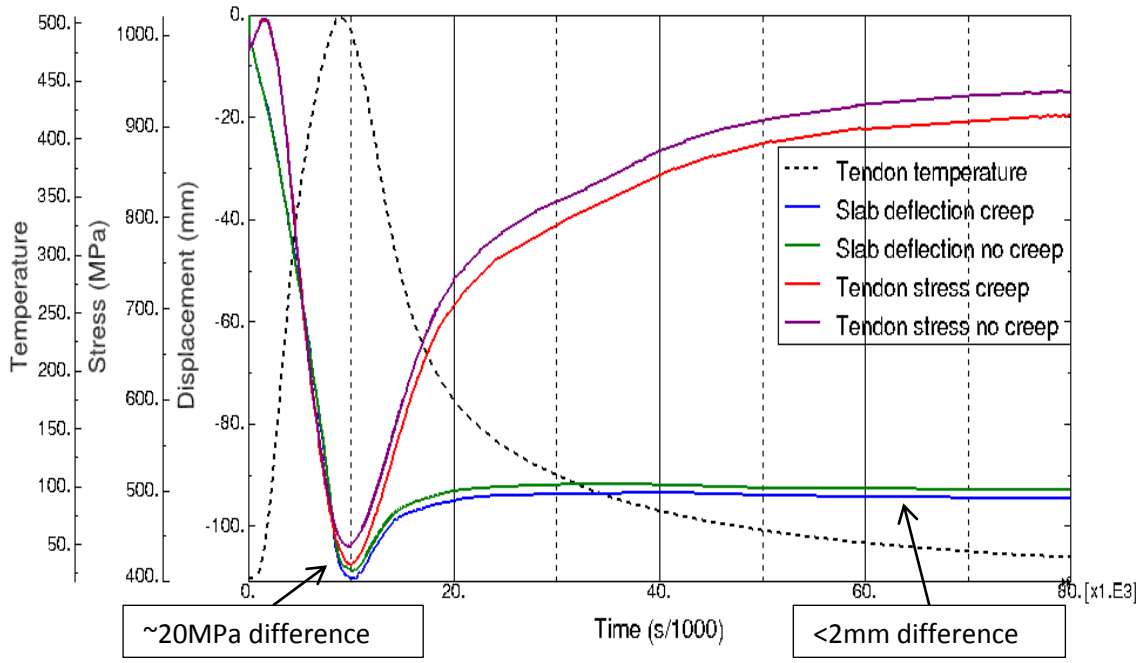

Figure 5-41; Tendon stress versus slab deflection with and without explicit creep modelling, 30mm minimum cover, 120 minute standard fire, BS 5897 prestressing steel.

Figure 5-38 and Figure 5-39 (90 minute standard fires) show only small differences in both tendon relaxation and slab central deflection. It is again noted however, the 25mm concrete cover model failed to converge as peak tendon temperature was approached. At this time, under sustained elevated temperature exposure, explicit creep models were beginning to display increased relaxation and resulting slab deflection with respect to the non-creep models. It is unlikely that the difference would have been significant however.

The main concern in these cases therefore does not seem to be the explicit consideration of creep with respect to predicting structural behaviour, but instead the tendon temperature profiles with respect microstructural evolution and long-term mechanical degradation of the prestressing steel. It is observed from Figure 4-17 there is, as with ASTM A416 [10] prestressing steel, an onset of secondary creep strain beyond 400^{o}C which may be linked to recrystallization. Therefore there is an associated permanent reduction in yield stress and an increase in ductility (Figure 2-6) dependent on the magnitude of temperature reached.

Figure 5-40 and Figure 5-41 show tendon relaxation and slab deflection for 25mm and 30mm concrete cover UPT slabs when exposed to a 120 minute standard fire and associated cooling. It is evident from Figure 5-40 that tendon relaxation curves are starting to diverge somewhat, as are slab deflection curves. Unfortunately the lack of convergence prevents observation of the ultimate difference. It may be assumed from the temperature exposure exceeding 500^{o}C and the expected time of exposure at low heating rates (<2^{o}C per minute), that Eurocode 2 [1] stress strain temperature reduction factors may not be able to sufficiently account for creep induced relaxation in this case. However to what degree of significance or concern the difference ultimately would be is uncertain. As with ASTM A416 [10] prestressing steel the inability of these 25mm concrete cover models to achieve numerical convergence again does not necessarily represent a structural collapse.

It may be due to contact difficulties between the slab and tendon with this particular cover and increased deflection. Or as postulated earlier it may represent rapid deflection of the slab resulting from large tensile strains in hogging or possibly due to extreme tensile strains and softening from crushing strain in a localised area of the base of the slab as shown in Figure 5-15 and Figure 5-17.

At 30mm concrete cover the tendon temperature exposure also touches 500^{o}C, however, despite a conservative compartmental cooling curve the difference in tendon relaxation and particularly resulting slab deflection are relatively small. It appears the need to explicitly account for creep in structural analysis of UPT concrete structures using BS 5896 [11] standard prestressing steel tendons is not really required except for the most extreme cases (standard fire exposure >120 minutes at minimum cover and concrete cover <=25mm). The temperature exposures in Figure 5-38 to Figure 5-41 however all warrant the replacement of tendons owing to the magnitude of the tendon temperature reached and the associated material microstructural evolutions. In this respect the conclusion is the same as for ASTM A416 [10] standard prestressing steel tendons; in order to prevent such microstructural changes a minimum of 35mm concrete cover is required. If standard fire duration is longer than 60 minutes, this cover would need to be increased further. Bearing this in mind the tendon temperature parametric plots of Section 5.2.2 are of most importance in deducing appropriate concrete covers and fire ratings.

It may be concluded with respect to BS 5896 [11] standard prestressing steel tendons, with the exception of extreme cases involving long duration standard fires and low concrete covers, that Eurocode 2 [1] temperature dependent stress-strain curves can implicitly account for creep to a satisfactory degree. The Eurocode 2 [1] stress-strain curves have a sufficient factor of safety with respect to inelastic strain accumulation during higher transience tendon heating to cover creep strain accumulation during low transience tendon heating within the parametric studies considered in this section. The extreme cases involve concrete covers far below that which would be recommended in typical design codes accompanied with long duration standard fires. The main consequence to consider is the degree of tendon temperature exposure and duration with respect to microstructural changes as outlined many times previously.

5.4 Summary

This section summarises the main outcomes of note from this chapter. Recommendations for design based around concrete covers to limit tendon temperature exposure are also summarised and finally the limitations of the previous modelling studies are presented. These limitations should inform areas of potential further study.

5.4.1 Key outcomes

- The following bullet points overview the key outcomes from the UPT concrete slab modelling study presented. In particular these summarise two notable conclusions. These are the importance of the consideration of compartment cooling post-fire and the difference in tendon relaxation and subsequent UPT concrete slab deformation when the slabs are prestressed by different tendons of different manufacturing standards. The validity of Eurocode 2 [1] stress-strain curves for prestressing steel to implicitly account for tendon creep and thus cover subsequent tendon stress relaxation and slab deflection is also summarised. The consideration of compartment cooling has been shown to be extremely important with respect to the continued relaxation of prestressing steel tendons within UPT concrete slabs and the resulting increase in slab deflection and concrete hogging damage. This is true even if the explicit consideration of creep is neglected (see Figure 5-22 to Figure 5-30). The rate of compartment cooling however, particularly after short duration standard fires, effects the magnitude of the peak tendon temperature reached and the duration of exposure at temperatures inducing significant creep strain (>300^{o}C, Figure 4-11, Figure 4-12). This can cause microstructural changes potentially damaging for continued tendon use, particularly if tendon temperature exceeds 400^{o}C (secondary creep and microstructural recrystallization). Examples of the effect of differing rates of compartment cooling were shown in Figure 5-7, Figure 5-8 and Figure 5-9.

- The standard to which prestressing steels are manufactured has been shown in Chapter 4 to make a significant difference to creep susceptibility and resulting stress relaxation in isolated prestressed tendons. This transfers to significant differences in UPT concrete slab deflection when ASTM A416 [10] standard tendons are used as opposed to BS 5896 [11] standard tendons. For example, when a UPT concrete slab with a minimum concrete cover of 30mm is heated for 90 minutes; with BS 5896 [11] standard tendons (Figure 5-39) as opposed to ASTM A416 [10] standard tendons (Figure 5-26), tendon relaxation is 50MPa less and permanent slab deflection 4-5mm less. These are respectively 9% and 7% relative increases in both parameters when ASTM A416 [10] standard tendons are used as opposed to BS 5896 [11] standard tendons. In this case the tendon temperature is at 384^{o}C after the 90 minute standard fire and reaches a peak beyond this of 444^{o}C, its temperature is beyond 400^{o}C for 61 minutes (Figure 5-11, Table 5-2). Comparing Figure 5-29 to Figure 5-41, whereby the same slab is subjected to a 120 minute standard fire, the relative increase in tendon relaxation is approximately 25% (105MPa). This results in an increase in permanent slab deflection of 10-11% (~10mm). In this case tendon temperature is 468^{o}C after the 120 minute standard fire and peaks at 505^{o}C.

- Time evolving creep strain accumulation during the compartment cooling period cannot be implicitly covered by Eurocode 2 [1] inelastic yield curves with respect to ASTM A416 [10] standard tendons if temperature exposure extends much beyond 350^{o}C. This results in a notable increase in predicted tendon relaxation and slab deflection when creep is explicitly considered (Figure 5-22 to Figure 5-30). Increases in concrete hogging damage are also noted, particularly during compartment cooling, relative to cases where creep is assumed

implicitly accounted for (Figure 5-31 to Figure 5-37). Whilst increases in tendon relaxation and slab deflection are also noted when creep is explicitly modelled in BS 5896 [11] standard tendons, these differences are generally small (Figure 5-38 to Figure 5-41). Differences of significance appear in Figure 5-40 where a 25mm minimum concrete cover slab is exposed to a 120 minute standard fire.

5.4.2 Recommendations

As mentioned in the main text of this chapter, Eurocode 2 [1] recommends 350^{o}C as a critical design temperature for exposure of unbonded prestressing steel tendons. A 15mm extra concrete cover allowance is recommended on top of ambient design specifications to prevent such exposure. MacLean [9] recommends tendons exposed to temperatures beyond 300^{o}C be considered damaged and necessary to be replaced, owing to mechanical degradation from microstructural evolution (yield stress reduction and ductility increase, Section 2.2). Based on the analysis of this chapter, 350^{o}C seems a reasonable maximum tendon design temperature. A key outcome of this thesis is however the need to consider compartment cooling when designing to such specific tendon temperatures. This is highlighted by Figure 5-11 where a 35mm minimum concrete slab displays a tendon temperature of 335^{o}C after a 90 minute standard fire, this rises to 410^{o}C during the early stages of compartment cooling. The heat transfer data displayed in Figure 5-10, Figure 5-11 and Figure 5-12 implies, to limit tendon temperature to no more than 350^{o}C, 35mm of minimum concrete cover must be specified and standard fire exposure must be no greater than 60 minutes. If designing UPT slabs to withstand longer fire durations according to a standard fire curve, an even greater degree of minimum concrete cover must be specified. Designing UPT concrete slabs to a maximum permissible tendon temperature of 350^{o}C after a given duration of fire exposure may also have other benefits with respect to the main outcomes above:

- It prevents the likely onset of internal recrystallization, likely to occur beyond 400^{o}C (Section 4.4.5) within the tendon wires and the associated decrease in yield stress and increase in ductility.
- It will limit the difference in UPT concrete slab deflection noted when ASTM A416 [10] standard prestressing steel tendons are used as opposed to BS 5896 [11] standard tendons. This makes the consequences of choosing one standard of tendon over the other less significant.
- In addition to this, the consequences of neglecting to account explicitly for the contribution of creep to tendon stress relaxation will also be minimised. This is under the assumption inelastic behaviour would be considered through the use of Eurocode 2 [1] temperature dependent stress-strain curve reduction factors.

5.4.3 Limitations

There are some notable limitations to the modelling study presented in this chapter. Most notably is the restriction of the analyses to heating subject only to the standard fire temperature-time curve [31]. Thermal gradients throughout a slab immediately post-fire are very important in dictating the ongoing heat transfer and temperature evolution of the tendon. This means only a very specific set or evolution of thermal gradients within a UPT concrete slab have been considered within the fire duration parametric studies. Coupled to this is the consideration of only one rate of air sink temperature cooling, this rate may be significant to further tendon relaxation and slab deflection after shorter duration standard fires such as 60 minutes. This chapter has highlighted the potential for significant ongoing tendon relaxation and associated UPT concrete slab concrete damage and deflection during compartment cooling. It cannot however be stated that the heating-cooling scenarios considered are necessarily characteristic of a real fire. It would be desirable to continue the modelling study of this chapter open to numerous more parameters including alternative temperature-time curves for both heating and cooling of a compartment.

A further significant limitation of this study and necessary addition to future models is the consideration of LITS. The effect of LITS during concrete cooling can be significant, as was outlined in Section 5.1. Therefore it must be incorporated in future FE models in order to perform a complete analysis of UPT concrete structures in fire. It could be particularly significant with respect to UPT concrete structures as opposed to standard reinforced concrete structures, owing to the addition of compressive prestress on the slabs from the tendons. Figure 13-1 and Figure 13-2 within Appendix F; Slab sectional compression-tension profile evolutions, show the evolution of longitudinal compression and tension across the slab cross-section. This highlights potential effective loading and unloading behaviour through parts of the slab cross-section as regions go from compression to tension and vice versa. During cooling this behaviour can reverse, though the unrecovered relaxation of the tendon ensures different conditions when the slab is fully cooled.

Some other limitations of this study are listed below, they largely relate to dangers in applying assumptions made from isolated slab models to larger continuous bay UPT concrete structures:

- Longitudinal hogging rebar should negate to some degree the significance of the tensile damage accumulated in hogging noted in Section 5.3.1.1.
- Edge beams free to rotate should also reduce the degree of hogging damage; the slab models presented were fixed in rotation.
- Single isolated UPT concrete slab models do not allow the effects of tendon relaxation on cold spans and resulting load redistribution to other areas of a structure to be considered.
- Transverse rebar should always be specified in UPT concrete with respect to transverse strain induced from compressing the slab. This was not specified in the slab models.
- In order to ease numerical convergence thermal expansion was restrained transversely thus preventing bowing. This may influence various facets of structural behaviour.
    - Tendon relaxation will vary to some degree dependent on transverse location within the slabs as deflection varies.
    - Stress conditions about supports will vary and other sectional behaviour will change dependent on location along the cross transverse span.

The final chapter is focussed largely on attempting to address the above limitations in drawing behavioural assumptions for continuous bay UPT concrete structures from the UPT concrete slab models of this chapter. This is to be achieved through the modelling of a section of a realistic one-way spanning UPT concrete structure. This may help understand the possible significance creep may have on potential hogging damage and failure with respect to realistic boundary conditions and specification of hogging rebar. Concerns regarding cold span behaviour may also be addressed. This could give an insight into likely failure mechanisms in a more realistic situation.

6 Modelling of one-way spanning UPT concrete structures exposed to fire

The limitations of the previous UPT concrete slab models were been outlined at the end of the last chapter. Amongst these were the lack of realistic structural boundary conditions and the lack of hogging rebar and their effects on minimising the hogging tensile damage noted in the slab models. The previous models for instance cannot consider load or moment redistribution to other regions and elements of a one way structure (such as columns and beams), as would happen in reality. They also do not consider the effect of tendon relaxation on cold spans. The following chapter aims to address some of these concerns by removing these limitations with larger scale modelling of a generic one way spanning building. Owing to time constraints it has not been possible to perform comparisons of models including explicit creep consideration in tendons versus those that do not. Creep however will be explicitly modelled within prestressing tendons throughout this chapter.

The structure modelled is a three by three bay one way spanning building of 5 storeys. Each bay spans 10 metres with a 6 metre transverse span. The structure is centred on a lift and/or stair shaft providing a solid core bracing the structure of dimension 6 metres by 3.6 metres. A schematic of the building and floor plan is displayed in Figure 6-1.

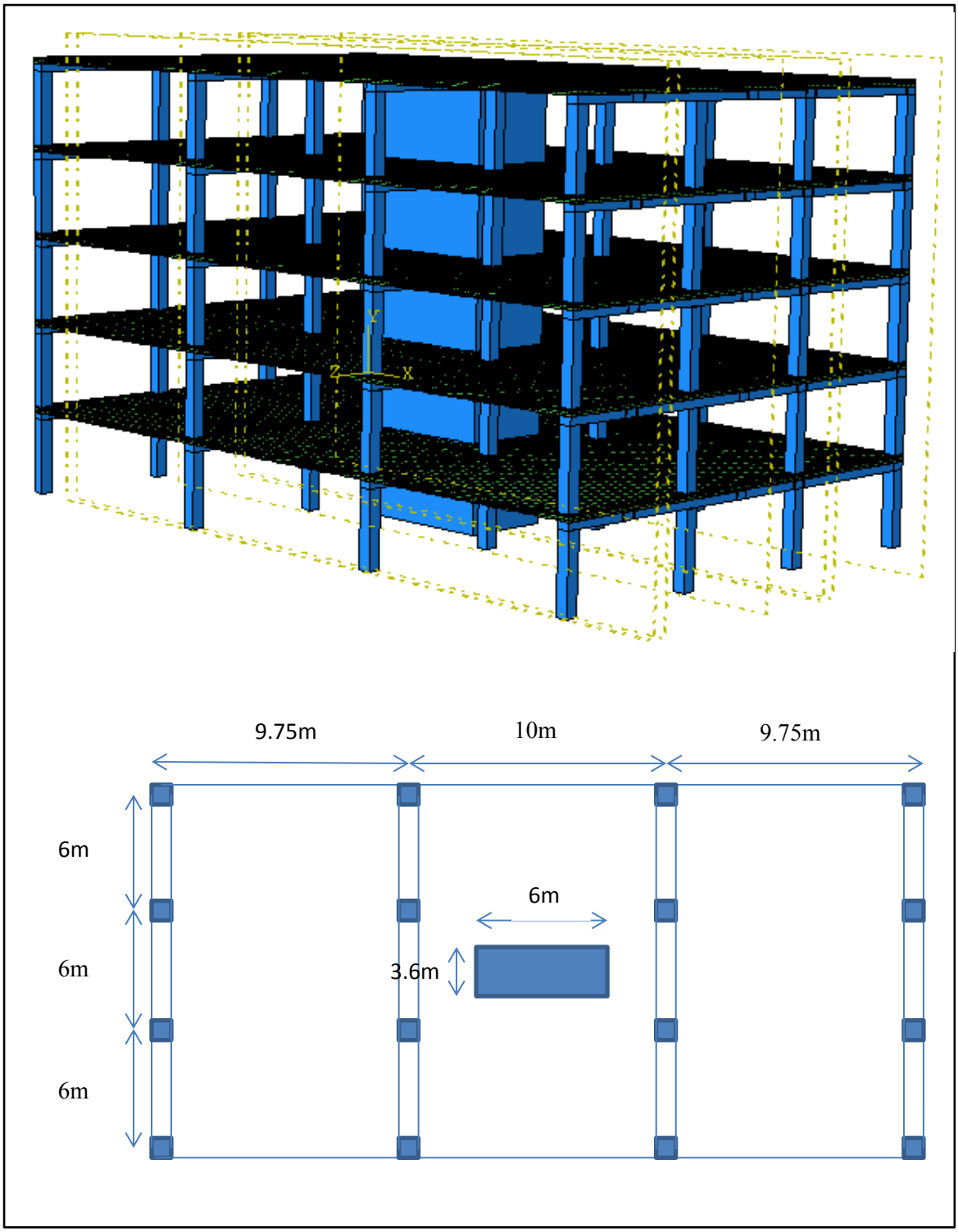

Figure 6-1; Building schematic and floor plan

The columns are square in cross-section with dimensions of 500mm by 500mm and 3 metres in height. The beams are 500mm in breadth and 300mm deep, thus allowing a 3.3 metre total floor clearance. The continuous slab is 250mm deep and mounted atop beams providing an effective beam depth of 550mm. The design of the structure has followed Eurocode 2 [32] guidelines. The span, the depth and number of tendons specified allow sagging rebar to be eliminated from the internal one way spans; transverse rebar however has been specified within these internal spans.

Sagging rebar is however specified in the end spans whilst hogging rebar is specified throughout. The slab is designed with ten tendons per transverse bay span, on 600mm centres with a minimum concrete cover of 30mm. The area of rebar specified in sagging and respective hogging regions is based on ensuring ultimate moment capacity exceeds the design moments for each span with appropriate factors of safety. The cross-sectional area of transverse rebar is specified at 50% of the sagging or hogging rebar specification. For the internal span where additional sagging rebar is not specified, the transverse rebar has been specified to the same area as the end span. The loads by which the structure is designed are as with the previous slab models; a $2KN/m^2$ static load and $3KN/m^2$ variable load with appropriate factors of safety. Bursting reinforcement has also been specified to restrain lateral and transverse induced tensile displacements. Rebar within the beams and columns is specified in accordance with the sizing of these respective concrete elements. The rebar within the end columns of the longitudinal span is specified with respect to one way bending based on criteria from Eurocode 2 [32]. Internal columns are also designed to bend about one axis however as they may bend in either direction about this axis as their rebar specification results in their capability of accommodating biaxial bending. Figure 6-2 shows a series of transparent structural views highlighting the specification and placement of additional tensile and bursting reinforcement throughout the section of the one-way spanning UPT structure.

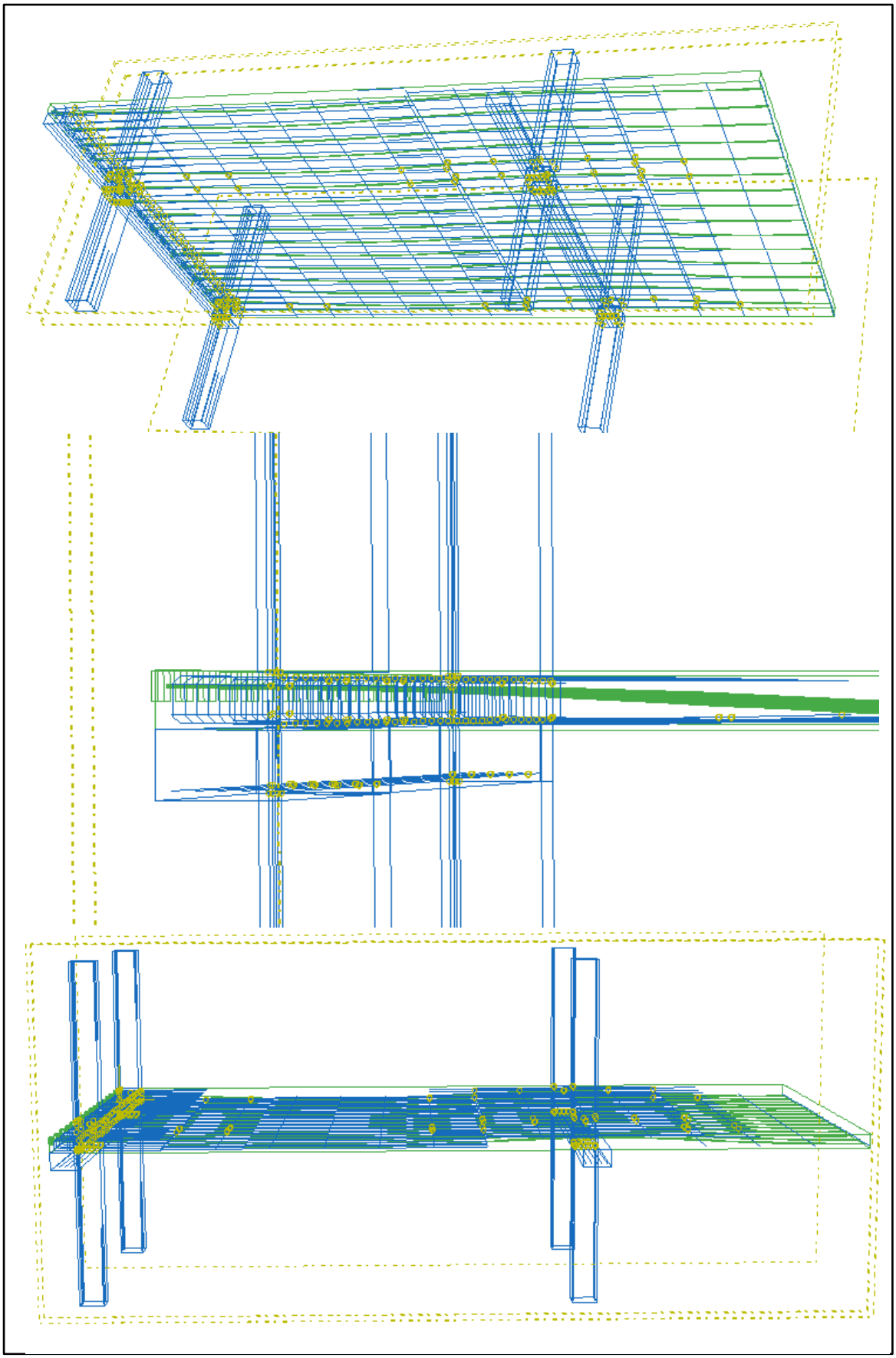

Figure 6-2; Additional reinforcement schematics throughout the structure section (three structural views)

As the models representing this structure will be large and require a relatively significant degree of computation, parametric studies are limited. This is further limited by time constraints regarding PhD completion. The previous UPT concrete slab models have provided an overview of the difference concrete cover and standard fire duration can make with respect to tendon temperature, particularly during cooling. The potential effect of the tendon temperature evolution during cooling on continued tendon stress relaxation and subsequent UPT slab deformation have been displayed. The aim now is to take a standardised case, and as previously described see how the slab behaviour relates to real behaviour. Therefore only one concrete cover has been modelled; a UPT concrete structure with 30mm of minimum concrete cover to tendons. The standard fire duration is taken as 120 minutes. Unfortunately however cooling could not be considered owing to numerical problems and insufficient time to find their solution. This is a major setback but the preceding UPT concrete slab models should give an idea of the likely continued structural behaviour post-fire within the forthcoming models. The fire is applied to a 6 metre by 6 metre square region on the base of the slab in the corner bay on the ground floor. Initially it was planned to model fires in numerous parts of the ground floor of the structure but sadly this has not been possible. Having outlined the structural details of the building the next section will detail the process of modelling such a building.

6.1 Model development

In order to reduce the size of the model only a quarter of the first floor (including ground and first floor columns) has been modelled using symmetry boundary conditions along the cut edges of the slab, beams and first floor column tops. The quarter ground and first floor cut model is displayed in Figure 6-3.

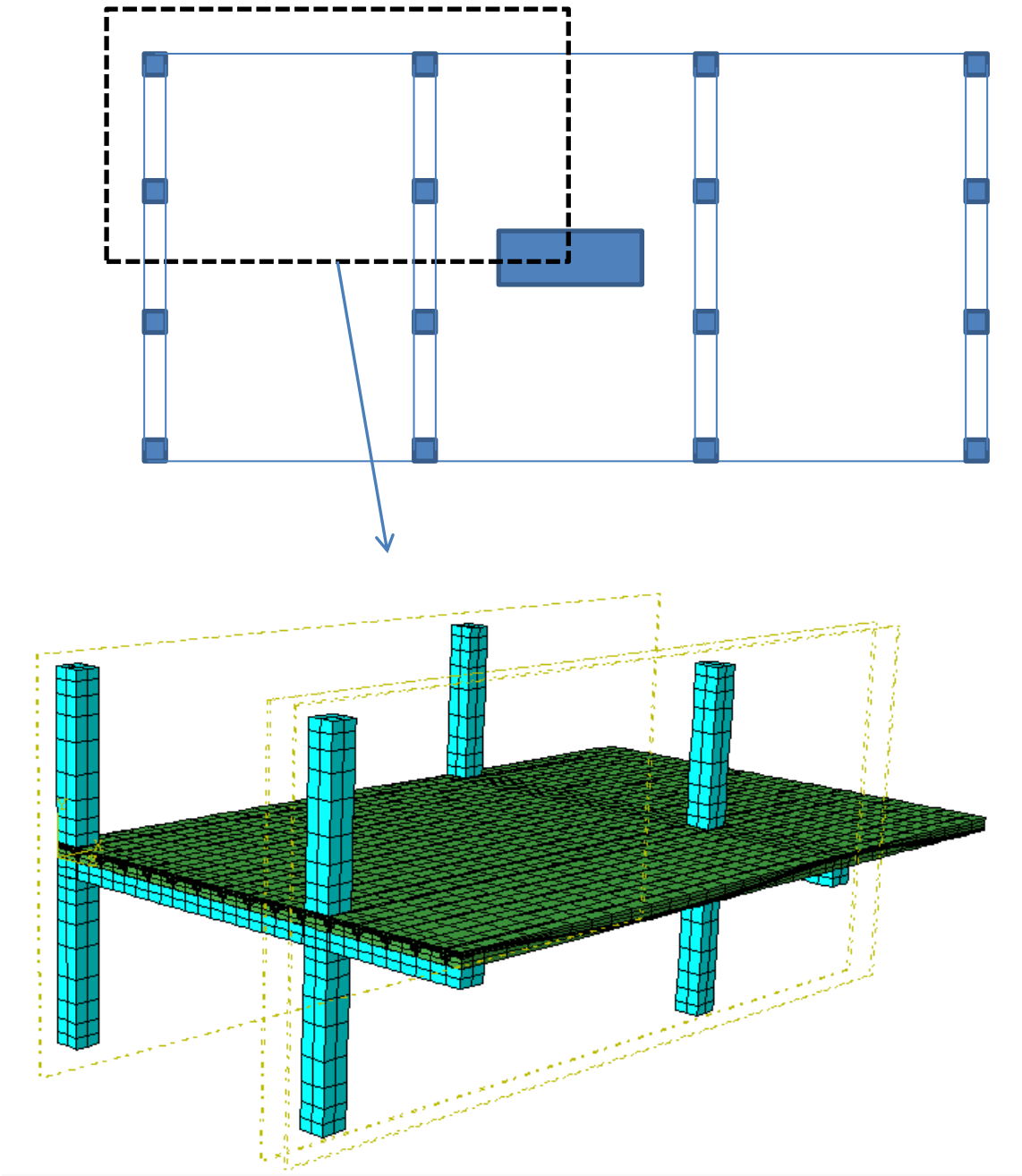

Figure 6-3; Modelled section of the structure

The column loads from upper levels are added as pressure loads on the top surface of each first floor column. It is assumed structural mass will dominate this column loading and as such individual

column loads are calculated according to the load/mass distribution scheme displayed in Figure 6-4. This load distribution is multiplied by the number of floors to approximate the load on each first floor column. The nodes lying on the cut column tops are thus allowed to displace vertically and rotate about the x-axis (longitudinal) and the z-axis (transverse). Column moments have not been calculated.

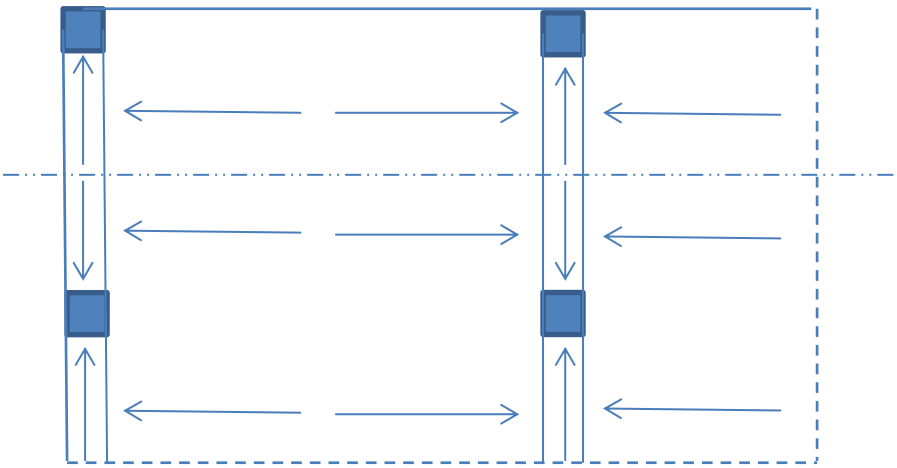

Figure 6-4; Floor mass distribution to columns

The central lift/stair core is not explicitly included within the model; instead the slab is modelled through the area the core should occupy and fixed in all degrees of freedom. This fixed area is illustrated in Figure 6-5.

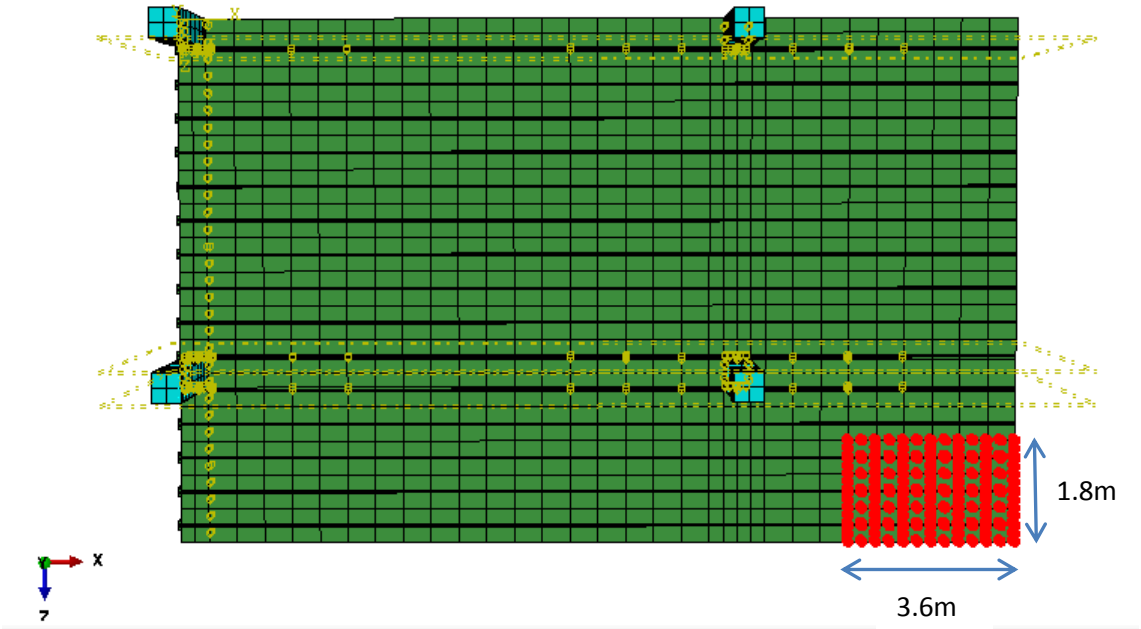

Figure 6-5; Fixed slab region representing central stiffening core.

As with the previous chapter, the slab is modelled using quadratic C3D20R reduced integration continuum elements with corresponding DC3D20 elements used for the heat transfer analysis. All other elements within beams, columns, tendons and anchors use linear C3D8R continuum elements and corresponding DC3D8 elements for the heat transfer analysis. Rebar is modelled using T3D2 truss elements embedded within relevant concrete host elements. The *embedded element* condition constrains nodes of the truss elements representing the rebar to the corresponding nearest plane of host element nodes. The truss elements thus stiffen the concrete continuum elements along their axis (truss element axis).

The nodal coordinates of the slab were generated within Excel in layers throughout the slab depth based around the chosen parabolic profile of the tendon. This parabolic profile is based around a minimum concrete cover of 30mm with points of contraflexure approximated using Matlab as described in the previous chapter, Section 5.1. The tendons pass through the slab mid-section at these points, with the gradient maintained from sagging to hogging; this allows the hogging concrete cover to be determined following a smooth continuous parabola. The slab nodal coordinates are then generated by filling in layers between the slab base and the tendon parabola line and again from the tendon parabola line and the top of the slab. Tendon ducts are created by defining nodes octagonal around tendon lines on a radius according to that of the tendon (15.7mm). These nodal coordinates are read from excel and listed in a text file in the form of an Abaqus input file using Matlab, within this process the slab elements are also defined. Tendon nodes and elements are also defined in this way with the input file imported into Abaqus cae where the beams, columns and rebar are defined and the structure assembled.

The fire as stated earlier is applied to a 6 metre by 6 metre square area on the base of the first floor slab (ground floor ceiling); this region is shown in Figure 6-6. This is applied as a boundary condition to the highlighted nodes in Figure 6-6. The temperatures used are determined through a simple slab model with base surface exposed to a 120 minute standard fire via convection and radiation with the sink temperature being the gas temperature corresponding to the standard fire curve. The nodal temperature evolution along the base of the simple slab forms the amplitude curves for heating and cooling referenced by the boundary condition applied to the nodes in Figure 6-6, within the full heat transfer model. The use of the standard fire temperature-time curve [31] with respect to the thermal gradients it creates within a slab was discussed in the previous chapter. The limitations in drawing comprehensive conclusions as to the behaviour of structures in fire during and post-fire were also discussed in the summary to Chapter 5 (Section 5.4). The use of alternative temperature-time curves relating to fire will have to wait for further study beyond this thesis. However, a main aim of this chapter is to observe whether the structural behaviour observed within the slab models of Chapter 5 are a concern in a realistic continuous structure. For example, will beam rotation and design code recommendations for rebar specification limit the consequences of the significant hogging damage noted in the previous slab models. Those models used standard fire temperature-time curves to heat the base of the slab and accordingly so should these initially.

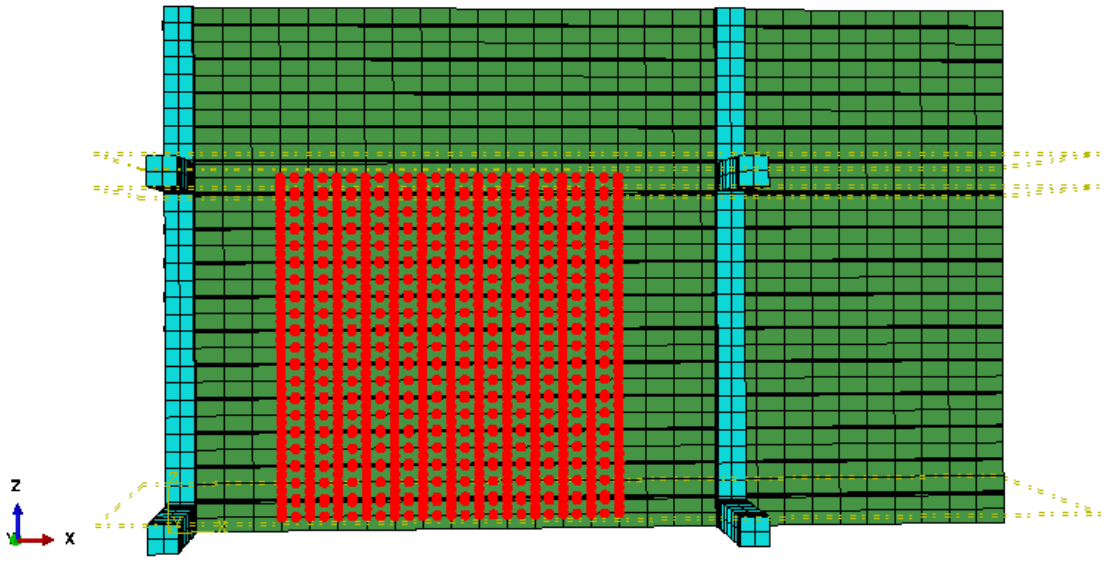

Figure 6-6; Heated ceiling nodes

Thermal and mechanical material properties are the same as those used in the previous slab models; these are listed in Appendix C for prestressing steel and Appendix D for concrete. LITS has again not been considered within the concrete material properties definition in the following continuous UPT concrete structural models, as with the UPT concrete slab models of the previous chapter. Mechanical properties including elastic modulus and inelastic yield curves with temperature for reinforcing steel are included in Appendix E, with other reinforcement properties being the same as those for prestressing steel. Tendons are tensioned using an *Initial Condition* of *type=stress*, tensioning the tendons to 1000MPa as with the slab models. Whilst the design load was taken from Eurocode 1 [31] the applied load has been taken as 3.75KN/m^2 applied across the entire surface of the continuous slab. Gravity is again treated as a body force and applies to the whole structure.

6.2 Heat transfer analysis

Figure 6-7 shows a temperature contour plot after a 120 minute standard fire applied to the ceiling of the ground floor of the modelled structure. Heat transfer horizontally from the heated region is negligible; within 0.25m the slab this goes from in excess of 1000^{o}C after a 120 minute standard fire to ambient. As such, the beams and columns are not exposed at all to elevated temperature within the model. This ensures that all ensuing mechanical behaviour is the direct result of elevated temperature tendon relaxation and concrete slab temperature exposure. Figure 6-8 shows the evolution of temperature throughout the slab depth when exposed to a 120 minute standard fire. As with the previous chapter, the moisture content of the concrete modelled has been taken as 1.5% by mass. The corresponding specific heat capacities are displayed in Table 11-5 and graphically represented in Figure 11-1. These values mean there is no significant kink in the temperature-time curves of Figure 6-8 as would be noted at higher moisture contents when the water boils and specific heat capacity spikes momentarily.

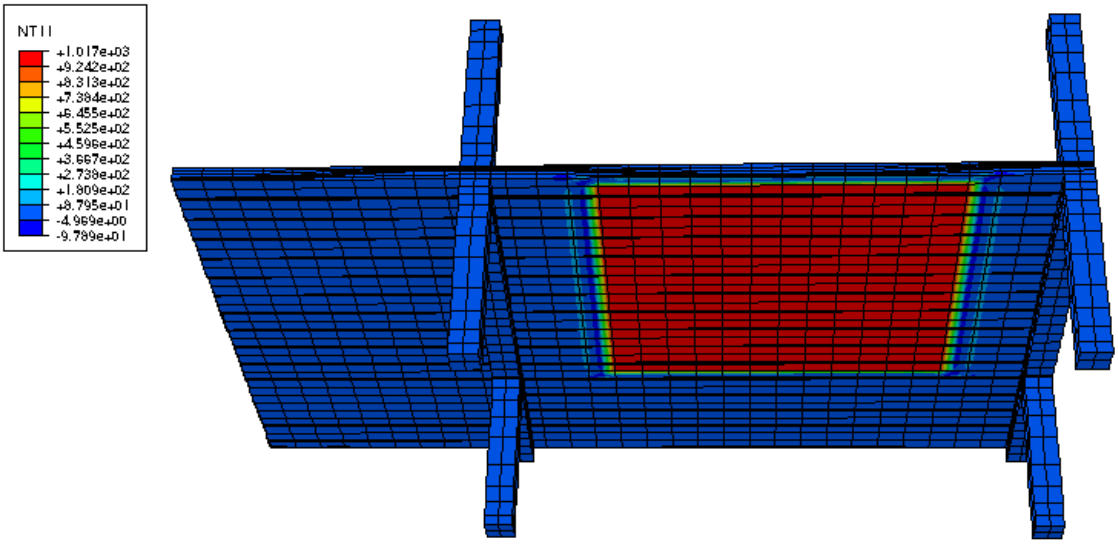

Figure 6-7; Temperature contour plot after a 120 minute standard fire applied to the ground floor ceiling.

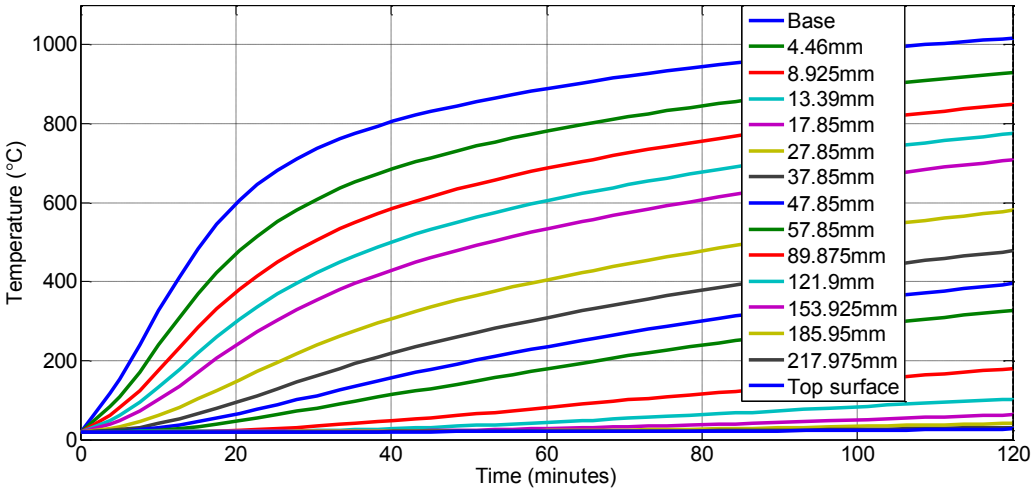

Figure 6-8; Slab temperature evolution with depth

Figure 6-9 shows the evolution of tendon temperature along its length from the point of minimum tendon cover to the edge of the heated region of the slab. As the tendon follows a parabolic profile tendon cover and thus temperature exposure decreases from the mid span outwards. A further impact of the combination of the heating area with regards to cooling (not modelled here) is the tendon temperature further from the mid span (the point of minimum cover) will continue to rise for a longer period of time post fire. Therefore there is the potential for continued creep induced tendon relaxation within a longer portion of the tendon if temperature is high enough. The longer the bay span the shallower the parabolic profile will be, also meaning an increased tendon length at lower concrete covers.

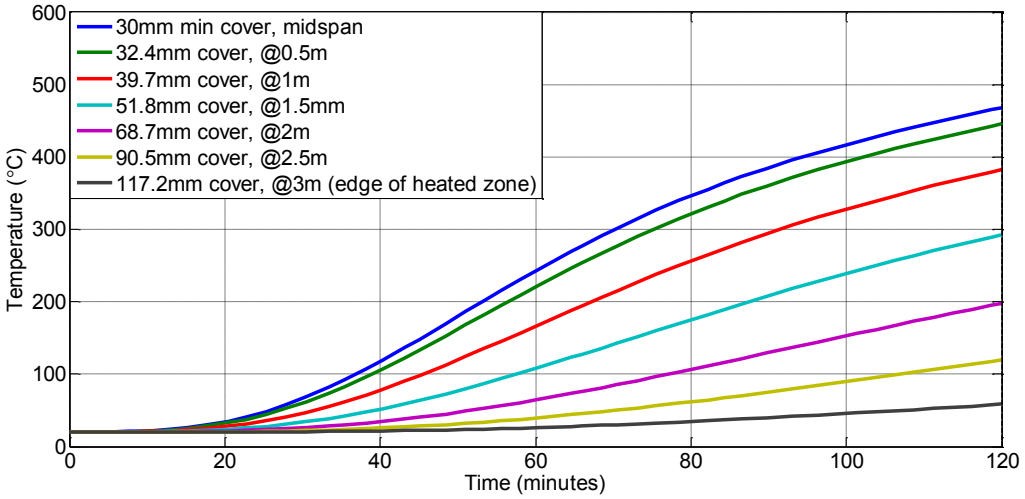

Figure 6-9; Tendon temperature evolution within heated region of the slab

Sagging reinforcement in both longitudinal and transverse directions within the heated corner bay is also exposed to elevated temperatures throughout the heated region. As such their tensile elastic capacity will drop should temperature be sufficient (Appendix E). Figure 6-10 shows the evolution of sagging rebar temperature within the heated region. This includes both 12mm diameter longitudinal rebar and 16mm diameter transverse rebar. These temperatures were taken from simple one-dimensional slab heat transfer models at depths corresponding to the rebar centres; rebar was not explicitly modelled within the heat transfer models (something that is not possible with rebar or truss elements). The temperature evolutions displayed below in Figure 6-10 are input as amplitude curves within the mechanical models to be referenced by heated rebar nodes at each time increment.

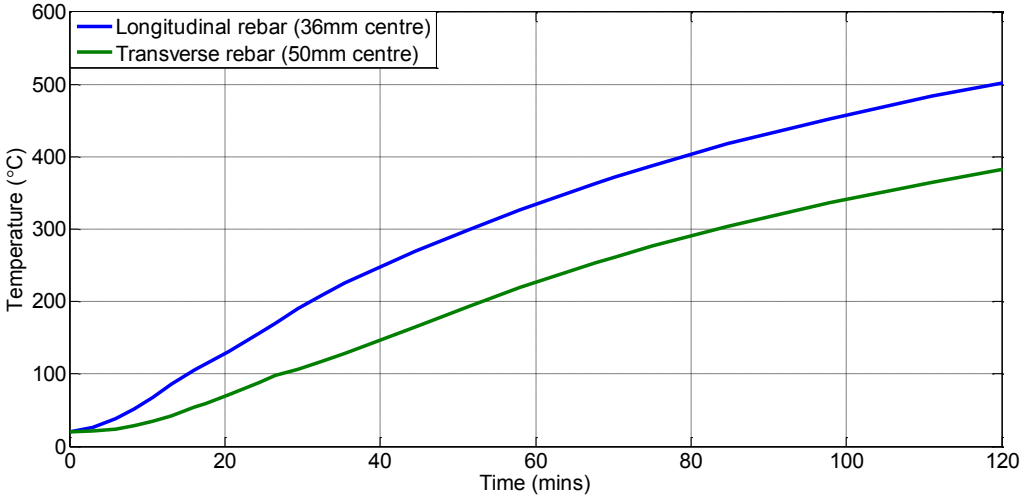

Figure 6-10; Sagging rebar temperature evolutions

6.3 Mechanical analysis

Within this section the results of the mechanical analysis are presented; within these models nodal temperature evolutions from the heat transfer analysis are used as input data. As stated in Section 6.1, material input data as a function of temperature can be viewed in Appendix C, Prestressing steel material parameters, and Appendix D; Concrete material parameters. The focus of this section is to elaborate on structural behavioural patterns observed in the Slab models of Chapter 5 through the consideration of realistic boundary conditions. In addition to this, cold span behaviour under relaxed tendon prestress resulting from fire in a different longitudinal bay of the same continuous span is a major concern with respect to fire in UPT concrete structures.

Figure 6-11 shows the deformation of the modelled section of the structure (Figure 6-3) after a 120 minute standard fire applied to a 6m by 6m square on the ceiling of the ground floor corner bay (Figure 6-6). When realistic boundary conditions are considered (where beams are allowed to bend and rotate as loads are transferred to the columns) the emergence of two way span behaviour is observed in the corner bay (as the slab begins to display transverse bending). This is partly due to bowing as thermal expansion is not restrained in the transverse direction, except by the colder regions of the slab depth towards the top surface. However the cold transverse bay also effectively becomes an additional beam as temperature rises in the heated bay, creating in effect a bay supported on three sides (note also the long edge base nodes are not heated, Figure 6-6).

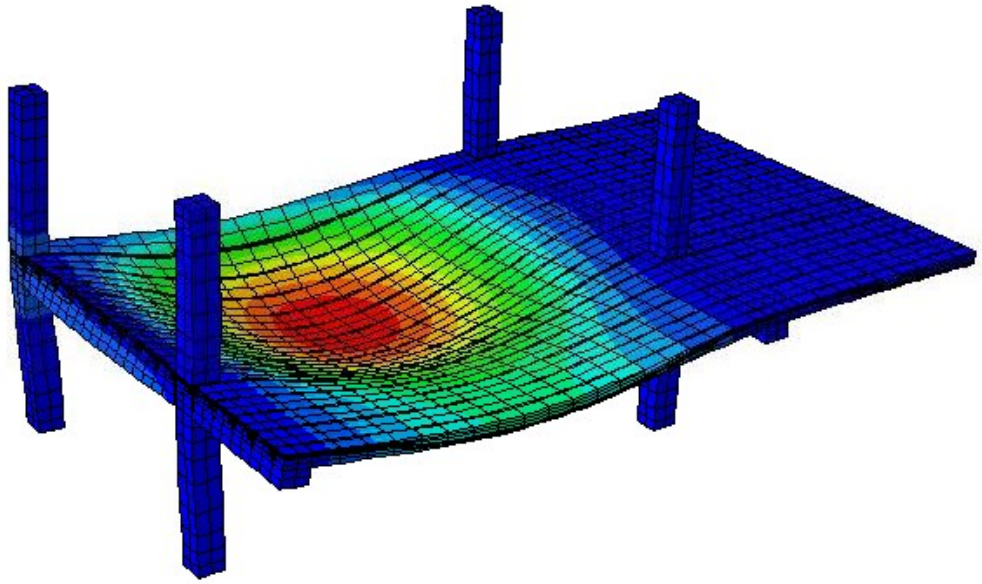

Figure 6-11; Deformation after a 120 minute standard fire in the corner ground floor bay

Figure 6-12 shows all maximum principal inelastic tensile strains throughout the modelled section of the one way structure after 120 minutes of standard fire exposure to the slab base. This is displayed as a series of arrows protruding from nodes throughout a transparent image of the model; the orientation of the double headed arrows indicates the orientation of the maximum principal inelastic tensile strain, with the colour indicating the magnitude. As has been noted previously the magnitude of principal inelastic tensile strain can be a useful indicator as to the degree of concrete

damage. Of equal importance is the orientation of the maximum principal tensile axis with respect to the global structural axis; this being indicative of the direction of plastic flow. Cracks would be expected normal to the maximum principal tensile direction.

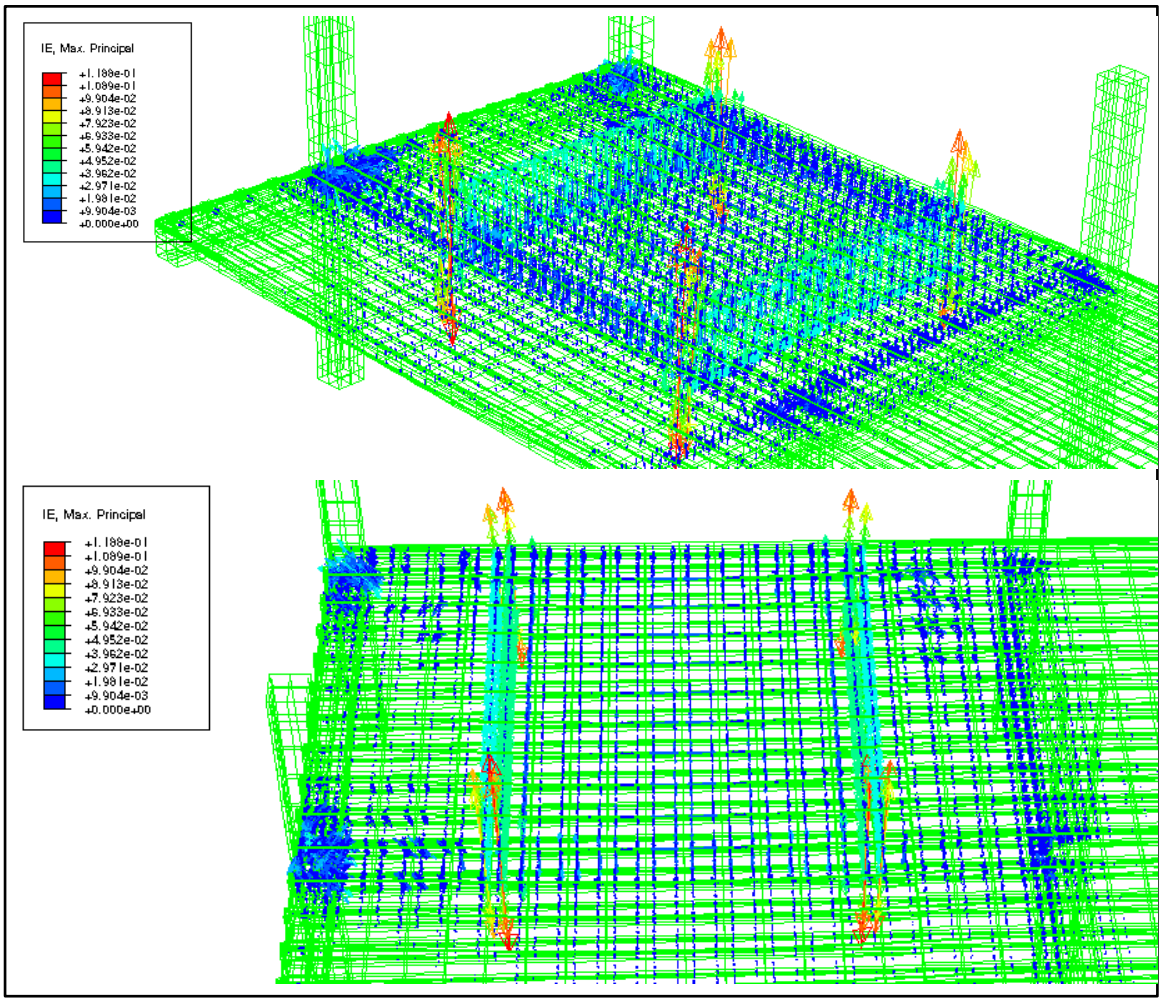

Figure 6-12; General view showing all maximum principal tensile strain. Notice action around anchors in vicinity of columns and through beams here.

The concentrations of arrows indicate regions of the slab where concrete damage should be expected. Figure 6-12 shows significant concentration of arrows about columns, particularly the edge columns of the main span. Arrows are also noticeable referring to hogging over the first internal beam support (in slightly greater concentration towards the internal column). The largest magnitudes of principal inelastic tensile strains are noted on the base of the slab near the four corners of the square heated region. These strains act laterally to the plane of the slab much like those noted on strips on the base of the slab models presented in Chapter 5. Such strips are clearly observable here in Figure 6-12; Figure 6-13 shows a clearer illustration highlighting these strains and others from the base of the slab. In these models, as opposed to the previous chapter, the emergence of two-way bending as heating evolves creates huge lateral inelastic tensile strains in the corners of the heated region. This implied significant damage would be expected here.

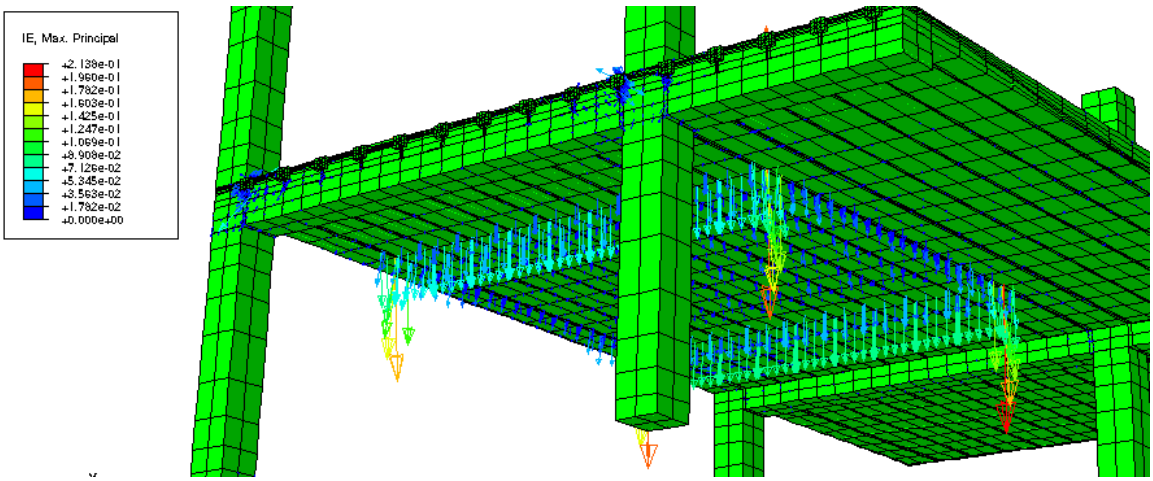

Figure 6-13; Tensile concrete damage accumulation on the base of the structure.

Figure 6-13 also shows smaller magnitude strips of induced lateral inelastic tensile strain in the longitudinal direction, again towards the edges of the heated region, with small lateral tensile inelastic strains relatively evenly distributed within these bounds across the entire heated region. This implies potential for concrete to fall off across the entire heated region but is highly likely in the corners.

The following sub sections focus on specific areas of damage highlighted in Figure 6-12 as well as trying to ascertain potential cold bay behaviour under relaxed tendon support. The first sub Section 6.3.1 deals with hogging damage observable in Figure 6-12 over the first internal beam support. This relates directly to concerns regarding the severe hogging damage observed in the slab models of Chapter 5 (Figure 5-14 and Figure 5-16) where hogging rebar was not included. Within this sub-section, slab deflection behaviour and tendon relaxation behaviour can be discussed as a matter of course. The actions noted within Section 6.3.1 influence longitudinal cold bay behaviour under reduced tendon prestress; this behaviour is subsequently analysed in Section 6.3.2. Following this the principal tensile strains observed in Figure 6-12 in the vicinity of the edge columns connecting to the edge beams and the slab are analysed and the resulting damage and possibly failure potential is discussed (Section 6.3.3). Finally the significant out of plane potential concrete damage highlighted in Figure 6-13, on the heated bay ceiling, is analysed in Section 6.3.4.The concerns arising in these analyses, limitations and suggestions for further study are summarised at the end of this chapter in Section 6.4.

6.3.1 Internal support hogging damage

Figure 5-14 and Figure 5-16 of Chapter 5 show significant tensile damage in hogging for an isolated slab, bonded to an imaginary beam fixed against rotation and lateral displacement. An end span beam is able to deflect and rotate to some degree, reducing the likely hood of such damage; this is of course dependent on the dimensions and design of the beam. However, over the first internal beam support, rotation of the beam may be restricted by the cold span on the other side, thus facilitating possible tensile hogging damage. This could be negated by the specification of hogging

rebar. As such design codes specify this inclusion and the considerations to be made in calculating the cross-sectional area of rebar required for a meter strip in the span direction. The models as detailed in Section 6.1 have been designed according to Eurocode 2 [32], and as such they contain an area of rebar through the slab cross section with sufficient factor of safety to theoretically prevent hogging failure. As shown in Figure 6-12, principal inelastic tensile strains have accumulated in this area of the model, hogging over the first internal beam. In order to analyse the significance of this it is necessary to examine the magnitude and direction of the principal inelastic tensile strains in the concrete and the tensile stress accumulated in the hogging rebar. Firstly however the degree of tendon relaxation and slab deflections in the respective bays is presented to illustrate the deformation behaviour of the continuous slab. Figure 6-14 displays the evolution of tendon stress for the modelled section of the structure for heating of the ground floor corner bay according to Figure 6-6.

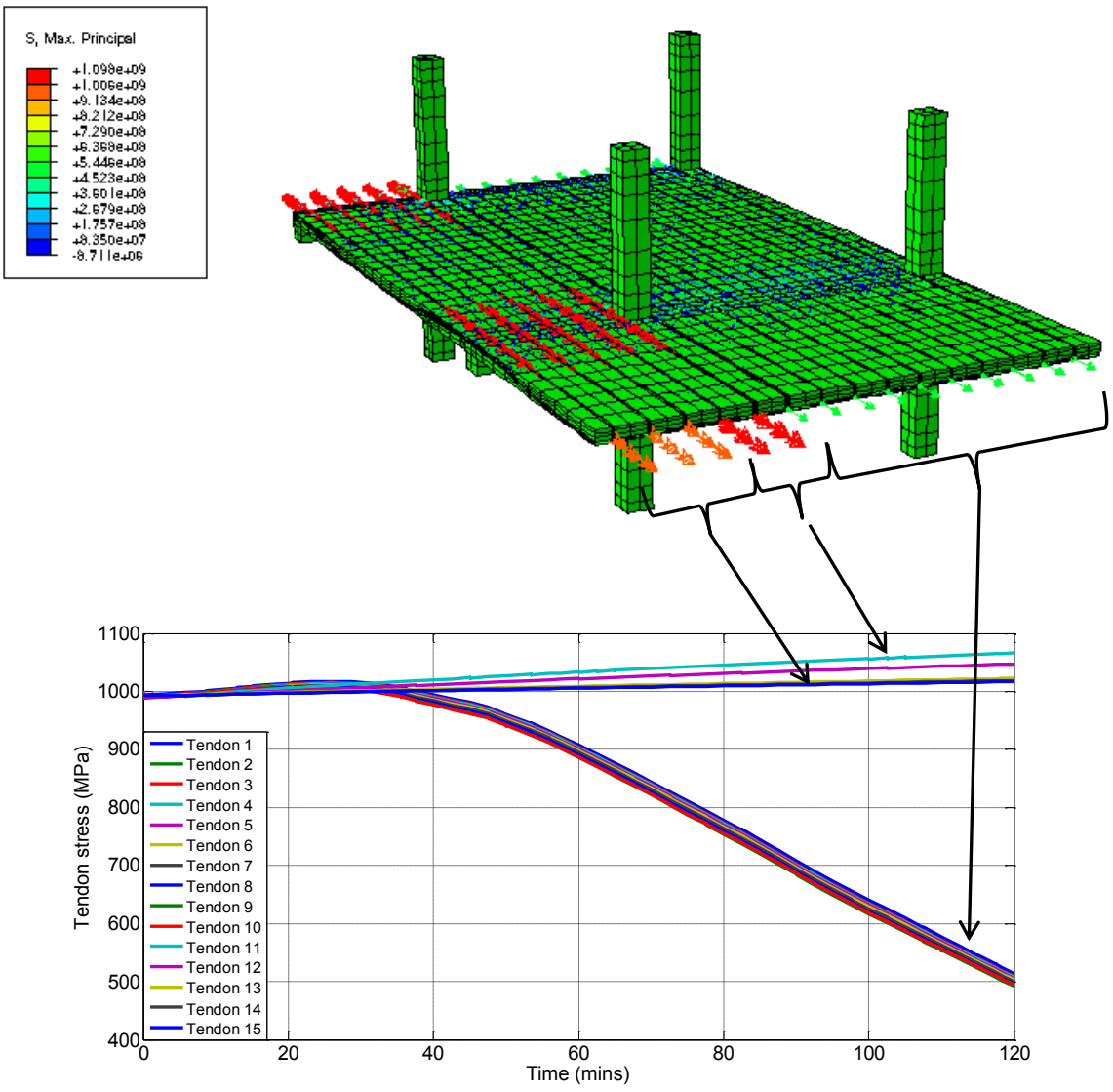

Figure 6-14; Tendon stress evolutions

Tendons exposed to elevated temperature relax by approximately 50% whilst cold tendons slightly increase in tension owing to increased deflection of the slab, effectively lengthening them. The small variation in relaxed stress of the heated tendons owes to the variation in deflection across the transverse span as shown in Figure 6-11. Figure 6-15 shows this structural deformation in more detail highlighting deflections at key points resulting from tendon relaxation and concrete thermal expansion effects. These thermal expansion effects manifest themselves as a result of various longitudinal, transverse and lateral restraint conditions imposed from the supports.

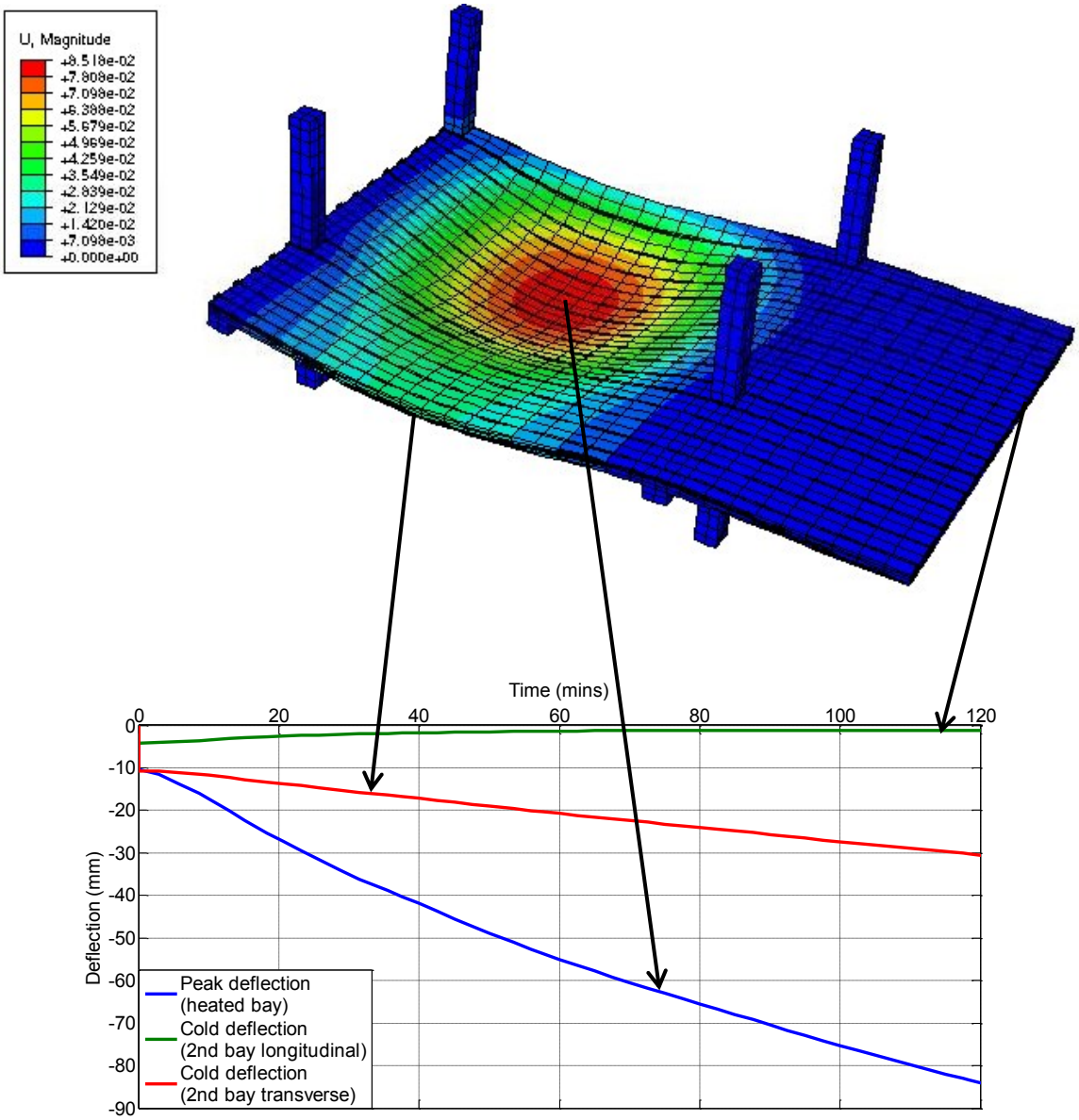

Figure 6-15; Deflection evolutions

Figure 6-15 clearly shows an induced deflection increase in the first transverse bay from the heated bay, hence the slight increase in cold tendon tension shown in Figure 6-14. It is however observed the deflection of the first longitudinal cold span actually decreases in magnitude. This implies that

hogging damage of concern from the slab models over this first internal support is either negligible and the concrete is still capable of transferring load in tension, or most likely the increased tensile load is taken largely by hogging rebar. This decrease in deflection is despite the 50% relaxation in tendon stress, implying significant tensile stress is transferred in hogging across the support from the increased deflection of the hot span, and the resulting moment across the beam. This creates an equivalent bowing action on the longitudinal cold span, increasing the length of the hogging zone over the internal beam and increasing the cross-section of the slab in compression. Figure 6-16 shows a contour plot highlighting an accumulation of inelastic strain in hogging prior to this support as well as a cut through the slab at this point. The cut reveals principal inelastic tensile strain arrows acting in the longitudinal span direction. This evolution of inelastic principal tensile strain is plotted alongside hogging rebar stress at the same location.

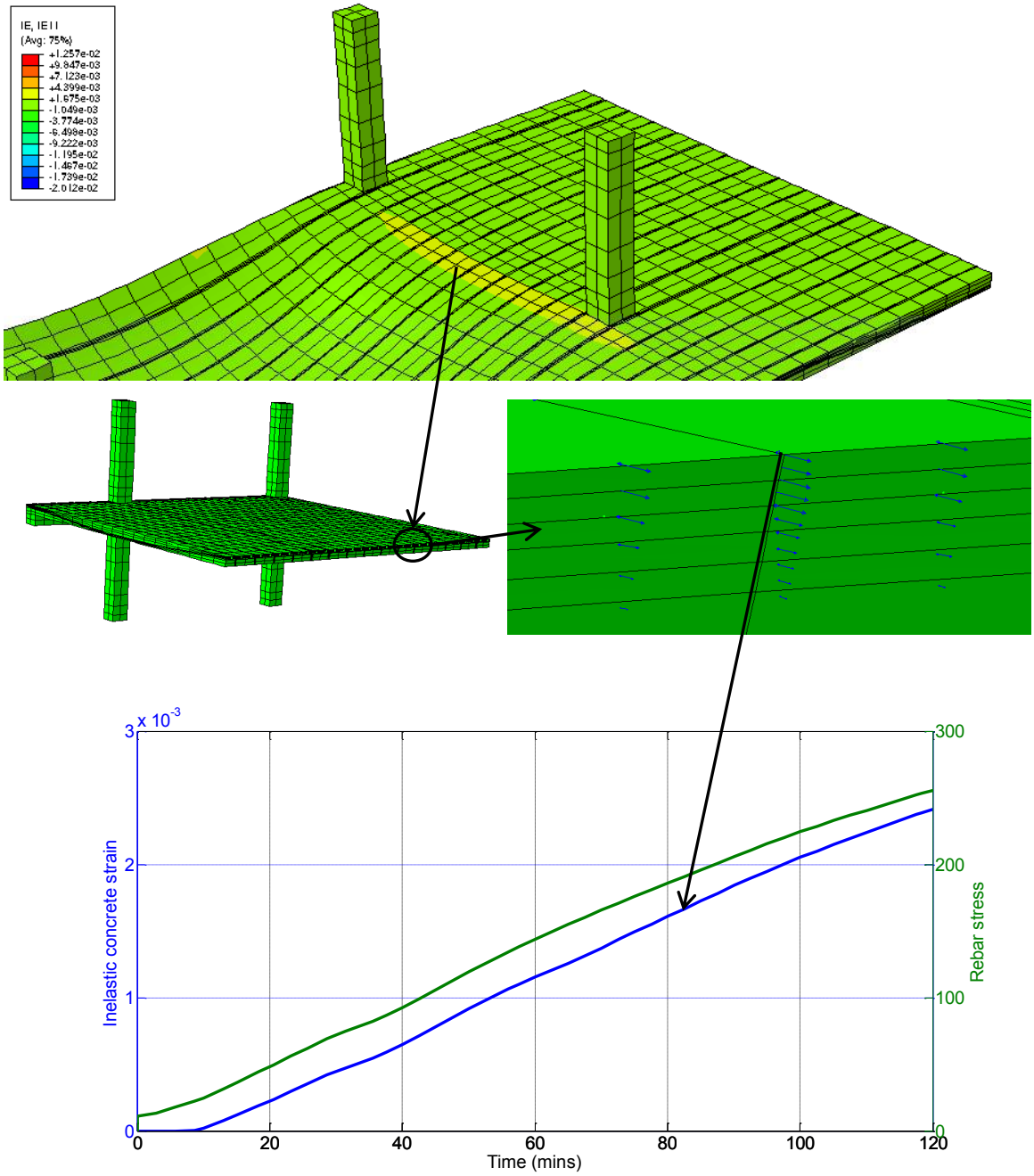

Figure 6-16; Maximum principal inelastic strain evolution (tensile) in concrete in hogging at cut with associated hogging rebar stress evolution (25mm cover to top surface)

The rebar stress evolution closely matches the concrete principal tensile strain evolution at the top surface, implying all tensile loads are being transferred in hogging across the support via the rebar. It is noted in Figure 6-16, the hogging rebar stress reaches just over 250MPa after a 120 minute standard fire. This is just over 50% of its 500MPa ambient yield stress as displayed in Table 12-2, Appendix E. The principal inelastic tensile strain may result in small concrete cracking normal to the principal direction; in this case normal to the longitudinal span direction. It is noted from Figure 6-16 principal inelastic tensile strain is first observed after 10 minutes of heating; this may imply the potential onset of cracking. The area of rebar specified per metre in the design is however clearly more than sufficient based on the tensile stress accumulated to take all tensile loads through this area in the event of concrete cracking. As a note of caution cooling has not been modelled here and

as observed in Chapter 5, Figure 5-29 and Figure 5-36, tendon relaxation, deflection and tensile damage can continue to increase significantly during the early stages of compartmental cooling. The rebar has been specified with a significant factor of safety as exemplified by it only being stressed to 50% of its capacity and thus should be capable of accommodating the continued increase in deflection and tensile stress. Should design codes be adequately followed, even considering the further evolution of damage during cooling, hogging failure over the first internal support should not be an issue based on the parametric study modelled, owing to the specification of adequate amounts hogging rebar. This however may not be the case for longer standard fire durations. The factor of safety with respect to hogging rebar specification, even accounting for increased hot span deflections when accounting explicitly for tendon creep, is particularly important in UPT concrete structures, given that in this modelled case the tendon stress has relaxed by 50% across the cold span. The resulting increase in compression induced across the cold cross section results from the increased counter rotation over the internal support which is only permitted by the adequate specification of the hogging rebar.

It must be considered however that although deflection decreased in the first longitudinal cold bay, the structural behaviour is no longer symmetrical owing to a fire in the corner bay. Cold longitudinal bays further removed from the heated bay will not be significantly influenced by the hogging action induced on the second bay by the heated bay and as such will have to resist the dead load in a normal bending manner with 50% of the original tensile tendon support.

Cold span behaviour with reduced prestressing tensile support from relaxed tendons is a major concern in UPT concrete structures exposed to fire. It is also one of the motivations for developing and analysing a large multiple bay model in this chapter. The following section presents data and analysis pertaining to cold span behaviour with relaxed tendon support.

6.3.2 Cold span behaviour subject to relaxed tendon tensile support

Within the global three bay structure of Figure 6-1 the hogging action over the first internal support influences the second span behaviour and in turn this influences the behaviour and rotation about the second internal beam support. It has been observed in Section 6.3.1 that the sufficient specification of rebar cross sectional area in hogging allows increased rotation of the first internal beam support extending the hogging zone of the second longitudinal span. As this span does not contain sagging rebar this may be of vital assistance given the tendon stress has reduced by 50% of its original value (Figure 6-14). The central deflection of this span decreases as a result (Figure 6-15). The third bay of this span of relaxed tendons (also a corner bay, Figure 6-1, Figure 6-3) however will not be directly assisted through this hogging action. In fact it is more likely the hogging action over the first internal support will induce a small counter rotation over the second internal beam support increasing the length of the sagging region in this span (and deflection).

In order to approximate this action on the second internal support and in order to determine possible third bay behaviour with 50% of the original prestress, an ambient model was subsequently performed on the identical symmetrical section of the structure, as in Figure 6-3. This model used a boundary condition at the cut slab face across the second longitudinal span restricting deflection to

1.3mm as shown after a 120 minute standard in Figure 6-15. Whilst it is noted the action about the second internal beam support will also influence the rotation about the first internal beam support it is assumed the first support action will dominate, and as such the cut deflection remains limited to 1.3mm in the ambient model. The tendons exposed to fire within the first bay were tensioned to 50% of the original 1000MPa used in the heated models (500MPa), corresponding to the average relaxed stress of those tendons after a 120 minute standard fire as shown in Figure 6-14. Non-heated tendons were stressed to 1000MPa as before. Figure 6-17 shows a deformation contour plot of the ground and first floor of the cold-quarter connecting longitudinally to the heated bay quarter of the structure.

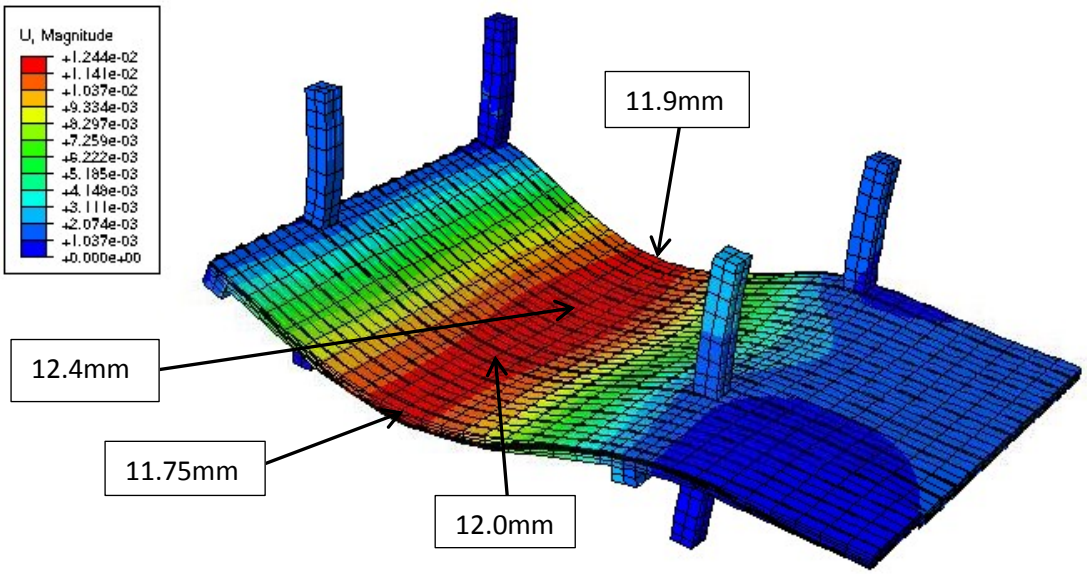

Figure 6-17; Third longitudinal bay deformation contour plot

Despite tendon stress across the edge bays being 50% of the original tensioned stress the cold quarter still behaves largely as if tendons were at full stress. The span barely deviates from total one way behaviour and only slightly larger deflections are noted in the bay supported by relaxed tendons. The sagging region of the cold corner span does increase slightly. The sufficient specification of hogging, sagging and transverse rebar clearly can accommodate the increased respective tensile stress and strain distributed to them as the tendons relax. As such they allow load redistribution to fully supported cold areas of the continuous floor slab and duly to the supports. The effect of the modelled fixed region, representing a stabilising elevator or stair core must also be considered and its effect on the action about the internal support. As such it may be necessary to consider structures with an increased number of longitudinal and transverse bays to consider the effect where a central stabilising core is a few bays further removed. In such structures there may however exist corner stair wells within a concrete core.

As has been previously stated should sufficient tendon numbers be used it is possible to design such that additional sagging reinforcement is not required. Additional reinforcement is only specified should there be a deficit with respect to the ultimate moment capacity of the UPT span with respect to maximum imposed moment. The one-way spanning model within this chapter has been designed such that no additional sagging reinforcement is required beyond the tendons in the internal span. With respect to this model this does not create concern when tendon stress is reduced by 50%,

owing to the hogging action over the first internal support. In addition the proximity of the central stabilising elevator/stair core provides support from a transverse direction assisted by transverse rebar and limiting potential deflection of this span. Therefore from the models of this chapter it cannot be certain in a larger bay structure, both longitudinally and transversely, how a bay without additional sagging reinforcement will behave further removed from a stabilising core. In order to visualise this, ambient models have also been developed and performed without a stabilising core, thus allowing the central bay to deflect fully. Figure 6-18 shows a contour plot of such a model with approximate deflections annotated; again tendons spanning longitudinally in the edge span are tensioned to 500MPa, this being the approximate relaxed stress after a 120 minute standard fire.

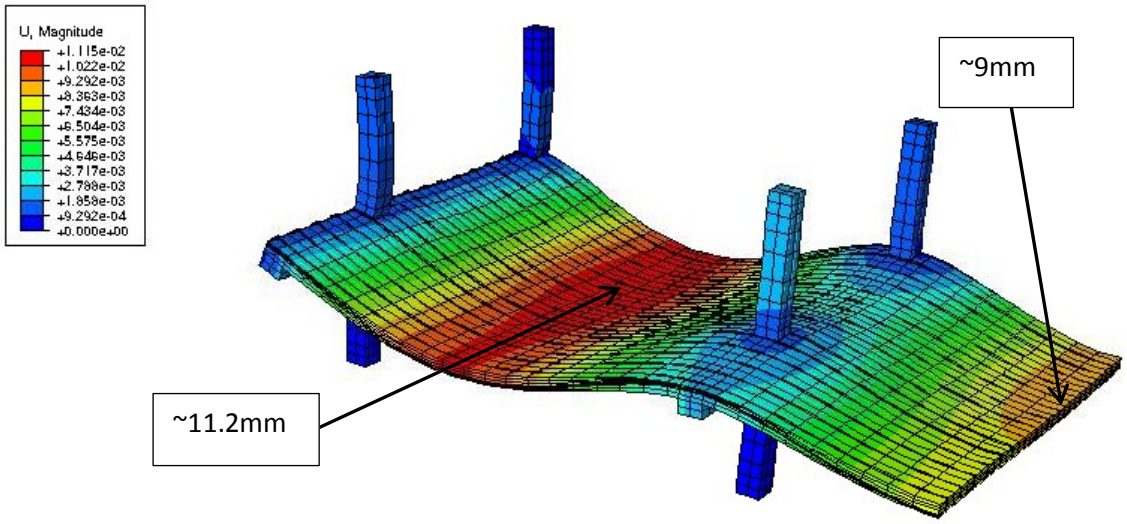

Figure 6-18; Cold model without a stabilising core.

The greatest deflection is still noted in the end span due to the edge beam rotation. This means over the internal support, a slight counter rotation is induced, marginally extending the hogging region of the middle bay. As noted at the end of the first paragraph of this sub-section, the end span deflection has reduced when the internal span has been allowed to deflect, owing to reduced rotation about the internal beam. The evidence of this sub-section and Section 6.3.1 suggest that design codes provide a significant enough factor of safety to allow for considerable tendon relaxation in cold regions. If design codes are adequately followed, a sufficient specification of hogging rebar in particular, as well as transverse rebar should prevent any significant cold span failure despite relaxed tendon support. However cooling has not been considered which conceivably, from Figure 5-29, could contribute to an extra 200MPa of relaxed tendon prestress in a slow bay cooling case. Figure 6-19 shows an ambient temperature model with the edge span tendons in the longitudinal direction tensioned to 300MPa, corresponding to the approximate minimum relaxed tendon stress achieved after 47 minutes of bay cooling from a 120 minute standard fire.

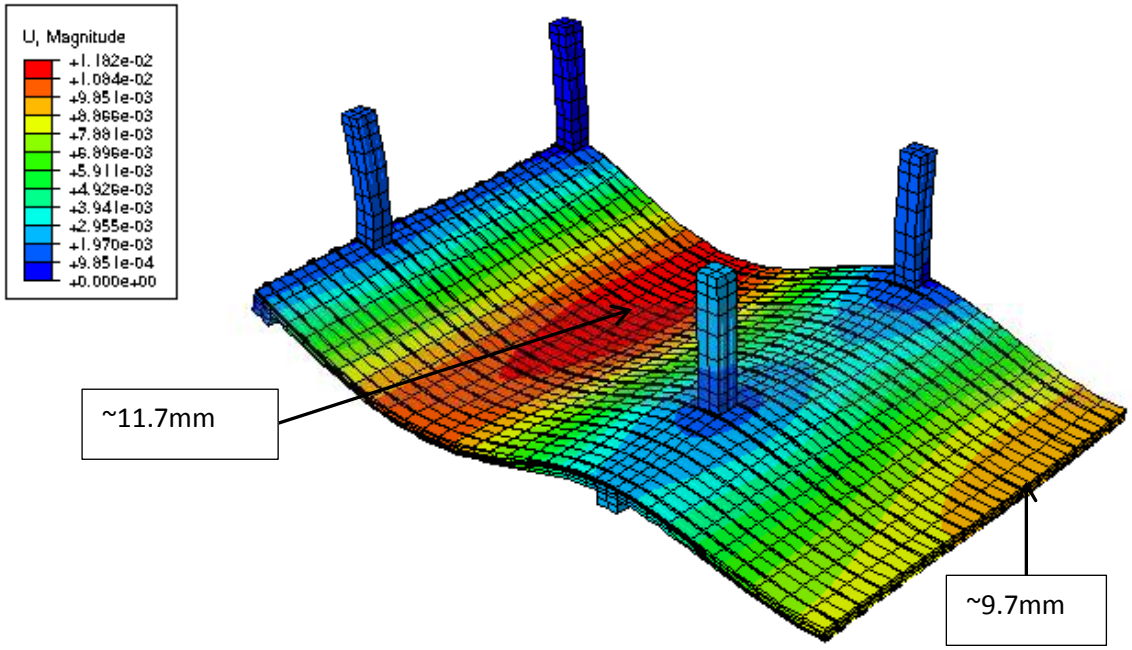

Figure 6-19; Cold model without a stabilising core and maximum tendon relaxation achieved during cooling from a 120 minute standard fire

Figure 6-19 shows a slight increase in deflection of the cold corner span with respect to the cold fully stressed span adjacent. In this case the relaxed tendons are at 300MPa, whilst the tendons in the adjacent span are at 1000MPa. The deflections as a result are still not significantly greater in the regions containing relaxed tendons than they were 47 minutes earlier at the end of the 120 minute standard fire, when tendon stress had relaxed to 500MPa. These deflections are also not significantly greater than the ambient deflection at full prestress shown earlier in Figure 6-15 (10.35mm). The cold transverse spans adjacent, with fully post-tensioned tendons therefore re able to assist the spans subject to reduced prestress. In part this is due to the transverse rebar extending into these regions being able to act as a tensile membrane as a degree of two-way spanning behaviour emerges. It is worth noting that damage to the concrete does occur in the corner bay of the relaxed cold span about the columns, in the same manner as in the hot corner bay but principal tensile strains are between one and two orders of magnitude smaller. These are observed in all the ambient models presented above (Figure 6-17, Figure 6-18 and Figure 6-19). Failure would then occur first in the heated bay around these edge columns but it is worth noting damage may also occur in the corner bay relaxed cold span in the same locations. In general however should design codes, in this case Eurocode 2 be followed there will be sufficient redundancy through hogging and transverse rebar, as well as stabilising cores, to prevent induced cold region failure as a tendon relaxation resulting from fire elsewhere in the structure.

6.3.3 Edge column damage

As stated in the introduction to the mechanical analysis Section 6.3 and displayed in Figure 6-12 there is a significant concentration of principal inelastic tensile strain about the structure end columns of the heated corner bay. This implies the potential for significant damage to occur in these

localities. Figure 6-20 shows a cut through the slab normal to the longitudinal span about the columns highlighting large principal inelastic tensile strains and their orientation (a large threshold was chosen to filter out smaller strain arrows masking the critical behaviour).

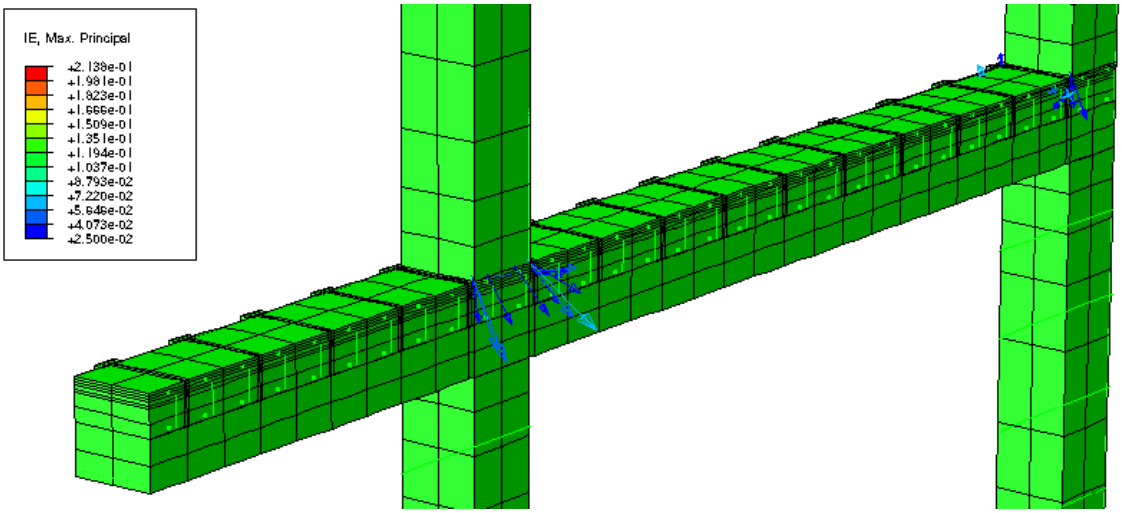

Figure 6-20; Cut showing only large principal inelastic tensile strains between edge columns and slab

Figure 6-21 shows side and plan views of the internal edge column to further illustrate the directions of these large principal inelastic tensile strain actions on the column. Through both Figure 6-20 and Figure 6-21 it is clearly observed large magnitude inelastic principal tensile strains of the order 0.03 to 0.05 are acting diagonally where the column contacts the slab top surface. As these strains do not match the normal span plane directions there must be shear strains acting on the cut vertical plane normal to the span direction.

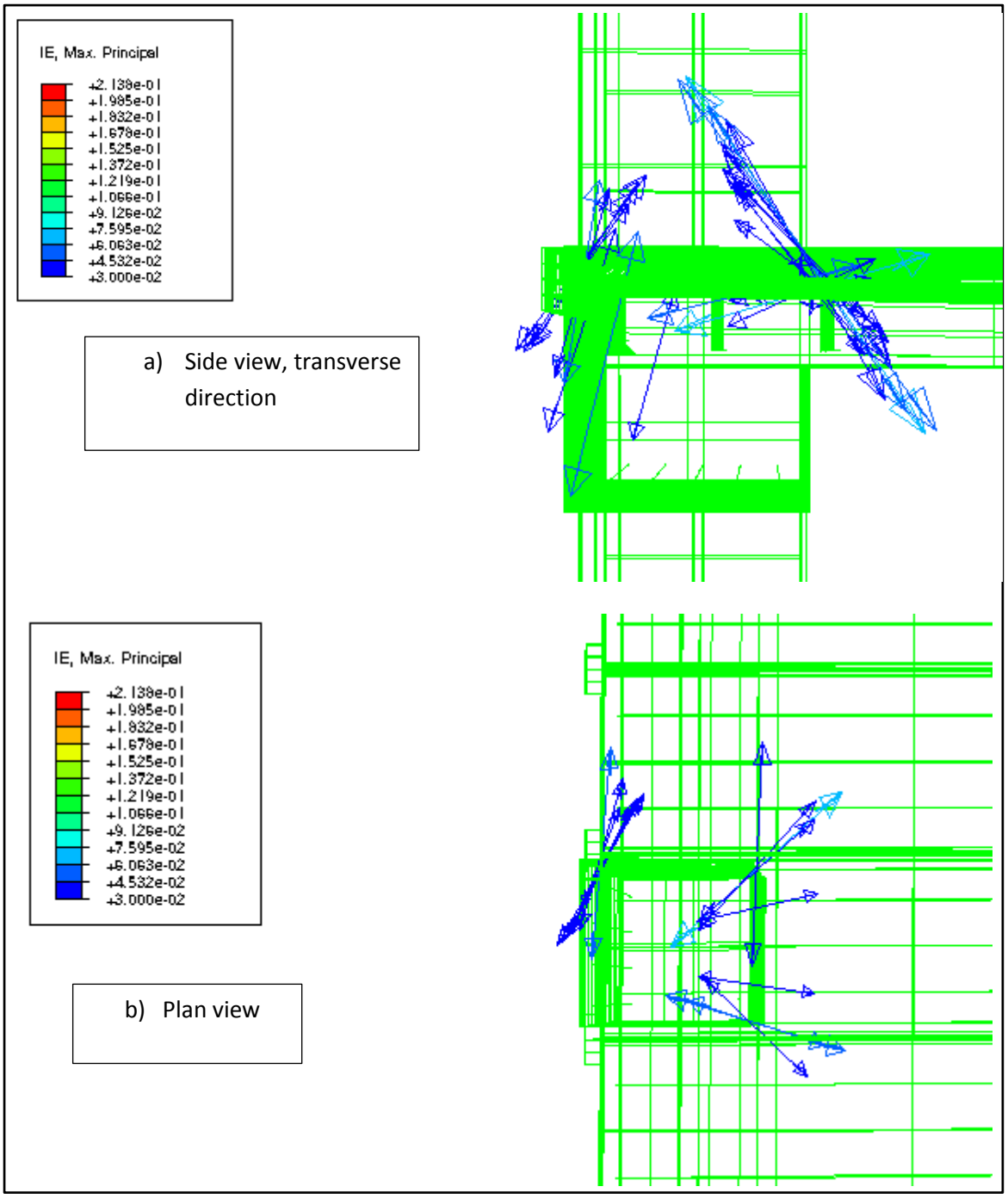

Figure 6-21; Internal edge column maximum principal tensile strains; a) side transverse view b) plan view

Figure 6-22 shows shear stresses do indeed exist on the cut column-slab section normal to the span, highlighting shear stress at five nodal points where the top of the slab contacts the column. Shear stress exists at these points prior to a fire in the bay as displayed by the zero time-stress intercept.

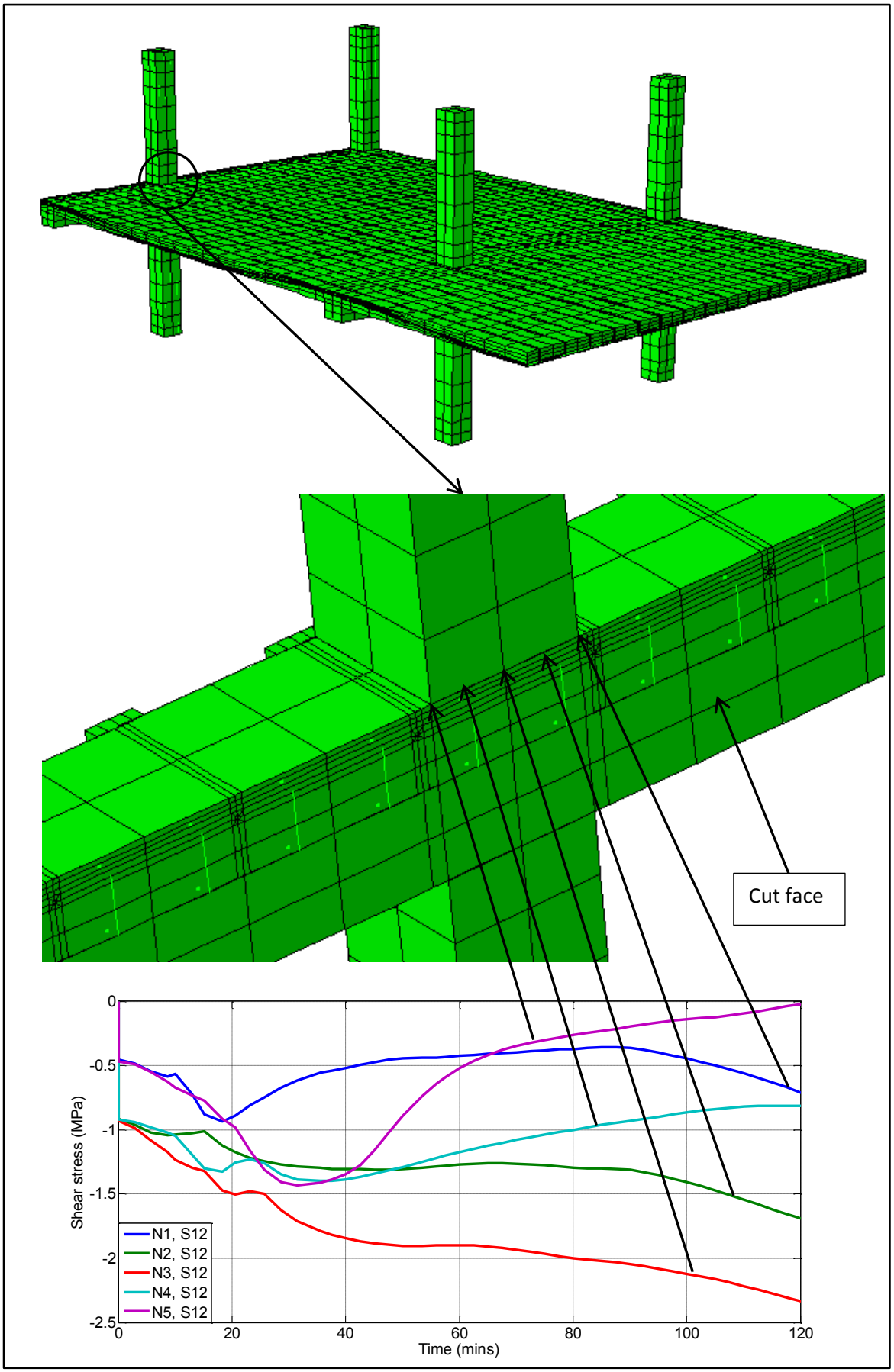

Figure 6-22; Shear stresses on top of vertical cut plane normal to span direction

Figure 6-23 shows the evolution of the diagonally acting maximum principal inelastic tensile strains at the same five nodal points as in Figure 6-22. Alongside this, inelastic strains normal, transverse and lateral to the span direction are displayed and noticeably smaller in magnitude than the maximum principal strains.

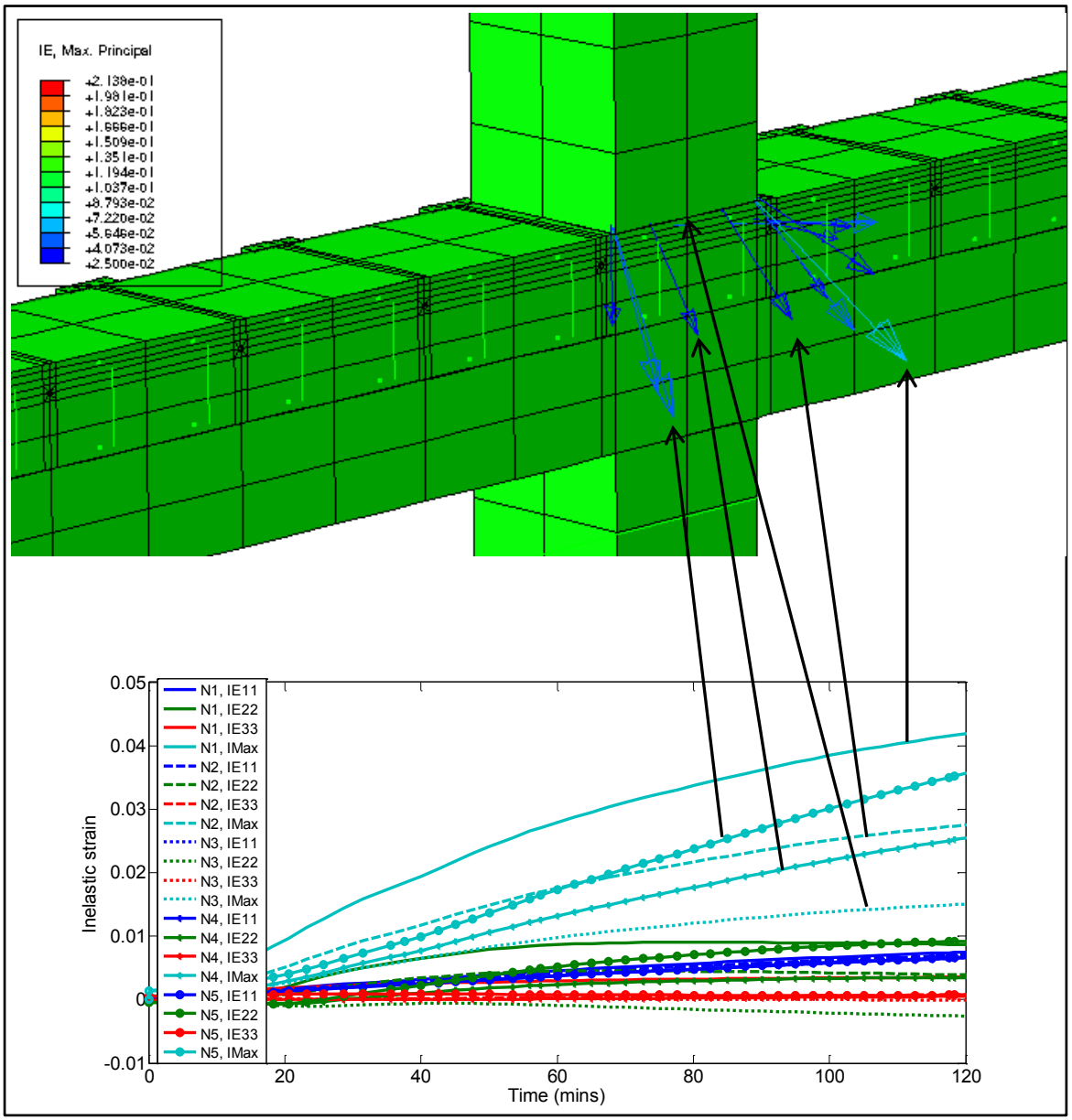

Figure 6-23; Principal inelastic tensile strain evolution at top of vertical cut plane normal to span direction

Figure 6-23 implies the possibility of concrete cracking normal to the direction of the principal inelastic tensile strains. These cracks therefore will be diagonal with respect to the span normal. Bursting rebar would however be included in structural design throughout this region providing tensile support to the concrete in longitudinal, transverse and lateral directions. Whilst bursting rebar is present in these models it can only constrain concrete displacement due to tensile stress, as ideal plasticity has been assumed with respect to tensile concrete behaviour. Maximum principal inelastic tensile strain behaviour is displayed about the corner column of the heated bay and ground floor of the whole structure in Figure 6-24. This shows the normal inelastic strains as well as the

maximum inelastic tensile strain magnitude evolution and direction from the corner node where the slab contacts the column.

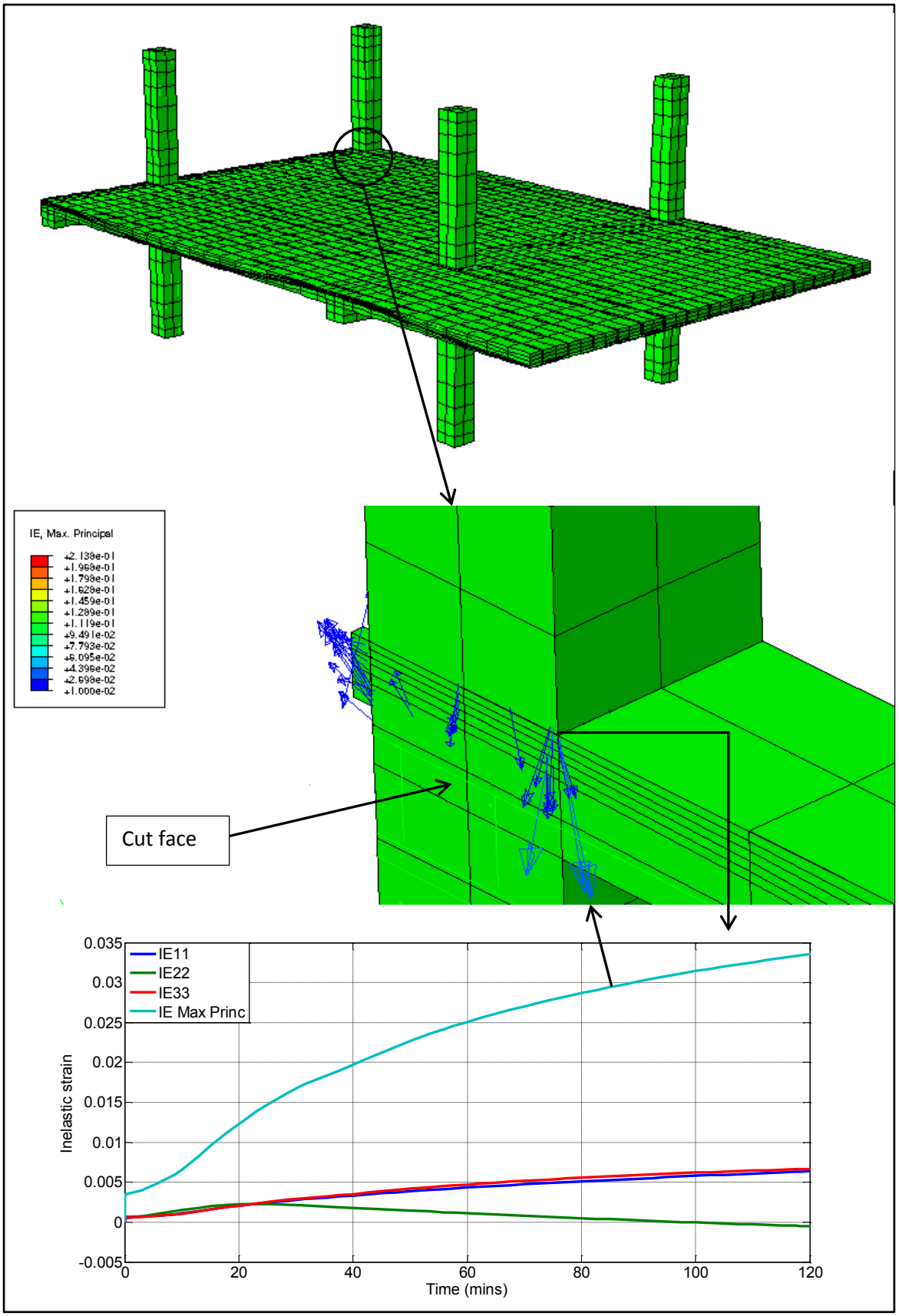

Figure 6-24; Corner column principal inelastic tensile strain directions and evolutions

As the maximum principal inelastic tensile strain is of far greater magnitude and oriented at an angle to structural normal inelastic strain magnitudes and directions, there again exists shear strains on vertical planes normal to the longitudinal and transverse span directions.

Often failure in concrete structures about columns, particularly in two-way spanning structures is labelled as shear failure, it is apparent from these models that shear stresses are present in the concrete slab about columns. However in these cases they are relatively small compared to ambient concrete compressive yield stresses, and from Figure 6-22, are nearer to the magnitudes associated to tensile yield. In order to reach the yield surface along the shear meridian it would be expected shear stress should be somewhat larger than is observed in Figure 6-22. Whether yield is reached on the shear meridian or tensile meridian however the direction of plastic flow is non-associated to the yield surface. As such the orientation of cracks and failure should follow the direction of maximum principal inelastic tensile strain; crack surfaces being most likely normal to this direction.

6.3.4 Vertical out of plane damage on the base of the heated corner bay

In Section 5.3.1.2 the emergence of a region on the base of the heated slab models showing significant out-of-plane tensile strain was described. These ‘strips’ also emerge in the one-way continuous quarter structure models of this chapter. However; owing to the support conditions and localised heated region, the induced two way spanning behaviour within the heated corner bay creates an amplified response towards the corners of the square heated zone. Figure 6-25 shows the region where large out of plane inelastic tensile strains are induced (in blue). These, in the longitudinal direction of the span are, as with the slab models, centred approximately 0.5m from the edge of the heated zone (illustrated by dotted lines). It should be noted again, as with the slab models previously, small inelastic lateral tensile strains exist right across the heated region (see Figure 6-13), but are substantially larger within these strips. These regions also extend somewhat towards the centre of the longitudinal heated span at the edges of the heated transverse span.

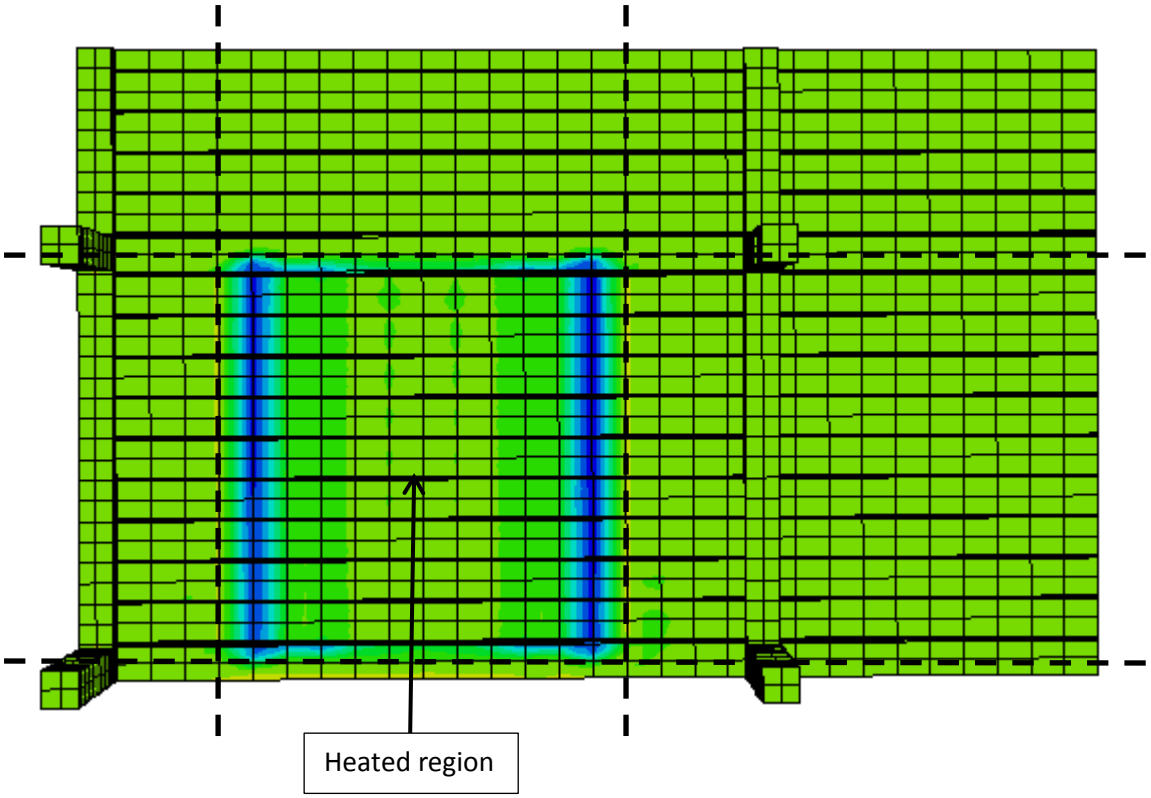

Figure 6-25; Large induced lateral tensile strain zones on base of heated bay ceiling

At the corners of the heated region within these strips shown in Figure 6-25 the out-of-plane vertical response is significantly amplified (despite being already substantial). Figure 6-26 confirms the maximum principal inelastic tensile stress directions illustrating the increased magnitudes at the corners of the yield strips. Longitudinal, transverse and out-of-plane inelastic strains are plotted for the corner displaying the highest tensile strain magnitudes, maximum principal tensile strain is plotted alongside. Longitudinal, transverse and out of plane normal stress, as well as Von Mises and equivalent hydrostatic stress are also plotted.

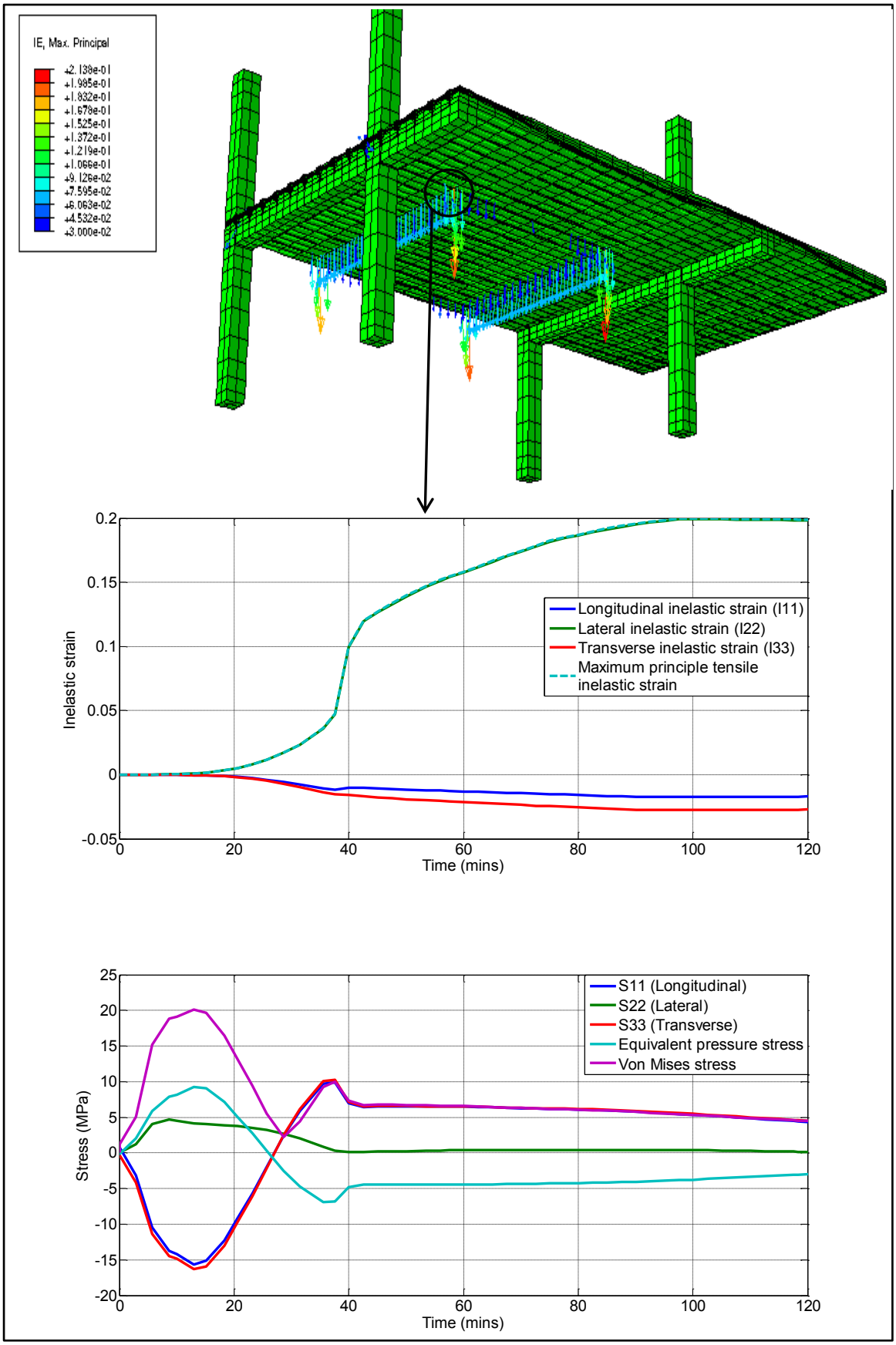

Figure 6-26; Maximum principal inelastic tensile strain evolution and stress evolutions on the slab base

Figure 6-26 displays the same trends as observed in Section 5.3.1.2, Figure 5-19 and Figure 5-20. It again confirms the maximum inelastic principal tensile strain is in the vertical out-of-plane direction, implying significant potential for cracks to form in the slab plane, in close proximity to the base. There is a very rapid rise from approximately 38 minutes to 40 minutes in out of plane tensile strain when the out-of-plane tensile stress reaches zero. Out-of-plane inelastic tensile strains (aligning with maximum principal inelastic tensile strain) are first observed around seven minutes. It may be concluded from the plots of Figure 6-26 that the concrete yield state is met relatively early during heating at this point on the slab base. The yield stress state then evolves towards total brittle tensile failure as the three normal stresses become tensile.

The depth to which the vertical out-of-plane tensile inelastic strains are observed extends from the base of the slab to approximately 20 to 30 mm into the slab. Figure 6-27 shows normal inelastic strain and maximum principal inelastic strain at nodal points from the base of the slab (where Figure 6-26 data is taken) and 19.6mm, 39.2mm, 58.8mm and 78.4mm vertically into the slab. Large tensile inelastic strains normal to the base of the slab are present at 19.6mm as well as on the base; again this corresponds to the maximum principal inelastic tensile strain. At 39.2mm from the base the lateral inelastic strain becomes compressive.

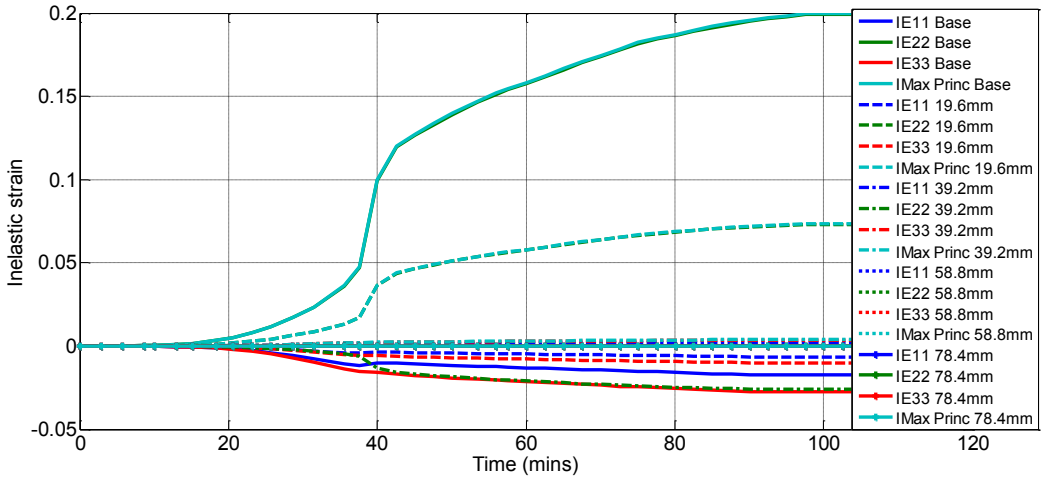

Figure 6-27; Inelastic strains with depth

Significant magnitude out of plane inelastic tensile strains are also observed all along the strips displayed in Figure 6-25 and Figure 6-26 to a similar depth. The data from these strips again matching the trends of Section 5.3.1.2, Figure 5-19 and Figure 5-20.

As has been observed, these regions of large out of plane inelastic tensile strain observed in both isolated slab models and the continuous bay one-way structural model of this chapter are located 0.5m from the edge of the slab base heated zones. These zones however are square with a clearly defined boundary between hot and ambient temperature exposure where heat transfer in-plane is negligible. As such the interaction of restrained thermal expansion and load induced deflection creates these clearly defined ‘resonant’ out of plane behavioural regions in precise areas through the Poisson effect. A realistic fire situation rather obviously will not be so uniform in terms of temperature profile and hot-cold boundaries in the slab-plane. As such the interaction of restrained thermal expansion and load induced deflection will not be clearly defined. This type of out-of-plane

behaviour in terms of location and magnitude will then be highly dependent on the heated region and in-plane thermal gradients. However, it may be less likely to observe such behaviour in a full bay fire. The 'strips' of out of plane behaviour observed in the slab and one way structural models in such a case will be located in very close proximity to the supports. In such cases it is possible this behaviour will be masked as support failure and likely significantly contributes to this type of failure.

The need to consider alternative fire temperature-time curves within FE UPT concrete slab models was summarised at the end of Chapter 5. The aim here would be to view the effect of different thermal gradients throughout the slab on tendon temperature evolution post-fire, and associated structural consequences. It would also be beneficial in understanding structural fire behaviour of general reinforced concrete (RC) buildings to undertake more modelling studies with varying heated regions within a bay. This would include full bay heating and circular or irregular heated zones on the base of a bay ceiling. The use of quadratic continuum elements assists in the observance of out-of-plane behaviour resulting from a combination of support conditions, restrained thermal expansion and slab loading. As stated in the introduction to this thesis it is difficult to truly understand (as opposed to hoping to quantify) such phenomenon as punching shear or spalling when the only approach is from the direction of large scale tests. The combination of modelling and material testing with such large scale modelling however provides three directions each capable of informing each other to truly assist understanding. The yield criteria for example used in metals and concrete is mathematically formulated about data from material experiment ([33] [34]). Therefore principal stress directions should not be dismissed in understanding or predicting concrete cracking behaviour.

6.4 Summary

Two concerns arising from Chapter 5 were the significant build-up of longitudinal inelastic tensile strains within the hogging region of the isolated UPT concrete slabs and the lack of consideration of continuous cold-span behaviour subject to reduced prestress. This chapter has addressed these concerns. Firstly it has been shown, Eurocode 2 [1] [32] guidelines specify sufficient hogging rebar over the first internal support to be able to accommodate the increase in hogging tensile stress across the beam resulting from the increased deflection of the heated bay. Chapter 5 however showed inelastic strain in this region can increase significantly during the early stages of compartment cooling (Figure 5-31 to Figure 5-37). However, after a 120 minute standard fire the hogging rebar specified within the parametric study modelled in this chapter had barely reached 50% of its elastic load capacity (Figure 6-16, Appendix E-Table 12-2). This implies there is sufficient factor of safety to accommodate the continued increase in tensile load to which the hogging rebar would be subjected during cooling. It should be aimed however to explicitly model cooling in large scale UPT concrete structural models in the future. Longer standard fire durations (greater than 120 minutes) followed by compartment cooling may also subject the hogging reinforcement to tensile stress approaching elastic yield.

The adequate specification of hogging rebar is also partly responsible for preventing cold-span concrete damage or failure when subject to relaxed tendon prestress. The first internal beam

support was permitted to rotate inwards towards the heated bay through the transference of tensile stress through the hogging rebar. This increased rotation actually reduced the observed slab deflection within the subsequent cold bay. This increased the cross-sectional area of the first cold-span in compression through increasing the length of the hogging region extending from the heated bay. The transverse cold-spans also offer significant support to the reduced prestress cold-spans, the specification of transverse rebar is able to act as a tensile membrane if needed, extending from fully prestressed areas. Figure 6-19 showed cold span behaviour of the modelled structure subject to the minimum prestress observed during compartment cooling from the equivalent UPT concrete slab model of Chapter 5 (300MPa, Figure 5-29). The transverse spans were fully prestressed through tendons tensioned to 1000MPa. The increase in deflection within the cold span was not noted to be significantly increased from the ambient deflection at full prestress noted in Figure 6-15, going from 10.3mm to 11.7mm.

The most significant area of potential concrete damage is in the region of the edge columns at the anchored end of the heated bay (Figure 6-12). Whilst greater inelastic tensile strains are noted protruding from the base of the slab it is the inelastic tensile strain in vicinity of the slab-column intersections that are most likely to induce some form of local structural collapse.

There are numerous limitations to the study performed in this chapter. Firstly the difference in structural response to standard fire exposure has not been compared where creep is explicitly considered within prestressing tendons as opposed to being assumed to be implicitly covered by Eurocode 2 [1] stress-strain curves. These differences may not have been so pronounced without the consideration of bay cooling however. The lack of consideration of cooling is the most notable limitation of the study in this chapter. This was mainly due to a lack of time to solve numerical issues, but it should be achievable and is a necessary future consideration based on the evidence from Chapter 5. Having demonstrated within Chapter 5 the importance of explicitly considering tendon creep during compartment cooling, possibly the next area of priority is the explicit consideration of LITS. This has not been considered in this thesis but could significantly further influence the cooling behaviour of UPT concrete structures.

The importance of considering alternative temperature-time curves for heating and cooling of the structure has also been discussed within Chapter 5. This could affect the cooling behaviour of the structure with respect to the thermal gradients within the slab post-fire and ongoing heat transfer to tendons. Beyond this there exists a further exhaustive list of potential future modelling studies to help visualise structural behaviour in fire of UPT concrete structures. Potential modelling studies of interest are the variation of heating zones, both with respect to the shape and area they cover as well as their locations within the structure. As outlined at the end of Section 6.3.4, this will influence the locations of the amplified out-of-plane tensile strains noted from the base of the slab. It will also influence load distribution to particular columns and beams. Additionally, it would have been desirable to model the effects of fire on an internal span where additional sagging reinforcement was not present. During heating the lack of additional sagging reinforcement would be negated by restrained thermal expansion of the base concrete. However during compartment cooling as observed in the previous chapter this effect in close proximity to the base will reduce rapidly whilst tendon relaxation may continue to increase for a given time (owing to continued heat transfer within the slab). As heat transfer continues within the slab there will be increased restrained thermal expansion deeper within the slab, but at much lower temperatures than experienced at the base.

Finally, a step further from the consideration of one-way spanning continuous UPT concrete structures is the consideration of two-way spanning structures. Whilst cold-span behaviour under relaxed levels of prestress was not an issue in the modelling study of this chapter it could well be an issue in two-way spans. In such cases the support from the transverse span will also be reduced due to tendon relaxation spanning in both directions. The prescription of bonded reinforcement could provide a tensile membrane assisting the cold spans, but it is possible should sufficient unbonded tendons be specified that the internal spans could be designed without additional reinforcement. Further to this, punching shear is a potential problem in two-way spanning structures. Section 6.3.3 showed within the one-way UPT concrete structure modelled, shear stresses exist at the slab-column boundary with maximum principal tensile inelastic strains acting diagonally to the slab plane. This behaviour could be further explored through the development of two-way spanning UPT concrete structures where this behaviour is more critical.

7 Conclusions and recommendations

The novelty of the research presented in this thesis is the validation and use of an explicit prestressing steel creep material model in the computational analysis of elevated temperature UPT concrete structural behaviour. Further, the analysis has also investigated the ongoing structural behaviour occurring through compartment cooling; this is a phase where assuming tendon creep is implicitly covered by Eurocode 2 [1] stress-strain curves can lead to underestimates in tendon relaxation. The standardised code to which prestressing steel tendon wires and strands are manufactured has also been considered within this thesis. Gales has shown grade 1860 ASTM A416 [10] and grade 1860 BS 5896 [11] prestressing steel wires (both with a quoted elastic yield stress of 1860MPa) to have different responses with respect to creep strain accumulation under external stress and temperature conditions. Therefore the respective structural response subject to fire exposure to the base of UPT concrete slabs, prestressed by each standard of tendon, has been considered. The following section overviews the key outcomes of this thesis. These are the outcomes most noteworthy and most significant with regards to structural fire safety design and analysis. The recommendations arising from these outcomes and those areas requiring further study are outlined in Section 7.2.

7.1 Key outcomes

This section outlines the areas to arise of most practical significance and also of concern as concluded from the modelling studies presented in this thesis. These points include:

- The significance of considering cooling with regards to the analysis of elevated temperature behaviour of UPT concrete structures.
- The observed difference in behaviour with respect to creep strain accumulation, stress relaxation and resulting UPT concrete slab deformation between the use of grade 1860 ASTM A416 [10] and grade 1860 BS 5896 [11] standard prestressing steel tendons.
- The ability and consequences of relying on Eurocode 2 [1] temperature dependent stress-strain curves to implicitly account for creep in the analysis of elevated temperature tendon and UPT concrete slab behaviour.

7.1.1 Consideration of compartment cooling

The magnitude of ongoing UPT concrete slab deformation and damage during cooling, post-fire, observed within this thesis is significant and an important consideration with respect to fire-safety analysis of UPT concrete structures.

Thermal gradients built up within a UPT concrete slab during fire exposure to the slab base do not immediately reverse throughout the entire slab depth post-fire. Therefore tendon temperature at a given depth within a slab must continue to rise until sufficient heat has been released beneath to

reverse the thermal gradient at that depth. For example Figure 5-11 shows and Table 5-2 show a tendon covered by 30mm of concrete to reach a temperature of 384^{o}C after a 90 minute standard fire; the tendon temperature goes on to reach a peak of 444^{o}C before it begins to cool.

Figure 5-10, Figure 5-11 and Figure 5-12 show the continued increase in temperature of 15.7mm diameter tendons at their centres, 37.85mm from the slab base, after heating for 60 minutes, 90 minutes and 120 minutes according to a standard fire curve. The sink temperature below the slab during cooling takes between 77 and 85 minutes across the three cases respectively to reach ambient. This sink cooling profile is linear and was determined following guidelines from Eurocode 1 [31]. Figure 5-7, Figure 5-8 and Figure 5-9 show temperature profiles obtained from simple one-dimensional concrete heat transfer models at a depth of 37.85mm from the base of a slab subject to increasingly rapid rates of sink temperature cooling (from the three standard fire durations). These sink cooling profiles are also based on Eurocode 1 [31] guidelines; they correspond to compartments with an increased area of open allowing heat to escape. These figures (Figure 5-7, Figure 5-8 and Figure 5-9) give an idea of the difference in time it could take for thermal gradients at a tendon depth to reverse subject to different rates of sink cooling.

In all cases, the rate of increase of tendon temperature slows until peak tendon temperature is reached, at which point it begins to cool. Therefore there is a period of time post-fire where not only does the tendon temperature increase but it remains elevated with an ever decreasing rate of thermal transience. This period of time of elevated low transience temperature exposure extends whilst the tendon itself cools.

This has been shown in Section 5.3.2 to be a key phase in the evolution of tendon relaxation and resulting UPT concrete slab deformation. This is the case even if the effects of elevated temperature creep on tendon relaxation are ignored by assuming Eurocode 2 [1] inelastic yield curves will implicitly account for this. For example, Figure 5-23 shows a UPT concrete slab with 30mm of minimum tendon concrete cover, subject to a 60 minute standard fire at its base to continue to deflect from a value of approximately 38mm at the centre span to a peak of 65mm whilst the compartment cools (almost an 80% increase). In this case, whilst the tendon temperature (at a peak of approximately 360^{o}C) is significant enough to elicit primary creep strain (Section 4.4.5, Figure 4-15 and Figure 4-16), the Eurocode 2 [1] computed yield curves largely cover the accumulated creep strain. A 2% increase in peak tendon relaxation is noted in this case when creep is explicitly considered however, which also translates to a 2% (1mm) difference in the post-fire fully ambient deflected state.

Creep should always be considered during this critical phase of tendon temperature evolution. Figure 5-10, Figure 5-11 and Figure 5-12 highlight the point at which the rate of tendon heating within the slab drops below 2^{o}C per minute. This is outside of the stated degree of transience where Eurocode 2 [1] stress-strain curves are said to implicitly account for creep. Further, the modelling study of Section 4.4 (Figure 4-10) shows, particularly considering ASTM A416 [10] standard tendons, insufficient factor of safety to cover the effects of time evolving creep on stress relaxation at steady state heating beyond 400^{o}C.

Figure 5-26 and Figure 5-29 show the response of 30mm minimum concrete cover slabs subject to 90 and 120 minute standard fires respectively. The recovered deflections of the slabs are approximately 7% and 11% greater when creep is explicitly considered, with 59MPa and 125MPa

respective differences in tendon relaxation being accumulated by the time peak tendon temperature is reached (~450^{o}C and ~500^{o}C respectively). Considerable increases in hogging concrete damage are also noted during compartment cooling and can be viewed in the figures of Section 5.3.2.

It is however of very significant note where UPT concrete slabs have been modelled with BS 5896 [11] standard prestressing steel tendons that only very small relative differences in tendon relaxation, slab deflection and concrete damage are noted where creep is explicitly modelled. This is when compared to models where creep is assumed implicitly covered during transient heating by Eurocode 2 [1] stress-strain curves. Figure 4-10 showed, with respect to isolated tendon relaxation during transient heating to 400^{o}C, the Eurocode 2 [1] yield curves had built up a significant enough factor of safety with respect to their predicted inelastic strains, to cover subsequent steady state heating stress relaxation for this steel for over 90 minutes. Relaxation during steady state heating is of course directly attributable to creep (Section 4.2). This leads to the next key outcome of this thesis; the significant difference in susceptibility to creep of two different types of prestressing steel and the subsequent difference noted in stress relaxation and UPT concrete slab deformation during and post fire. These prestressing steels are manufactured to different standards [10] [11] but to the same ambient yield stress (1860MPa); this difference in behaviour, its consequences and reasons behind it are discussed in the following Section 7.1.2.

There is however significant scope for further analysis with regards to considering compartment cooling post-fire and subsequent UPT concrete structural behaviour. This will be discussed in greater detail in the recommendations for further study section of this concluding chapter (Section 7.2.2).

7.1.2 Steel type

The next significant outcome noted from this thesis, is the large difference in UPT concrete slab behaviour, during and post-fire, when slabs are prestressed by grade 1860 BS 5896 [11] steel tendons as opposed to grade 1860 ASTM A416 [10] steel tendons. Large differences in stress relaxation are noted between the two when isolated and heated at a fixed length (Figure 4-10). This follows on from Gales [6] noting a significant difference in creep strain response to stress and temperature during transient heating creep tests, between the two standards of steel. This difference is represented by the creep parameters determined from those tests as a function of stress as displayed in Table 3-1 [6] [7]. Naturally as these parameters were used in the explicit modelling of creep undertaken in this thesis, it was expected to notice a difference in stress relaxation between the two standardised steels considered. The magnitude of the stress relaxation difference noted is significant however. Figure 4-10 shows an approximate difference in relaxed stress, after heating to 400^{o}C at 10^{o}C per minute, of 35MPa, this is an approximate 4% increase in relaxation when using ASTM A416 [10] standard steel as opposed to BS 5896 [11] standard steel. After 90 minutes of subsequent steady state heating this difference in stress relaxation however extends to approximately 115MPa; this is an approximate 15% increase in relaxation when using ASTM A416 [10] standard steel as opposed to BS 5896 [11] standard steel. The 500^{o}C curve in Figure 4-10 shows significantly greater relative differences; a 25% increase in relaxation is noted using ASTM A416 [10] standard steel after heating to 500^{o}C at 10^{o}C per minute. After 90 minutes of subsequent steady state heating at this temperature the relative increase in relaxation when using

ASTM A416 [10] standard steel extends to 48%. These numbers are relative to the BS 5896 [11] standard relaxation curve.

These differences in stress relaxation can transfer to significant differences in UPT concrete slab deflection and damage, particularly during the early stages of compartment cooling, where tendon temperature is less transient but still of significant magnitude (>350^{o}C). For example, comparing Figure 5-26 to Figure 5-39, when a slab is exposed to a 90 minute standard about the point of minimum tendon cover, this being 30mm, a 50MPa difference in tendon relaxation and approximately a 4-5mm difference in permanent slab deflection are noted. These are respectively 9% and 7% relative increases in both parameters when ASTM A416 [10] standard tendons are used as opposed to BS 5896 [11] standard tendons. In this case the tendon temperature is at 384^{o}C after the 90 minute standard fire and reaches a peak of 444^{o}C, its temperature is beyond 400^{o}C for 61 minutes (Figure 5-11, Table 5-2). Comparing Figure 5-29 to Figure 5-41, in the case of a UPT concrete slab of minimum tendon cover 30mm, subject to a 120 minute standard fire, the relative increase in tendon relaxation is approximately 25% (105MPa) resulting in an increase in permanent slab deflection of 10-11% (approximately 10mm). In this case tendon temperature is 468^{o}C after the 120 minute standard fire and peaks at 505^{o}C.

Both the ASTM A416 [10] and BS 5896 [11] standard steels tested by Gales [6], and the creep parameters resulting from those tests and used in this thesis, specify ambient tensile yield strengths of 1860MPa. Both standards specify tendon strands should be formed from six cold-drawn wires woven about a seventh of slightly larger diameter. In both cases the completed strand should then be given a further thermo-mechanical treatment to remove any residual stresses between wires. As this is a standardised method of manufacture used globally [37] for tendon strands then attention naturally must focus on the noticeable difference in respective chemical compositions of the wires tested by Gales [6] (Table 4-1).

Of particular note is the increased concentrations in the ASTM A416 [10] wires tested by Gales [6] of phosphorus and sulphur. These elements are said to ease the cold-drawing process implying they ease the process of tensile elongation and grain alignment [9]. Stress relaxation induced by secondary creep is also a result of subgrain formation, alignment and growth (Section 2.2.4). Both standards specify similar mandatory ambient force relaxation requirements must be met with respect to strands; these are outlined in Section 4.1.The loads specified for these relaxation tests (70% and 80% of breaking force) however are not yield inducing. The relaxation noted can technically be called creep, but this can occur in the elastic regime (viscoelasticity), the strains noted are of a low order of magnitude in comparison to elevated temperature inelastic creep. The loads used to cold-draw wires, by default, have to be loads capable of inducing inelastic yielding behaviour. Hence an increased input of phosphorus and sulphur to ease the cold-drawing process need not affect the ambient force relaxation noted from the manufacturing standard tests owing to the non-yielding forces being applied. It also needn't necessarily affect initial ambient yield and inelastic behaviour given this is a dislocation based process (Chapter 2). It may however affect elevated temperature yield behaviour, particularly as this tends towards secondary creep and recrystallization based plasticity (Section 4.4.4).

Singling out phosphorus and sulphur and indeed the differing chemical composition in general as the reason for differing creep strain accumulation, and resulting stress relaxation, is postulation at

present. Being the standout difference between the two standard types of wire tested by Gales [6] however, the effect of chemical composition on elevated temperature creep strain accumulation and stress relaxation warrants further study.

A final point for consideration is the potential for different chemical composition steel rods to be used in prestressing steel manufactured to the same standard. For example, a wire and strand manufacturer switching supplier with respect to the raw material, or different manufacturers who use different suppliers. BS 10020 [27] does not specify exact chemical compositions for steels to be used for prestressing concrete; only limiting values of certain elements are detailed. This raises potential for differing elevated temperature creep strain accumulation and stress relaxation responses with respect to steels manufactured to the same standard.

7.1.3 The validity of Eurocode 2 implicit elevated temperature creep accountability

Eurocode 2 [1] quotes temperature dependent reduction factors to be applied to elastic modulus and ambient yield stress through which temperature dependent inelastic yield curves are computed. These inelastic yield curves are then said to implicitly account for creep strain accumulation during transient heating within the range $2℃/min \leq \dot{T} \leq 50℃/min$. Outwith this domain it is stated creep should be explicitly considered (no means as to how to do so is provided). It has been shown throughout the modelling study of this thesis, tendons within UPT concrete slabs subject to fire will at some stage of the heating-cooling process be subject to temperature exposure outside the above domain. Through Section 5.3.2 it has been shown in some cases that neglecting to explicitly account for creep does not make a significant difference to modelled UPT slab behaviour. These cases depend on steel type with respect to the tendon and the magnitude of the tendon temperature reached. As a guideline, ensuring tendon temperature does not exceed 350^{o}C should ensure it is not critical to explicitly account for creep (Figure 5-24 for example). Eurocode 2 [1] stress-strain curves over-predict inelastic strain during early transient heating, which covers the phase of lower transience heating. It should be noted however, the standard fire curve [31] is the only temperature-time curve that has been applied to UPT concrete slab models within this thesis as well as only one cooling curve. The consideration of other fire specific temperature-time profiles with respect to heating and cooling is of significant importance beyond this thesis and forms a recommendation for further study as detailed in Section 7.2.2. Time evolving thermal gradients within the slab dictate the transience and magnitude of tendon temperature exposure. To base all recommendations on thermal gradients induced from one temperature-time curve is a significant over-sight given how potentially significant the thermal gradients at the point the fire ceases are to continued creep strain accumulation within tendons.

During transient heating at 10^{o}C per minute of isolated ASTM A416 [10] standard prestressing steel tendons, Eurocode 2 [1]derived stress-strain curves contribute sufficient inelastic strain to the total strain Equation 4-1 to account for experimentally observed stress relaxation [9] to 400^{o}C (Figure 4-8). They fail to account for transient heating relaxation for this steel beyond this temperature, implying they under predict the contribution of creep to stress relaxation. It is worth noting they fall approximately 20MPa (4%) short of predicting the modelled transient heating stress relaxation to 500^{o}C where creep is explicitly considered.

With respect to modelled stress relaxation of BS 5896 [11] standard prestressing steel tendons the Eurocode 2 [1] stress-strain curves contribute to an over-prediction of stress relaxation, compared to modelled curves explicitly considering creep during 10°C per minute heating to 500°C (Figure 4-10). This is quite a significant over-prediction of approximately 115MPa or a 17% relative increase in predicted relaxation. The modelled ASTM A416 [10] standard prestressing steel stress relaxation curves, explicitly accounting for creep, showed an approximate error of 15% as 500°C was reached with respect to the experimental relaxation curves [9] (Figure 4-8). No experimental stress relaxation curves exist for BS 5896 [11] standard prestressing steel. Creep parameters as a function of stress used within the creep modelling process for both steels were determined by the same author [6]. Assuming the same error to experiment with respect to BS 5896 [11] standard steel would ensure the Eurocode 2 [1] determined relaxation curves cover the experimental relaxation also. Ultimately it therefore may be deduced, Eurocode 2 [1] derived yield curves do implicitly account for creep during transient heating at 10°C per minute, within the stated $2°C/min \leq \dot{T} \leq 50°C/min$ range, up to 400°C for ASTM A416 [10] and 500°C for BS 5896 [11] standard prestressing steels.

7.2 Recommendations

Within this section the main recommendations, both for design of UPT concrete structures, and with respect to areas requiring further study are presented. These recommendations are largely based on consideration of the key outcomes of this thesis outlined in Section 7.1. They relate largely to the consideration and further analysis of the effect of compartment cooling on UPT concrete structural behaviour. The investigation of potential differences in elevated temperature creep and relaxation properties between steel types is also discussed, along with guidelines as to mitigation against differing performance.

7.2.1 Performance recommendations

Eurocode 2 [1] recommends with respect to temperature exposure of unbonded prestressing steel tendons, the design process should consider 350°C as a critical temperature. Accordingly it recommends increasing concrete cover by 15mm from ambient design cover to prevent this temperature being exceeded. It specifies a greater critical temperature should only be used if more accurate methods are used to determine the effects of increased deflections. MacLean [9] recommends replacement of tendons or their consideration as damaged, if exposed to temperatures beyond 300°C. No significant changes in mechanical properties were noted to 300°C [9] but irreversible microstructural changes do occur between 300°C and 400°C mainly relating to dislocation motion as outlined by the recovery process (Section 2.2). These changes initiate the processes and thus set the material along the irrecoverable path leading to more serious microstructural evolutions with respect to structural integrity such as recrystallization. Assuming tendons are damaged beyond 300°C therefore provides a factor of safety against the significant degradation of mechanical properties associated to recrystallization (decrease in yield strength, increase in ductility) observed in metallurgical tests beyond 400°C.

On the evidence of this thesis concrete cover and fire ratings should be specified to ensure tendon temperature does not exceed 350^{o}C. It may still be prudent to follow MacLean's advice and replace any tendons that have been exposed to greater than 300^{o}C however. Critically, cooling of the compartment must be considered in determining fire durations and concrete covers that limit this temperature being reached. Under the sink temperature cooling curves used in this thesis a tendon covered by 35mm of concrete reaches 197^{o}C after 60 minute of standard fire exposure to the base of the slab, this rises to 337^{o}C over the following 45 minutes post-fire (Figure 5-10, Table 5-1). The same slab subject to a 90 minute standard fire shows a tendon temperature of 335^{o}C immediately post-fire, this rises to 410^{o}C over the following 38 minutes (Figure 5-11, Table 5-2). To limit tendon temperature to no more than 350^{o}C, the heat transfer data displayed in Figure 5-10, Figure 5-11 and Figure 5-12 implies 35mm of minimum concrete cover must be specified and standard fire exposure must be no greater than 60 minutes. If designing UPT slabs to withstand longer fire durations with respect to a standard fire curve, an even greater degree of minimum concrete cover must be specified.

In limiting tendon temperature exposure to 350^{o}C it is possible to:

- Apply a factor of safety against the degradation of mechanical properties such as rapidly decreasing yield stress coupled with rapidly increasing ductility that onset with recrystallization and noted secondary creep strain onset beyond 400^{o}C.
- Limit the difference in UPT concrete slab deflection noted when ASTM A416 [10] standard prestressing steel tendons are used as opposed to BS 5896 [11] standard tendons.
- Limit the consequences of neglecting to account explicitly for the contribution of creep to tendon stress relaxation. This is under the assumption inelastic behaviour would be considered through the use of Eurocode 2 [1] temperature dependent stress-strain curves.

As a side note, when considering standard bonded reinforcement, 400^{o}C is used as a critical temperature by Eurocode 2 [1]. In design, to limit temperature exposure of reinforcement to below this threshold, slab cooling should also be considered. Whilst creep and stress relaxation are not of concern in this case, material degradation is, and could significantly reduce the elevated temperature moment capacity of a slab.

7.2.2 Further study

The main recommendations for further study relate to three areas of analysis. These are:

- The further consideration of compartment cooling. This includes alternative temperature-time curves for the entire heating and cooling phases and the explicit consideration of LITS within the concrete material model.
- An investigation into the reasons for differing elevated temperature creep accumulation with respect to different manufacturing standards of prestressing steels of the same ambient yield stress. This should include an analysis of mechanical properties as a function of temperature and particularly differences in chemical composition between prestressing steels.

- The development and analysis of two-way spanning UPT concrete structures to analyse cold-span behaviour subject to prestress relaxation in two directions.

These points are elaborated on below:

Further analysis of post-fire cooling UPT concrete slab behaviour

The continued deflection and damage of UPT concrete slabs post-fire during cooling has been shown to highly significant. For example, Figure 5-23 shows a 30mm minimum tendon cover UPT concrete slab subject to a 60 minute standard fire increasing in central deflection, post-fire, by almost 80% at its peak. The UPT concrete slab models of Chapter 5 and larger continuous one-way UPT concrete structural models of Chapter 6 are all heated subject to the standard fire curve detailed in Eurocode 1 [31] (Figure 5-4). The accuracy of this curve often comes under scrutiny. In addition to this its use does impose a limited range of fire scenarios for analysis; these are simply to increase the duration of the fire. Shorter duration standard fires to the base of a slab impose steep initial thermal gradients within the slab owing to the rate of heating from the curve in its early stages. This result is the 45 minutes it takes for a tendon covered by 35mm of concrete to reach peak temperature after a 60 minute standard fire and the 140^{o}C increase during this period noted in Figure 5-10 and Table 5-1. As the gas temperature of the curve plateaus with time so to do the thermal gradients. Longer duration fires therefore elicit a smaller relative tendon temperature increase within UPT concrete slabs during compartment cooling. The relative time frame of the continued tendon heating is also smaller as the thermal gradients within the slab reverse more rapidly; being shallower immediately post-fire. For example Figure 5-12 and Table 5-3 show a 35mm cover tendon to reach its peak temperature 34 minutes after a 120 minute standard fire with an increase of 45^{o}C during this period.

The rigidity of only using the standard fire curve therefore imposes rigid post-fire cooling behaviour with respect to continued tendon relaxation and slab deflection. Exploration of alternative temperature-time curves enforcing different thermal gradients within slabs at different times will influence and broaden the analysis of cooling behaviour within the tendon. Further to alternative heating temperature-time profiles, alternative cooling profiles should also be studied. To some extent this has been alluded to in Section 5.2.1. Varying the rate with which the sink-temperature cools influences the rate at which thermal gradients reverse post-fire.

Thermal gradients within a UPT concrete slab are also highly important with respect to the consideration of creep on tendon relaxation. Shallow thermal gradients, maintaining a tendon at high temperatures beyond 350^{o}C for significant durations, mean creep strain accumulation could become significant. This has implications on the standard of prestressing steel used (ASTM A416 [10] as opposed to BS 5896 [11]) and the factors of safety built up during transient heating by Eurocode 2 [1] stress-strain curves with respect to stress relaxation, should creep not be explicitly considered.

In summary, a comprehensive analysis of UPT concrete slab behaviour considering a variety of heating and cooling temperature-time curves should be undertaken. This should continue to compare the response of slabs using different manufacturing standards of prestressing steel tendon. It should also continue to consider the effects of implicit versus explicit creep consideration within the tendons.

The models presented within this thesis, whilst taking a step forward in the explicit consideration of tendon creep have not explicitly considered LITS as a concrete property. This is a significant component of total compressive concrete strain again said to be implicitly accounted for in Eurocode 2 [1] stress-strain curves. It is however an irrecoverable strain component which begins to accumulate from an early stage during transient heating of concrete. As a result its implicit inclusion is often treated as elastic when Eurocode 2 stress-strain curves are incorporated into commercial FE software packages. This can seriously distort the cooling and unloading behaviour of concrete as outlined in Section 5.1. The combination of heating and cooling on tendon prestress and flexural deformation create a variety of loading and unloading stress conditions throughout a UPT concrete slab cross section. As a result the addition of LITS within the concrete material definition is a necessary addition, alongside tendon creep, to future UPT concrete structural modelling studies. In particular the difference in UPT concrete slab deformation during compartment heating and cooling where tendon creep and LITS are explicitly considered as opposed to implicitly considered by Eurocode 2 [1] could form an interesting set of parametric studies.

Experimental studies as to the effect of chemical composition on elevated temperature stress relaxation in prestressing steels.

A significant outcome of this thesis has been the difference in susceptibility to elevated temperature creep strain accumulation between grade 1860 ASTM A416 [10] prestressing steel and grade 1860 BS 5896 [11] prestressing steel. The effect this difference has on tendon stress relaxation and UPT concrete slab deflection has been extensively covered in Chapters 4 and 5 and is overviewed in Section 7.1. The reasons for this difference requires further study in order to ensure prestressing steel tendon strands are manufactured to the highest possible standard with respect to elevated temperature stress relaxation. Neither ASTM A416 [10] or BS 5896 [11] specify elevated temperature performance criteria to be met by the manufacturer.

Both standards specify the same general procedure for manufacture of tendon wires and strands; involving cold-drawing and various thermo-mechanical treatments (Section 4.1). This implies the difference may be due to different chemical compositions with respect to the steel wires tested by Gales [6] manufactured to each standard. Before assuming this to be the difference, a review of the manufacturing process of high yield prestressing steel wires and strands worldwide should be undertaken. This should ascertain what, if any, differences are noted in the cold-drawing and thermo-mechanical treatment processes. Mechanical properties such as elastic modulus reduction (and thus shear modulus reduction) as a function of temperature could also affect creep strain susceptibility, particularly primary creep accumulation, as inter-atomic bonds relax reducing shear resistance against inelastic deformation through dislocation motion. Given the microstructure of prestressing steel is dominated by pearlite it is unlikely this should be significantly different between the different steels.

Chemical composition, with respect to the concentration of various impurities within the steel should be assumed to influence elevated temperature yield and ductility behaviour; just as it does at ambient temperature. Reasons for this assumption can be deduced from Chapter 2, suffice to say the size, concentration and whether they are interstitial or substitutional can significantly increase,

or reduce the formation of energy barriers resisting inelastic deformation. The transient heating tensile creep tests as undertaken by Gales [6] should provide a good reference for the design of an experimental study to compare creep strain accumulation with respect to variation in chemical composition.

In particular a difference in the composition of phosphorus and sulphur was noted with respect to the two standards of steel wire tested (Table 4-1). The ASTM A416 [10] standard wires tested by Gales [6] had just over three times the concentration by mass of phosphorus and nearly nine times the concentration by mass of sulphur as compared to the BS 5896 [11] wires tested. It has been noted previously the addition of phosphorus and sulphur eases the cold drawing process. It may therefore be a good starting point to test the elevated temperature creep response of similar steels containing varying concentrations of these two elements. The potential for these two elements to influence particularly secondary creep behaviour has been postulated at the end of Section 4.4.4 and overviewed in Section 7.1.2.

Two-way spanning UPT concrete slab and structural modelling analysis

Only one-way spanning UPT concrete structural models have been developed and analysed within this thesis. One of the main reasons for the development of the large scale continuous UPT concrete structural model of Chapter 6 was to observe the cold-span behaviour resulting from a loss of prestress in tendons exposed to heating in a different part of the structure. These models were also intended to analyse hogging behaviour over the first internal supports from a heated bay. Increased concrete damage was noted in these regions in certain UPT concrete slab models (Chapter 5) explicitly considering tendon creep (Figure 5-36 for example). Therefore it was necessary to examine if design code [32] hogging rebar specifications could cover the increased tensile stresses developing in these regions. In both cases of cold-span and hogging behaviour it appears from the model presented concerns are unfounded. In fact the adequate specification of hogging rebar allows a significant counter rotation over the first internal support of the first cold-span, increasing the compressive cross-sectional area within the slab and decreasing its deflection.

Two-way spanning continuous UPT concrete structures do not have the same rigidity provided by beams between columns. Further, a single bay fire will relax tendons in two directions, significantly increasing the load on the cold span tendons spanning perpendicular. Therefore there is potentially less redundancy with respect to cold-span behaviour. In cases where a sufficient number of tendons are specified such that no additional standard sagging reinforcement is required, cold-spans in the direction of relaxed tendons could be particularly susceptible to sagging damage. Of further concern is the potential for punching shear in two-way spanning structures. It follows that continuous bay two-way spanning structural models could be of significant use in addressing concerns over the behaviour of such structures in fire. Naturally, a comparison of explicit versus implicit creep accountability in prestressing tendons coupled with the consideration of cooling would be of significant benefit. This can address whether design codes are adequate in specification of various cross-section dimensions and standard reinforcement to account for possibly increased tendon relaxation, slab deflection and concrete damage.

8 Appendix A; Classical plasticity constitutive relations

In order to fully understand the constitutive representation of viscoplasticity (creep) presented in Chapter 3 it is necessary to be familiar with a few preliminaries. In this Appendix a brief overview of the stress tensor is presented followed by a description of the Von Mises yield surface and stress as a background to the flow equations presented in Chapter 3.

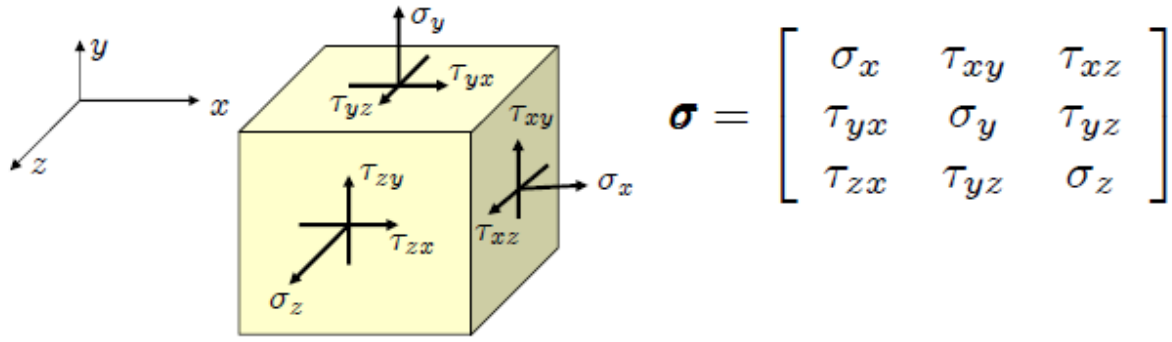

Figure 8-1; The stress tensor and its components as visualised acting on an infinitesimal cube

The stress tensor is a *field*, that is to say it varies with position throughout a material giving 9 stress components at each point describing the stress state at each point. It is a second rank tensor meaning in three dimensional space it has 3^2 or nine components (note a vector is a rank 1 tensor with 3^1 components and a scalar is a rank 0 tensor with 3^0 components). The stress tensor can then relate to a tensor of strain describing the deformed state at each point in a material leading to a strain field described by nine components at various points throughout its volume. In order to link stress and strain tensors a tensor of elasticity is required, this is a rank 4 tensor with 3^4 or 81 components (Equation 8-1).

$$\sigma_{ij} = \sum_{k,l} E_{ijkl}\varepsilon_{kl}$$

Equation 8-1

In reality for a three dimensional solid material in equilibrium typically only three separate values exist within the tensor of elasticity one of which is unity. The other two values can be described by two scalar quantities, one being the uniaxial elastic modulus and the other Poisson's ratio (these two being able to describe the shear modulus).

The stress tensor is a symmetric tensor, that is to say that the shear stresses $\sigma_{ij} = \sigma_{ji}$ where $I \neq j$. If this were not the case the infinitesimal point being described by the stress tensor would be rotating and not in equilibrium. This symmetry allows the stress tensor to be described by an ellipsoid; the deformed shape of any infinitesimal cube subjected to a deforming action described by a symmetric stress tensor will deform to an ellipsoid. Under equal compressive (or tensile) stresses in the absence of shear stresses (a hydrostatic stress state) it will deform to a sphere. Conceptually it is then possible to rotate the coordinate axis centred on the point being considered so the ellipsoid is created purely by pushing and pulling stresses; axial stresses in the new coordinate system. This is a

unique property of symmetric tensors. The fundamental definition of a tensor is that under rotation of a coordinate axis the tensor will also transform via rotation matrices (two in the case of a rank 2 tensor) to represent the same physical state in a new coordinate orientation. Within this description then it should be and is possible to find a new local axis orientation where the stress tensor transforms to represent the stress state via three axial stress components, otherwise known as principal stresses. This allows the stress state at a point to be represented by a vector with 3 components in a localised axis (local to the point being considered), this system or space is often referred to as principal stress space.

Should the deformed shape be represented by a sphere then the point is experiencing a hydrostatic pressure stress of either uniform compression or tension. A commonly observed property of metals is their immunity to yield under any magnitude of hydrostatic pressure stress, be it positive or negative. This implies yield is achieved in a metal through some form of distorting stress independent of volume change. If such volume changing hydrostatic stresses can be separated from the stress tensor then perhaps a more appropriate tensor (or vector in principal stress space) can be found representing the distorting stress state most likely produce elastic yield. Referring to principal stress space for ease and clarity a mean axial stress λ can be found through averaging the principal stresses (Equation 8-2).

$$\lambda = -(\sigma_1 + \sigma_2 + \sigma_3)/3$$

Equation 8-2

This mean stress can equally be taken from the axial components of the stress tensor in any coordinate axis orientation and represents an equivalent mean hydrostatic stress state in that space when considered along each axis (the mean hydrostatic stress is actually an invariant property of the stress tensor, it doesn't change with coordinate rotation). It is therefore possible to split the stress tensor into a hydrostatic spherical deforming component and a distorting or *deviatoric* elliptically deforming stress state (Equation 8-3).

$$\sigma_{ij} = S_{ij} + \lambda\delta_{ij}, \qquad \delta_{ij} = \begin{cases} 1, & i = j \\ 0, & i \neq j \end{cases}$$

Equation 8-3

The deviatoric stress state tensor is known as the stress deviator tensor, S_{ij}. δ_{ij}, is known as the Kronecker delta and is multiplied by the mean hydrostatic stress λ to give an effective hydrostatic stress state. The stress deviator tensor then represents the pure elliptically deforming and ultimately yield inducing stress state of a metal.

In order to visualise this and to visualise the elastic stress domain at a given point within a metal the Von Mises yield surface is used (Figure 8-2). This describes a cylinder about a hydrostatic axis ($\sigma_1 = \sigma_2 = \sigma_3$) in principal stress space, all points within the cylinder represent an elastic stress state. The deviatoric stress state lies perpendicular to this hydrostatic axis with its magnitude being the radius of the cylinder and the effective yield stress of the material.

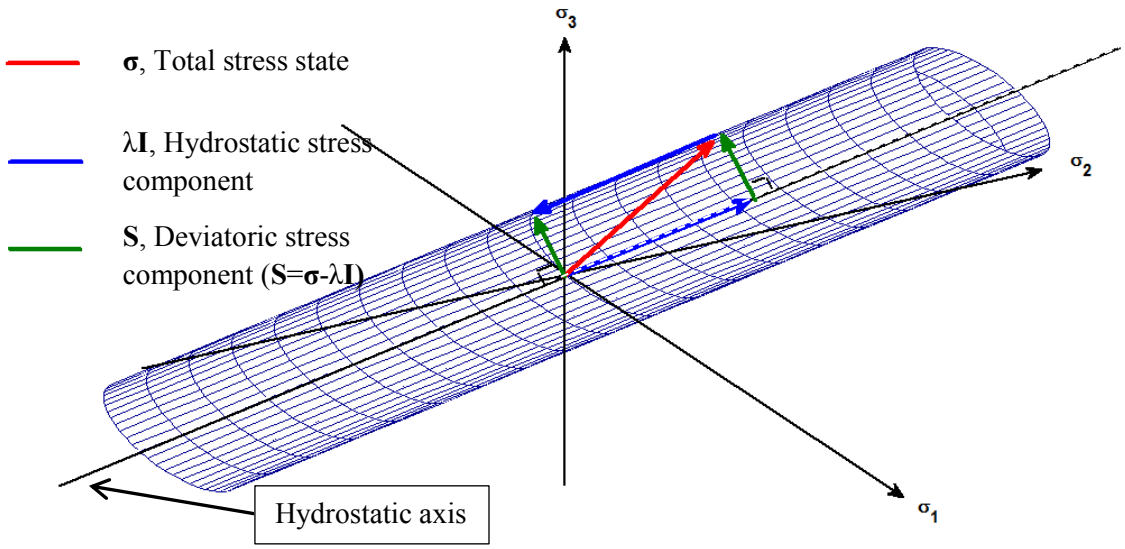

Figure 8-2; The Von Mises yield surface

Figure 8-2 shows a stress state lying on the yield surface; elastic yield has therefore been reached. The arrows depict the vector summation involved displaying the deviatoric stress lying in the *deviatoric plane* (a disc centred on the origin whose plane is perpendicular to the hydrostatic axis). Any plastic deformation from here is observed perpendicular to the yield surface in principal strain space showing plastic deformation to be dependant only on the deviatoric stress and independent of hydrostatic stress.

Typically yield stresses for metals are quoted as a uniaxial tensile yield stress obtained through experiment. If such a state is considered in Figure 8-2 whereby the stress state lies on the yield surface with principal stress components $\sigma_1 = a$, $\sigma_2 = \sigma_3 = 0$ (a being the uniaxial tensile yield stress) then the radius of the yield surface can be derived from Equation 8-3 and Equation 8-2. The stress state is defined as $\underline{\sigma} = (a, 0, 0)$, the mean stress from Equation 8-2 is $\lambda = a/3$.

$$\underline{S} = \underline{\sigma} - \lambda\left(\underline{i} + \underline{j} + \underline{k}\right) = (\sigma_1 - \lambda)\underline{i} + (\sigma_2 - \lambda)\underline{j} + (\sigma_3 - \lambda)\underline{k}$$

$$\underline{S} = \left({}^{2a}/_{3}\right)\underline{i} + \left({}^{-a}/_{3}\right)\underline{j} + \left({}^{-a}/_{3}\right)\underline{k}$$

Equation 8-4

The deviatoric stress as a vector in principal stress space then shows biaxial equal magnitude compressive components (in themselves create extension in the third component) and a tensile component in the remaining axis creating an elongated ellipsoid. The magnitude of the deviatoric stress vector in Equation 8-4 is the radius of the yield surface and implies the magnitude of the elliptical extension.

$$|S| = \sqrt{2/3}\, a$$

Equation 8-5

So; the pure deviatoric stress required to cause yield is actually $\sqrt{2/3}$ smaller than the quoted uniaxial tensile yield stress of the metal. In order to keep things simple it is desirable to only have one quoted yield stress for a material, the uniaxial tensile yield stress is something easy to measure and quantify so it would be of practicality to quote only this stress. In constitutive terms when looking at pure yield under multi directional stress states it is then useful to be able to equate the radius of the yield surface (the magnitude of the deviatoric stress in principal stress space) to the quoted tensile yield strength in order to establish when yield has been reached. Therefore the Von Mises stress is defined as $\sqrt{3/2}$ multiplied by the magnitude of the deviatoric stress in principal stress space. When yield is reached represented by the stress state lying at some point on the yield surface the Von Mises stress then equals the uniaxial tensile yield stress. Therefore by computing the Von Mises stress at a given time yield can always be quantified by comparison to the quoted uniaxial tensile yield stress. It should be noted the Von Mises stress is often known as the *equivalent Von Mises stress* or the *effective stress*. In both cases these names indicate that the Von Mises stress is not a *real* stress as such but a measure of the magnitude of the elliptical distorting component of the stress state scaled to the uniaxial tensile yield stress.

$$\sigma_{vm} = \sqrt{\left(\frac{3}{2} S_{ij} S_{ij}\right)} = \sqrt{3J_2}$$

Equation 8-6

It should be noted that as would be expected given that the Von Mises stress is essentially a magnitude that it is an invariant quantity of the stress deviator tensor. That is to say that its value will remain the same no matter what orientation of coordinate axis the stress deviator tensor is defined. Strictly speaking it is not a direct invariant but proportional to a direct invariant known as the second invariant of the stress deviator tensor, J_2. Considering the relation of the stress deviator tensor to the stress tensor the Von Mises stress can then be defined in terms of components of the stress tensor as in Equation 8-7 (where the shear stresses equal zero in principal stress space).

$$\sigma_{vm} = \sqrt{\frac{1}{2}[(\sigma_{11} - \sigma_{22})^2 + (\sigma_{22} - \sigma_{33})^2 + (\sigma_{33} - \sigma_{11})^2 + 6(\sigma_{12}^2 + \sigma_{23}^2 + \sigma_{31}^2)]}$$

Equation 8-7

9 Appendix B; Creep strain rate functions of viscous stress

It has been established that the total internal stress state of a material beyond elastic yield, at elevated temperatures, consists of an effective viscous stress state and yield stress state. This total internal stress state at small strains, in most practical situations can be taken as matching the magnitude of the external applied stress state (where inertial forces are negligible). As a result yield stress will be a lot lower than classically predicted where viscous stress is ignored. The examples presented earlier in Section 3.3 all attempt to predict the flow rate, $\dot{p}$, with respect to the norm of the deviatoric component of the total internal stress state, which is typically taken as the Von Mises stress. This as has been presented in Chapter 3 however, does not directly dictate the creep strain rate; the viscous stress decomposed from the Von Mises stress does (Figure 3-4, Equation 3-6). In this section possible representations for the flow rate $\dot{p}$ as a function of viscous stress are explored as opposed to the examples in Section 3.3 where the external or total internal stress state is used.

Forms for a representation of the flow rate as a function of viscous stress have been proposed and briefly reasoned within Section 3.2.1 through Equation 3-13 and Equation 3-14. From a practical standpoint using the viscous stress to predict creep strain rate, as has been stated previously, is troublesome in that if the actual yield stress at a given strain is unknown, then the viscous stress is unknown. Practically then it is usually more useful to use a less theoretically concise form using the total deviatoric stress state represented by the Von Mises stress instead, if there is sufficient grounds to believe in accuracy. It would however be of much use both theoretically and practically to have yield curves as a function of temperature determined viscoplastically, these curves may then include strain rate as an additional field variable. If experimental creep strain rates are available then using a strain rate function of the form Equation 3-13 or Equation 3-14 may allow viscous stress and yield stress as a function of plastic strain to be approximated.

It was noted in Section 2.3 in Equation 2-7 and Equation 2-8[1] that creep strain rate often appears to be proportional to either a power of the applied stress, or at higher stresses an exponential of the applied stress. A means to accommodate a wide range of applied stresses within one representation may be to adapt and expand Equation 2-8 as in Equation 9-1. This is achieved by simply subtracting unity from the exponential and expanding as a Maclaurin series, as displayed below.

$$\dot{p} = \dot{\varepsilon}_0 \left[exp\left(\frac{\sigma_A}{D}\right) - 1 \right] g(T) = \dot{\varepsilon}_0 \left[\frac{\sigma_A}{D} + \left(\frac{\sigma_A^2}{2!\, D^2}\right) + \left(\frac{\sigma_A^3}{3!\, D^3}\right) + \cdots + \left(\frac{\sigma_A^n}{n!\, D^n}\right) \right] g(T)$$

Equation 9-1

In Equation 9-1, *g(T)* represents a function of temperature, this typically being the Arrhenius relation. In a constitutive form temperature effects can be included via their effects on the viscoplastic potential, Ω. At low total stress magnitudes (small σ_A/D), Equation 9-1 reduces towards a

[1]

$$\dot{p} = \dot{\varepsilon}_0 exp\left(\frac{\sigma_A}{D}\right) exp\left(\frac{-Q_{cr}}{Rt}\right)$$

power law as large power terms tend towards zero, whilst at high applied stresses (large σ_A/D) Equation 9-1 tends towards an exponential as the *-1* factor becomes negligible.

Clearly in Equation 9-1 there is a fundamental problem in that there is no distinguishing between yield and non-yield states. This requires constants to be chosen such that creep strain rate only begins to become significant when elastic yield is exceeded; something that can be done through appropriate choosing of the activation energy in Equation 2-8. Using the viscous stress, as is desirable from a theoretical constitutive standpoint naturally eliminates this; the function is such that when the viscous stress equals zero, the strain rate equals zero. Equation 3-14[2] presents a form of the flow rate similar to that in Equation 9-1, where the flow rate or creep strain rate is a function of the viscous stress. This form ensures separation between elastic and viscoplastic domains through the *-1* factor (ensuring $\dot{p} = 0$ when $\sigma_{vis} = 0$) and thus conveniently expands in the same way as Equation 9-1. It thus ensures that the flow rate can be treated as a form of power law or exponential function of the viscous stress.

To make Equation 3-14 specifically applicable requires determination of the rate constant $\dot{\varepsilon}_0$, an appropriate constant or variable drag stress *D*, and a knowledge of the evolution of the radius of the yield surface ($\sqrt{2/3}$ of the uniaxial tensile yield stress). The radius of the yield surface can naturally be represented in terms of the uniaxial tensile yield stress which in turn is a function of plastic strain, strain rate, temperature, heating rate and any other applicable field or internal state variables. Equation 3-14 then allows the effects of strain hardening to be encompassed through its natural inclusion of the yield stress as shown in Equation 9-2, obtained by substituting Equation 3-6[3] into Equation 3-14.

$$\dot{p} = \dot{\varepsilon}_0 \langle exp\left(\frac{\sigma_{vis}}{D}\right) - 1\rangle = \dot{\varepsilon}_0 \langle exp\left(\frac{\sqrt{2/_3}\,\sigma_{vm} - \sqrt{2/_3}\,\sigma_y}{D}\right) - 1\rangle$$

Equation 9-2

The drag stress, *D*, is a necessity to dimensionally balance Equation 9-2, it however also has the potential to be used to incorporate hardening and softening effects, as was demonstrated in Section 3.3.1, Figure 3-6.The appropriate choice of the form of the drag stress then will make a considerable difference either to the computed strain rate or to the calculation of yield stress (should strain rate evolution with viscous stress be known). At first glance the rate constant, $\dot{\varepsilon}_0$, may also appear as a candidate to consider hardening and softening effects but it may be best intended as a representative of initial conditions. If the flow rate, $\dot{p}$, is integrated with respect to the viscous stress

2

$$\dot{p} = \dot{\varepsilon}_0 \langle exp\left(\frac{\sigma_{vis}}{D}\right) - 1\rangle$$

3

$$\sigma_{vis} = \sqrt{2/_3}\,\sigma_{vm} - \sqrt{2/_3}\,\sigma_y$$

to produce a function for the viscoplastic potential, according to Equation 3-11, then the rate constant, $\dot{\varepsilon}_0$, is shown to be directly proportional to the viscoplastic potential as well as the flow rate. This constant then could be considered to reflect the magnitude or order of creep strains that would be expected to be observed and may be considered as representative of the effects of such initial conditions as dislocation density, which in turn dictates subgrain formation size and so on. It may also be a function of the total applied stress state.

In order to consider strain hardening and softening effects an effective hardening parameter can be extracted from Equation 9-2 as displayed via Equation 9-3, Equation 9-4 and Equation 9-5. The uniaxial tensile yield stress as stated above provides a natural means of considering strain hardening and softening effects on the magnitude of the viscous stress. Within this, temperature effects can also be included, bearing in mind their influence on first elastic yield through reduction of bond stiffness as well as its effect on the degree of strain hardening, through vacancy concentration effectively *saturating* the effect of dislocation pile up.

$$\dot{p} = \dot{\varepsilon}_0 \langle exp\left(\frac{-\sqrt{2/3}\,\sigma_y}{D}\right) exp\left(\frac{\sqrt{2/3}\,\sigma_{vm}}{D}\right) - 1\rangle$$

Equation 9-3

$$\dot{p} = \dot{\varepsilon}_0 \langle H\left(T, \dot{T}, p, \dot{p}\right) exp\left(\frac{\sqrt{2/3}\,\sigma_{vm}}{D}\right) - 1\rangle$$

Equation 9-4

$$H\left(T, \dot{T}, p, \dot{p}\right) = exp\left(\frac{-\sqrt{2/3}\,\sigma_y}{D}\right)$$

Equation 9-5

The drag stress, *D*, may be also be assigned the role of representing hardening and softening behaviour as stated above. In these cases it is often linked to the yield stress, σ_y, in some form of linear relationship as in Equation 9-6. The approach taken by Perzyna [38] [39] is to assign *A=0* and *B=1*, such that the drag stress is taken as equal to the yield stress.

$$D = A + B\sigma_y$$

Equation 9-6

If this approach is taken, where $B = \sqrt{2/3}$, then the hardening parameter, Equation 9-5, ceases to be a parameter and becomes a constant, with hardening included directly by the yield stress evolution. The flow rate form reduces to Equation 9-7.

$$\dot{p} = \dot{\varepsilon}_0 \langle exp\left(\frac{\sigma_{vm}}{\sigma_y} - 1\right) - 1 \rangle$$

Equation 9-7

If it is desired to use the drag stress as some form of evolving hardening parameter evolving with accumulated strain, then it makes sense to tie its evolution to the yield state rather than having two separately evolving parameters that in essence represent the same physical occurrence. If the decomposition of yield into first elastic yield and evolving yield is considered, this makes some sense. The coefficient of friction of the friction slider in Figure 3-1 effectively evolves drag with accumulated plastic strain, whilst the reduction of first yield with increasing temperature accounts for the reduction of bond stiffness on drag. To be complete, the coefficient of friction must then also account for the saturation effect of vacancies on strain hardening and must also have temperature dependence.

A method of sorts to account for the saturation effect of vacancies has already been presented within Section 3.3.1; temperature compensated time. The Arrhenius function can be viewed from Chapter 2 as broadly representing vacancy concentration at a given time whilst summing over time normalises their effects over time. The rate forms of Equation 2-7, Equation 2-8 and Equation 2-9 naturally include temperature compensated time through the time derivative acting on the Arrhenius relation.

The rate constant, $\dot{\varepsilon}_0$, also requires determination. As stated earlier, it would appear best representative of the effect of initial conditions such as dislocation density on creep strain rate. It may also possibly vary with total stress. In all, this leaves too many variables and evolutions to be determined from experimental strain rate data, even if drag stress and yield stress can be tied. So for now it seems existing representations from Chapter 2.3.2 and similar based forms within Section 3.3 and Section 3.3.1, as a function of total stress, with an Arrhenius temperature dependence will have to suffice. These can be adopted into a constitutive framework through defining the uniaxial creep strain rate. This is until accurate yield curves considering viscoplastic effects can be determined from experiment, allowing a fully constitutive approach to creep modelling to practically applicable.

10 Appendix C, Prestressing steel material parameters

E (MPa)	Poisson ratio	Temp (ºC)
200000	0.3	20
196000	0.3	100
190000	0.3	200
176000	0.3	300
162000	0.3	400
108000	0.3	500
82000	0.3	600
20000	0.3	700
14000	0.3	800
6000	0.3	900
0	0.3	1000

Table 10-1; Elastic modulus reduction with temperature EC2 [1]

Expansion coefficient, α	Temp (ºC)
0	20
8.38E-06	100
9.79E-06	200
1.05E-05	300
1.11E-05	400
1.16E-05	500
1.21E-05	600
1.25E-05	700
1.27E-05	735
1.29E-05	800
1.34E-05	900
1.38E-05	1000
1.42E-05	1100

Table 10-2; Thermal expansion coefficient with temperature EC2 [1]

Stress (MPa)	Inelastic strain	Temperature (ºC)
1860.00	0.0000	20
1860.00	0.0407	20
0.10	0.0907	20
1264.80	0.0000	100
1466.54	0.0015	100
1713.39	0.0055	100
1825.86	0.0095	100
1860.00	0.0135	100
1860.00	0.0435	100
0.10	0.0935	100
948.60	0.0000	200
1198.87	0.0020	200
1313.09	0.0035	200
1484.63	0.0070	200
1586.60	0.0110	200
1618.20	0.0150	200
1618.20	0.0450	200
0.10	0.0950	200

595.20	0.0000	300
801.66	0.0016	300
1072.41	0.0056	300
1187.71	0.0086	300
1274.64	0.0126	300
1302.00	0.0166	300
1302.00	0.0516	300
0.10	0.1016	300
241.80	0.0000	400
570.82	0.0035	400
756.95	0.0075	400
908.91	0.0145	400
930.00	0.0185	400
930.00	0.0585	400
0.10	0.1085	400
130.20	0.0000	500
347.36	0.0038	500
456.30	0.0078	500
545.59	0.0148	500
558.00	0.0188	500
558.00	0.0688	500
0.10	0.1138	500
93.00	0.0000	600
186.88	0.0039	600
225.25	0.0079	600
242.70	0.0109	600
256.13	0.0149	600
260.40	0.0189	600
260.40	0.0689	600
0.10	0.1189	600
55.80	0.0000	700
78.28	0.0022	700
96.31	0.0062	700
109.78	0.0132	700
111.60	0.0172	700
111.60	0.0722	700
0.10	0.1172	700

Table 10-3; Eurocode 2 inelastic stress-strain temperature reduction curves [1]

Conductivity (W/m.K)	Temp (ºC)
53.334	20
50.67	100
47.34	200
44.01	300
40.68	400
37.35	500
34.02	600
30.69	700
27.36	800
27.3	900
27.3	1000

Table 10-4; Thermal conductivity with temperature, EC2 [1]

Specific heat capacity (J/kgK)	Temperature (ºC)
439.8018	20
487.62	100
529.76	200
564.74	300
605.88	400
666.5	500
759.92	600
1008.158	700
1388.333	720
5000	735
1482.895	750
1001.923	770
803.2609	800
650.4438	900
650	1000

Table 10-5; Specific heat capacity with temperature, EC2 [1]

11 Appendix D; Concrete material parameters

Density (kg/m^3)	Temp (ºC)
2.500	20
2.500	115
2450	200
2412.5	300
2375	400
2353.125	500
2331.25	600
2309.375	700
2287.5	800
2265.625	900
2243.75	1000

Table 11-1; Concrete density as a function of temperature

E (GPa)	Poisson ratio	Temp (ºC)
17928	0.2	20
11205	0.2	100
7905	0.2	200
5827	0.2	300
3810	0.2	400
2211	0.2	500
1076	0.2	600
771	0.2	700
484	0.2	800
269	0.2	900
108	0.2	1000

Table 11-2; Concrete elastic properties with temperature, EC2 [1]

Expansion coefficient α	Temp (ºC)
0	20
6.18E-06	100
6.62E-06	200
7.35E-06	300
8.36E-06	400
9.65E-06	500
1.12E-05	600
1.31E-05	700
1.52E-05	800
1.36E-05	900
1.22E-05	1000

Table 11-3; Thermal expansion coefficient with temperature, EC2 [1]

Conductivity (W/mK) (middle bound)	Temp (ºC)
1.642	20
1.498	100
1.332	200
1.182	300
1.049	400
0.932	500
0.832	600
0.748	700
0.680	800
0.629	900
0.595	1000

Table 11-4; Thermal conductivity with temperature, middle bound values, EC2 [1]

Specific heat capacity (1.5% moisture) J/kgK	Temp C
900	20
900	100
1470	101
1470	115
1000	200
1050	300
1100	400
1100	500
1100	600
1100	700
1100	800
1100	900

Table 11-5; Specific heat capacity at 1.5% moisture content with temperature, EC2 [1]

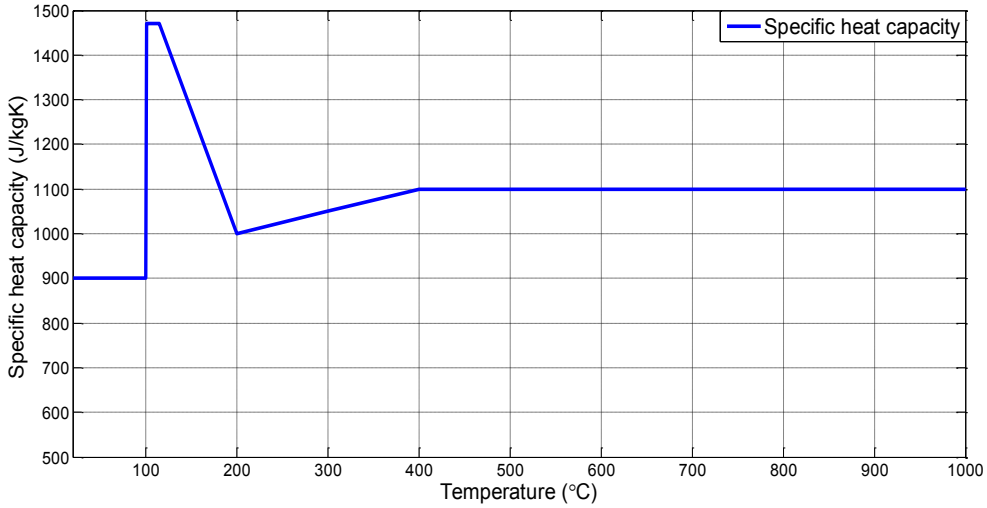

Figure 11-1; Specific heat capacity at 1.5% moisture content with temperature, EC2 [1].

Dilation Angle	Eccentricity	f_b/f_{c0}	K	Viscosity parameter
15	0.1	1.16	0.666	0

Table 11-6; Concrete damaged plasticity parameters defining yield surface/state

Stress (Mpa)	Inelastic strain	Temp (ºC)
17.4419	0.0000	20
24.3682	0.0001	20
28.6624	0.0004	20
30.0000	0.0008	20
0.0000	0.0200	20
17.4419	0.0000	100
24.3682	0.0002	100
28.6624	0.0006	100
30.0000	0.0013	100
0.0000	0.0225	100
8.6952	0.0000	200
16.9186	0.0001	200
23.6372	0.0003	200
27.8025	0.0009	200
29.1000	0.0018	200
0.0000	0.0250	200
8.1574	0.0000	300
15.8721	0.0001	300
22.1751	0.0004	300
26.0828	0.0011	300
27.3000	0.0023	300
0.0000	0.0275	300

7.6195	0.0000	400
14.8256	0.0001	400
20.7130	0.0006	400
24.3631	0.0016	400
25.5000	0.0033	400
0.0000	0.0300	400
6.6335	0.0000	500
12.9070	0.0002	500
18.0325	0.0008	500
21.2102	0.0024	500
22.2000	0.0050	500
0.0000	0.0325	500
5.3785	0.0000	600
10.4651	0.0003	600
14.6209	0.0014	600
17.1975	0.0040	600
18.0000	0.0083	600
0.0000	0.0350	600
3.8546	0.0000	700
7.5000	0.0003	700
10.4783	0.0014	700
12.3248	0.0040	700
12.9000	0.0083	700
0.0000	0.0375	700
2.4203	0.0000	800
4.7093	0.0003	800
6.5794	0.0014	800
7.7389	0.0040	800
8.1000	0.0083	800
0.0000	0.0400	800
1.3446	0.0000	900
2.6163	0.0003	900
3.6552	0.0014	900
4.2994	0.0040	900
4.5000	0.0083	900
0.0000	0.0425	900
0.5378	0.0000	1000
1.0465	0.0003	1000
1.4621	0.0014	1000
1.7197	0.0040	1000
1.8000	0.0083	1000

0.0000	0.0450	1000

Table 11-7; Concrete compression hardening with inelastic strain and temperature, EC2 [1]

Stress (MPa)	Inelastic strain	Temp (ºC)
3.39	0	20
3.39	0	100
2.71	0	200
2.03	0	300
1.36	0	400
0.68	0	500
0.00	0	600

Table 11-8; Concrete tension stiffening data

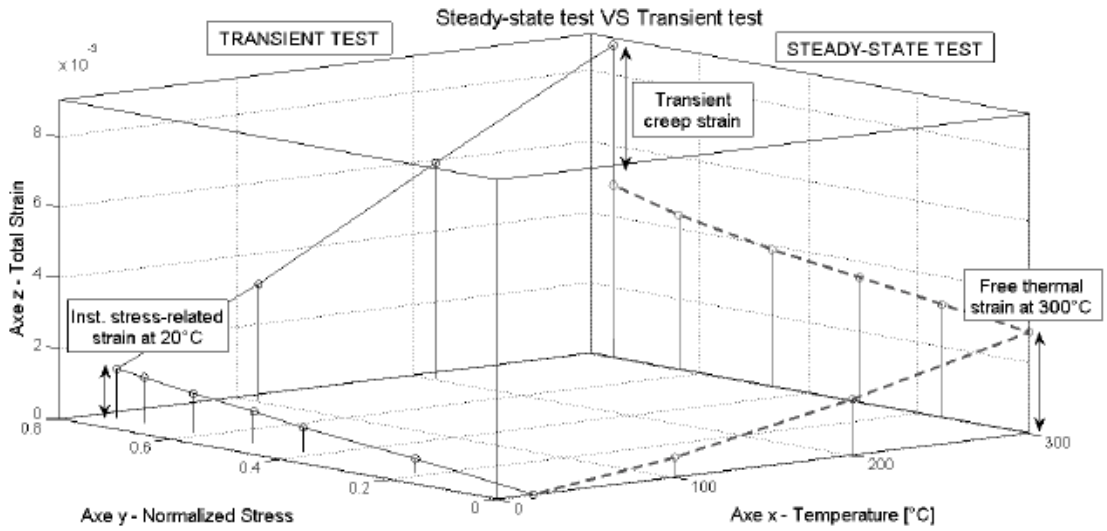

Figure 11-2; Transient creep strain in concrete ([36])

12 Appendix E; Reinforcing steel material parameters

E (MPa)	Poisson ratio	Temp (ºC)
210000	0.3	20
210000	0.3	100
189000	0.3	200
168000	0.3	300
147000	0.3	400
126000	0.3	500
65100	0.3	600

Table 12-1; Reinforcing steel elastic modulus and Poisson ratio with temperature, EC2 [1]

Stress (MPa)	Strain	Temp (ºC)
500	0	20
500	0.147619048	20
0.000001	0.197619048	20
500	0	100
500	0.147619048	100
0.000001	0.197619048	100
405	0	200
462.9382862	0.003857143	200
486.677706	0.008857143	200
500	0.017857143	200
500	0.147857143	200
0.000001	0.197857143	200
305	0	300
379.6439359	0.001684524	300
431.3344496	0.004684524	300
461.7876296	0.007684524	300
491.9721931	0.013184524	300
500	0.018184524	300
500	0.148184524	300
0.000001	0.198184524	300
210	0	400
308.1325148	0.001571429	400
398.6757498	0.005071429	400
449.0122628	0.008571429	400
492.3858187	0.014571429	400
500	0.018571429	400
500	0.148571429	400
0.000001	0.198571429	400
180	0	500
253.1477084	0.001571429	500
317.8841873	0.005071429	500
353.7315932	0.008571429	500
384.585842	0.014571429	500
390	0.018571429	500
390	0.148571429	500
0.000001	0.198571429	500

90	0	600
128.3384873	0.001117512	600
179.1313913	0.004617512	600
206.3616143	0.008117512	600
228.951163	0.013617512	600
235	0.018617512	600
235	0.148617512	600
0.000001	0.198617512	600

Table 12-2; Reinforcing steel inelastic yield curves with temperature, EC2 [1]

13 Appendix F; Slab sectional compression-tension profile evolutions

The following Figure 13-1 and Figure 13-2 show contour plots displaying longitudinal compression (blue) and tension (red) through the course of a 120 minute standard fire and natural cooling returning to an ambient state. Figure 13-1 displays the cold surface viewed from the top, Figure 13-2 displays the fire exposed surface viewed from below.

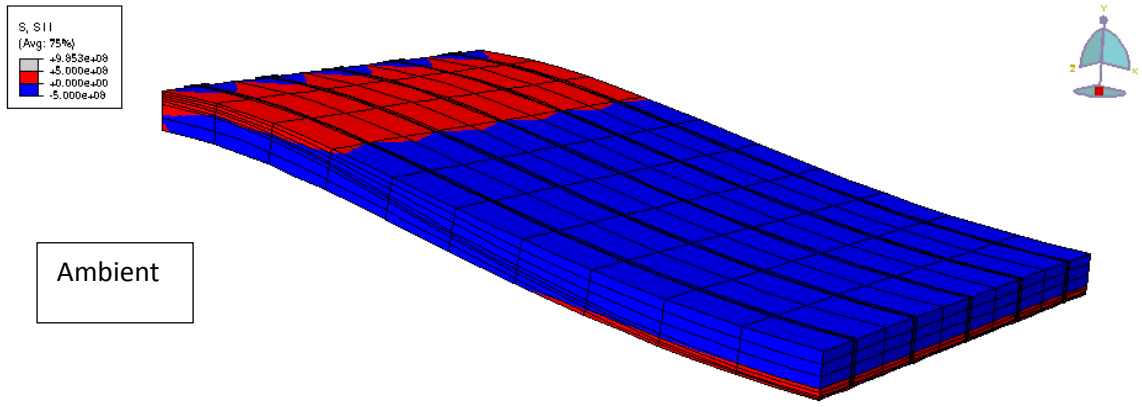

Ambient

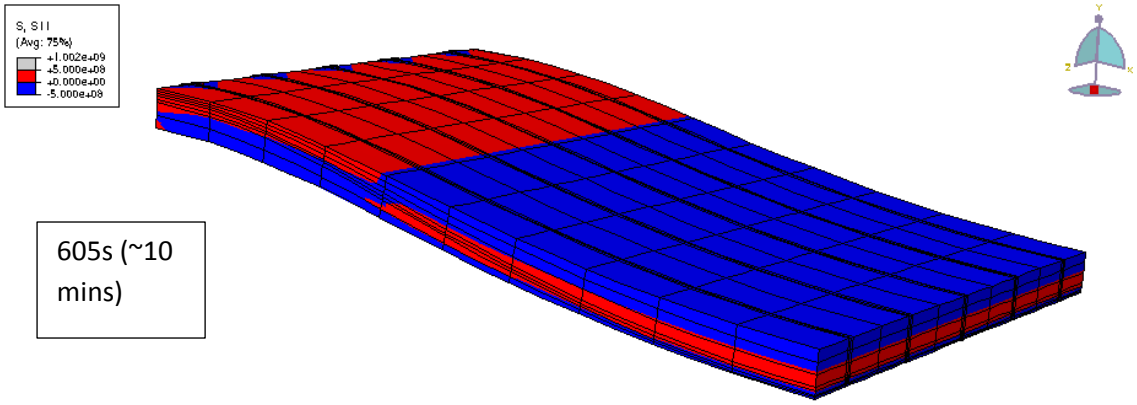

605s (~10 mins)

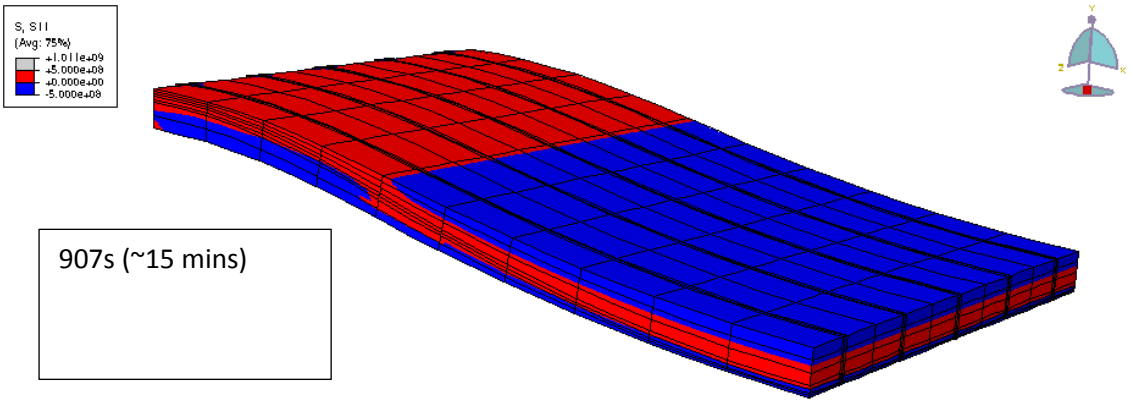

907s (~15 mins)

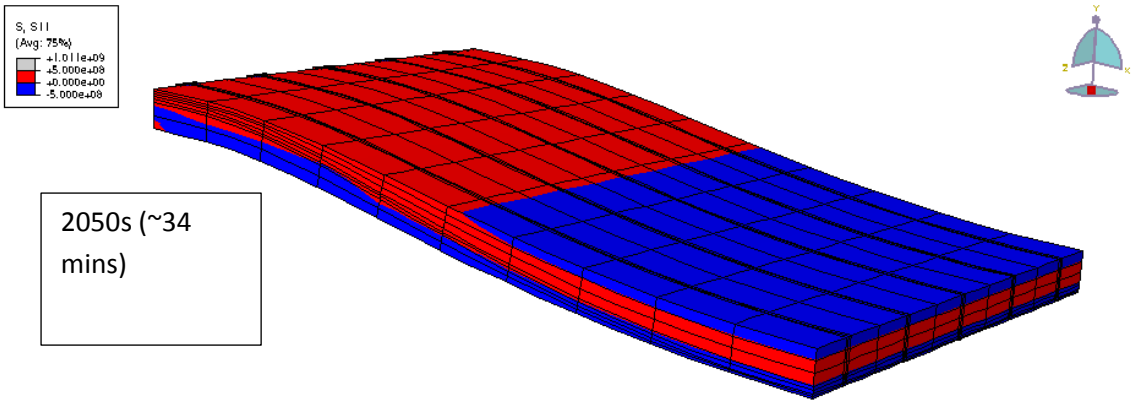

2050s (~34 mins)

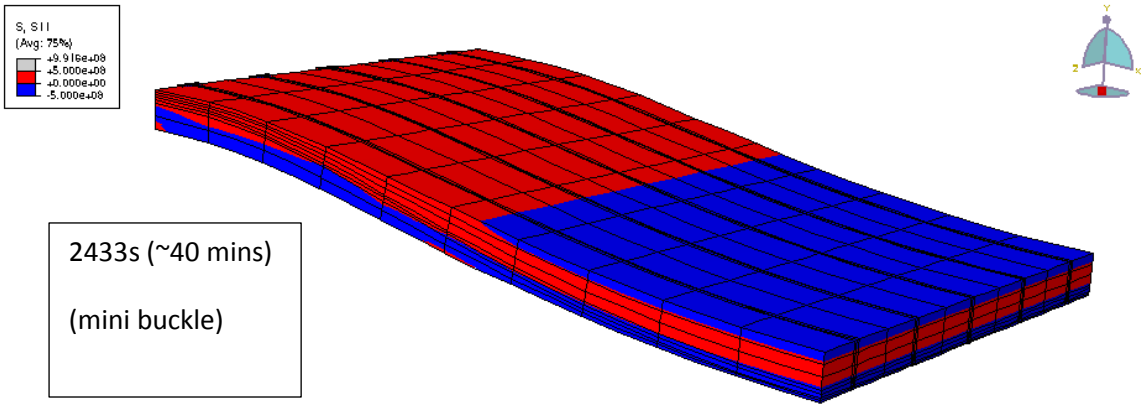

2433s (~40 mins)

(mini buckle)

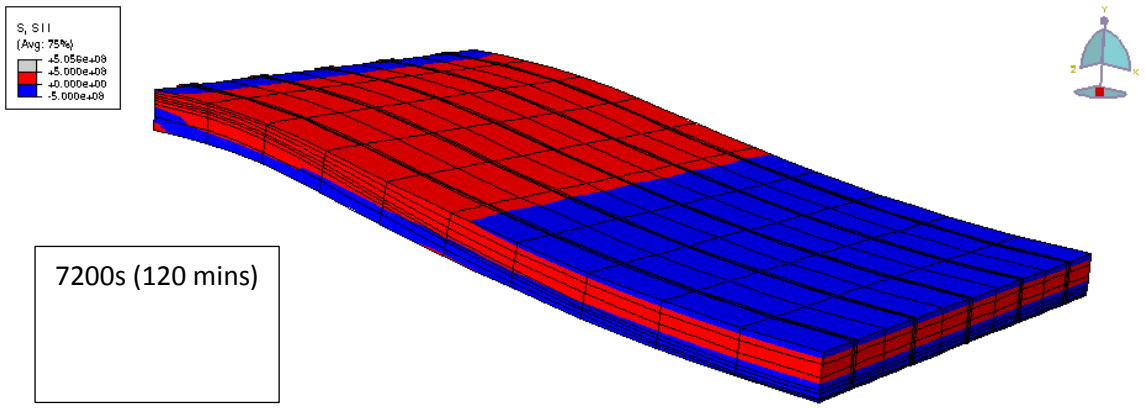

7200s (120 mins)

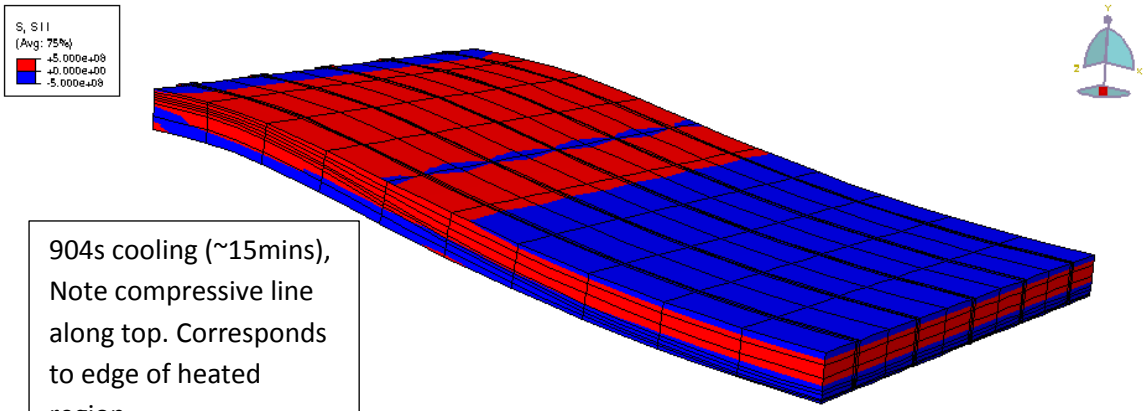

904s cooling (~15mins), Note compressive line along top. Corresponds to edge of heated region

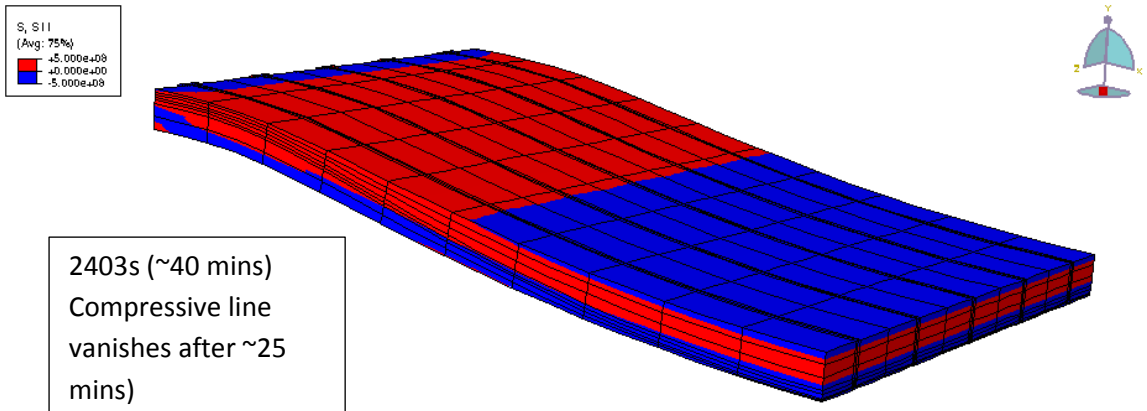

2403s (~40 mins) Compressive line vanishes after ~25 mins)

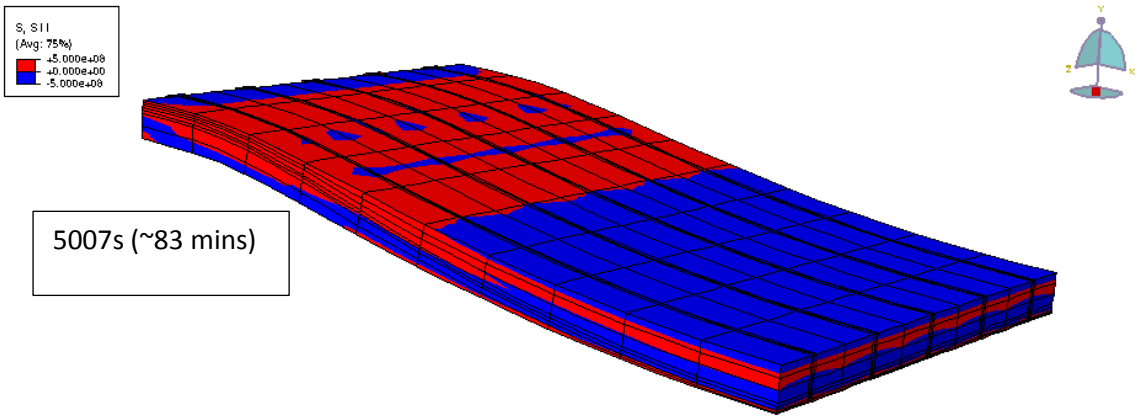

5007s (~83 mins)

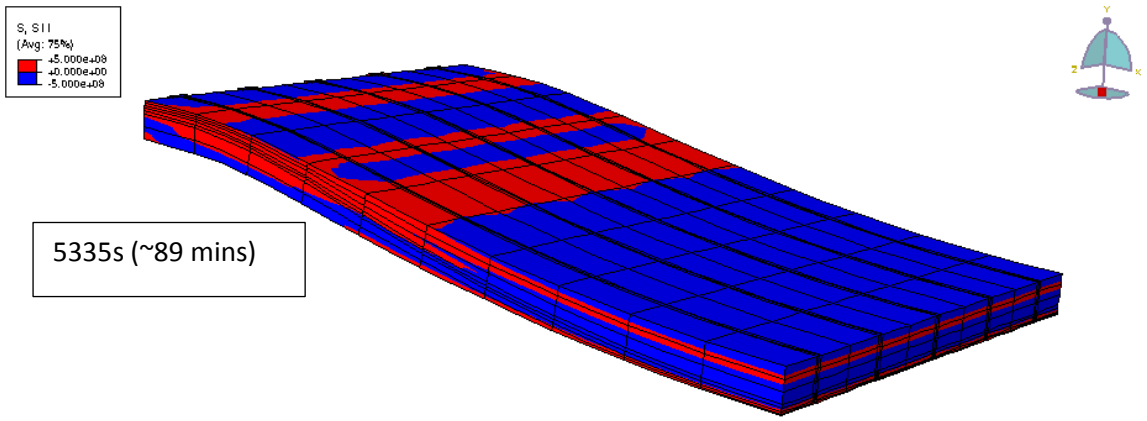

5335s (~89 mins)

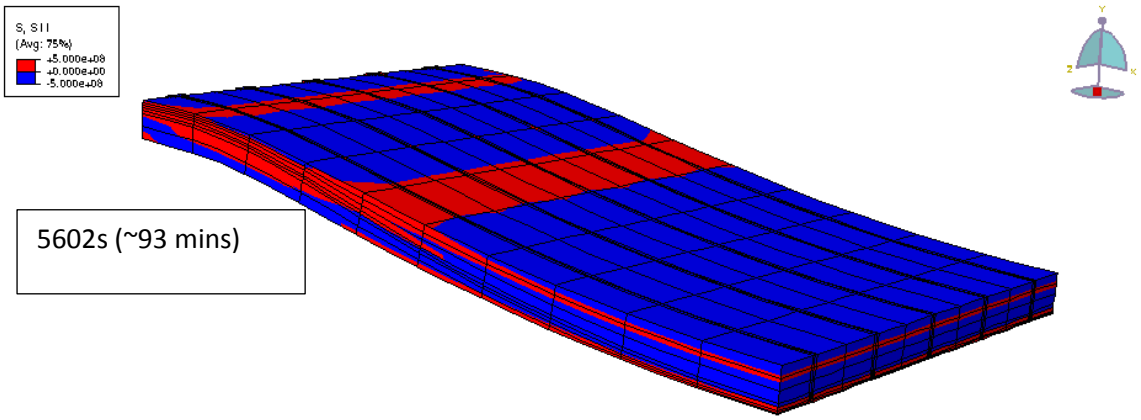

5602s (~93 mins)

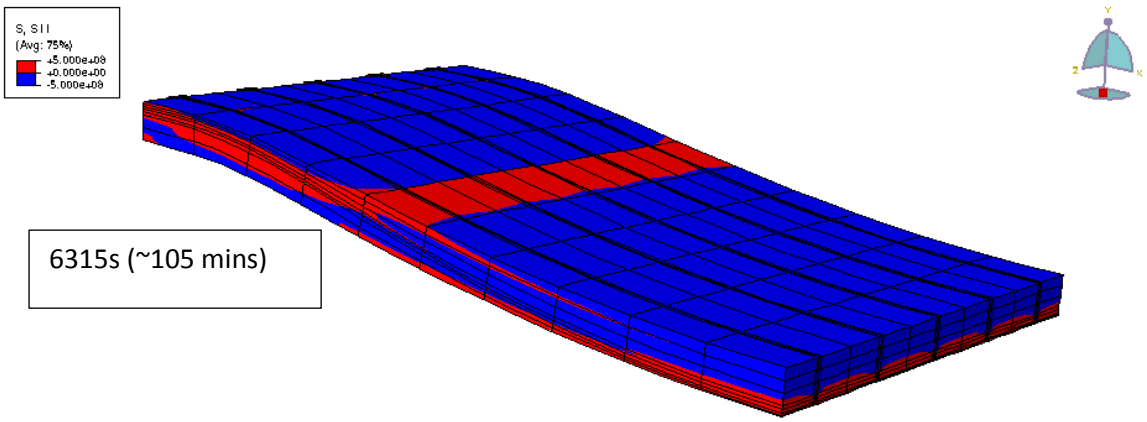

6315s (~105 mins)

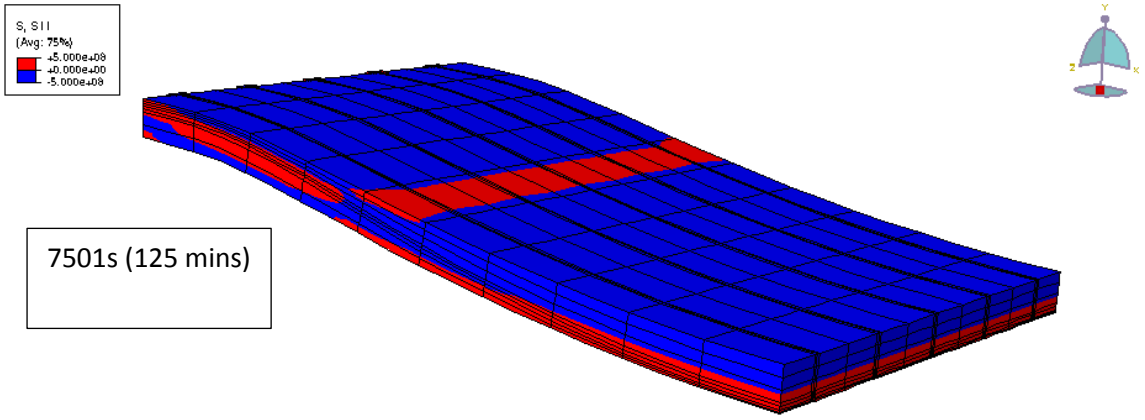

7501s (125 mins)

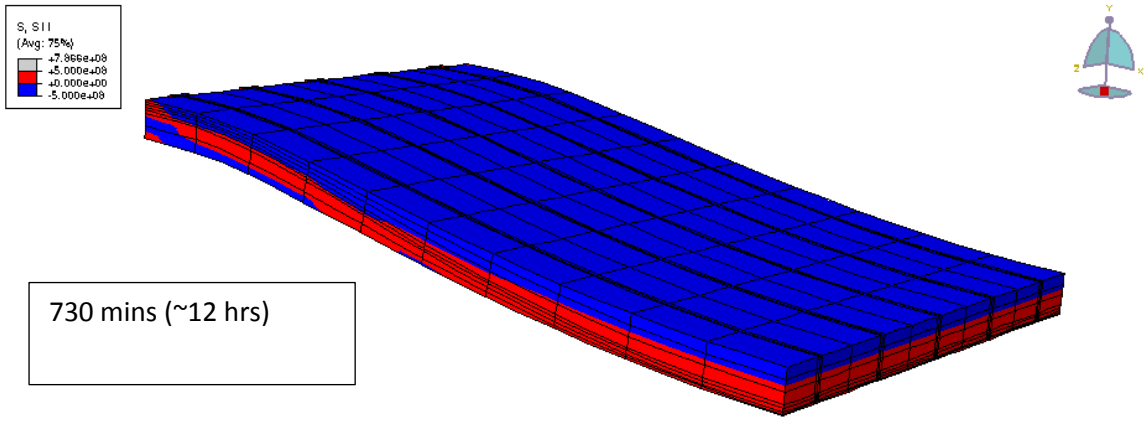

730 mins (~12 hrs)

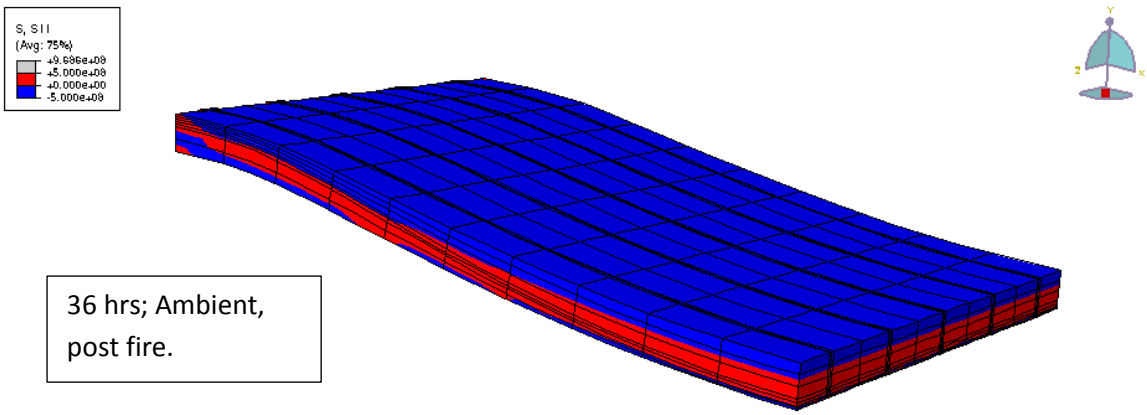

Figure 13-1; Compression tension contour plots top view

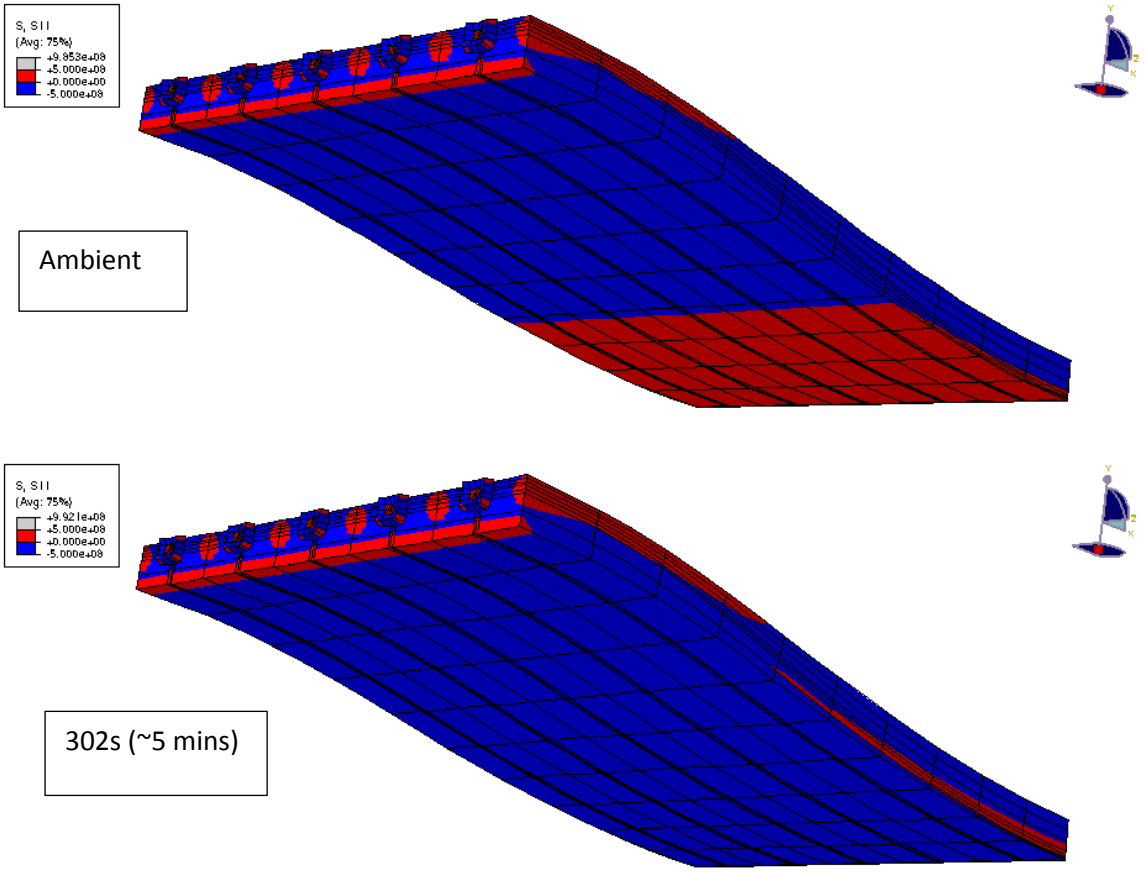

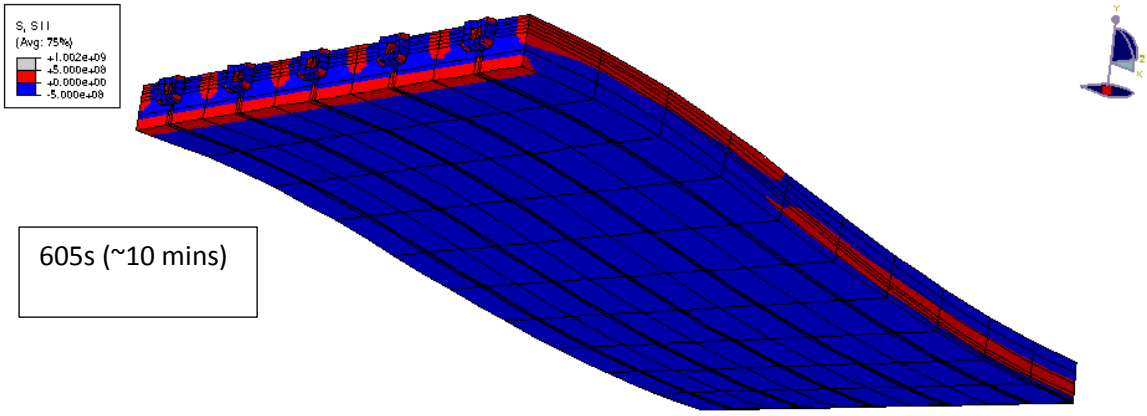

605s (~10 mins)

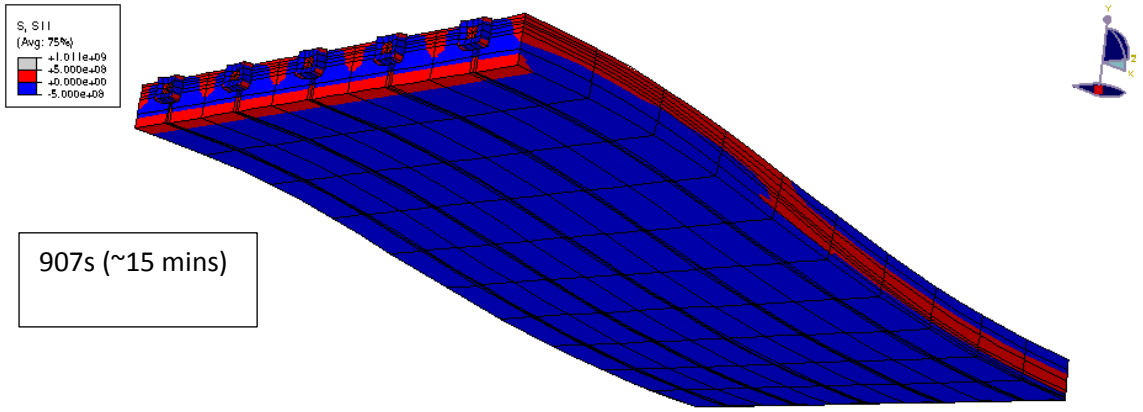

907s (~15 mins)

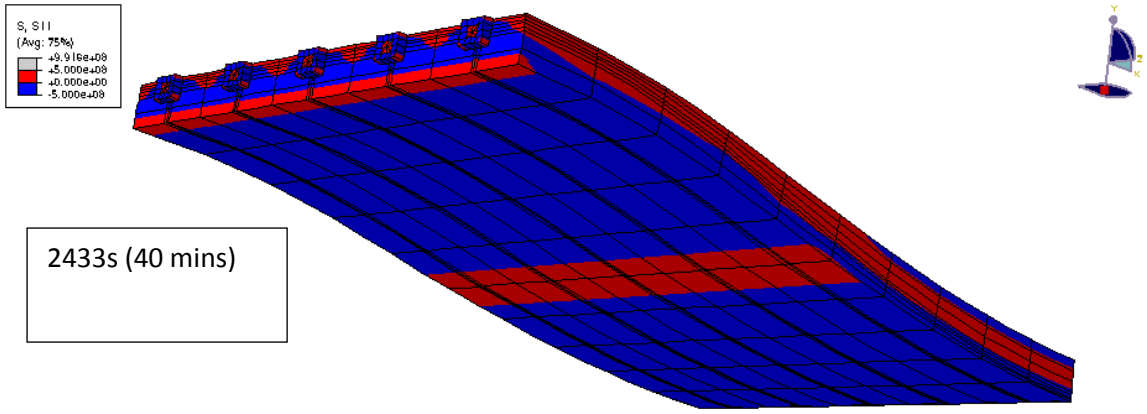

2433s (40 mins)

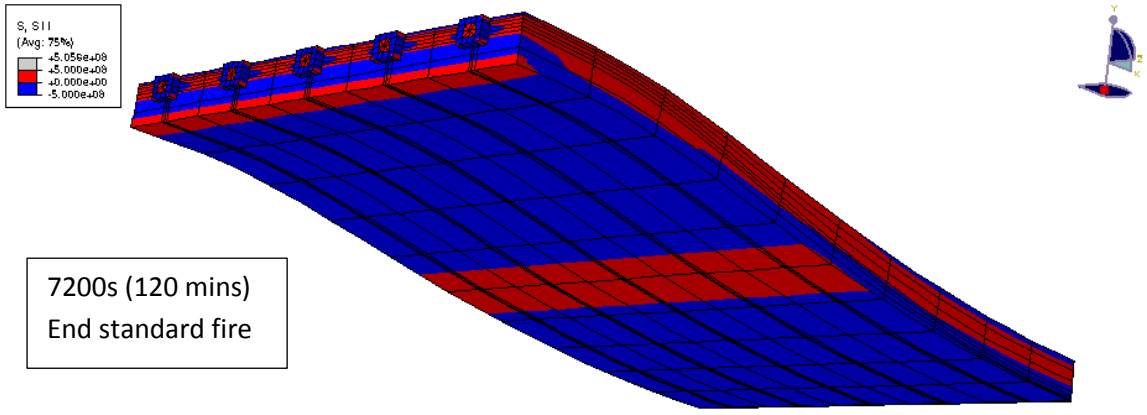

7200s (120 mins)
End standard fire

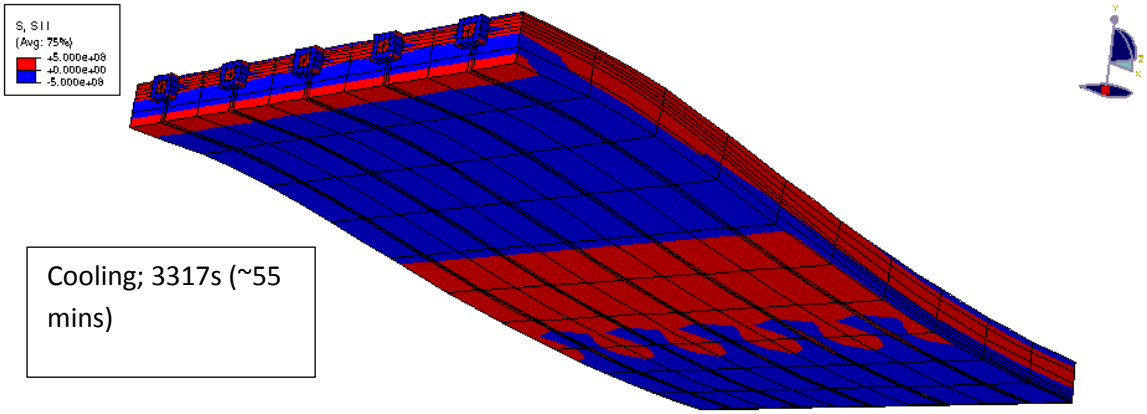

Cooling; 3317s (~55 mins)

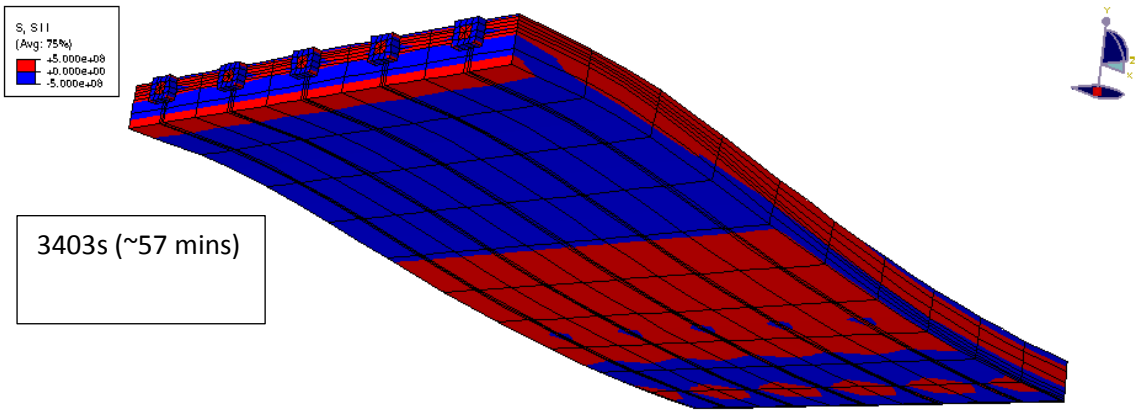

3403s (~57 mins)

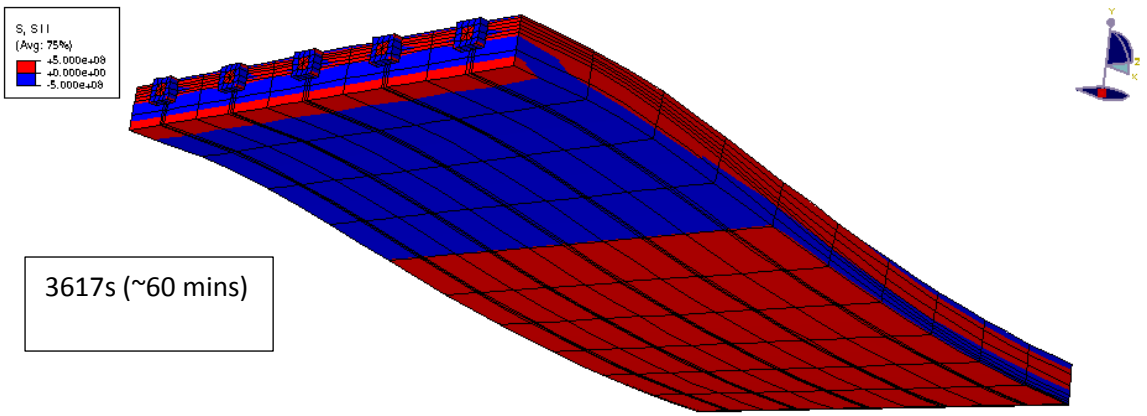

3617s (~60 mins)

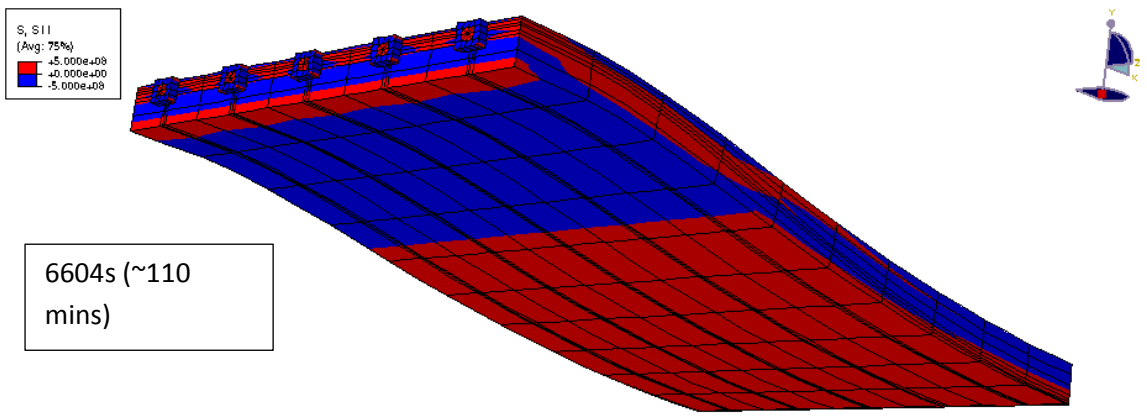

6604s (~110 mins)

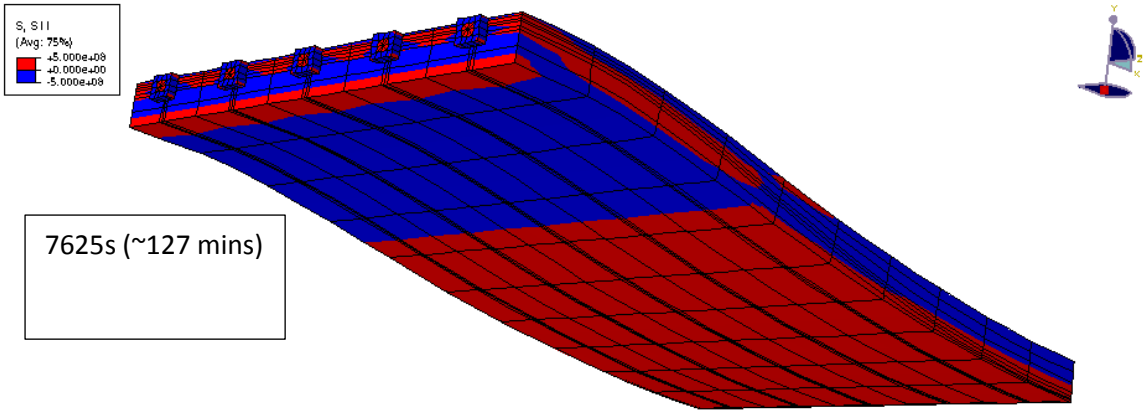

7625s (~127 mins)

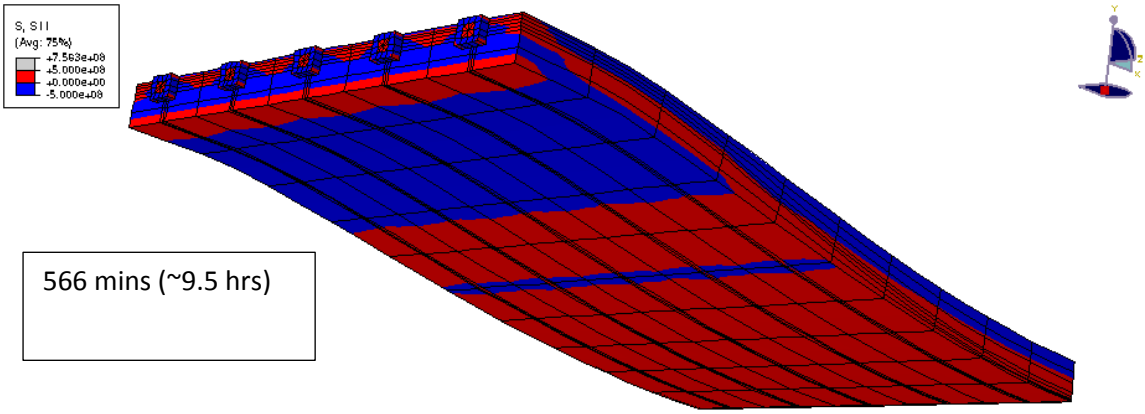

566 mins (~9.5 hrs)

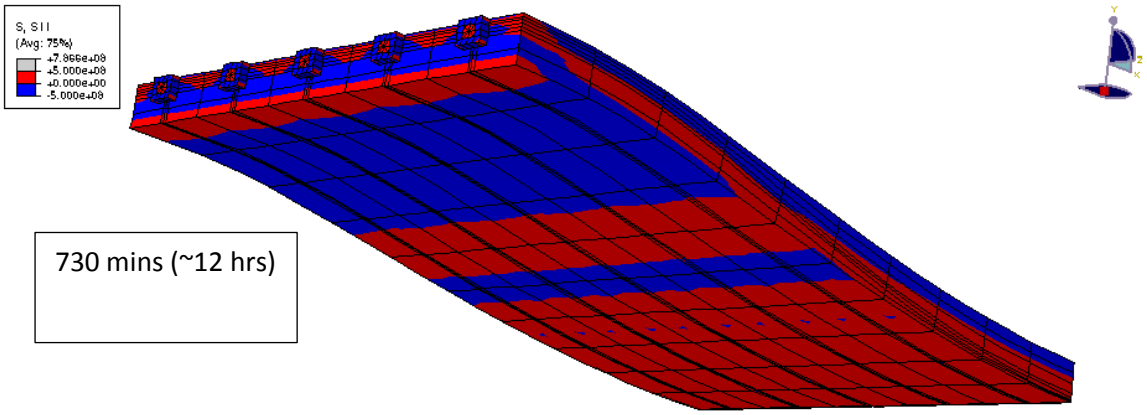

730 mins (~12 hrs)

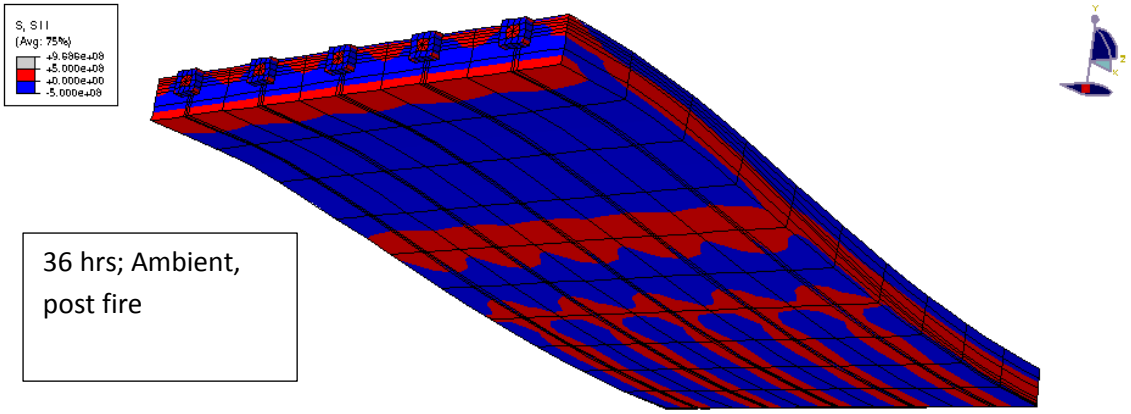

Figure 13-2; Compression tension contour plots bottom view

14 References

[1] ENV-1992-1-2, “Eurocode 2: Design of concrete structures, Part 1-2: General rules-Structural fire design,” European Committee for Standardization, Brussels, 2004.

[2] ACI, “Corrosion and Repair of Unbonded Single Strand Tendons,” American Concrete Institute, Farmington Hills, MI, 1998.

[3] The Concrete Centre, “Post-tensioned Concrete Floors,” 2008.

[4] D. Lee and C. Bailey, “The Behaviour of Post-Tensioned Floor Slabs in Fire Conditions,” in *International Congress on Fire Safety in Tall Buildings*, Santander, Spain, 2006.

[5] I. Stern, “Restoration of long span plate post-tensioned with unbonded tendons,” in *FIB Congress*, Osaka, Japan, 2002.

[6] J. A. Gales, L. Bisby and T. Stratford, “High Temperature Creep Deformation and Failure Behaviour of Prestressing Steel,” in *Proceedings of the 7th International Conference on Structures in Fire*, Zurich, 2012.

[7] T. Z. Harmathy and W. W. Stanzak, “Elevated-Temperature Tensile and Creep Properties of some Structural and Prestressing Steels,” *American Society for Testing and Materials Special Technical Publication,* p. 186, 1970.

[8] T. Z. Harmathy, “A Comprehensive Creep Model,” *Transactions of the ASME Journal of Basic Engineering, Vol 89, Series D, No.3,* pp. 496-502, 1967.

[9] K. MacLean, *Post-Fire Assessment of Unbonded Post-Tensioned Concrete Slabs: Strand Deterioration and Prestress Loss,* Department of Civil Engineering, Queens University, Kingston, ON, Canada, 2007.

[10] ASTM, “A416/A416M-02 Standard Specification for Steel Strand, Uncoated Seven-Wire for Prestressed Concrete,” American Society for Testing and Materials, West Conshohocken, Pa, 2002.

[11] BS EN 5896, “High tensile steel wire and strand for the prestressing of concrete-specification,” BSI, London, 2012.

[12] W. D. Callister, Materials Science and Engineering an Introduction, Seventh Edition, New York: John Wiley & Sons, 2006.

[13] L. Bragg and J. F. Nye, “A Dynamical Model of a Crystal Structure,” in *Proceedings of the Royal Society of London, Vol 190*, 1947.

[14] D. Holmes and A. Bridges, “DoITPoMS,” [Online]. Available: http://www.doitpoms.ac.uk/tlplib/dislocations/printall.php.

[15] H. J. Frost and M. F. Ashby, Deformation Mechanism Maps, Oxford: Pergamon Press, 1982.

[16] Y. Gorash, *Development of a Creep-Damage Model for Non-Isothermal Long Term Strength Analysis of High-Temperature Components Operating in a Wide Stress Range,* Kharkiv: National Technical University , 2008.

[17] B. Babu, *Physically Based Model for Plasticity and Creep of Ti-6Al-4V,* Department of Applied Physics and Mechanical Engineering, Lulea University of Technology, Sweden, 2008.

[18] Dassault Systemes, Abaqus Theory Manual, 2012.

[19] R. P. Feynman, R. B. Leighton and M. Sands, The Feynman Lectures on Physics, Volume II, Addison-Wesley Publishing Company, 1964.

[20] C. M. Young, S. L. Robinson and O. D. Sherby, “Effect of Subgrain Size onthe High Temperature Strength of Polycrystalline Aluminium as Determined by Constant Strain Rate Tests,” *Acta Metallurgica, Vol 23,* pp. 633-639, 1975.

[21] V. Levitin, High Temperature Strain of Metal and Alloys, Weinheim: Wiley VCH, 2006.

[22] O. D. Sherby and P. M. Burke, “Mechanical Behaviour of Crystalline Solids at Elevated Temperature,” *Progress in Material Science,* vol. 13, no. 7, pp. 325-390, 1967.

[23] J. J. Jonas, C. M. Sellars and W. J. M. Tegart, “Strength and Structure Under Hot Working Conditions,” *Metallurgical Review,* vol. 14, pp. 1-24, 1969.

[24] O. D. Sherby and J. E. Dorn , “An analysis of the Phenomenon of High Temperature Creep,” *Proceedings, Society for Experimental Stress Analysis ,* vol. 12, p. 139, 1953.

[25] C. Zener and J. H. Hollomon, “Effect of strain rate upon plastic flow of steel,” *Journal of Applied Physics,* vol. 15, p. 22, 1944.

[26] ASTM, “A421/A421M-02 Standard Specification for Uncoated Stress-Relieved Steel Wire for Prestressed Concrete,” American Society for Testing and Materials, West Conshohocken, Pa, 2002.

[27] BS EN 10020, “Definition and classification of grades of steel,” BSI, London, 2000.

[28] J. A. Gales, L. Bisby and M. Gillie, “Unbonded post-tensioned concrete slabs in fire - Part I - Experimental response of unbonded tendons under transient localized heating,” *Journal of Structural Fire Engineering,* no. 2(3), pp. 139-153, 2011.

[29] Y. Anderberg, “The Impact of Various Material Models on Structural Fire Behaviour,” in *Fifth International Conference on Structures in Fire*, Singapore, 2008.

[30] Dassault Systemes, Abaqus Analysis Users Manual, 2012.

[31] ENV-1991-1-2, “Eurocode 1: Actions on structures, Part 1-2: General actions-Actions on structures exposed to fire,” European Committee for Standardization, Brussels, 2002.

[32] ENV-1992-1-1, “Eurocode 2: Design of concrete structures- Part 1-1: General rules and rules for buildings,” European Committee for Standardization, Brussels, 2004.

[33] J. Lubliner, J. Oliver, s. Oller and E. Onate, “A Plastic-Damage Model for Concrete,” *International Journal of Solids and Structures,* vol. 25, no. 3, pp. 299-326, 1989.

[34] J. Lee and G. L. Fenves, “A plastic-damage concrete model for earthquake analysis of dams,” *Earthquake Engineering and Structural Dynamics,* vol. 27, no. 9, pp. 937-956, 1998.

[35] A. Law and M. Gillie, “Load induced thermal strain; implications for structural behaviour,” in *SiF*, Singapore, 2008.

[36] T. Gernay, “Effect of Transient Creep Strain Model on the Behaviour of Concrete Columns Subjected to Heating and Cooling,” *Fire Technology,* no. 48, pp. 313-329, 2012.

[37] J. A. Gales , *Transient High-Temperature Prestress Relaxation of Unbonded Prestressing Tendons for use in Concrete Slabs,* Department of Civil Engineering, Queens University, Kingston, ON, Canada, 2009.

[38] P. Perzyna, “Fundamental Problems in Viscoplasticity,” *Advances in Applied Mechanics,* pp. 243-377, 1966.

[39] J. L. Chaboche, “A Review of some Plasticity and Viscoplasticity Constitutive Theories,” *International Journal of Plasticity, Vol 24,* pp. 1642-1693, 2008.

[40] ENV-1993-1-2, “Eurocode 3: Design of steel structures, Part 1-2: General rules-Structural fire design,” European Committee for Standardization, Brussels, 2005.